DOCTORAL SCHOOL
UNIVERSITA' *MEDITERRANEA* DI REGGIO CALABRIA

DIPARTIMENTO DI INGEGNERIA DELL'INFORMAZIONE, DELLE INFRASTRUTTURE E DELL'ENERGIA SOSTENIBILE (DIIES)

PHD IN
INFORMATION ENGINEERING

S.S.D. FIS/01
XXXI CICLO

ETHANOL-CVD GROWTH OF LARGE SINGLE-CRYSTAL GRAPHENE AND GRAPHENE-BASED DERIVATIVE FOR PHOTOVOLTAIC APPLICATIONS

CANDIDATE
Andrea GNISCI

ADVISOR
Dr. Giuliana FAGGIO

COORDINATOR
Prof. Tommaso ISERNIA

REGGIO CALABRIA, FEBRARY 2019

Finito di stampare nel mese di **Febbraio 2019**

Edizione

Quaderno N. 41
Collana *Quaderni del Dottorato di Ricerca in Ingegneria dell'Informazione*
Curatore *Prof. Tommaso Isernia*

ISBN 978-88-99352-32-5

Università degli Studi *Mediterranea* di Reggio Calabria
Salita Melissari, Feo di Vito, Reggio Calabria

Andrea Gnisci

ETHANOL-CVD GROWTH OF LARGE SINGLE-CRYSTAL GRAPHENE AND GRAPHENE-BASED DERIVATIVE FOR PHOTOVOLTAIC APPLICATIONS

The Teaching Staff of the PhD course in
INFORMATION ENGINEERING
consists of:

Tommaso ISERNIA (coordinator)
Giovanni ANGIULLI
Pier Luigi ANTONUCCI
Giuseppe ARANITI
Francesco BUCCAFURRI
Rosario CARBONE
Riccardo CAROTENUTO
Salvatore COCO
Maria Antonia COTRONEI
Claudio DE CAPUA
Francesco DELLA CORTE
Aimè LAY EKUAKILLE
Giuliana FAGGIO
Fabio FILIANOTI
Patrizia FRONTERA
Sofia GIUFFRE'
Antonio IERA
Gianluca LAX
Giacomo MESSINA
Antonella MOLINARO
Andrea Francesco MORABITO
Rosario MORELLO
Fortunato PEZZIMENTI
Sandro RAO
Domenico ROSACI
Giuseppe RUGGERI
Maria Teresa RUSSO
Valerio SCORDAMAGLIA
Domenico URSINO
And also:
Antoine BERTHET
Dominique DALLET
Lubomir DOBOS
Lorenzo CROCCO
Ivo RENDINA
Groza VOICU

…to my dearly loved sister, Daniela

"To Infinity and Beyond!"
Buzz Lightyear
of Star Command

Contents

CONTENTS .... **I**

LIST OF FIGURES .... **III**

INTRODUCTION **1**

GRAPHENE **5**

1.1 INTRODUCTION 5
1.2 THE PHYSICS OF GRAPHENE 6
1.2.1 CARBON HYBRIDIZATION OF GRAPHENE *6*
1.2.2 GRAPHENE CRYSTAL STRUCTURE *8*
1.2.3 THE BAND STRUCTURE OF GRAPHENE *10*
1.3 GRAPHENE PROPERTIES 14
1.3.1 ELECTRONIC TRANSPORT PROPERTIES OF GRAPHENE *14*
1.3.2 SCATTERING IN GRAPHENE *15*
1.3.3. OPTOELECTRONIC PROPERTIES OF GRAPHENE *16*
1.3.4 THERMAL CONDUCTIVITY IN GRAPHENE *18*
1.3.5 PHYSICAL PROPERTIES OF GRAPHENE *19*
1.3.6 CHEMICAL AND SURFACE PROPERTIES *19*
1.4 GRAPHENE SYNTHESIS 20
1.4.1 MECHANICAL EXFOLIATION *21*
1.4.2 LIQUID PHASE EXFOLIATION *22*
1.4.3 EPITAXIAL GROWTH ON SIC *23*
1.4.4 CHEMICAL VAPOUR DEPOSITION (CVD) *25*
1.4.5 OTHER GROWTH METHODS *29*
1.5 TRANSFER OF CVD GRAPHENE 30

CHARACTERIZATION TECHNIQUES **33**

2.1 INTRODUCTION 33
2.2 OPTICAL MICROSCOPY 34
2.3 SCANNING ELECTRON MICROSCOPY (SEM) 35
2.4 MICRORAMAN SPECTROSCOPY 38
2.4.1 PRINCIPLES OF RAMAN SPECTROSCOPY *39*
2.4.2 RAMAN FEATURES OF GRAPHENE *47*
2.5 ATOMIC FORCE MICROSCOPY (AFM) 51
2.5.1 PROBING FORCES WITH A CANTILEVER *54*
CANTILEVER MOTION DETECTION *55*
NOISE CONSIDERATIONS AND OPTIMAL RESOLUTION *56*
2.5.2 MODE OF OPERATION *57*
CONTACT MODE AFM (C-AFM) *57*
NON-CONTACT MODE AFM (NC-AFM) *58*
ATTRACTIVE AND REPULSIVE FORCES *59*
TAPPING MODE AFM *61*
AMPLITUDE MODULATION AFM *62*
FREQUENCY MODULATION AFM *63*
2.5.3 ANOMALIES IN THICKNESS MEASUREMENTS OF GRAPHENE BY TM-AFM *65*
2.5.4 SIMULTANEOUS AFM-RAMAN *70*
2.6 KELVIN PROBE FORCE MICROSCOPY (KPFM) 71
2.7 GRAPHENE FIELD EFFECT TRANSISTOR (GFET) FOR MOBILITY MEASUREMENTS 73
2.8 SOLAR CELL CHARACTERIZATION 76
2.8.1 EXTERNAL QUANTUM EFFICIENCY (EQE) *76*
2.8.2 PHOTOVOLTAIC PARAMETERS *77*

ETHANOL-CVD SYNTHESIS OF LARGE GRAPHENE DOMAINS **81**

3.1 INTRODUCTION 81
3.2 THE CVD SYSTEM AT ENEA 84
3.3 OPTIMIZED CYCLODODECANE-BASED GRAPHENE TRANSFER METHOD 86
3.4 INITIAL STAGES OF THE GROWTH OF GRAPHENE 91
3.5 LARGE GRAPHENE DOMAINS GROWTH 94
3.5.1 NUCLEATION DENSITY REDUCTION 94
3.5.2 EFFECT OF ETHANOL FLOW: TOWARDS LARGE GRAPHENE GRAINS 97
3.5.3 HIGH-TEMPERATURE GROWTH OF LARGE GRAPHENE GRAINS 100
3.5.4 ELECTRICAL PROPERTIES OF SUB-MM GRAPHENE GRAINS BY ETHANOL-CVD 102

GRAPHENE BASED DERIVATIVE INTERLAYER IN GRAPHENE ON SILICON SCHOTTKY BARRIER SOLAR CELLS 105

4.1 INTRODUCTION 105
4.2 THE SCHOTTKY JUNCTION 107
4.2.1 THE SCHOTTKY BARRIER 108
4.2.2 THERMIONIC EMISSION AND I–V CHARACTERISTIC 114
4.2.3 ANALYSIS OF I-V CHARACTERISTIC 119
4.3 GRAPHENE ON SILICON SCHOTTKY JUNCTION WITH GBD INTERLAYER 120
4.3.1 GRAPHENE ON SILICON SCHOTTKY JUNCTION 120
4.3.2 THE INTERFACE ENGINEERING IN SCHOTTKY JUNCTION 125
4.3.3 DEVICE REALIZATION 126
SUBSTRATE PREPARATION 126
FILMS GROWTH AND TRANSFER ON SUBSTRATE 129
4.3.4 GBD AND FEW LAYER GRAPHENE CHARACTERIZATION 132
4.4 SOLAR CELL CHARACTERIZATION 135
4.4.1 ELECTRICAL CHARACTERIZATION 135
4.4.2 PHOTOVOLTAIC CHARACTERIZATION 138
4.5 DOPING TREATMENT 139

CONCLUSIONS 144

REFERENCES 147

LIST OF PUBLICATIONS 187

ACKNOWLEDGMENTS 189

List of Figures

Figure 1.1. The carbon family and the considered material dimensionality. (a) Diamond (3D) (b) Graphite (3D) (c) Fullerenes (0D) (d) Nanotube (1D) (e) Graphene (2D)....6
Figure 1.2. The orbital evolution from a ground state energy carbon atom to a sp^2 hybridised graphene atom....8
Figure 1.3. (a) The honeycomb lattice of graphene showing the two sublattices marked A and B [7]. (b) Lattice structure of graphene showing the two sublattices marked A and B; a_1 and a_2 the lattice unit vectors; δi i=1, 2, 3 the nearest neighbor vectors [6]. 9
Figure 1.4. First Brillouin zone of graphene with the reciprocal lattice vectors defined as b1 and b2. High symmetry k-points are labelled as Γ, M, K and K' [6]. 10
Figure 1.5. Band structure of graphene. In the vicinity of the Dirac points at the two nonequivalent corners K and K' of the hexagonal Brillouin zone, the dispersion relation is linear and hence locally equivalent to a Dirac cone [8]. The energy dispersion is a function of the wavevector components kx and ky, as obtained from Eq. 1.3. Valence (π) and conduction bands ($\pi *$) are seen touching at the Fermi level at the K and K' points with a linear conical relation among them. 12
Figure 1.6. (a)Calculated density of states of graphene. Close to the Fermi level, the density of states ϱ(ε), is linear with respect to the energy [6]. (b) Ambipolar transport characteristic of graphene. Field induced by gate voltage, Vg can control concentration and polarity of charge carriers. Positive (negative) gate voltage increases Fermi level increasing carrier concentration of holes (electrons) [11] 15
Figure 1.7. Scan profile showing the intensity of transmitted white light through air, single layer and bilayer graphene respectively [35].... 17
Figure 1.8. (a) Transmittance for different transparent conductors and (b) thickness dependence of the sheet resistance [10]. 18
Figure 1.9. Graphene quality vs mass production cost of different graphene fabrication methods [68].... 21
Figure 1.10. (a) Scotch tape mechanical exfoliation [70], (b) Exfoliated graphene on 300 nm thick SiO_2, the number of layers increases with flake contrast, the number of layers are labelled, image adapted from [71]. 22
Figure 1.11. Liquid phase exfoliation technique [70]. 23
Figure 1.12. Growth on SiC. Gold and grey spheres represent Si and C atoms, respectively [70]. 24
Figure 1.13. Schematic representation of graphene mechanism growth (a) precipitation over Ni substrate and (b) adsorption over Cu substrate.

The growth mechanisms have been studied by the use of two different carbon isotopes ^{12}C ^{13}C [88]. 27
Figure 1.14. (a) Sketch of CVD system. (b) Time dependence of experimental parameters: temperature, pressure and composition/flow rate for graphene growth by methane (CH_4) in hydrogen (H_2) flow [54]. 29
Figure 1.15. The wet PMMA support layer transfer process. a) Graphene grown via CVD on metal substrate. b) PMMA is spin coated onto the graphene surface. c) The metal growth substrate is etched away. d) The target substrate is used to scoop the graphene/PMMA sample out. e) The graphene/PMMA is allowed to dry to the target substrate surface. f) The PMMA is removed with a solvent or annealing [67]. 31
Figure 2.1. Optical image of graphene (a) on Si/SiO_2 and (b) on copper substrates. 35
Figure 2.2. Schematic diagram of ray traces in a typical SEM, ray divergence is exaggerated for clarity. 36
Figure 2.3. (a) Interaction of Radiation-matter interaction processes: backscattered electrons, secondary electrons, X-rays and Auger electrons and their creation mechanisms; (b) Schematic diagram of the interaction volume for electrons incident on a material. The penetration of electrons to different depths produces different imaging signals. Adapted from references [127].- 37
Figure 2.4. SEM micrographs of graphene on copper substrate: single and multilayer graphene on copper. Scale bar represents 20μm [129]. 38
Figure 2.5. Raman spectrum of carbon tetrachloride showing Rayleigh, Stokes and anti-Stokes Raman bands. 41
Figure 2.6. Schematic representation of quantum energy transitions for Rayleigh and Raman scattering. 42
Figure 2.7. Diatomic linear lattice with M_1 and M_2 atoms mass and lattice spacing 2a. 44
Figure 2.8. Dispersion curve in biatomic crystal. Optical and acoustical branches are shown. 45
Figure 2.9. Phonon dispersion relation of graphene showing the iLO, iTO, oTO, iLA, iTA and oTA phonon branches [136]. 46
Figure 2.10. Role of the electron dispersion (Dirac cones, shown by solid black lines) in Raman scattering: (a) intravalley one-phonon G peak, (b) defect-assisted intravalley one-phonon D peak, (c) intravalley two-phonon 2D peak, (d) defect assisted intervalley one-phonon D' peak, (e) intervalley two-phonon 2D' peak. Vertical solid arrows represent interband transitions accompanied by photon absorption (upward arrows) or emission (downward arrows) [140]. 48
Figure 2.11 Carbon motions in the G modes namely E_{2g} and D modes namely A_{1g} [134]. 48
Figure 2.12. Typical Raman spectrum of graphene showing the main Raman features, the D, G and 2D bands. 49
Figure 2.13. Sketch of an AFM probe showing the tip's radius of curvature r_c 53
Figure 2.14. AFM image of graphene film: (a) image with artefacts due to contaminations of the sample that can damage the tip, (b) same

graphene film region after measurement post-processing. In (b) the artefact due to the tip are eliminated and tears in the film are visible........ 54
Figure 2.15. Diagram of a piezoelectric actuator exciting a cantilever, the oscillatory motion of the cantilever is indicated... 55
Figure 2.16. Sketch the laser beam deflecting onto the quadrant photodiode......... 56
Figure 2.17. Diagram of a contact mode AFM, the cantilever scans across the sample whilst in direct contact with the sample. 57
Figure 2.18. Resonance curve for a single harmonic oscillator (solid line) and under the influence of attractive and repulsive forces (dashed lines), A = oscillation amplitude. 58
Figure 2.19. Sketch of the force exerted on the tip of the AFM cantilever by the surface, F_{ts}, versus tip-sample separation distance, z, illustrating the repulsive and attractive regimes. 60
Figure 2.20. Sketch of tip oscillation in tapping-mode AFM...................................... 61
Figure 2.21. Schematic illustration of non-contact AFM operation mode: (a) Amplitude modulation mode and (b) Frequency modulation mode. Both AM and FM modes maintain constant tip–sample separation. AM mode uses oscillation amplitude changes as a feedback signal while FM mode uses frequency changes as feedback signal [160]. 65
Figure 2.22. Typical measured thickness of graphene as a function of RH. The RH range is divided into three approximate sections: Low, Middle, and High RH [161]. 68
Figure 2.23. Structure of exfoliated FLG trapping the water adlayer on the oxide substrate. Figure not shown to scale [161]. 69
Figure 2.24. Schematic mechanism of improving AFM imaging accuracy with increasing peak force set point. As the pressure applied increases from (a) low to (b) medium to (c) high the AFM tip is able to disrupt the underlying buffer layer and subsequently measure a more accurate value for graphene height [170]. 69
Figure 2.25. (a) AFM and Raman instrumentation Schematic of AIST-NT SPM AFM integrated with LabRamHR Evolution HORIBA Scientific Raman system allowing for the capture of simultaneous AFM-Raman. (b) The Raman laser (red shaded area) and AFM probe (blue) are both focused onto the same area of the sample and held in a fixed position. The z position of the stage is controlled by phase feedback from the probe, the stage is then moved in the x-y direction when scanning the sample. 70
Figure 2.26. Electronic energy levels of the sample and AFM tip for three cases: (a) tip and sample are separated by distance d with no electrical contact, (b) tip and sample are in electrical contact, and (c) external bias (V_{dc}) is applied between tip and sample to nullify the CPD and, therefore, the tip–sample electrical force. E_v is the vacuum energy level. E_{fs} and E_{ft} are Fermi energy levels of the sample and tip, respectively. 72
Figure 2.27. Schematic cross section of a GFET [207]. 73
Figure 2.28. Ideal drain current versus gate voltage... 74
Figure 2.29. FET transfer characteristics showing I_D (on a logarithmic scale on the left and a linear scale on the right) versus the gate–source

voltage V_{GS}. Above threshold, the change in I_D for a given change in V_{GS} is called the terminal transconductance, g_{mt} [61]. 76
Figure 2.30. J-V curves acquired under illumination with photovoltaic parameters.. 77
Figure 2.31. The effects of series and shunt resistance on the J-V curve. Optimal values are R_{series} = 0 ohm cm^2 and R_{shunt} = ∞ ohm cm^2................ 80
Figure 3.1. Scheme of CVD apparatus at ENEA. 84
Figure 3.2. Temperature-time profile during a typical growth. (I) Insertion in the chamber, (II) evacuation and setting of the gas flows for annealing (Ar, H_2), (III) insertion in the furnace hot zone and annealing, (IV) growth, (V) extraction from the hot zone and rapid cooling under Ar, (VI) filling with Ar and extraction from the chamber. Adapted from [227].. 86
Figure 3.3. 10X optical image of cyclododecane diluted in hexane (a) 20mg/ml and (b) 200mg/ml spin coated at 1000rpm for 40s.. 88
Figure 3.4. Scheme of cyclododecane transfer method process of graphene, from Cu native substrate to Si/SiO_2 substrate. 89
Figure 3.5. (a) Monolayer graphene films and (b) graphene islands transferred with different concentration 0f 40%, 44% and 50% of CDD in hexane. 89
Figure 3.6. (a) and (b) AFM characterization of monolayer graphene film and graphene islands, respectively, (c) and (d) Raman maps of I_D/I_G and I_{2D}/I_G ratios of monolayer graphene film and graphene islands, respectively.. 90
Figure 3.7. Schematic representation of reduction of nucleation density and increase of crystallinity... 91
Figure 3.8. Raman spectra of graphene samples grown in the conditions of Table 3.1; the graphene was grown in different conditions (Temperature, growth time, pressure, flow of ethanol) [251]. 92
Figure 3.9. Graphene grown at 1070°C and 65 Pa for 15 s with (a-c) Q_{eth} = 0.1 sccm and (d-f) Q_{eth} = 1.5×10^{-2} sccm with g) averaged Raman spectra. (a,d) SEM micrographs of the as-grown graphene on the Cu substrates. (b,c) Raman mapping images (50 x 50 μm in size, 0.5 μm resolution) for A_D/A_G and I_{2D}/I_G after transfer on SiO_2/Si. The blue arrow indicates tear caused by transfer. (e,f) Raman mapping images (17 x 17 μm in size, 0.25 μm resolution) for A_D/A_G and I_{2D}/I_G of graphene islands after transfer on SiO_2/Si. The sample is composed of isolated monolayer graphene grains of 1 - 3 μm with smaller disorder level [251]. 93
Figure 3.10. (a) AFM image of the graphene grains on copper foil facets (t = 15 s, T = 1070 °C, P = 65 Pa, and Q_{eth} = 1.5×10^{-2} sccm). (b) Higher resolution AFM image of a single grain on Cu. Some grains show hexagonal shape with rounded corners. c) AFM image after transfer on SiO_2/Si. (d) Height profile from (c) shows a step of 0.8 nm [251]. 94
Figure 3.11. Nucleation density of graphene grown on Cu substrate with different pre-oxidation (250°C in air) time (t_{OX}) ranging from 0 to 150 min. (a-e) Optical microscopy of the graphene grown on Cu in

the various cases. (f) Nucleation density trend *vs* pre-oxidation time. Adapted by [251]. 95
Figure 3.12. (a-c) Nucleation density of graphene grown on pre-oxidized Cu substrate (250°C in air for 150min) with different pre-growth Ar annealing times (t_{ann}). Isolated grains grew only with 1 min Ar annealing, while in the other cases continuous films grew. Adapted by [251]. 96
Figure 3.13. (a) AFM image of pre-oxidized Cu foil, (b) the effect of oxygen on copper. Reprinted from [256]. 97
Figure 3.14. Optical images of graphene (30 min, 1000° C, 130 Pa) grown on pre-oxidized Cu foil with (a) 1.5×10^{-2} sccm and (b) 1.5×10^{-3} sccm of ethanol. (c) The corresponding Raman spectra. [251] 98
Figure 3.15. Analysis of a 50-μm grain (sample P2) after transfer onto Si/SiO_2. (a) Optical micrograph of the grain, (b) AFM topography image with thickness line profile of ~ 1 nm. The value is larger than the inter-plane spacing of graphite (0.335 nm) due to intercalated molecules and to the interaction forces between graphene-substrate-tip, as found for CVD-graphene in similar experimental and environmental (relative humidity) conditions [161]–[163]. Raman mapping images of (b) A_D/A_G and (c) I_{2D}/I_G peak ratio (60 μm × 60 μm area, 0.5 μm spatial resolution) [251]. 99
Figure 3.16. Optical and SEM images of the single-crystal graphene grains grown at 1070 °C with 1.5×10^{-3} sccm of ethanol: (a) 130 Pa, 30 min (P3); (b) 400 Pa, 30 min (P4); (c) 400Pa, 60 min (P5). (d) Raman spectra of the samples transferred onto Si/SiO_2[251]. 100
Figure 3.17. Analysis of a 350-μm graphene grain (P5: 1.5×10^{-3} sccm ethanol, 1070° C, 130 Pa, 60 min). (a) SEM image and (b) AFM topography image with thickness line profile of the grain edge. Raman mapping images of (c) A_D/A_G and (d) I_{2D}/I_G [251]. 101
Figure 3.18. Optimization steps performed to reduce nucleation density δ_n according to Table 1. Grain size and A_D/A_G are also reported. 102
Figure 3.19. (a) Optical image of graphene devices with TLM geometry. (b) Transfer curve (I_D-V_G) of a representative graphene device. The inset shows the output curves (I_D-V_D) at different gate voltages. (c) Histogram of field-effect mobilities measured from eleven graphene devices [251]. 103
Figure 4.1. (a) Work function Φ_M and Fermi energy E_{FM} in a metal and (b) work function Φ_S, electron affinity X and band structure with a bandgap between E_c and E_v and Fermi energy E_{FS} in a n-type semiconductor. (c) Charge at the metal/semiconductor junction. (d) Schematics of equilibrium band diagram for the junction. The junction is set at x = 0. Φ_i is the energy barrier to the flow of electrons (black dots) from the semiconductor to the metal, while Φ_B is the Schottky barrier height (SBH) for the electron flow in the opposite direction. w is the extension of the depletion layer. (e) Schematics of equilibrium band diagram of a metal with a p-type semiconductor under the assumption that $\Phi_M < \Phi_S$ (empty circles represent holes). [270] 110

Figure 4.2. Energy band diagram between a metal surface and vacuum, showing (red continuous line) how the application of an external electric field E lowers the effective barrier height by the amount $\Delta\Phi_B$ 113
Figure 4.3. (a) Principal transport processes across a Schottky junction: TE = thermionic emission, TFE = thermionic field emission, FE = field emission and electron–hole recombination. (b) Schematic of the voltage bias of the junction. (c) Ideal I–V characteristic of a Schottky junction. (d) Band diagrams at the ideal metal/n-type semiconductor Schottky junction in forward bias (V > 0) and in (e) reverse bias (V < 0). The arrows associated with currents in (d) and (e) indicate the direction of the electron flow [270]. 114
Figure 4.4. Band diagrams of an ideal Gr/Si junction at (a) zero, (b) forward and (c) reverse bias [270]. 121
Figure 4.5. Schematic representation of the e-beam evaporator. 128
Figure 4.6. Schematic illustration of (a) silicon wafer, (b) PDMS mask 3 mm of side on the silicon substrate, (c) SiO_2 layer surrounding the silicon window, (d) hollow squared and 5 mm of side PDMS masks on the substrate, (e) Cr-Au evaporated contact, (f) final device. 129
Figure 4.7. The inductively heated CVD reactor used to grow FLG and GBD 130
Figure 4.8. (a) Silicon substrate with HF on active area just before the layers transfer, (b) Schematic illustration of the fabricated devices left, reference solar cell based on FLG/n-Si junction (FLG/n-Si), right, solar cell with single GBD between single FLG and n-Si (FLG/GBD/n-Si) [351]. 131
Figure 4.9. (a) Raman spectra of FLG and GBD, (b) AFM measurement on FLG/GBD stack on Si/SiO2 with relative height profile, (c) transmittance of FLG/GBD stack onto quartz substrates, compared with transmittance of graphene, (d) scanning work function of FLG onto Si substrate [351]. 133
Figure 4.10. (a) AFM and (b) CPD maps, Raman mapping images of (c) 2D intensity, (d) I_D/I_G and (e) I_{2D}/I_G. 134
Figure 4.11. (a) Experimental setup, (b) Dark ln(J)-V characteristics with corresponding lnJ-V curves (inset) and (c) plots of dV/dln(I) versus I for FLG/n-Si (blue), FLG/GBD/n-Si (red) and FLG/2GBD/n-Si SBSCs (black curve) SBSCs [351]. 135
Figure 4.12. Schematics of band diagrams for (a) FLG/n-Si, (b) FLG/GBD/n-Si and (c) FLG/2GBD/n-Si SBSCs [351]. 136
Figure 4.13. EQE curves without (a) and with (b) OB of G /n-Si (blue) and FLG/GBD/n-Si (red) SBSCs [351]. 138
Figure 4.14. Schematic diagrams of the Gr/Si solar cell and HNO_3 doping. Adapted from [364]. 139
Figure 4.15. G-2D Correlation map for GBD layer. The solid black line and the solid grey line represent the pure strain and pure doping, respectively. The dashed line represent the projection on strain and doping axes [351]. 140
Figure 4.16. J-V curve of FLG/GBD/n-Si under illumination in standard condition, before and after doping treatment with HNO_3 [351] 141

Figure 4.17. Doping, ageing and recovery effect on illuminated J-V curve of FLG/GBD/n-Si SBSC: before the doping (blue), immediately after doping (red), after 2 hours (light) and after re-doping process (green) 142

Introduction

The discovery of graphene unquestionably marks the beginning of a new era in electronics and optoelectronics. Graphene, a single layer of graphite, was the first two dimensional (2D) material to be isolated in 2004 by K. Novoselov and A.K. Geim and their team at Manchester University. Its unique and outstanding properties spurred the scientific community to produce many other forms of graphene derivatives vastly extending the already broad range of graphene applications.

Although it has been almost 15 years, the expected disruptive impact of such materials is still to come, due to current limitations related to the production and processing. Electronic-grade graphene is usually achieved in single-crystal samples obtained by mechanical exfoliation, but it has proven hard to match those properties in large-area samples produced by even the most advanced techniques, such as chemical vapor deposition (CVD).

The CVD growth process involves the catalytic decomposition of a carbon source both in vapor and liquid phase, such as methane or ethanol, on a transition metal. CVD samples are typically made of polycrystalline graphene, and the presence of grain boundaries are known to have a negative impact on graphene's physical properties, such as mobility, electron conductivity, and mechanical strength. For this reason, an extensive effort was devoted to suppress the formation of grain boundaries and increase the size of graphene grains, mainly by decreasing the nucleation density. If a few graphene *nuclei* are widely spaced, they can grow as isolated single crystals and eventually merge into a continuous graphene film with reduced grain boundaries. Alternatively, all graphene *nuclei* were reported to grow with the same crystalline orientation. Being epitaxially correlated on an identically-oriented surface, they grow aligned along the same crystalline direction and ultimately merge into a single-crystal film without grain boundaries. However, this approach is still out of reach in the case of the polycrystalline Cu foil substrate, that is widely used to grow

highly crystalline graphene, due to an efficient catalytic activity (low carbon diffusion and surface-mediated growth) combined with a limited cost.

The first part of the thesis work is to demonstrate the growth of large single-crystal graphene on copper foils by ethanol CVD. Ethanol is an efficient precursor which can be used instead of methane, the most commonly used carbon source, and can provide various advantages. Being liquid at standard atmospheric temperature and pressure, ethanol is safer than methane and can decompose at a lower temperature, accelerating the growth. Continuous graphene films were grown on Cu foils at low partial pressures of ethanol (< 2 Pa) in seconds *i.e.,* much faster than conventional growth times (in the order of minutes) of methane-based CVD processes. Shorter growth times are crucial for industrial production and can also limit growth kinetic issues related to Cu sublimation. Most of the recent studies on the growth of large single crystal graphene covered the CVD of methane, while ethanol as a carbon source has not been investigated in this respect yet and up to date, only one group reported the growth of mm-sized single crystal graphene by CVD of ethanol with pre-oxidized Cu enclosures. The enclosure approach is not ideal because it introduces uncertainties to the CVD process: It is impossible to define the gaseous environment inside the enclosure's internal surfaces. The goal of this work is to systematically explore the process parameters of ethanol-CVD to obtain full control over the nucleation rate, grain size and crystallinity of graphene on flat Cu foils, which are of interest for any realistic production in large scale.

The development of 2D materials with tailored electronic properties is attractive and promising for future photovoltaic (PV) devices. Graphene and graphene based derivatives (GBDs) with tuneable optoelectronic properties can be synthetized by ethanol-CVD. These graphene derivatives maintain the 2D character, but their properties can be tuned over a wide range. Such derivatives can be obtained both by a post-growth processing of graphene and by properly tuning the synthesis processes. The possibility of using GBDs with desired properties to function as interfacial, buffer and active layers offers an unprecedented opportunity for photovoltaics.

Schottky barrier solar cells (SBSCs) based on graphene/n-Si junctions represent an innovative and interesting case study for the integration of 2D materials into consolidated cell architectures and fabrication processes. Graphene and related materials are ideally suited for the fabrication of stacked structures, either in novel device configurations or in conjunction with "classic" PV materials. Graphene in the SBSC serves not only as transparent conductive electrode, but can also contribute as an active layer for carrier separation and hole transport. This kind of solar cell represents a low-cost and high-efficient alternative to traditional Si solar cells based on p-n junctions. In fact, these cells can be fabricated by simply transferring a graphene film onto n-Si substrate at room temperature, making the fabrication process less expensive and easier in comparison to traditional Si solar cells. Power conversion efficiency (PCE) of graphene/n-Si SBSCs passed from 1.5 to 15.6% in only 5 years, by implementing various kinds of graphene films and optimization strategies: multilayer films, chemical doping treatments, the introduction of antireflection coatings or light-trapping layers, the engineering of interface between graphene and Si. The engineering of the interface between absorber and front electrode is crucial for reducing the dark current, blocking the majority carriers injected into the electrode, and reducing surface recombination in Schottky heterostructures based on graphene. The presence of tailored interfacial layers between the metal electrode and the semiconductor absorber can improve the cell performance. The second part of this thesis clarifies the role of a non conductive GBD as interfacial layer between few-layer graphene (acting as transparent conductive electrode) and n-Si (the absorber). The effect of GBD interlayer on the electrical and photovoltaic solar cell parameters will be discussed.

The thesis has been arranged in four chapters. Chapters 1 and 2 are related to theory and experimental methods used during the study, whereas in Chapter 3 and 4 the results on the synthesis of large graphene grains and the effect of GBD as interlayer in a SBSC are reported, respectively. In Chapter 1, graphene is presented, together with its crystal and electronic structure, and CVD method, largely used in the research activities, is also discussed. An overview of the experimental techniques used to characterize graphene and to

test the photovoltaic device is reported in Chapter 2. Optical, electron and atomic force microscopy and Raman spectroscopy have been used to investigate the graphene structure and properties, whereas to characterize the solar cell, analysis of J-V curve, external quantum efficiency and power conversion efficiency have been evaluated. Synthesis of large graphene domains by ethanol CVD with direct exposition of Cu foil to precursor flow is discussed in Chapter 3. The process parameters of ethanol-CVD are systematically explored to obtain full control over the nucleation rate, grain size and crystallinity of graphene, which are of interest for any realistic production in large scale. Fabrication and testing of photovoltaic device are discussed in Chapter 4. The SBSCs are characterized and tested in dark conditions and as solar cells under standard conditions; electrical and photovoltaic parameters are extracted and discussed. A physical model to better explain the effect of non conductive interlayer in the diode structure is also discussed.

The experimental activity here presented was carried out in different laboratories, specifically at the University Mediterranea of Reggio Calabria, at the ENEA Casaccia and ENEA Portici Research Centers.

1
Graphene

Because of its extraordinary versatility, graphene is playing an important role in nanotechnology and microelectronics, envisaged as the main protagonist of optoelectronic devices of the future and in particular for photovoltaic applications.
The aim of this chapter is to introduce the physics of the graphene and the techniques used to produce it. Firstly, graphene structures and properties will be pointed out, then synthesis and transfer methods will be briefly discussed.

1.1 Introduction

Graphene was originally explored as a theoretical exercise in solid state physics and its linear dispersion relation was predicted by P. R. Wallace in 1947 [1]. Before 2004 the consensus was that graphene and 2D crystals were completely theoretical materials. In 2004 a flake of graphite with monoatomic thickness was isolated and characterized by A.K. Geim, K. Novoselov and their team [2] at Manchester University, giving the beginning to the revolution in reduced dimension materials and the age of 2D materials. This revolution had a surprising origin: the original technique used to isolate graphene for the first time derived from the technique used to create fresh graphite surfaces for scanning tunneling microscopy using scotch tape [3]. In the "scotch tape method", highly ordered pyrolytic graphite (HOPG) is repeatedly shed of its layers using scotch tape until a monolayer is left on the tape, a technique we can all recreate at home. Initially not everyone saw the potential of graphene and the journal Nature rejected the teams original submission with the quip that it 'did not constitute a sufficient scientific advance' [3]. The journal Science did not feel the same and accepted it and Geim and Novoselov went on to promptly receive the 2010 Nobel Prize in physics for 'groundbreaking experiments regarding the two-dimensional material graphene'. Since then, graphene has attracted great research interests in areas such as physics,

chemistry, nanoelectronics, materials science and bioscience because of its fascinating electronic, optical, mechanical and thermal properties.

1.2 The Physics of Graphene

Graphene can be considered the building material of all other carbon allotropes, such as being rolled into 1D nanotubes or wrapped into 0D fullerenes. Figure 1.1 shows the structure and dimensionality of the carbon allotrope family. In this chapter the crystal structure of graphene and its optical and electronic properties will be described.

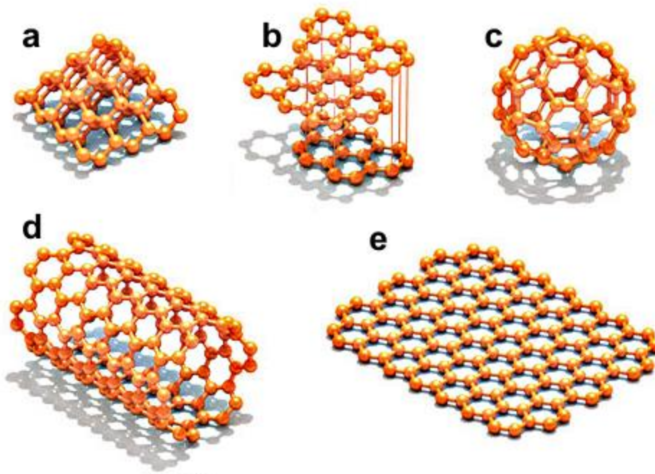

Figure 1.1. The carbon family and the considered material dimensionality. (a) Diamond (3D) (b) Graphite (3D) (c) Fullerenes (0D) (d) Nanotube (1D) (e) Graphene (2D).

1.2.1 Carbon hybridization of graphene

Graphene is composed of covalently bonded, sp^2 hybridized, carbon atoms in a two dimensional hexagonal atomic structure that resembles honeycomb. Bonding hybridisation refers to the mixing of valence electron states. Carbon is the 6th element in the periodic table and has six electrons, two electrons with opposite spins fill the first shell (principal quantum number (n = 1) and four partially fill the second shell (n = 2). The shell with n=2 is the valence shell of carbon and two electrons fill the first sub-shell (2s) and the remaining two partially fill the second sub-shell (2p) as reported in Figure 1.2. The electron configuration of a carbon atom is described as $1s^2 2s^2 2p^2$. The p sub-shell is

capable of holding 6 electrons in total, with pairs of electrons with opposite spin states occupying the x (px), y (py) and z (pz) axis (orbital). The 1s sub-shell has an orbital energy of E ≈ -285 eV [4] and thus the $1s^2$ electrons are not considered in the majority of theoretical predictions and carbon interaction and bonding are attributed to n = 2 shell. The 2p and 2s orbitals have an energy difference (≈ 4 eV [5]) and thus it is energetically favourable to fill the lower energy 2s orbital first. However, in the presence of other carbon atoms it becomes energetically favourable to excite a single 2s electron to fill a third 2p orbital state in order to form covalent bonds known as sp^x hybridised covalent bonds with the neighbouring atoms (Figure 1.2). The sp^x orbital has three common forms sp^1 (acetylene), sp^2 (graphene) and sp^3 (diamond) where the order of the sub-shell indicates the number of electrons involved in the hybridised bonding from that sub-shell. Graphene is sp^2 hybridised and forms a three fold planar bonding between a single 2s orbital and two 2p orbitals (2px and 2py) with the same electron orbitals of three other neighbouring carbon atoms (Figure 1.2). The hybridisation becomes the core orbital and one electron is left over from the n = 2 valence band per carbon atom, from the energy minimisation from hybridised bonding this becomes a 2pz un-hybridised orbital which has an orbital volume out of plane to the sp^2 hybridised covalent sigma bonds and acts to form p covalent bonds with neighbouring 2pz electrons. For clarity $1s^2 2s^2 2p^2$ (non-hybridised) became $1s^2 2s^1 2p^3$ (sp^2 hybridised) as the external potential from bonding with other carbon atoms favours the hybridised energy state even though it costs ≈ 4 eV to promote a 2s electron to the 2pz orbital state. Figure 1.2 shows the orbital form of ground state carbon orbitals and their respective formation into sp^2 hybridised orbitals in the graphene lattice. It is the 2pz orbital that is capable of joining the de-localised extended states that form the valence and conduction bands of graphene and facilitates graphene's electrical properties.

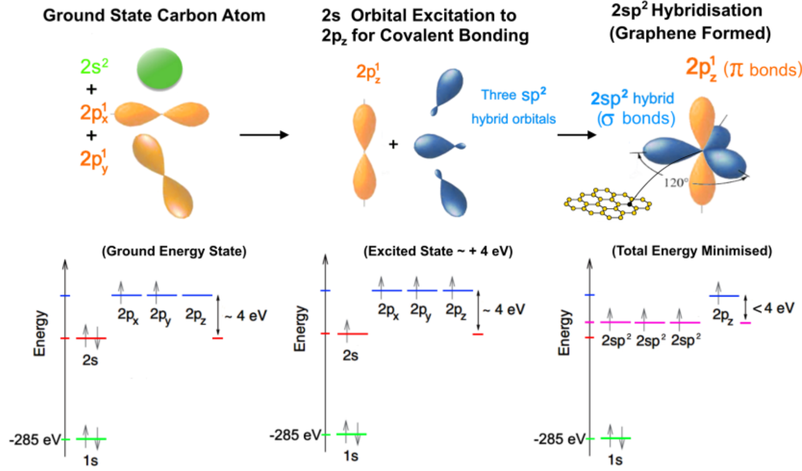

Figure 1.2. The orbital evolution from a ground state energy carbon atom to a sp^2 hybridised graphene atom.

1.2.2 Graphene crystal structure

Graphene is a carbon allotrope in which atoms are arranged forming a honeycomb 2D lattice due to their sp^2 hybridization, with an inter-atomic length of a_{cc}=1.42 Å. A theoretically pristine crystal is formed from an infinite array of repeating atomic positions. A Bravais lattice can be formed by using the atomic positions. The unique electronic properties of graphene are due to this honeycomb lattice arrangement, which can be seen as two non-equivalent interpenetrating hexagonal lattices with a two-atom basis (A and B), as depicted in Figure 1.3a. Both sublattices are Bravais lattices characterized by two base vectors *a* and *b*, with an angle of 120° between them. The lattice vectors forming the basis of the unit cell (Figure 1.3b) are [6]:

$$\alpha\vec{a}_1=\frac{a}{2}(3\hat{x},\sqrt{3}\hat{y}) \qquad \vec{a}_2=\frac{a}{2}(3\hat{x},-\sqrt{3}\hat{y}) \qquad 1.1$$

where a ≈ 1.42 Å and is the C-C bond length and the lattice constant can be given as $\vec{a} = a\sqrt{3} = |\vec{a}_1| = |\vec{a}_2| \approx 2.46$Å, $\hat{x}$ and $\hat{y}$ are the Cartesian basis vectors (unit vectors).

Any linear combination of the vectors a_1 and a_2 generates all the points in the lattice.

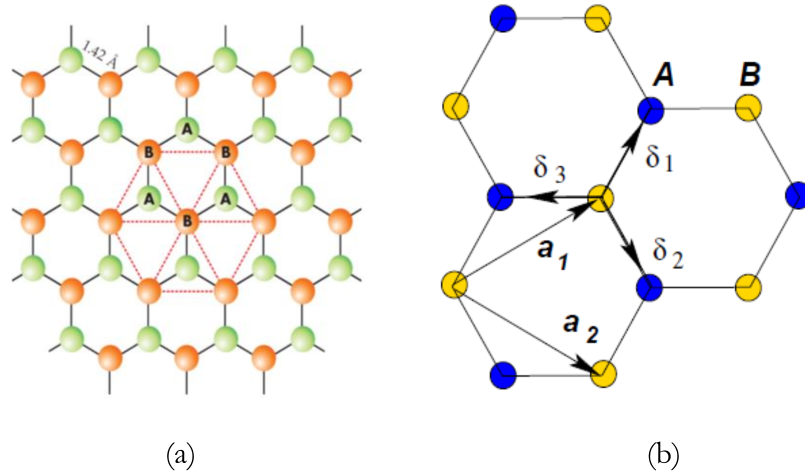

(a) (b)

Figure 1.3. (a) The honeycomb lattice of graphene showing the two sublattices marked A and B [7]. (b) Lattice structure of graphene showing the two sublattices marked A and B; a_1 and a_2 the lattice unit vectors; $\boldsymbol{\delta_i}$ i=1, 2, 3 the nearest neighbor vectors [6].

The vectors $\boldsymbol{\delta_{1,2,3}}$ connect in real space any site on the A sublattice to any of its three nearest neighbours which all reside on the B sublattice and they can be defined as:

$$\overrightarrow{\delta_1} = \frac{a}{2}\left(+\sqrt{3}\hat{y}\right) \qquad \overrightarrow{\delta_2} = \frac{a}{2}\left(\hat{x} - \sqrt{3}\hat{y}\right) \qquad \overrightarrow{\delta_3} = -a\hat{x} \qquad 1.2$$

Reciprocal space (k-space, momentum space) is a construct used for theoretical analysis of periodic structure. The real space and reciprocal space vectors satisfy the relation $\hat{a}_i \cdot \hat{b}_j = 2\pi\delta_{ij}$ where δ_{ij} is the Kronecker delta. The reciprocal lattice vectors $\vec{b}_1$ and $\vec{b}_2$ of the graphene Bravais lattice are defined as

$$\vec{b}_1 = \frac{2\pi}{3a}\left(1\hat{x}, \sqrt{3}\hat{y}\right) \qquad \vec{b}_2 = \frac{2\pi}{3a}\left(1\hat{x}, -\sqrt{3}\hat{y}\right) \qquad 1.3$$

and shown in Figure 1.4 relative to the first Brillouin zone (BZ). Importantly, the BZ is the reciprocal analogue of the real space Wigner-Seitz cell and can be defined as the area of available reciprocal space that does not cross any Bragg planes drawn about a lattice point.

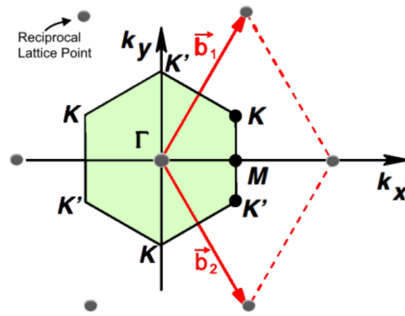

Figure 1.4. First Brillouin zone of graphene with the reciprocal lattice vectors defined as b1 and b2. High symmetry k-points are labelled as Γ, M, K and K' [6].

The area within the first BZ is closer to the origin than any other lattice point and importantly this means that any point in reciprocal space has an equivalent in the first BZ due to the periodic nature of the lattice. Every wave vector within the BZ is unique and non-equivalent to another in the BZ, therefore any wave vector in any periodic state of the crystal has a single wave vector equivalent within the BZ. Here a wave vector $\vec{k}$ (wavenumber k $= |\vec{k}|$) is related to momentum via $\vec{p} = \hbar\vec{k} = \frac{2\pi\hbar}{\lambda}$ and is often referred to as the crystal momentum. Considering the reciprocal space of the honeycomb lattice, it is easy to see that the first Brillouin zone is an hexagon [7].

1.2.3 The band structure of graphene

Due to the sp^2 hybridization of carbon valence orbitals, the 2s valence orbital mixes with the 2px and 2py ones forming three equivalent sp^2 hybrid orbitals lying in the xy plane. Three in-plane carbon atoms are bonded to other nearby carbon atoms by covalent bonds by sigma bond by overlapping their sp^2 orbitals and are not available for the conduction process, as well as the electronic bands of the 1s state, which is completely filled. The remaining 2pz orbital, with an axis normal to the xy plane, can overlap with a neighboring 2pz orbital forming π bonding and π^* antibonding orbitals [14]. Overlap between 2pz orbitals of neighboring carbon atoms in graphene results in the formation of a delocalized π system. Each atom in the unit cell is characterized by the π bond and thus can donate one electron to the lattice, almost completely

delocalized, free to move and actively participate to conduction. Most of the spectacular electronic properties of graphene are related to its π and π^* electron energy bands. The form of the π energy bands in graphene was first derived by Wallace in 1947 within the approximation of tight-binding electrons [1]. Considering only interactions between 23 nearest neighbors in the lattice this will be

$$E(k) = \pm t\sqrt{1 + 4\cos\left(\frac{\sqrt{3}}{2}a_0 k_x/2\right)\cos\left(\frac{1}{2}a_0 k_y\right) + 4\cos^2\left(\frac{1}{2}a_0 k_y\right)} \quad 1.4$$

where a_0 is the carbon-carbon distance and t ≈ 2.8 eV is the nearest neighbor hopping energy. The minus sign applies to the lower π band, which is fully occupied, and the plus sign to the upper π^* band, which is empty. These bands come in contact, without overlapping, at six points in the reciprocal lattice, which are commonly referred to as the *K* points, coincident with the boundary of the first Brillouin zone. Graphene's BZ shows four distinct vector positions from the origin, $\vec{\Gamma}$, $\vec{\mathrm{M}}$, $\vec{\mathrm{K}}$, $\vec{\mathrm{K}}'$ and are positioned at:

$$\vec{\Gamma} = 0\hat{x} + 0\hat{y}, \qquad \vec{\mathrm{M}} = \frac{2\pi}{3a}\hat{x}, \qquad \vec{\mathrm{K}} = \frac{2\pi}{3a}\left(\hat{x} + \frac{\hat{y}}{\sqrt{3}}\right), \qquad \vec{\mathrm{K}}' = \frac{2\pi}{3a}\left(\hat{x} - \frac{\hat{y}}{\sqrt{3}}\right) \quad 1.5$$

K and *K'* represent a set of non-equivalent points in the reciprocal space which may not be connected one to another by a reciprocal lattice vector. The corners of the Brillouin zone, where the band crossing occurs are K and K´ points. The *K* and *K'* points are the primary points of interest when studying the electronic properties of graphene. This crossing point is called the Dirac point and its energy position is exactly at the Fermi level. A representation of the graphene energy bands is shown in Figure 1.5. Fermi energy lies exactly at the *K* points for undoped graphene and the Fermi surface of graphene consists thus of only six points.

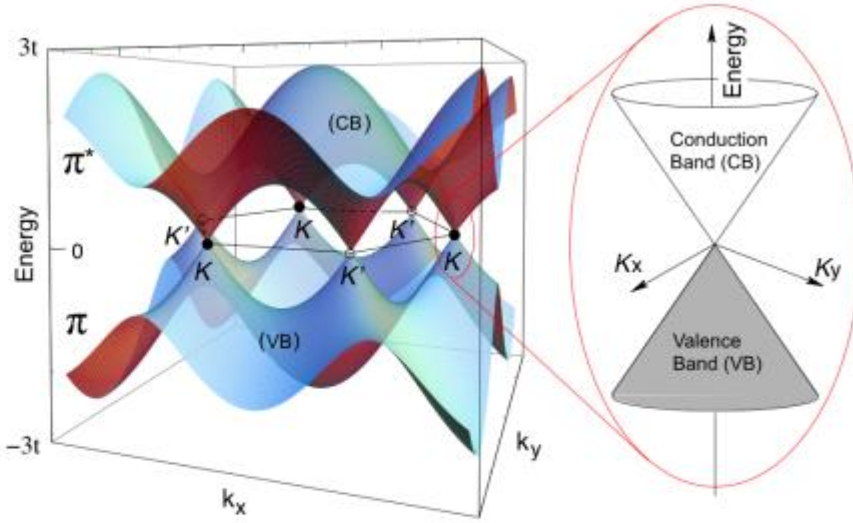

Figure 1.5. Band structure of graphene. In the vicinity of the Dirac points at the two nonequivalent corners *K* and *K′* of the hexagonal Brillouin zone, the dispersion relation is linear and hence locally equivalent to a Dirac cone [8]. The energy dispersion is a function of the wavevector components k_x and k_y, as obtained from Eq. 1.3. Valence ($\boldsymbol{\pi}$) and conduction bands ($\boldsymbol{\pi}^*$) are seen touching at the Fermi level at the K and K' points with a linear conical relation among them.

Near these points the relationship of the energy versus momentum becomes linear, which has significant consequences for the electronic transport and optical properties of graphene. The linear dispersion region is well-described by the Dirac equation for massless Dirac fermions, particles with relativistic speed and no mass [9]

$$E(k)=\pm\hbar v_F\left|\vec{k}-\vec{K}\right| \tag{1.6}$$

with $\hbar$ reduced Planck constant, k the wave vector of the electron and $v_F \approx 10^6 ms^{-1}$ is the Fermi velocity (responsible of the ballistic transport) [10]. In the usual case with parabolic valence and conduction bands the dispersion relation is $E(\vec{k}) = E(0) + \frac{\hbar^2\vec{k}^2}{2m^*}$ and the velocity $v = \sqrt{2E/m}$ is proportional to the energy. Comparing these relations to Einstein's relativistic energy relation ($E = \sqrt{(mc^2)^2 + (cp)^2}$) for massive particles in the nonrelativistic limit $E \approx mc^2 + \frac{p^2}{2m}$ and massless relativistic particles $E = c|p|$ there is a clear parallel between parabolic dispersion relations and massive particles and

graphene's dispersion relation and massless particles [6]. Therefore in the low energy limit in the Dirac valleys the electronic states can be described by the Dirac equation for m = 0, as a consequence the charge carriers in graphene are quasiparticles and are known as massless Dirac fermions. It should be noted that frequently graphene is described as having a zero effective mass using $m^* = \hbar^2 \left(\frac{d^2E^{-1}}{dk^2}\right)$ as is used in semi-conductors, however this gives m^*= 1 in the linear Dirac valleys or zero at the Dirac point. The effective mass of graphene's charge carriers becomes anomalous at the Dirac points ($E = E_F$) as the wavenumber k = 0 and instead can be described as [6]:

$$m^* = \frac{1}{2\pi}\frac{\partial A(E)}{\partial E} \tag{1.7}$$

where $A(E) = \pi E^2/v_F^2$ and is the area in reciprocal space enclosed by the 2pz orbit. The charge carrier effective mass can then be related to E_F, the carrier density n and the Fermi momentum $k_F(k_F^2 = n\pi)$ by [6]:

$$m^* = \frac{E_F}{v_F^2} = \frac{k_F}{v_F} = \sqrt{\frac{\pi n}{v_F^2}} \tag{1.8}$$

Again, note $\hbar$ needs to be applied for the correct units. It can be seen clearly that at the Dirac Point where n=0 the effective mass is zero.

Linear dispersion graphene π bands close to the Dirac points result, also, in a linear dependence of density of states on the energy. The density of states per unit cell can be written as [6]

$$\rho(E) = \frac{2A_C|E|}{\pi\hbar^2 v_F^2} \tag{1.9}$$

where A_C is the unit cell area. At the Dirac point the density of states is in principle zero. Despite that, graphene exhibits a minimum quantum conductivity of the order of $4e^2/h$ [11]. The linear dispersion of the Dirac valleys creates a linear change in the density of states until reaching the Dirac

point where the density of states is zero. Increasing E above E_F induces electrons into conduction band, decreasing E below E_F increases the hole density. At the Dirac point (at 0 K thus zero probability of excitation states above E_F) graphene should exhibit an infinite resistance/zero conductivity as the zero density of states indicates a zero charge carrier density [12].

1.3 Graphene Properties

Since graphene discover, its electronic properties have attracted the interest of researchers, who looked at graphene as the substitute of silicon in the fabrication of electronic devices.

1.3.1 Electronic transport properties of graphene

The electronic transport and optical properties of graphene are greatly influenced by the physics of the charge carriers near the Dirac points. Charge carrier mobility (μ) of up to 1000000 cm^2/Vs at low temperature (~5 K) [13] has been observed in pristine, suspended graphene, where interactions with the substrate are eliminated. At room temperature, the mobility has been measured to typically range from 10000 to 200000 cm^2/Vs [14], [15] [16]. This value is at least 100 times faster than what is observed in silicon. Scattering in graphene does not depend strongly on temperature for $T < 400$ K [17] but it is influenced by the charged impurities of the supporting substrate and other extrinsic impurities that may be present [6], [14], [15], [17], [18]. For instance, the carrier mobility is typically on the order of 10000 cm^2/Vs for polar SiO_2 substrate limited by the graphene-SiO_2 interaction [6] On the other hand, graphene placed on more inert, hexagonal boron nitride (BN) substrate exhibited the mobility of 500000 cm^2/Vs [19], [20]. Substitutional defects are unlikely in graphene as the carbon atoms form strong in-plane bonds and graphene seems to form perfect crystal without vacancies in the range of microns at room temperature [21]. Furthermore, graphene forms corrugations or puddles of charges which can act also as scattering centres [22]. Conductivity of graphene can be tuned by doping through fabrication of a field effect device structure

where the application of gate voltage modulates the Fermi level (Figure 1.6). Figure 1.6a depicts the density of states and ambipolar transport in graphene where it can be seen that both the hole and electron densities can be easily controlled with the gate voltage [23]. Because the density of state increases linearly away from the charge neutrality point, the conductivity also varies linearly with gate voltage (Figure 1.6b). The mobility, however, remains constant over a wide range of gate induced doping. At low temperatures, graphene approaches a universal conductivity of $4e^2/h$ and does not undergo metal to insulator transition as theoretically expected for a material even with very low concentration of charge carriers near the Dirac point [11]. This minimum quantized conductivity has been predicted by the theory describing the 2D Dirac fermions. The high mobility makes graphene a potential material for nanoelectronics especially in high-frequency applications [24].

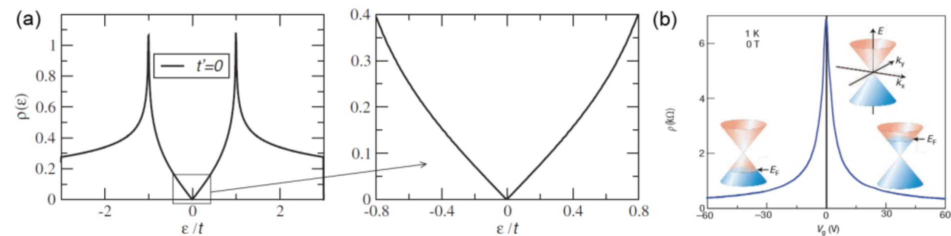

Figure 1.6. (a)Calculated density of states of graphene. Close to the Fermi level, the density of states ϱ(ε), is linear with respect to the energy [6]. (b) Ambipolar transport characteristic of graphene. Field induced by gate voltage, Vg can control concentration and polarity of charge carriers. Positive (negative) gate voltage increases Fermi level increasing carrier concentration of holes (electrons) [11]

1.3.2 Scattering in graphene

The charge-carrier mobility in graphene, which is around 10000 cm^2/Vs at room temperature, is believed to be limited by scattering of charge carriers [25]–[27]. There are various sources of scattering in a graphene system, such as phonons, charged impurities, neutral point defects and ripples (microscopic corrugations of a graphene sheet). Although intrinsic scattering such as scattering produced by interaction with phonons cannot be eliminated at room temperature, which eventually raises a fundamental limit on the mobility in

graphene, the electron-phonon scattering in graphene is found to be weak enough that mobility can still reach around 200000 cm^2/Vs at room temperature if extrinsic disorder is eliminated [14]. On the other hand, extrinsic disorders such as charged impurities, ripples and neutral point defects are considered the source of scattering that is expected to suppress the mobility in graphene. Short-range scattering generated by neutral point defects, or impurities, has limited effect on graphene's resistivity ρ, comparing to conventional nonrelativistic two-dimensional electron system [27], [28]. This fact may help to understand the remarkably high mobility in graphene. On the other hand, long-range Coulomb scattering from the random charged impurities located near the interface between the graphene and the substrate can be another possible candidate that limits the charge carrier mobility in graphene [26], [29], [30]. It explains the experimental fact that resistivity ρ is inversely proportional to charge carrier density n and mobility is independent of charge carrier density. The typical concentration of charged impurities in graphene samples with mobility limited to ~ 10000 cm^2/Vs is estimated to be ~ 10^{12} cm^{-2} [30]. In addition to charged impurities, ripples in graphene should create a similar long-range scattering effect on the mobility [31]. Large-scale ripples were also observed in graphene on SiO_2 [32], while nanometre-sized ripples were observed in scanning-probe study of graphene [33], [34]. This kind of ripples is unavoidable, because strictly 2D crystals are extremely flexible and soft, and the existence of ripples can help stabilize the crystal by lowering the total energy.

1.3.3. Optoelectronic properties of graphene

Graphene shows remarkable optical properties. For instance, despite being only a single atom thick, it can be optically visualized. For freestanding single layer graphene (SLG) transmittance (T) can be derived by applying the Fresnel equations in the thin-film limit for a material with a fixed universal optical conductance [10]:

$$T = (1 + 0.5\,\pi a)^{-2} \approx 1 - \pi a \approx 97.7\% \qquad 1.10$$

where α is the fine-structure constant [35]. Graphene only reflects <0.1% of the incident light in the visible region, rising to ~2% for ten layers. Thus, it can be assumed the optical absorption of graphene layers to be proportional to the number of layers, each absorbing $A \approx 1 - T \approx \pi\alpha \approx 2.3\%$ over the visible spectrum (Figure 1.7).

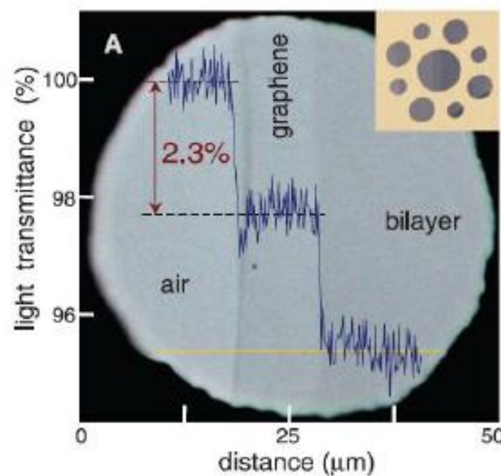

Figure 1.7. Scan profile showing the intensity of transmitted white light through air, single layer and bilayer graphene respectively [35].

Its transparency makes graphene ideal for its use in optoelectronic devices such as displays, touchscreen and solar cells, where materials with low sheet resistance R_s and high transparency are needed. It could replace the current transparent conducting materials, as indium tin oxide (ITO) [10], [36]. ITO is commercially available with $T \approx 80\%$ and R_s as low as 10 Ω/sq on glass and ~60−300 Ω/sq on polyethylene terephthalate. However, ITO suffers severe limitations: an ever-increasing cost due to indium scarcity, processing requirements, difficulties in patterning and a sensitivity to both acidic and basic environments. Moreover, it is brittle and can easily crack when used in applications involving bending, such as touch screens and flexible displays [10]. For these reasons new transparent conducting materials with improved performance are needed and graphene seems to be a good alternative. Graphene films have a higher transmittance over a wider wavelength range than

single-walled carbon nanotube (SWNT) films, thin metallic films (ZnO/Ag/ZnO e TiO_2/Ag/TiO_2) and ITO (Figure 1.8a) [10].

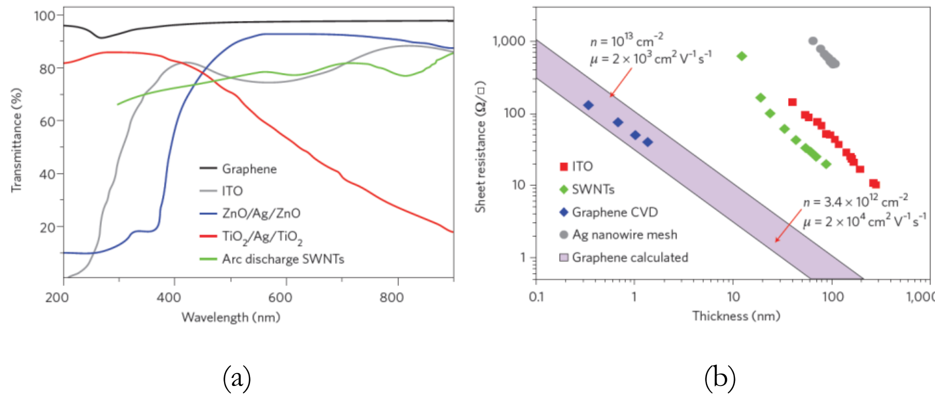

(a) (b)

Figure 1.8. (a) Transmittance for different transparent conductors and (b) thickness dependence of the sheet resistance [10].

It has been calculated that for an ideal intrinsic SLG with T ≈97.7% resistance sheet value is about 6 kΩ/sq. Thus, an ideal intrinsic SLG would beat the best ITO only in terms of T, not R_s. However, real thin films are never intrinsic. The range of T and R_s that can be realistically achieved for graphene layers of varying thickness can be estimated by taking n= 10^{12}-10^{13} cm^{-2} and μ = 1000 - 20000 cm^2 V^{-1} s^{-1}. As shown in Figure 1.8b, graphene can achieve the same R_s as ITO, ZnO/Ag/ZnO, TiO_2/Ag/TiO_2 and SWNTs with a similar or even higher transmittance [10]. It has been also demonstrated that the optical properties of graphene can be significantly modulated by the doping which can lead to novel optoelectronic effects and devices [37].

1.3.4 Thermal conductivity in graphene

Thermal conductivity of graphene can also occur through ballistic phonon transport with theoretical values of the thermal conductivity predicted to be ~8000 W/mK while indirect measurements have yielded values ranging from 600 to 5000 W/mK that are comparable to that of bulk graphite (≤2000 W/mK) [38]–[42]. This thermal properties makes graphene promising for thermal management and in particular for heat dissipation and transport applications [43], [44].

1.3.5 Physical properties of graphene

Graphene attracts much interest also for its mechanical properties. Numerical methods and experimental techniques have proved graphene intrinsic mechanical properties, characterized by high strength, hardness and elasticity [45], [46]. For instance, the spring constant of suspended graphene sheets is in the range 1-5 N/m and the value of the Young's modulus equal to 1.0 teraPascal (TPa) was measured for monolayer graphene by Atomic Force Microscopy (AFM), assessing graphene as the strongest material ever measured [45]. These mechanical properties make graphene a strong material and lead to a promising potential of utilising graphene in Nanoelectromechanical systems (NEMS) [47].

1.3.6 Chemical and Surface Properties

Like graphite, graphene is generally a chemically stable material and it is thermally stable in air up to temperatures of ~500 °C [48]. Graphene has a very large surface area, ~2600 m^2/g [49] which is useful for catalyst and energy storage applications. Graphene can also serve as a support for sensing adsorbing gas molecules [50] or for forming nanoparticle assemblies [51].
Graphene can be functionalized through chemical modifications such as oxidation, hydrogenation, and fluorination. Oxidation renders graphene hydrophilic and allows further alteration of the functional groups by organic molecules (e.g. acylation followed by $SOCl_2$ activation for polymer linkage and treatment by diazonium salts for improved solubility in polar organic solvents) [52], [53]. Hydrogenation can render graphene insulating [54], [55] and may have implications in hydrogen storage [56]. Fluorination of graphene makes it strongly hydrophobic, induces p-type doping, and can also open up a band gap [57], [58]. Through functionalization, the optoelectronic, chemical, and surface properties of graphene can be engineered for multitude of applications.

In conclusion, crystal and electronic structure of the graphene, give it interesting properties, such as:

- Density of 0.77 mg/m^2
- Thickness of ≈ 3.4 Å

- Surface area to volume ratio 2630 m^2/g
- Massless, relativistic Dirac quasiparticle charge carriers [2]
- Room temperature mobility ≈ 200000 cm^2/Vs [14], [17]
- Low temperature mobility ≈ $6 \cdot 10^6$ cm^2/Vs (T = 4 K) [59]
- Higher current density capacity (milliamps through ribbons microns wide) [60]
- Tunable band gap with length [61]
- Tunable hole and electron densities with an applied electric field [2], [23]
- Half integer quantum Hall effect at room temperature [9]
- Room temperature quantum Hall effect [62] and unconventional Hall effects [63], [64]
- Transparent - absorbs ≈ 2.3% of normal incident light [10], [16], [65]
- Softest material possible against transverse deflection, flexible and stretchable [66]
- Young's modulus ≈ 1TPa [45]
- Intrinsic strength of 130 GPa [45]
- Thermal conductivity ≈ 5000 W/mK [43]
- Cheap to produce [67]

1.4 Graphene Synthesis

Graphene does not exist in nature as isolated 2D material, but it can be extracted from graphite. Mechanical cleavage, thermal decomposition of silicon carbide, liquid phase exfoliation of graphite, molecular assembly and chemical vapor deposition (CVD) are the most commonly used synthesis methods of graphene. Anyway, it should be pointed out that no one of the aforementioned synthesis techniques can be considered as the best one in absolute. Since each of these methods is suitable to obtain graphene with different characteristics, the choice of a specific technique derives by the role of graphene in the specific application.

Figure 1.9 compares the available methods with regards to graphene quality and cost. CVD is described in detail due to its relevance to the study and further detail of the process is included in the results section.

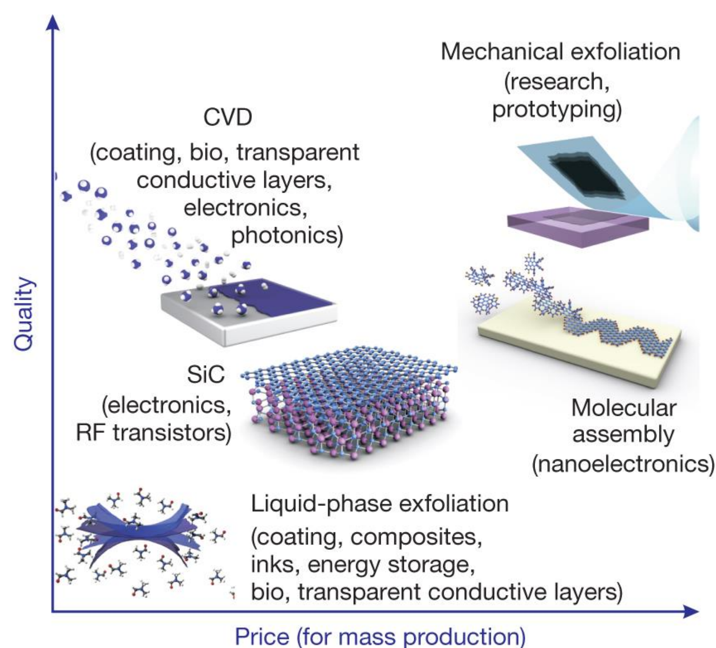

Figure 1.9. Graphene quality vs mass production cost of different graphene fabrication methods [68].

1.4.1 Mechanical exfoliation

Mechanical exfoliation can be regarded as the mother of all techniques for graphene production, since it was the first technique through which graphene was successfully isolated by Geim and Novoselov [2]. It basically consists in the exfoliation of a High Oriented Pyrolytic Graphite (HOPG) block through the so called "scotch-tape technique". HOPG can be considered as a significant stack of monolayer graphene with distance of 3.34 Å, and stacked interacting with each other via van der Waals forces. Such forces are weak and for graphite the energy needed to cleave layers from each other is 0.39 ± 0.02 J/m^2 [69] (ABAB stacked). Thus graphene layers are easily peeled/cleaved/exfoliated from each other without any effort and this is the fundamental principle of this method [2]. In this method, an adhesive can be used to peel off the graphite flakes, as depicted in Figure 1.10a. With the first

step, several layers of bulk graphite are removed from the planar side of HOPG sample. The first piece of tape is then repeatedly cleaved by other sticky pieces till to obtain an almost invisible powder on the starting tape. With any luck a few flakes of single or bi-layer graphene will be isolated Finally, at the end of the exfoliation process, the tape is transferred onto another substrate that usually is silicon dioxide on Si wafer (SiO_2/Si). In Figure 1.10b an optical image of a mechanical exfoliated multilayer graphene flake is show

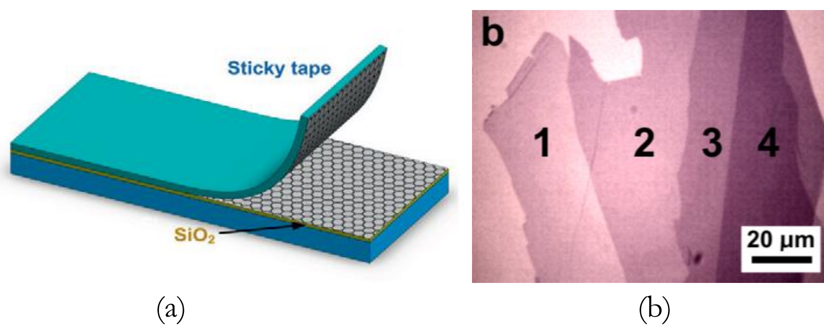

(a) (b)

Figure 1.10. (a) Scotch tape mechanical exfoliation [70], (b) Exfoliated graphene on 300 nm thick SiO_2, the number of layers increases with flake contrast, the number of layers are labelled, image adapted from [71].

The costless and advantageous of the technique brought many research groups to use it to produce high quality graphene layers. Graphene produced by this technique show mechanical and electrical quality comparable to the theoretical predictions. However, the real dimensions are significantly limited. The largest measured monolayer flakes are no bigger than 1 mm in any planar dimension [72] and the position of the flakes are uncontrollable. In order to be used for the fabrication of nanoelectronic devices, this process needs improvements for both the large-scale production and transfer method.

1.4.2 Liquid Phase Exfoliation

One of the promising routes to synthesize large quantities of graphene for large area applications is to exfoliate graphite in solution to produce a dispersion of graphene flakes. Graphite can be exfoliated in liquid environments exploiting ultrasounds to extract individual layers, (Figure 1.11). Such exfoliation method relies on covalent and non-covalent interactions

introduced by external molecules to disrupt the van der Waals interactions between the graphene sheets. The liquid-phase exfoliation (LPE) process generally involves the dispersion of graphite in special solvents able to minimize the interfacial tension between the liquid and graphene flakes. Indeed, if the interfacial tension is high, the flakes tend to adhere to each other and the work of cohesion between them is high, hindering their dispersion in liquid. Liquids with surface tension $\gamma \sim 40$ mN/m, are the best solvents for the dispersion of graphene and graphitic flakes, since they minimize the interfacial tension between solvent and graphene [70]. The solvents that mainly match this requirement are N-methyl-pyrrolidone (NMP) and Dimethylformamide (DMF) even if toxic and harmful to the environment. In order to favor the splitting of graphite into individual platelets, the solution should be sonicated for a long time. Finally, the surnatant phase of the suspension, the thinner exfoliated flakes, must be separated from the unexfoliated ones. Centrifugation process is generally used to this purpose [73]. Since this technique is regarded as one of the most promising for mass production, high concentration of exfoliated graphene is desirable. It is important to note that the yield of the process is strongly affected by each parameter involved in the procedure.

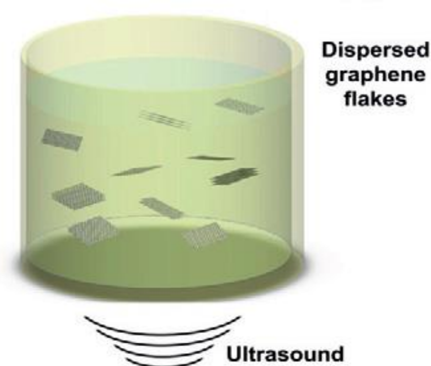

Figure 1.11. Liquid phase exfoliation technique [70].

1.4.3 Epitaxial Growth on SiC

Graphene can be synthesized by the thermal decomposition of silicon carbide [70], [74] (Figure 1.12). This growth technique is usually referred to as "epitaxial growth" even though there is a very large lattice mismatch between

SiC (3.073 Å) and graphene (2.46 Å) and the carbon rearranges itself in a hexagonal structure as Si evaporates from the SiC substrate, rather than being deposited on the SiC surface, as would happen in a traditional epitaxial growth process. The process is possible due to the lower sublimation temperature of Si compared to C and when elevated temperatures ≈ 1200°C and ultra-high vacuum (UHV) are applied to SiC. The annealing of the substrates results in the sublimation of the silicon atoms while the carbon-enriched surface undergoes reorganization and, for high enough temperatures, graphitization [70]. The typical range of annealing temperatures goes from 1500°C to 2000°C and the usual heating and cooling rates are 2-3°C/sec [75]. The thermal decomposition, however, is not a self-limiting process and areas of different film thicknesses may exist on the same SiC crystal. The graphene growth is also very sensitive to the crystallographic orientation of SiC and processing before growth is often essential [76].

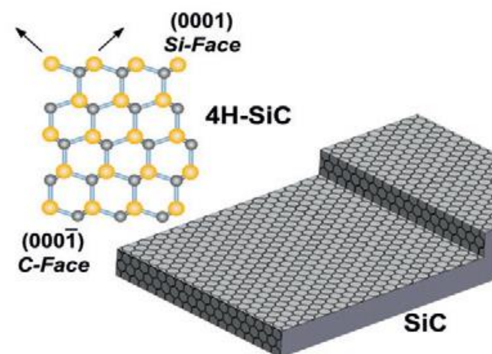

Figure 1.12. Growth on SiC. Gold and grey spheres represent Si and C atoms, respectively [70].

The dimensions of graphene produced are moderately larger in comparison to mechanically exfoliated graphene and can be on the order of 100 μm [11] but are not significant enough for non-research use. Graphene obtained on SiC single crystals has has shown a mobility of > 3400 cm^2/Vs [77]. Mobility has seen more recent improvements to $11000 cm^2/Vs$ but this is at a temperature of 0.3K and after a H_2 intercalation process [78]. Graphene produced by epitaxial growth on SiC may be limited to devices on SiC only, since transfer to other substrates such as SiO_2/Si might be difficult, with all the

drawbacks involved in the transfer process. Moreover, it is an expensive technique because of the SiC wafers cost.

1.4.4 Chemical Vapour Deposition (CVD)

Chemical Vapor Deposition (CVD) is a widely used method to grow thin films from many different carbon precursors both in vapor and liquid phase, such as methane (CH4), methanol (CH_3OH) and ethanol (C_2H_5OH) [54], [79]–[85] that are dissociated at high temperature using transition metal substrates such as Fe [86], Co [87], Ni [88]–[93], Cu [54], [94]–[100], Ru [87], Ir [87], [101], Pt [102]–[104] and Au [105], [106].

Graphene growth morphology is heavily dependent upon the growth substrate, with the grain orientation, grain size, grain boundary density and importantly the number of layers all being variable. At elevated temperatures and pressures, C dissolves into the surface of the substrate during CVD. The amount of C that the substrate intakes is defined as its solubility. The C solubility is a critical factor for optimizing graphene growth in terms of crystalline quality and number of layers. Low C solubility suppresses the formation of multi-layer graphene as C adatoms are predominantly restricted to the substrate surface. Graphene forms into small nuclei, which coalesce and grow into a full surface coverage at which point the precursor gas can no longer dissociate at the catalyst surface and thus no more C atoms can be added to the system, creating a self-terminating monolayer graphene growth. On very low C solubility materials, minimal bi-layer formation is shown such as on Cu it is often found that the graphene coverage is ≈ 95% monolayer Cu [54], [65], [94]–[100], [107], but this can be quite variable with CVD parameters such as temperature, pressure, growth time and C concentration. Graphene growth is also strongly affected by interaction with metallic substrate and surface orientation [87]. It is important to take into account lattice mismatch between graphene and substrate caused by C atoms forced from the most energetically favorable adsorption positions on the metal surface when incorporated into a graphene lattice. Weaker bonding creates an elongated distance between the metal surface and graphene and this often corresponds to a decreased C

solubility [87]. Ir, Pt, Ag, Au and Cu have the greatest bond separation of all the transition metals. With a greater graphene metal separation, the graphene will beneficially grow over substrate defects such as grain boundaries and step edges without any detriment as demonstrated with Cu [108]. However a weak lattice interaction allows domains do not have a favored crystal orientation and grow into a polycrystalline coverage [87] making the growth of large area single crystal graphene difficult. Ir shows the greatest bond separation between graphene and the metal surface (34 nm). Ir is very promising for graphene CVD, and has shown self-terminating monolayer graphene growth, low energy graphene-Ir interface, structural coherence over Ir step edges and even preferred nucleation orientation at higher temperature allowing for a reduced polycrystallinity [101]. However it is less favored if compared to Cu because it is more probable to obtain bi-layer graphene [109] due to its higher C solubility. Similar argument can be used for Pt, which shows self terminating monolayer growth, weak bonding interaction but a more polycrystalline graphene sheet and is not favored due to a greater formation of bi- multi-layer graphene areas [104]. In summary, Cu and Au are the most promising CVD candidates due to negligible disruption of graphene from step edges and defects due to their weak interfacial bonding with surface and low solubility. Because of cost, grain size, etchability, and their wide use and acceptance by the semiconductor industry, Cu and Ni have received the most attention as graphene substrates [88]. Indeed, graphene and few-layer graphene have been grown on polycrystalline Ni [93] while large area graphene has been grown on Cu substrates [54]. Two different CVD mechanism growth have been proposed on account of the different substrates [88]. Graphene on Ni is due to a C precipitation process. The solubility of carbon in Ni is high, thus carbon diffuses into the metal first before segregating and precipitating to the surface. A fast cooling rate is needed to suppress the formation of multiple layers (Figure 1.13a). Indeed, nonuniform layers are obtained with a variation in thickness from a monolayer to many layers over the metal surface.

On the other hand, when Cu substrates are used a surface adsorption mechanism is involved. Cu is one of the most used catalyst due to the low solubility of carbon in it even at a very high temperature. During growth, C

atoms nucleate on the substrate surface and then nuclei grow to form domains. Large-area graphene films with uniform thickness, due to the low solubility of C in Cu, are obtained. In this case, graphene growth is surface mediated and self-limiting (Figure 1.13b).

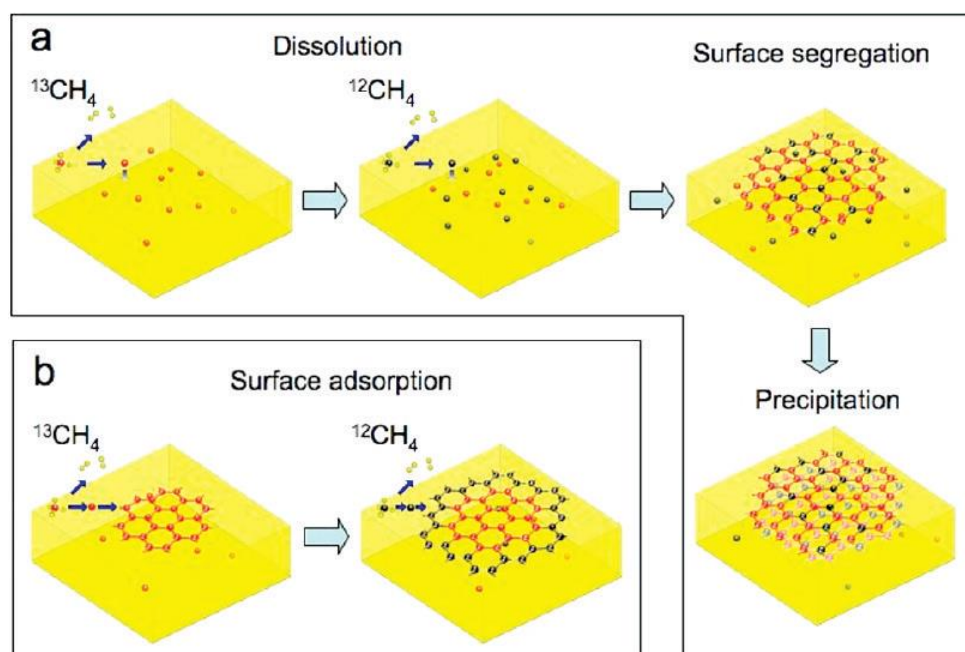

Figure 1.13. Schematic representation of graphene mechanism growth (a) precipitation over Ni substrate and (b) adsorption over Cu substrate. The growth mechanisms have been studied by the use of two different carbon isotopes ^{12}C ^{13}C [88].

CVD on Cu has demonstrated more promising and successful results, with large graphene domain dimensions of up to 0.5 mm achieved by minimizing graphene nucleation density, even on polycrystalline Cu foil [107]. It has also been hypothesized that the electronic properties of graphene on Cu are comparable to that of freestanding graphene [87]. However the high temperatures at which graphene growth is seen ≈ 700 - 1070 °C can cause the sublimation of Cu step edges, but with a graphene surface layer the escape of Cu atoms is restricted and thus deforms the Cu surface which can act to perturb the graphene growth [87]. To minimize the surface roughness and grain boundary density of graphene one method is the Cu annealing. Pre CVD annealing is also important for obtaining a low graphene nucleation density.

The precursor flow in CVD is made up of a C source (methane, ethanol, methanol) as well as a buffer gas and hydrogen (H_2). The buffer gas is a neutral gas species such as Ar and is uninvolved in the growth mechanisms of graphene but is used to help keep a viscous flow and push oxides that bond with H out of the system towards the pump. H_2 is often used as a cleaning gas as it bonds to oxide species on the Cu surface or in the atmosphere, thus reducing Cu_2O and CuO contaminating surface species. It is used in both pre CVD annealing as well as in the growth process. The type of C source is important as it has proportionalities with the growth kinetics of graphene at the Cu surface. As some species need higher/lower temperatures and pressures for dissociation to atomic C, this will have an effect on the rate of growth and the continuity of graphene also. Gaseous hydrocarbon sources have been heavily investigated. In particular methane (CH_4) represents the standard to grow graphene in CVD technique. Another important precursor it is represented by ethanol [79], [81], [82], [84], [110], [111]. In fact, ethanol is cheaper than methane and the presence of O atoms accelerate the growth kinetics. Ethanol allow to obtain graphene film in few second rather than hour as reported in methane CVD [82]. It is very difficult to control the graphene growth in ethanol CVD and in particular to obtain isolated graphene domains with high quality and high crystallinity.

Typical CVD apparatus is reported in Figure 1.14a and a detailed discussion on the instrumentation used to grow the samples characterized in this thesis is reported in Chapter 3.

The rapid cooling of the substrate in inert atmosphere down to room temperature, is critical in suppressing formation of multiple layers [112].

It is fundamental to control the synthesis of graphene by controlling the CVD growth parameters such as temperature, gas composition, gas flow rate, deposition time as well as heating and cooling rate. Time dependence of experimental parameters is reported in Figure 1.14b.

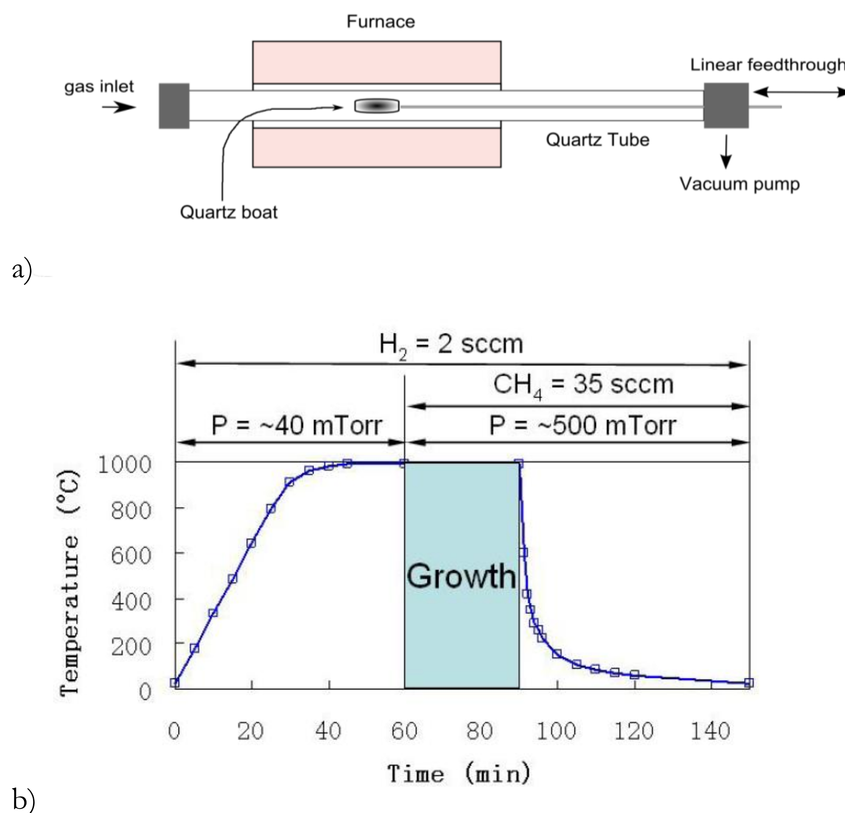

Figure 1.14. (a) Sketch of CVD system. (b) Time dependence of experimental parameters: temperature, pressure and composition/flow rate for graphene growth by methane (CH_4) in hydrogen (H_2) flow [54].

Compared to the other graphene synthesis processes, as previously reported, CVD growth on metal substrates has the distinct advantage of being able to provide very large-area graphene films of good crystalline quality and more easily transferrable to other substrates. The study of the effects of substrate pre-treatment, temperature, pressure, and gas flow are central in this thesis. These parameters have been optimized to control the growth of large area graphene in ethanol CVD.

1.4.5 Other growth methods

There are many other techniques to grow graphene, but it is unlikely that they will become commercially available in the next decade. Nevertheless, some of these methods have certain advantages and should be researched further. Surface-assisted coupling of molecular monomer precursors into linear

polyphenylenes with subsequent cyclodehydrogenation is an exciting way to create high-quality graphene nanoribbons and even more complex structures using a chemistry-driven bottom-up approach [113]. Molecular beam epitaxy has been used to grow chemically pure graphene [114], but it is unlikely to be used on a large scale because of its much higher cost than CVD methods. Laser ablation is a potentially interesting growth technique allowing the deposition of graphene nanoplatelets on arbitrary surfaces [115]. This relatively expensive method is in direct competition with the other ones, so it is unlikely to be widely used.

1.5 Transfer of CVD Graphene

Graphene, after growth, has to be transferred from metallic substrate to interest substrate, for characterization or to realize electronic device. The successful transfer from metal to a target substrate is crucial for the application of graphene to both research and industry. The transfer process can affect the quality of the transferred films and compromise their application in devices. Indeed, the removal and transfer process from the growth substrate to a more useful one is a critical step since it can provoke damages or cracks, resulting in discontinuous graphene films.

Several transfer processes have been developed and can be mainly classified as wet, when graphene is in contact with a liquid, or dry, when one face of graphene is protected from contacting any liquid, while the other is typically in contact with a polymer, eventually removed by solvents.

The first published transfer of graphene from a metal substrate was done in 2009 using graphene grown on Ni and was performed by using a protective layer of Poly-methyl methacrylate (PMMA, $C_5O_2H_8)_n$) [93], typically used in the silicon industry. Basically, a thin layer of PMMA is spin-coated on the graphene/substrate, then chemical etching of the metallic substrate is performed. Typical etchant are hydrochloric or nitric acid (HCl or HNO_3) and ammonium persulphate ($(NH_4)_2S_2O_8$). After etching, graphene film is transferred to a clean bath of deionized water for rinsing (graphene side down) and finally transferred to the substrate of interest (e.g., SiO_2/Si wafer).

Graphene strongly bonds to the surface (of most materials) via van der Waals interaction, the PMMA is then washed away using acetone (a solvent of PMMA) and thermal treatment leaves graphene on the insulating SiO_2 surface, Figure 1.15 shows the generic process.

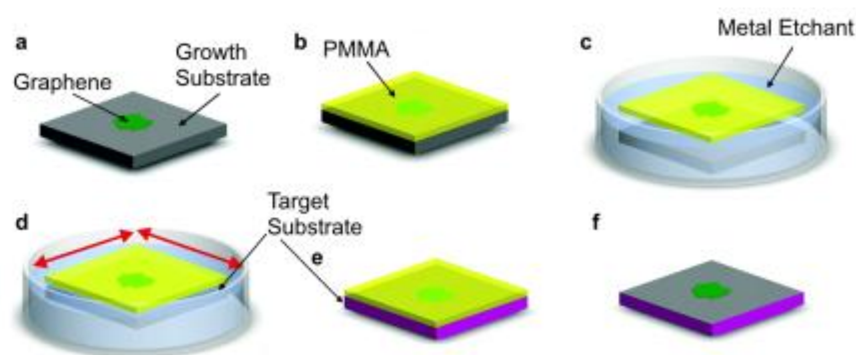

Figure 1.15. The wet PMMA support layer transfer process. a) Graphene grown via CVD on metal substrate. b) PMMA is spin coated onto the graphene surface. c) The metal growth substrate is etched away. d) The target substrate is used to scoop the graphene/PMMA sample out. e) The graphene/PMMA is allowed to dry to the target substrate surface. f) The PMMA is removed with a solvent or annealing [67].

Several parallel processes have been tested using a variety of etchants, polymer supports and methodology. The process represents the initial gold standard for graphene transfer, however significant issues still remain such as introduction of graphene wrinkle structure or graphene discontinuity, and PMMA residue on graphene, inducing defects and affecting its electronic properties [116].

Recently, a very efficient transfer method has been reported [117], based on the use of Cyclododecane ($C_{12}H_{24}$), a non-toxic and eco-friendly organic compound. Cyclododecane can be spin coated on graphene, and after assisting the wet etching of the copper catalyst, it completely sublimates at ambient conditions providing a clean means of transferring atomic-thick films, without introducing unwanted contaminants and thus not requiring any further restoring process [117]. Thus, it can be considered an eco-friendly process since it does not require the use of solvents for its removal and it can be in principle recovered after the process. The transfer method results simple, effective and capable of maintaining intact the intrinsic features of graphene films, in terms

of both properties and defects. The well-established method is currently used in place of the standard reported ones [117].

All sample grown and characterized in this thesis, and the solar cell realized and tested, have been transferred by using cyclododecane method. Further refinement of this promising technique is needed and a brief study of optimization of this process is discussed in Chapter 3.

2
Characterization techniques

In this chapter, the general principles behind the experimental equipment and techniques used over the course of this research will be outlined. The opening sections will describe the use of optical and electronic microscopy. Subsequently a brief explanation of how Raman spectroscopy was used and the ability to understand the electronic structure of graphene produced by Chemical Vapour Deposition. Scanning probe techniques and graphene field effect transistor will be also introduced to complete the electronic characterization of graphene. External quantum efficiency and extraction of photovoltaic parameters such as fill factor and power conversion efficiency will be described as tools to characterize solar cell.

2.1 Introduction

Several techniques are usually employed for carbon-based materials characterization. Among these, the most commonly used is Raman spectroscopy. It is the principal tool used to investigate the vibrational dynamics of carbon materials and to provide structural characterization. It is recognized to be unambiguously able to provide the fingerprint of the carbon materials as well as that of all the other Raman active materials.

Other supporting characterization techniques used in this thesis that will be discussed in the following are the Optical and Scanning Electron Microscopy (SEM). The complementary information about the morphology of the graphene have been obtained by using Atomic Force Microscopy (AFM). By using the interaction between a tip and the sample it is possible to determinate the morphology of sample, estimate the thickness of the graphene films and evaluate the quality of transfer methods. In order to obtain electronic information about the surface potential and electron mobility, Kelvin Probe Force Microscopy (KPFM) and graphene field effect transistor (GFET) have been used respectively. Finally, the photovoltaic parameters of solar cell integrating graphene and graphene based derivative have been extracted by

analyzing the external quantum efficiency and evaluating fill factor and power conversion efficiency from J-V curves acquired under standard illumination. Physical principles of each technique used in this research work will be discussed in this chapter.

2.2 Optical Microscopy

The difficult part of growing and characterize graphene is how to "see" graphene. In 2004 [2] Geim and Novoselov observed the monolayer graphene on oxidized silicon wafer for the very first time by employing interference-like contrast under optical microscope. When graphite flakes are deposited on silicon wafer with selected silicon oxide (SiO_2) coating thickness, thin flakes are sufficiently transparent to add to an optical path, which gives a feeble interference-like contrast with respect to an empty wafer. Although a number of modern visualization techniques, such as Atomic Force Microscopy (AFM) and Raman Microscopy are capable of characterizing monolayer graphene, none of these can find micron-sized graphene without using an optical microscope. The most efficient way to find monolayer graphene remains the same as when graphene was discovered and observed for the first time: search graphene flakes under optical microscopes.

Optical microscopy represents the most rapid optical methods to obtain detailed qualitative data from graphene samples and in particular allows a rapid and non-destructive characterization and identification of graphene. Optical microscopy is the first step of graphene characterization and by this analysis is immediately possible to estimate the number of graphene layers. Defining the graphene layer number using optical methods is possible depending by the substrate. In fact, free-standing graphene is invisible. Some optical methods such as contrast spectroscopy using a charge coupled device (CCD) [118] or total color difference methods [119] allow for an accurate differentiation between graphene layers, but these methods are complex and time-consuming if compared to using an optical microscope and the human eye. For characterization, graphene is often transferred onto a reflective substrate (typically Si) with a thin dielectric layer (typically SiO_2) separating the graphene

and substrate to enhance interference of incident light. The opacity of freestanding graphene is 2.3% for white light and can be defined from the Fresnel equations for transmittance (T) in the thin film limit $T_{optical} = 1 - \left(\frac{\pi\alpha}{2}\right)^{-2} \approx 0.977$ where $\alpha = \frac{e^2}{\hbar c}$ is the fine structure constant [120], [121]. The small percentage of light that is reflected from the graphene is sufficient to increase the optical path length of light when it is transferred to a dielectric/reflective substrate stack and hence causes a relative interference color change with respect to the substrate. For white light SiO_2 thickness should be ≈ 90 nm or ≈ 300 nm for maximum contrast [122]. It is possible also observe graphene on different substrate (Figure 2.16.). Using copper oxidation at 180°C is also possible to observe graphene on native substrate after the CVD process. This is possible because graphene avoids the oxidation of metallic substrate (Figure 2.16.b) [123].

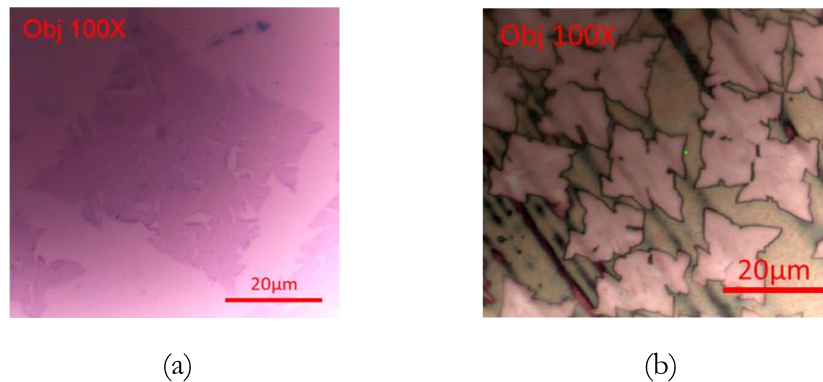

Figure 2.16. Optical image of graphene (a) on Si/SiO_2 and (b) on copper substrates.

2.3 Scanning Electron Microscopy (SEM)

A scanning electron microscope (SEM) consists of an electron optical column, where a beam of electrons is generated by a suitable source, typically a tungsten filament, and accelerated through a high voltage between 20 and 60 kV. First invented in 1938 [124], [125] and further developed in the 1950s [126] the scanning electron microscope has become a highly effective tool for imaging surfaces in many different scientific fields. SEM probes the surface of a conductive sample with a beam of medium energy (1-50 kV) electrons [127],

ensuring a very high spatial resolution imaging of the surface. Electrons are produced by an electron gun and accelerated by a high voltage applied to an anode (V_B). The beam is rastered back and forth to build up a complete image of the surface. The arrangement of magnetic lenses used to deflect and optimize the electron beam on the sample can be seen in Figure 2.17, in which the electron beam passes into the column and is concentrated via a condenser lens. The beam then passes into an objective lens which focusses the incident beam into a precise probe of diameter d. The magnetic lenses produce a rotationally symmetric magnetic field which the electron beam passes through. This causes electrons travelling through the magnetic field to feel a force allowing them to be carefully directed by small changes in the magnetic field to form a highly focused beam. SEM provides a substantially higher level of magnification than optical microscopes, accompanied by excellent depth of focus. This is the consequence of the beam geometry which ensures a large depth (~2 μm), in comparison to the probe size (~5 nm), remains in reasonable focus around the area of optimal imaging.

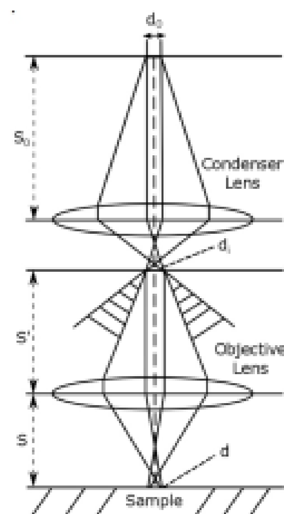

Figure 2.17. Schematic diagram of ray traces in a typical SEM, ray divergence is exaggerated for clarity.

The incident electrons (primary electrons) have several interactions with the sample and several emitted radiation characteristics can be measured, including backscattered electrons, secondary electrons, X-rays and Auger

electrons and their creation mechanisms are shown in Figure 2.18a. Each interaction can provide information on the material composition, surface topography or both. The penetration of electrons to different depths provides different signals as shown in Figure 2.18b. As graphene resides on the sample surface, the primary electron interaction with graphene is negligible. The closest measurable interactions to the surface and graphene are secondary electrons and Auger electrons (first few nm into the sample), but Auger electrons need specialist set-ups for detection. Secondary electrons are produced via inelastic collisions within the material, specifically with weakly bound electrons which may be ejected. The ejected electrons typically have an energy of $E \leq 50$ eV, meaning that those produced close to the surface will have enough energy to overcome the work function of 2-6 eV, escape the material and be measured [127].

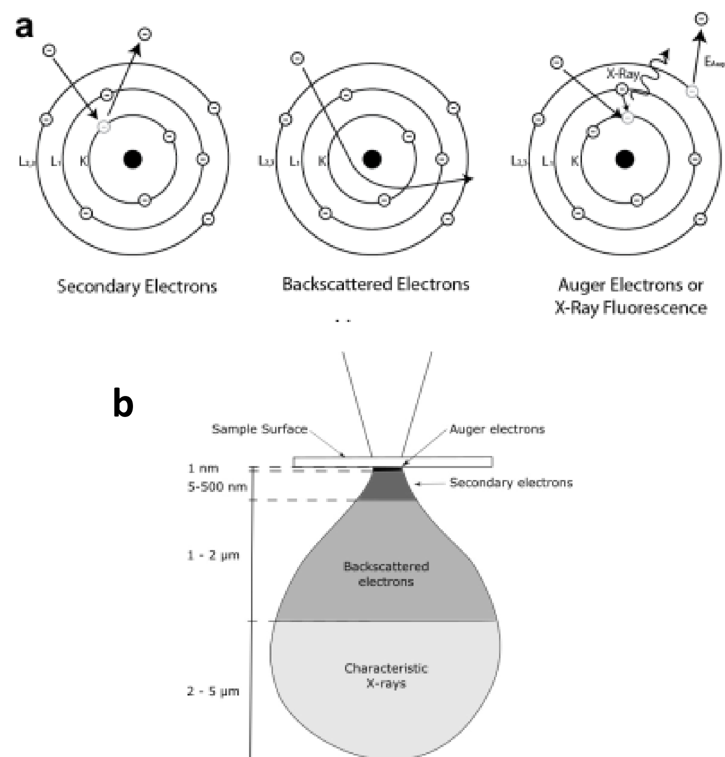

Figure 2.18. (a) Interaction of Radiation-matter interaction processes: backscattered electrons, secondary electrons, X-rays and Auger electrons and their creation mechanisms; (b) Schematic diagram of the interaction volume for electrons incident on a material. The penetration of electrons to different depths produces different imaging signals. Adapted from references [127].-

This causes the signal produced by secondary electrons to be highly surface sensitive and ideal for imaging graphene domains on Cu substrates. They can be used to determine the topography of the sample as their energy is not characterized by the chemical composition of the material and are often used to detect the presence of graphene due to their higher resolution compared to backscattered electrons. A general rule of characterization is that lower V_B creates better graphene contrast due to reduced penetration depth and greater probability of graphene interaction. The contrast of graphene with layer number cannot be said to be caused directly by graphene interaction with the incident electron beam due to the spatial resolution limited to ≈ 10 nm by aberrations and diffraction as well as the interaction volume of secondary electrons in graphene that is deeper than the graphene thickness. However, it is suspected that graphene acts as a potential barrier for electrons ejected from the underlying substrate and has an energy attenuating effect [128], as a consequence increasing the graphene layers will decrease the number of secondary electrons reaching the detector and thus reduce the intensity output of the signal over graphene layers (Figure 2.19).

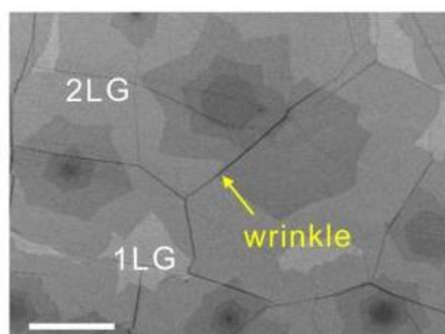

Figure 2.19. SEM micrographs of graphene on copper substrate: single and multilayer graphene on copper. Scale bar represents 20μm [129].

2.4 MicroRaman Spectroscopy

Micro-Raman spectroscopy is one of the most versatile, non-destructive, and high throughput methods to identify and characterize graphene. In this work, the main uses of the technique involved the identification of graphene structure, thickness and defects. The ambient condition of the measurement

without much need for sample preparation allows the facile acquisition of the Raman spectra with the lateral scale and resolution of optical microscopy (~ 1 μm).

2.4.1 Principles of Raman Spectroscopy

The Raman phenomenon was detected in 1928 by the Indian physicists Raman and Krishnan [130]. Raman spectroscopy is based on the inelastic scattering of light by crystal lattices or molecules where the incident light interacts with lattice vibrations (phonons) [131]. It can involve either emission (Stokes scattering) or absorption (anti-Stokes scattering) of phonons. The loss of incident light energy, EL (usually fixed in the visible – UV light range) leads to shift in the wavelength of the scattered light (measured in cm^{-1}) which depends on the electronic structure and phonon dispersion of the specimen. The photons exchange energy with crystal or molecule vibration modes, accomplished with electrons being the medium. The basics of the Raman scattering can be explained using classical and quantum mechanical theories. Both formulations are based on the idea that the origin of scattered radiation is considered to be the oscillating electric dipole moments induced in a molecule by the electromagnetic fields of the incident light waves [132].

In the classical approach, the incoming electromagnetic radiation can be described as a sinusoidal plane electromagnetic wave. The oscillating electric field (Eq. 2.11) induces a dipole moment in a molecule (Eq. 2.12):

$$E = E_0 \cos 2\pi \, \nu_0 t \qquad 2.11$$

$$p = \alpha E = \alpha \, E_0 \cos 2\pi \, \nu_0 t \qquad 2.12$$

where ν_0 is the oscillation frequency of the electric field and α is the polarizability of the molecule. The polarizability of a vibrating molecule is not a constant since it depends upon the molecular conformation which changes with the displacements of the nuclei during the vibrations. Let $q(t) = q_0 \cos(2\pi\nu_{vib} t)$ be the variation of the nuclear distance during a vibration at frequency ν_{vib}, q_0 being the maximum variation.

Although the variation law of $\alpha(t)$ is not known, it can be approximated at the first order as:

$$\alpha = \alpha_0 + \left(\frac{\partial \alpha}{\partial q}\right)_0 q + \cdots \qquad 2.13$$

where α_0 is the polarizability of the molecule in the equilibrium geometry and the second term represents the polarizability change due to the molecular vibration.

The classical theory of electromagnetism states that an electric dipole oscillating at frequency ν emits electromagnetic radiation at the same frequency with intensity given by:

$$I = \frac{16\pi^4\, \nu^4}{3c^2}\, |p|^2 \qquad 2.14$$

thus, for $\nu = \nu_0$

$$I = \frac{16\pi^4 \nu_0^4}{3c^2}\, \alpha^2 E_0^2 \cos^2(2\pi\, \nu_0 t) \qquad 2.15$$

By considering the change of α due to a molecular vibration, it is possible to obtain the expression of the oscillating dipole (Eq. 2.16) and the emitted intensity (Eq. 2.17):

$$\begin{aligned} p(t) = {} & \alpha\, E_0 \cos(2\pi\, \nu_0 t) \\ & + \left(\frac{\partial \alpha}{\partial q}\right)_0 \frac{q_0 E_0}{2} \cos[2\pi(\nu_0 + \nu_{vib})t + \varphi] \\ & + \left(\frac{\partial \alpha}{\partial q}\right)_0 \frac{q_0 E_0}{2} \cos[2\pi(\nu_0 - \nu_{vib})t + \varphi] \end{aligned} \qquad 2.16$$

and

$$I = \frac{16\pi^4}{3c^2} E_0^2 \left\{ \nu_0^4 \alpha_0^2 \cos^2(2\pi\nu_0 t) + (\nu_0 + \nu_{vib})^4 \left[\left(\frac{\partial\alpha}{\partial q} \right)_0 \frac{q_0}{2} \right]^2 \cos^2[2\pi(\nu_0 + \nu_{vib})t + \varphi] + (\nu_0 - \nu_{vib})^4 \left[\left(\frac{\partial\alpha}{\partial q} \right)_0 \frac{q_0}{2} \right]^2 \cos^2[2\pi(\nu_0 - \nu_{vib})t - \varphi] \right\} + cross - terms \quad 2.17$$

An oscillating dipole moment emits therefore with the frequency of the incident field (Rayleigh scattering) and in phase with it. In addition, the molecule radiates with two frequencies that are modulated by the frequency of the excited normal vibration and phase shifted (Raman scattering). The Raman scattered light has a lower frequency than the incident light (Stokes-Raman scattering) or a higher frequency (anti-Stokes Raman scattering) and are in both case incoherent because of the phase factor [132].

In the spectrum of the scattered radiation, the new frequencies are termed Raman lines, or bands, and they constitute the Raman spectrum, as depicted in Figure 2.20, where the typical recorded Raman spectrum of carbon tetrachloride (CCl_4) is reported.

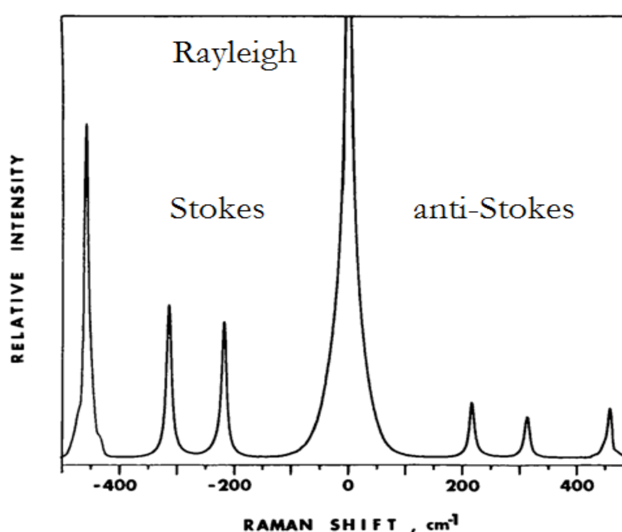

Figure 2.20. Raman spectrum of carbon tetrachloride showing Rayleigh, Stokes and anti-Stokes Raman bands.

The patterns of bands observed in the spectra are entirely consistent with the classical theory. The spectra also show that Rayleigh scattering is much more intense than Raman scattering, and that Stokes Raman scattering is more intense than anti-Stokes Raman scattering with the ratio of the intensity of anti-Stokes to Stokes Raman scattering dependent on ν_{vib}. One of the failures of the classical theory is that the ratio of the Stokes and anti-Stokes intensities should theoretically be <1:

$$\frac{I_{Stokes}}{I_{anti-Stokes}} = \left(\frac{\nu_0 - \nu_{vib}}{\nu_0 + \nu_{vib}}\right)^4 \quad 2.18$$

Actually, as experimentally shown it is not correct since Stokes Raman scattering is more intense than the anti-Stokes Raman scattering. The quantum theory of the Raman scattering overcomes this problem.

When light beam aims at substances, the electromagnetic wave of the light beam induces the electric dipole moment $p = \alpha E$ in the material. Here α is the polarizability of the material and E is the electric field of the light wave. The electric dipole moment will then exert electrostatic force on ionic core of atoms in the substance and exchange energy with vibration modes. The amount of energy the phonon can accept or release is quantized due to the quantization of phonon energy as shown in Figure 2.21.

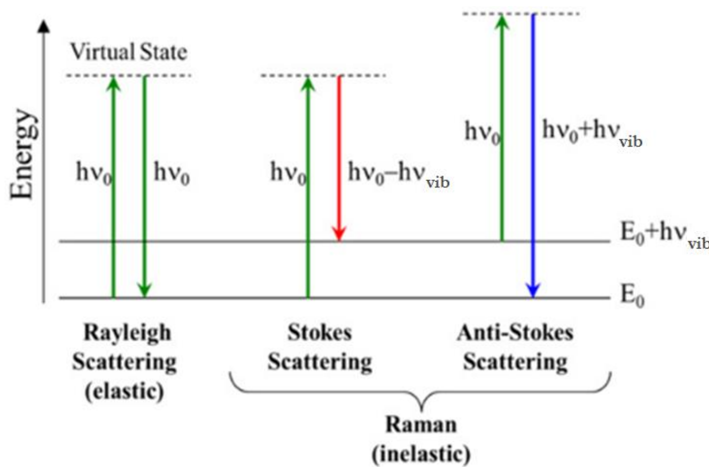

Figure 2.21. Schematic representation of quantum energy transitions for Rayleigh and Raman scattering.

The electric field of frequency ν excites the lower energy phonons to a higher virtual energy level. When the phonons relax back to a ground state, it will release the surplus energy by means of emitting light indirectly. Depending on the relative position of original and final state, the light emitted by the material comprises three parts as illustrated in Figure 2.21. If the phonon relaxes to exactly the same ground state that it has been actuated from, the scattered light has the same wavelength of the incident light (left part of Figure 2.21). Such process represent the Rayleigh scattering, which is elastic and the photon gain or lose no energy. On the other hand, the phonon can either relax back to a higher (middle part) or lower (right part) energy level than the original one, absorbing or releasing an amount of energy ΔE_P, and the scattered light frequency will shift by $\Delta E_P/h$ where h is the Planck's constant. The lower frequency component is the Stokes line, while the higher frequency one anti-Stokes line [133]. In order for an anti-Stokes process to take place, the system must be in an excited vibrational state in the first place. In typical conditions, this may only occur through thermal excitation and this implies that the anti-Stokes signal depends at equilibrium on temperature. The Stokes lines are more intensive than anti-Stokes line because it is more likely that the low energy phonons are excited to higher states. In the quantum mechanical model the intensity depends on the occupation of the initial state. This is determined by the Boltzmann distribution. Thus, the intensity ratio is dependent on temperature T as:

$$\frac{I_{amti-Stokes}}{I_{Stokes}} = \frac{(\nu_0 + \nu_{vib})^4}{(\nu_0 - \nu_{vib})^4}\frac{N'}{N} = \frac{(\nu_0 + \nu_{vib})^4}{(\nu_0 - \nu_{vib})^4}\exp\left[-\frac{\Delta E}{kT}\right] \quad 2.19$$

where N and N' are the number of molecules in the ground and excited states.

Usually Raman measurements are performed considering only Stokes lines. In fact, since the anti-Stokes lines are due to the scattering from molecules in excited states, the intensity of the anti-Stokes lines is considerably lower than Stokes lines due to scattering from molecules in the ground state, simply because of the lower population of the excited states with respect to ground state, according to the Boltzmann statistics.

The vibrational frequency depends on the binding strength and is a characteristic of the molecule. Thus, the shift in frequency of the scattered light from a given material is unique and gives information about the vibrational modes of the molecules, resulting in an unambiguous identification of the sample.

Typical experiment consists in a sample illuminated with a laser beam. Back-scattered radiation is collected with an objective lens and sent through a monochromator. The wavelength corresponding to the Rayleigh scattering is filtered out, while the remaining light is dispersed onto a diffraction grating. The intensity of the shifted light versus frequency results in a Raman spectrum of the sample. Generally, Raman band positions will lie at the frequencies corresponding to the energy levels of the vibrations of different functional groups. Rayleigh band lies at 0 cm^{-1}.

The interpretation of the Raman spectra of carbonaceous materials has been widely discussed in the literature with studies covering a wide range of carbon structures [134]–[136]. As for the interpretation of the Raman spectra, an understanding of the phonon dispersion is essential. Therefore, by considering the interaction of the lattice vibrations with the electromagnetic radiation, we can gain insight into the Raman spectra of the crystals [137], [138]. Considering a diatomic linear lattice as shown in Figure 2.22, the mass of the atoms are taken as M_1 and M_2, respectively. The lattice spacing is 2a.

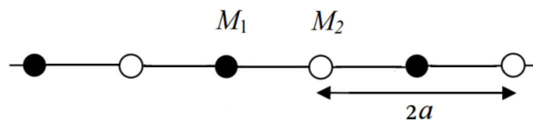

Figure 2.22. Diatomic linear lattice with M_1 and M_2 atoms mass and lattice spacing 2a.

If it is assumed nearest neighbor interaction only, by imposing the periodic boundary conditions, the solutions of motion equations are:

$$\Omega^2 = C\left[\left(\frac{1}{M_1}+\frac{1}{M_2}\right) \pm \sqrt{\left(\frac{1}{M_1}+\frac{1}{M_2}\right)^2 - \frac{4\sin Ka}{M_1 M_2}}\right] \qquad 2.20$$

with C the force constant between adjacent atoms. The equation gives the relationship between Ω and k, called the dispersion relation $\Omega = \Omega(\mathrm{k})$. For each wavevector k two Ω values are obtained (Figure 2.23). The solution corresponding to the plus sign is called the optical branch. It can be shown that for transverse displacements of the particles at $k = 0$, the two atoms vibrate against each other with a fixed center of mass. This shows that the two atoms of masses M_1 and M_2 move in the opposite directions. If these atoms carried charges of opposite sign, this type of vibration could be excited by an optical field and hence the name optical branch. The solution corresponding to the minus sign is called the acoustical branch and has the characteristic of being linearly proportional to k for small k values [138]. In general, electromagnetic waves propagating within the crystal will interact only with lattice vibrations of the same wavelength and frequency.

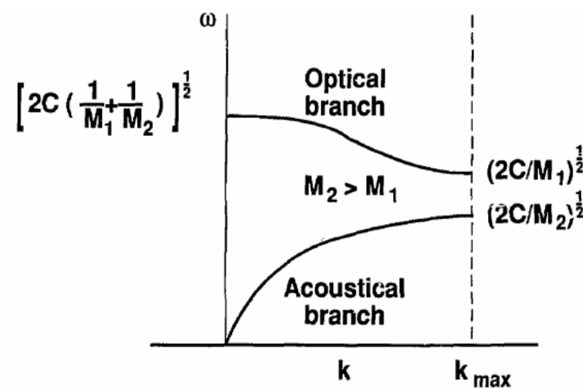

Figure 2.23. Dispersion curve in biatomic crystal. Optical and acoustical branches are shown.

The above discussion can be extended to the case of more than two atoms per unit cell. For p atoms in the primitive cell there will be 3p equations of motion. Three equations will correspond to the acoustical modes. The remaining $3(p - 1)$ modes will each have a nonzero frequency in the long wavelength limit and are the optical modes [138].

Since the unit cell of monolayer graphene contains two carbon atoms, A and B, there are six phonon dispersion bands, in which three are acoustic branches (A) and the other three are optic (O) phonon branches [136] (Figure 2.24). Specifically, for one acoustic branch (A) and one optic (O) phonon

branch, the atomic vibrations are perpendicular to the graphene plane, and they correspond to the out-of plane (o) phonon modes. For two acoustic and two optic phonon branches, the vibrations are in-plane (i) [136]. Generally, the phonon modes are classified as longitudinal (L) or transverse (T) according to vibrations parallel with the A-B carbon-carbon directions or perpendicular to it. Therefore, as shown in Figure 2.24, along the high symmetry ΓM and ΓK directions, the six phonon dispersion curves are assigned to LO, iTO, oTO, LA, iTA, and oTA phonon modes [136].

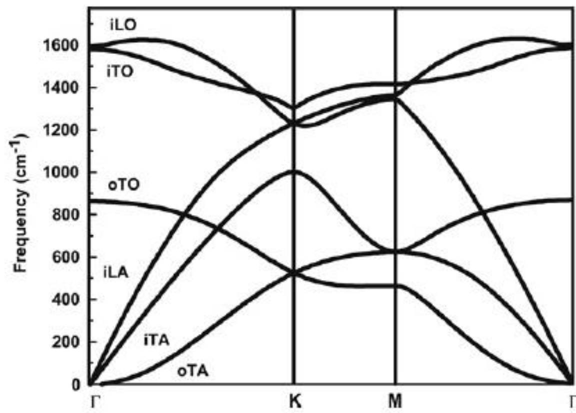

Figure 2.24. Phonon dispersion relation of graphene showing the iLO, iTO, oTO, iLA, iTA and oTA phonon branches [136].

In the inelastic scattering of light in a crystal, an incident photon of wave vector k_i and frequency ω_i is widespread in the direction determined by the wave vector k_s. The frequency of the scattered photon changes to a new value ω_s, as a phonon lattice (wave vector q_j and frequency Ω_j) is created or destroyed. The conservation conditions for Raman scattering are the energy (Eq. 2.21) and momentum conservation (Eq. 2.22):

$$\hbar\omega_i = \hbar\omega_s \pm \hbar\Omega_j \tag{2.21}$$

$$\hbar k_i = \hbar k_s \pm \hbar q_j \tag{2.22}$$

The number of emitted phonons before relaxation of the lattice can be one, two, and so on, respectively, one-phonon, two-phonon and multi-phonon Raman processes. The order of a scattering event is defined as its number in the sequence of the total scattering events, including elastic scattering by an

imperfection (such as a defect or edge) of the crystal. The lowest order process is the first-order Raman scattering process which gives Raman spectra involving one-phonon emission [139].

Raman scattering measurements in this thesis were carried out at room temperature with a HORIBA Scientific LabRAM HR Evolution Raman spectrometer with an integrated Olympus BX41 microscope and 532 nm laser (2.33 eV) was focused on the sample surface using a 100 objective with a spot size of approximately 1 μm. Low laser power of < 1 mW minimized degradation or damages of graphene. The Raman spectra were acquired by filtering the scattered light through a monochromator over the range of 1200 to 3300 cm^{-1} with a resolution of ~ 1 cm^{-1}. The system also contains a motorized stage that can automatically capture a map of Raman spectra in the x and y directions.

2.4.2 Raman Features of Graphene

The most prominent features that are commonly found in the Raman spectra of graphene are the G peak appearing at 1582 cm^{-1} and the 2D peak at about 2700 cm^{-1}[135]. In the case of disordered samples, or at the sample edges, the disorder-induced D-peak is also detected around 1350 cm^{-1}. The activation mechanism of the peaks is schematically shown in Figure 2.25. In detail, the G peak is associated with the doubly degenerate (iTO and LO) phonon mode (E_{2g} symmetry, due to the bond stretching of all pairs of sp^2 atoms in both rings and chains, Figure 2.26) at the Brillouin zone center. In fact, the G-band is the only band coming from a normal first order Raman scattering process in graphene [136], [141]. D peak is due to the A_{1g} breathing mode of six-atom rings (Figure 2.26) and is not Raman active for pristine graphene, but can be activated when symmetry is broken by structural disorder, as edges or defects. It originates from a second order process involving one iTO phonons and one defect around *K* [95]. The two scattering processes consist of one elastic scattering event by defects of the crystal and one inelastic scattering event by emitting or absorbing a phonon.

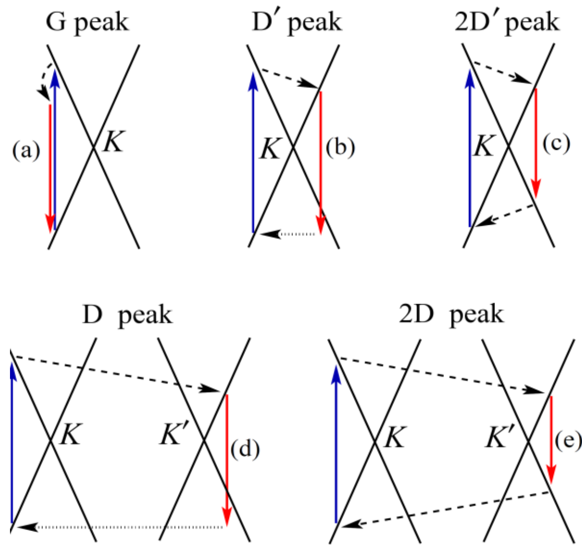

Figure 2.25. Role of the electron dispersion (Dirac cones, shown by solid black lines) in Raman scattering: (a) intravalley one-phonon G peak, (b) defect-assisted intravalley one-phonon D peak, (c) intravalley two-phonon 2D peak, (d) defect assisted intervalley one-phonon D' peak, (e) intervalley two-phonon 2D' peak. Vertical solid arrows represent interband transitions accompanied by photon absorption (upward arrows) or emission (downward arrows) [140].

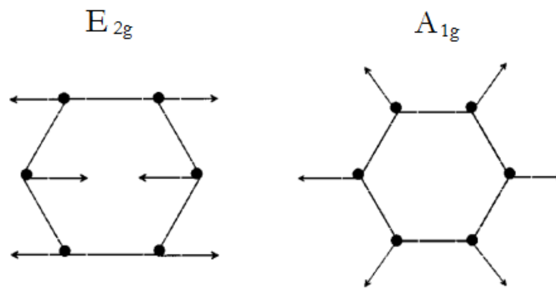

Figure 2.26 Carbon motions in the G modes namely E_{2g} and D modes namely A_{1g} [134].

The 2D peak, approximately twice of the D band frequency, originates from a second-order process too, involving two iTO phonons near the *K* point [136]. The two involved phonons give rise to inelastic scattering events. This double resonance mechanism is an inter-valley process that connects points in circles around nonequivalent *K* and *K'* points in the first Brillouin zone of graphene.

A weaker feature can be also detected, namely D’, centered roughly at 1620 cm^{-1}. The double resonance process responsible for the D’ band is an intra-valley process, since it connects two points belonging to the same circle around the *K* or *K’* point. Finally, 2D' peak is the second order of D' peak.

The typical graphene Raman spectrum is shown in Figure 2.27.

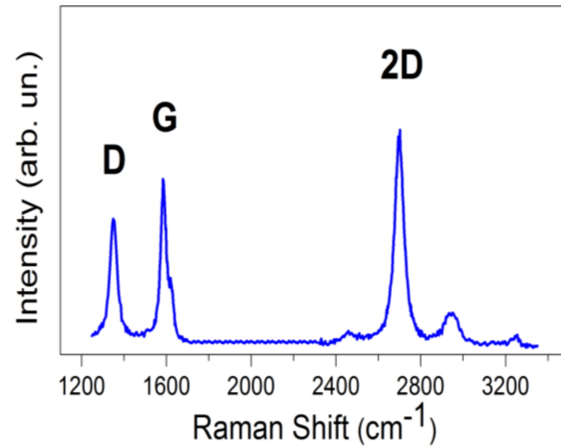

Figure 2.27. Typical Raman spectrum of graphene showing the main Raman features, the D, G and 2D bands.

The D band intensity to the G band intensity ratio I_D/I_G serves as an indicator for degree of disorder [134], [142]. Traditionally, the relationship between I_D/I_G has been described by the Tuinstra and Koenig relation in nanocrystalline graphite where I_D/I_G is inversely proportional to the mean grain size, L_a [143]. This relation is expected to be held until $L_a \sim 2\ nm$ where the significant proportion of ideal sp^2 rings within the sample starts to decrease to reduce I_D/I_G. Recently, vacancy-like defects with the mean inter-defect distance, L_D, has been shown to give rise to D peak with relationship, $I_D/I_G \propto 1/L_D^2$ for $L_D > 10\ nm$ [144]. Below $L_D{\sim}10\ nm$, I_D/I_G still increases till about $I_D/I_G{\sim}14$ at EL = 2.41 eV and decreases as $I_D/I_G \propto L_D^2$ for $L_D < 3\ nm$. In low defect regime, where I_D/I_G increases with the degree of disorder, it has been recently shown that by comparing I(D) with the intensity of another small defect related, D’ peak $I_{D'}$ at ~1620 cm^{-1}, which is generated by the intravalley process, the nature of defect can be identified as vacancies [where $I_D/I_{D'}{\sim}7$], sp^3 functionalization induced defects [$I_D/I_{D'}{\sim}13$], and grain boundaries [$I_D/I_{D'}{\sim}3.5$] [145]. Since a typical graphene sample in a real

condition cannot contain purely one type of defects, the precise identification and quantification of the defects, however, remain as a challenge. It must also be noted that the D peak cannot identify other kinds of disorder that are not Raman active, but still may degrade the electronic properties of graphene. They include zigzag edges, physically adsorbed dopants, and uniaxial and biaxial strains [144]. The 2D band (also known as G' peak) which occurs at twice the frequency of D peak (~ 2700 cm^{-1} at EL = 2.41 eV) corresponds to the overtone of D band [134]. This process involves two electron scattering events by phonons of opposite momentum (q, -q) so that the total momentum is conserved. This makes the 2D band Raman active even for a defect free graphene lattice with EL dependent dispersive relationship (~ 100 cm^{-1}/eV) [146]. The shape of the 2D peak is a very useful indicator to identify stacking order and thickness of the graphene layers. The monolayer has a single Lorentzian 2D peak with a narrow FWHM (~25 cm^{-1}) [136]. For turbostratic multilayers the peak tends to get broader (FWHM > 40 cm^{-1}) and shifted toward higher wavelength (> 10 cm^{-1}). In AB stacked few layer graphene where the interlayer interaction is more significant, the 2D peak can be de-convoluted into four Lorentzian peaks with FWHM of ~ 24 cm^{-1} due to the splitting of the electronic band structure in valence and conduction bands [136]. The evolution of the 2D bands can be a useful indicator for the thickness identification of AB stacked multilayer. For higher thicknesses (> 10 layers), 2D band approaches that of natural graphite which is described by a convolution of two Lorentzian peaks. In the case of G band, the E_{2g} modes are no longer degenerate in few layer graphene and split into the symmetric (E_g) and anti-symmetric (E_u) modes leading to the G peak broadening or splitting especially for supported or doped few layer graphene [136]. Raman spectroscopy also can determine the degree of mechanical strain and doping in monolayer graphene.

In CVD graphene, the shape difference of the 2D-peak for one or more than one layer could be not as clear as in exfoliated graphene, due to the lower electronic coupling between layers with not-ordered stacking. A narrow Lorentzian line (~30–40 cm^{-1}) can be used to fit the 2D-peak of both 1L and 2L CVD graphene, while for number of graphene layer ≥ 3 the width of 2D (Lorentzian) peak increase up to ~70 cm^{-1}. The 2D to G intensity ratio (I_{2D}/I_G)

is used as a qualitative parameter to evidence the presence of very few graphene layers, being in this case $I_{2D}/I_G > 1$.

In the case of CVD graphene, which is produced at a high temperature, a large biaxial compressive stress is induced during cooling due to the mismatch between the thermal expansion coefficients of the graphene overlayer and substrate. The 2D and G peak will blue-shift by up to ~30 cm^{-1} and ~20 cm^{-1}, respectively with biaxial strain of -0.5 % as determined by the CVD graphene grown on Cu at high temperature (> 1000 °C) [147]. Doping can always be present in graphene due to the wet processing, substrate, unintentional contamination, air, moisture, and substrate that lead to changes in the Raman spectra [148], [149]. Das et al. [23] has observed the shifts in the G and 2D peaks by electrochemically doping graphene in a top-gated structure where the 2D peak is blue-shifted by up to 15 cm^{-1} by p doping ($n_h \sim 3 \times 10^{13}\ cm^{-2}$), and red-shifted by up to 10 cm^{-1} with n-doping ($n_e \sim 3 \times 10^{13}\ cm^{-2}$). On the other hand, G peak always blue-shifts upon both types of doping (~20 cm^{-1} when $n_e = 3 \times 10^{13}\ cm^{-2}$). The ratio I_G/I_{2D} and the FWHM are to also increase due to doping. Recently, for twisted multilayers, misorientation angle dependent symmetry conditions have been shown to generate additional double resonance Raman scattering process resulting in additional Raman peaks near the D peak. They are called either R band [150] or I band [151]–[153]. These peaks have an important implication in the study of multilayers produced by CVD or solution-processed films where stacking orders different from Bernal stacking are present. In addition to the R band, also recently, C band has been found at a very low wavenumber (30 – 50 cm^{-1}) which arise from in-plane E^{2g} shear mode and it tends to red-shift with increase in number of graphene layers due to the interlayer interactions [154].

2.5 Atomic Force Microscopy (AFM)

Atomic force microscopy (AFM) has been utilised for several parts of this thesis so it is useful to give an overview of its mechanism and related techniques. AFM has been primarily used as an imaging tool to investigate surface contamination and roughness as well as to determine the thickness of

the graphene domains. The field of scanning probe microscopy (SPM) was born with the inventions of the first scanning tunneling microscope (STM) [155] and atomic force microscope [156] (AFM) in the 1980s. AFM became the instrument of choice for nanoscientists interested in areas of biology, chemistry and physics throughout the world. The primary function of an AFM is to produce nanoscale topographical images of surfaces by probing the forces encountered at the surface, but AFM also allows the measurement of surface properties such as stiffness, elasticity and potential. The AFM is a combination of the principles of STM and the stylus profilometer, but while STM imaging is confined to conducting surfaces, the forces of both conducting and insulating surfaces can be mapped using AFM. The most striking difference between AFM and STM is that instead of a static tip measuring the electron tunnelling effect, AFM typically requires a cantilever to measure the surface forces. In all cases SPM techniques involve measuring physical properties with a very fine, needle like probe close to the sample surface. The major strengths of SPM techniques are the following:

1. High lateral resolution: many different properties can be measured on very local scale, less than 10 nm.
2. High vertical resolution, which can be below 1 Å: surface topography can be measured with high accuracy–important for investigating surface properties.
3. Large degree of flexibility in the measured properties; mechanical, electrical, magnetic and optical.
4. SPMs can be used invasively to perform lithographic patterning [157] and even manipulation/arrangement of single molecules [158].

AFM has become a widely used tool in investigations of material surfaces on the nanoscale. Graphene is by definition entirely composed of surface and AFM is a tool that has been widely used in graphene research. Most commonly, AFM is used to image surface topography but quantitative measurements can be made; mechanical properties of graphene such as stiffness [45] and friction [159] have been investigated with these techniques for instance. Another important technique is the Kelvin Probe where a probe is used to locally map

potential of a sample [160]. In this section, the theory of the AFM will first introduce and how the measurements can be made will be explained. The general idea behind AFM is that a needle like probe (Figure 2.28) with a very sharp tip is brought into contact with the surface of a sample and scanned over the surface by use of a piezoelectric motor.

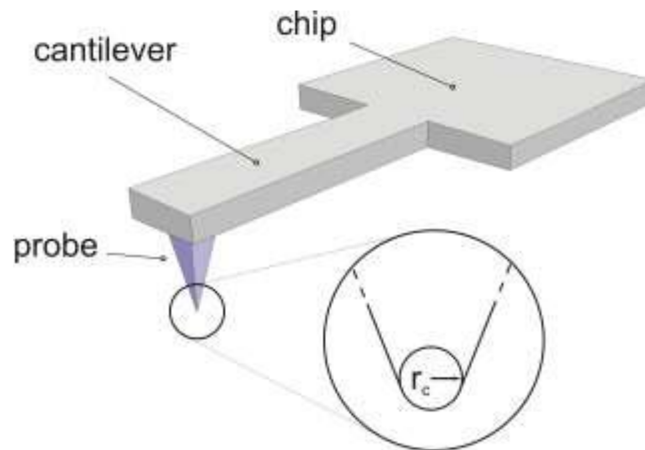

Figure 2.28. Sketch of an AFM probe showing the tip's radius of curvature r_c

The sample-probe interaction can be measured and the height of the tip is usually adjusted accordingly to maintain a constant interaction force; this can be interpreted as the surface topography. The technique and apparatus allow measurement of very localised forces and so samples can be mapped with a resolution in the subnanometer range in the vertical dimension and better than 10 nm in the lateral dimension. The precision in the lateral dimension is limited by the probe's radius of curvature r_c (Figure 2.28). The lateral resolution of AFM is typically limited by the tip radius and the condition of the tip. The typical materials used in the tips are silicon and silicon nitride, which have high hardness and stiffness. The radius of curvature of typical Si/Si_3N_4 based tip is not usually sharper than 2-3 nm. In ambient conditions, the maximum lateral resolution of 5 nm can be achieved. However, tips can easily worn out and attract small loose particles reducing the lateral resolution. Artefacts and ghost images can be seen in an AFM image produced by a damaged tip which needs replacement (Figure 2.29).

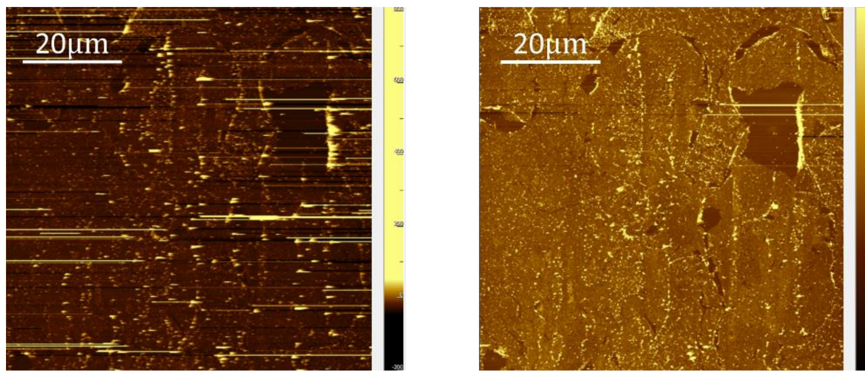

Figure 2.29. AFM image of graphene film: (a) image with artefacts due to contaminations of the sample that can damage the tip, (b) same graphene film region after measurement post-processing. In (b) the artefact due to the tip are eliminated and tears in the film are visible.

The height resolution in the vertical direction is expected to be as small as Angstroms, however, due to the effect of surface adsorbates in ambient condition, the measured thickness can be much thicker than the actual thickness [135], [161]–[163]. Therefore, a caution must be exercised when determining number of layers of multilayer stack of graphene as it can overestimate the thickness. Other practical limitations of AFM are the low scan speed, smaller scan area (typically < 100 μm × 100 μm) compared to SEM and optical microscope, and difficulty in imaging large features with height differences greater than 1 μm.

2.5.1 Probing Forces with a Cantilever

A topographical image of a surface can be generated by using an AFM measuring the forces acting on the sharp tip of an AFM cantilever while the tip is scanned over the sample surface. The surface forces are experienced by the cantilever tip due to the close proximity of the tip to the surface of the sample (down to sub-nanometre separation). A feedback mechanism adjusts the cantilever-sample distance so the average force on the tip is constant and the variation in cantilever-sample distance is recorded. Topographical AFM images are produced starting from this data. To move the sample, Piezoelectric transducers are necessary for the movement of the cantilever system in the Z direction - which requires a feedback loop. Piezoelectric transducers are also

incorporated into the mechanical design of an AFM to allow movement of the sample with respect to the probe in the X-Y plane. Depending on the mode of operation (Contact Mode, or Dynamic Methods) the cantilever of an AFM oscillates either at or close to its natural resonant frequency, f_0, while it scans the sample surface. The amplitude of these oscillations is of the order of 0.01-100 nm depending on the AFM mode of operation. There are several ways to excite the cantilever, acoustically, magnetically or electrically. The latter technique is associated with piezoresistive cantilevers and tuning forks. The acoustic (also called mechanical) excitation of the cantilever is a commonly adopted method that requires a piezoelectric actuator attached in close proximity to the cantilever-tip ensemble, as shown in Figure 2.30.

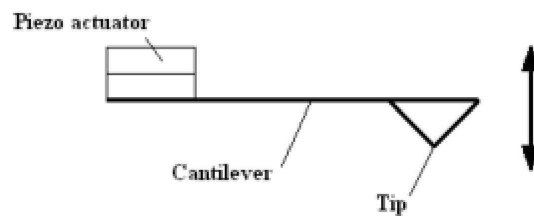

Figure 2.30. Diagram of a piezoelectric actuator exciting a cantilever, the oscillatory motion of the cantilever is indicated.

When an oscillating voltage is applied to the piezoelectric actuator, the piezo vibrates and thus the cantilever oscillates. The frequency of the waveform applied to the piezo can be varied to modify the oscillation frequency of the cantilever. By measuring the displacement of the cantilever as the cantilever oscillates at a range of frequencies, the value of f_0 can be acquired.

Cantilever Motion Detection

When the AFM was first developed by Binnig, Quate and Gerber [156], an STM system was used to monitor the cantilever displacement. Although electron tunnelling as a sensor was extremely sensitive, a technique that was not as prone to surface contaminant degradation but still provided sub-Angstrom resolution without perturbing the cantilever was preferred. Optical methods are the most common motion detection systems incorporated into ambient condition AFMs, which are divided into interferometry and beam deflection

techniques. A laser beam is incident on the cantilever and the reflected light detected by a four-piece photodiode. This gives the four signals labelled A, B, C and D in Figure 2.31 and their relative proportions depend on the laser spot position and hence the cantilever motion can be deduced. These variations are mapped as a function of lateral position and hence local information is revealed about the sample surface.

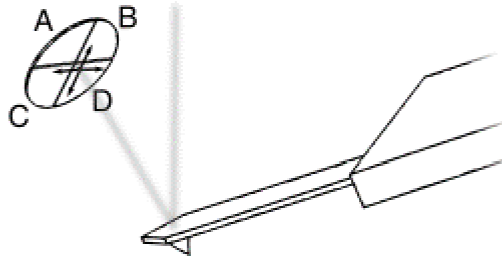

Figure 2.31. Sketch the laser beam deflecting onto the quadrant photodiode.

Noise Considerations and Optimal Resolution

Topographical images of a surface can be generated using an AFM and there are two separate resolutions, 'lateral' and 'vertical'. The vertical resolution is limited by both noise from the detection system and thermal fluctuations of the cantilever. In general, the lateral resolution depends on tip size, tip-surface separation and tip-surface force. Mechanical noise can cause a significant problem in vertical resolution for AFM. However, from Reference [164], the immunity of an AFM to external vibration depends on the frequency, f, of the vibration relative to the lowest resonant frequency, f_0, of the mechanical system. The amplitude of the relative tip displacement due to noise is attenuated by a factor (f/f_0) in the limit $f \ll f_0$. Thus if the lowest resonant frequency of a cantilever is greater than 20 kHz, a typical 20 Hz building vibration of amplitude 1 μm results in relative vertical tip motion of less than 0.01Å, nearly insignificant. Cantilevers have a very high value of f_0 so the limiting factor is typically the AFM mechanical structure, thus mechanical components that are rigid and compact are constructed to reduce the effect of mechanical noise. The tip radius must be as sharp as possible to minimise any

broadening effects in the AFM images. Thus, atoms in the tip further from the sample than the tip apex will contribute to the total force experienced by the AFM cantilever, rather than just the tip apex. Therefore, surface features that are smaller than the tip radius can appear broader. Cantilevers can be microfabricated from silicon, SiO_2 or Si_3N_4 using photolithographic techniques to achieve a sharp tip apex. This technique can produce cantilever lateral dimensions in the order of 100 μm and 1 μm in thickness.
There are several AFM operational modes and for the highest quality images the mode selected typically depends on the surface being studied.

2.5.2 Mode of operation

The different modes of AFM operation can be segregated into 'contact mode' and 'dynamic methods', often called non-contact AFM (NC-AFM). Tapping Mode AFM (TM-AFM) is a particular non-contact mode. Dynamic modes can be further organised into amplitude modulation AFM (AM-AFM) and frequency modulation AFM (FM-AFM) modes.

Contact Mode AFM (C-AFM)

AFM was originally only operated in contact mode, where the cantilever is in physical contact with the surface while the sample surface is scanned and the static deflection of the cantilever is recorded. Figure 2.32 shows a diagram of a cantilever in contact mode.

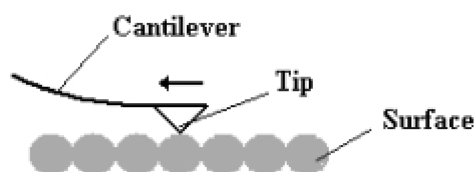

Figure 2.32. Diagram of a contact mode AFM, the cantilever scans across the sample whilst in direct contact with the sample.

However, the contact between the tip and atoms of the surface during the measurement, can damage the surface itself. In contact mode AFM has a loading force of 10^{-7} N to 10^{-11} N. Atomic resolution has been achieved in

contact mode for graphite in 1987 [165] and has also been achieved for other layered materials such as molybdenum sulphide and boron nitride in 1988 [166].

Non-Contact Mode AFM (NC-AFM)

In contact mode the interaction is dominated by relatively short-range repulsive interatomic forces. When the tip is displaced from the sample by 10-100 nm and an oscillating cantilever is adopted, the tip is subjected to longer range forces - such as magnetic, electrostatic and van der Waals forces. The tip-cantilever ensemble can be modelled as a point-mass spring, when driven, the motion of the tip can be approximately described by a non-linear, second-order differential equation, as in Eq. 2.23.

$$m\ddot{z} + \frac{m\omega_0}{Q}\dot{z} + kz = F_{ts} + F_0 \cos(\omega t) \qquad 2.23$$

F_0 and ω are the amplitude and angular frequency of the driving force respectively. Q, ω_0 and *k* are the quality factor (or Q-factor), angular resonant frequency and the spring constant of the free cantilever respectively [167]. F_{ts} contains the tip-surface interaction forces in the Z direction. In the absence of any tip-surface forces (that is when the tip is away from the surface) $F_{ts} = 0$ and Eq. 2.23 describes the motion of a forced harmonic oscillator with damping. By substituting $F_{ts} = 0$ into Eq. 2.23, the shape of the resonance curve, as illustrated in Figure 2.33, can be described.

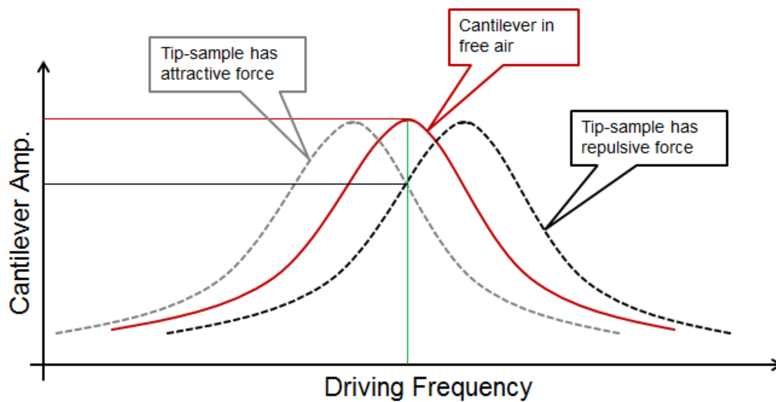

Figure 2.33. Resonance curve for a single harmonic oscillator (solid line) and under the influence of attractive and repulsive forces (dashed lines), A = oscillation amplitude.

At low driving frequencies with respect to f_0 the response is controlled by the stiffness of the spring, that is, the cantilever moves in phase with the driving force and with an amplitude close to F_0/k. At frequencies very large compared to f_0, $kz \ll \ddot{z}$ the response is controlled by inertia, causing a relatively small amplitude with a phase shift of 180°.

Attractive and Repulsive Forces

The presence of a force gradient in the Z direction, $(\partial F_{ts})/\partial z$, modifies the effective spring constant of the cantilever, k_e:

$$k_e = k - \partial F_{ts}/\partial z \qquad 2.24$$

If the sample exerts a negative force gradient on the cantilever, the spring constant will effectively soften. This then affects the resonant frequency of the cantilever with mass m_0.

$$f_0 = \left(\frac{1}{2\pi}\right)\left(\frac{k_e}{m_0}\right)^{1/2} \qquad 2.25$$

From Eq. 2.25, a softer cantilever leads to a decrease in f_0. If the cantilever was driven at its resonant frequency before the force gradient was experienced by the cantilever, the amplitude of oscillations of the cantilever will decrease due to the change in f_0. When a positive force gradient is exerted by the sample, the spring constant will effectively stiffen. Thus f_0 will increase, affecting the amplitude of the oscillations, as shown in Figure 2.33. From Figure 2.33, the force gradient of the external force, F_{ts}, produces a shift of the resonant curve without introducing any shape or size modifications. This is the case when the resonance curves are derived by modelling the cantilever as a weakly perturbed harmonic oscillator as in Reference [167]. However, this does not take into account that the shape of the resonance curve changes with variation in the separation distance of cantilever and sample. The peak becomes more and more truncated at the centre of the curve the smaller the tip-sample separation distance. Whether a positive or negative force gradient is exerted on the tip by

the sample is dependent on the tip-sample distance. In the absence of any field being applied externally, the dominant forces are van der Waals interactions, short-range repulsive interactions and capillary forces. Capillary forces are attractive forces that arise due to a thin film of water between tip and sample. This thin film is always present in ambient conditions. If the tip is in contact with the thin film of water the capillary force acts by creating a bridge between the tip and sample. Van der Waals forces are long-range attractive interactions that arise from spontaneous fluctuations of electrons. Van der Waals forces are exerted upon the cantilever tip by all types of surfaces as these fluctuations are always present. Pauli repulsion causes the short-range repulsive forces between atoms and molecules. The different forces exerted on the cantilever tip by the surface lead to two different regimes, as shown in Figure 2.34, with the arbitrary point $z = 0$ separating the two regimes. From Figure 2.34, the 'attractive regime' describes AFM operation when the tip-sample distance, z, is positive and the 'repulsive regime' describes operation when $z < 0$. The repulsive regime is defined as the distance in which repulsive forces act on the tip and is very short-range (fractions of nm). The attractive regime is for tip-sample distances beyond the repulsive regime where the forces acting on the tip are only attractive (up to 100 nm). Thus the force gradient changes from negative (attractive forces for $z > 0$) to positive (repulsive forces for $z < 0$), as the mean tip-sample separation distance, z, decreases.

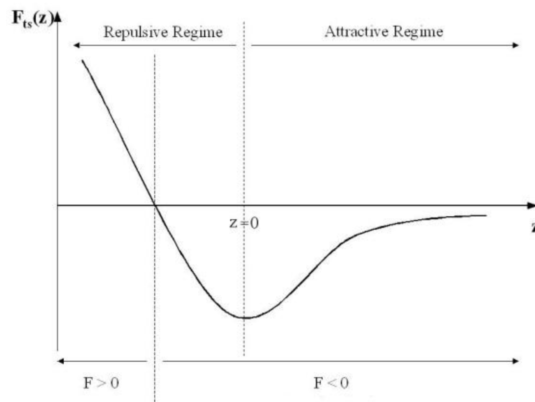

Figure 2.34. Sketch of the force exerted on the tip of the AFM cantilever by the surface, $\boldsymbol{F_{ts}}$, versus tip-sample separation distance, z, illustrating the repulsive and attractive regimes.

Figure 2.34 shows how the resonant frequency is affected by the two different types of forces. The longer range attractive forces decrease the resonant frequency, f_0 , and the shorter range repulsive forces increase f_0. Therefore in practical terms, there are two different stable states in which an AFM can operate. In Frequency Modulation AFM (FM-AFM) mode the feedback system must be able to control the tip-cantilever assembly in the Z direction for either increases or decreases in f_0 (due to both positive and negative force gradients) accordingly, depending on the regime of operation. An AFM can be operated in NC-AFM mode (attractive forces), 'tapping' AFM mode (where the cantilever still experiences attractive forces, but also repulsive forces for a fraction of its oscillation cycle) or contact mode (which primarily probes repulsive forces) without requiring the ability to alter the feedback polarity. In FM-AFM mode, care must be taken in the selection of a frequency shift set-point because of the trough in the F_{ts} versus z curve (Figure 2.34). Operation in this trough is very difficult as practically only one polarity of feedback is possible at any one time. Thus, the tip may crash into the sample if the polarity of the feedback mechanism is incorrect.

Tapping Mode AFM

In Tapping Mode AFM (TM-AFM) the probe is repeatedly tapping on the surface (Figure 2.35).

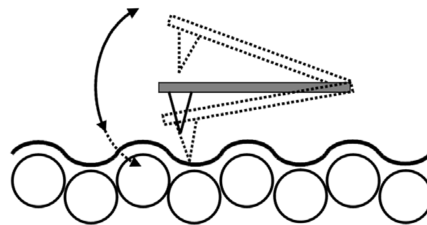

Figure 2.35. Sketch of tip oscillation in tapping-mode AFM.

The equation of motion of a damped, driven cantilever has a term dependent on the probe-sample interaction and thus the system's resonant frequency is dependent on this force. The Eq. 2.23 describes the tip motion in tapping mode. The tip vibration leads to an oscillating output voltage of the photodiode and the amplitude is tracked as the probe is scanned across the

surface and encounters regions of varying height. A feedback loop keeps a constant probe-surface distance by maintaining a constant oscillation amplitude. If the height increases the probe-sample force will increase and the probe will be retracted to compensate. In the simplest case, a trace of the probe's path is interpreted as the topography of the sample.

Amplitude modulation AFM

In Amplitude Modulation AFM (AM-AFM) mode the measured oscillation amplitude, A, is the feedback parameter. The excitation amplitude (and excitation frequency) is kept constant throughout, but the oscillation amplitude, A, is monitored and the Z direction feedback piezo adjusts the mean Z-position of the cantilever to maintain A at a constant value. The topography of the surface is therefore mapped by recording the movement of the Z direction piezo. AM-AFM is sometimes referred to in the literature as tapping mode and FM-AFM referred to as NC-AFM. This is because AM-AFM was historically operated in an intermittent contact mode and FM-AFM in a non-contact mode. However, both these dynamic modes of AFM can now be implemented together. Nowadays AM-AFM is the dominant mode of AFM for experiments in air and in liquids, whereas FM-AFM is primarily implemented in UHV. However, atomic resolution of Si(111)-(7×7) was achieved in UHV in 1997 for AM-AFM mode [168]. AM-AFM typically involves excitation amplitudes in the 1-100 nm range and is used for biomolecular imaging, for imaging DNA, membrane proteins and polymers. It may also be used to manipulate at the nanometre scale, the manipulation of single 50 nm diameter gold nanoparticles as an example [169]. This operation mode is also used to characterize the graphene [161], [163]. The tip dynamics of AM-AFM can be described in terms of a tip-sample interaction potential with long-range van der Waals forces and short-range Pauli repulsive forces. However, even with simplified assumptions, these forces have power law dependencies on the tip-surface separation. Therefore, the non-linearity of the tip-sample interactions has large implications in the resulting tip motion, making it difficult to find analytical solutions, but the action of a cantilever in AM-AFM can be understood qualitatively for ease of understanding. If the cantilever was excited by a driving

force, F_0, at the natural resonant frequency of the cantilever, f_0, and then approached towards the surface, the cantilever tip would experience forces exerted by the sample. These forces would modify the resonant frequency which in turn implies a modification of the cantilever oscillation amplitude, A (as shown in Figure 2.33). Therefore, the new oscillation amplitude would be smaller than the free oscillation amplitude. However, if the cantilever was initially off resonance, the oscillation amplitude, A, could decrease or increase depending on the modified resonant frequency and the driving force frequency both with respect to f_0.

Frequency modulation AFM

Frequency Modulation AFM (FM-AFM) monitors the resonant frequency of the cantilever and utilizes it as the Z direction piezo feedback parameter. FM-AFM is the AFM mode primarily used in UHV and has achieved atomic resolution for over a decade. FM-AFM has led to an increased sensitivity over AM-AFM through the ability to use higher Q-factor cantilevers without any restriction on bandwidth. In FM-AFM mode the oscillation amplitude, A, of the cantilever may or may not be kept constant at A_0. The example of the 'constant amplitude' mode will be assumed, where the oscillating amplitude of the cantilever, A, is fixed and equal to the amplitude set point, A_0. Initially the resonance of the cantilever is measured while the tip-sample distance is large and $F_{ts} = 0$, thus f_0 can be recorded and the associated amplitude at f_0 defined as A_0. While scanning the sample in constant amplitude mode, a feedback loop monitors the oscillation amplitude, A, as an input signal from the cantilever motion detector and modifies the excitation amplitude accordingly to force the cantilever to oscillate at the amplitude set point, A_0.
In FM-AFM, a feedback loop called the phase-locked-loop (PLL) varies the frequency of the driving signal in order to excite the cantilever at resonance conditions. The PLL maintains the phase of the driving signal at the phase set-point. The frequency of the driving signal is modified according to the polarity of the phase shift. Therefore the cantilever will always be driven at its effective resonant frequency, f_e, even though this parameter varies due to the tip-sample

interaction. The frequency shift, df, caused by forces from the surface, is equal to $f_e - f_0$ and the tip-sample distance is varied with the Z direction piezo to maintain df at a desired frequency shift set-point. The movement of the Z direction piezo during a scan of the sample is then plotted as a topography map of the surface. The cantilever motion in FM-AFM mode can be described as a weakly perturbed harmonic oscillator with a modified frequency due to the tip-surface interaction, as the AM-AFM mode was previously. However, the FM-AFM model has been proven to be justified by previous calculations [167]. Using this model Eq. 2.23 can be modified into Eq. 2.26 to describe FM-AFM operation.

$$m\ddot{z} + \frac{mQ}{\omega_0}\dot{z} + kz - F_{ts}[A + z_c] = F_{exc} \qquad 2.26$$

where z_c is the cantilever support distance from the surface (compared to z which is the tip-surface separation), and F_{exc} is the excitation term that describes the excitation of the cantilever motion due to the cantilever being driven. The numerical results from this model described in Equation 2.16 and the experimental results measured for the frequency shift for varying tip-sample separation distance are described in Reference [167].

Intermediate and non-contact mode AFM with the tip–sample interaction perturbed by attractive and repulsive forces that cause amplitude or frequency changes in the oscillation of the AFM tip is illustrated schematically in Figure 2.36.

AFM measurements in this thesis are performed in amplitude modulation tapping-mode using a AIST-NT SmartSPM, equipped with a conventional piezoscanner (maximum xy range 100 µm and maximum z range 15 µm) and a four-segment photodetector for cantilever deflection monitoring. MikroMasch Silicon-SPM-probes with Al backside reflex coating having spring constant $k = 1.8 \div 13Nm^{-1}$, oscillation frequency from 110 to 220 kHz and a tip apical diameter of 8 nm are used. All the scans were executed at room temperature. At least three areas for each sample were measured in order to take into account inhomogeneity which might derive from the sample preparation.

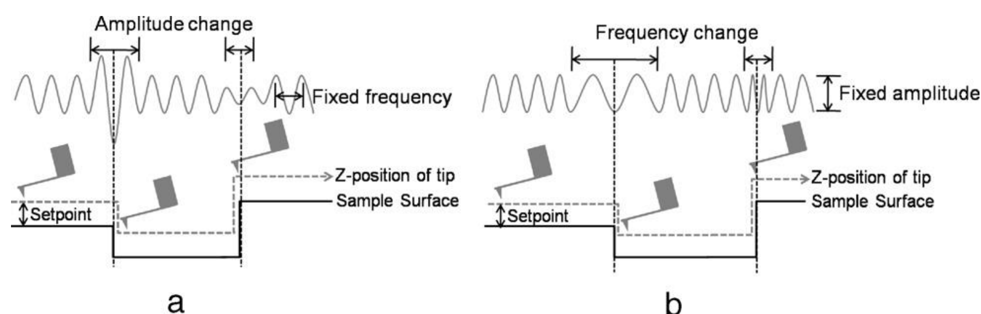

Figure 2.36. Schematic illustration of non-contact AFM operation mode: (a) Amplitude modulation mode and (b) Frequency modulation mode. Both AM and FM modes maintain constant tip–sample separation. AM mode uses oscillation amplitude changes as a feedback signal while FM mode uses frequency changes as feedback signal [160].

2.5.3 Anomalies in thickness measurements of graphene by TM-AFM

AFM is used extensively since it provides three-dimensional images that enable the measurement of the lateral dimensions of graphene films as well as the thickness, and by extension the number of layers present. However, in the literature AFM has proven to be inaccurate with a wide range of measured values for single layer graphene thickness reported (between 0.4 and 1.7 nm) [170] which varies widely when compared to the inter-plane spacing of graphite (0.335 nm) [171]. Indeed various groups reported different thickness measurements for graphene layers, with thicknesses ranging from 0.35 to 1 nm, relative to the SiO_2 substrate. Novoselov et al. measured platelet thicknesses of 1–1.6 nm [2]. Gupta et al. have measured an instrumental offset induced by the AFM, of 0.33 nm, i.e., 0.7 nm height for a single layer [172]. Other authors have also reported varying step heights for few layer graphene supported on silicon oxide [173]–[175].

Despite the disparity in measured single layer graphene thickness via AFM, it is common to use the following equation to determine N via AFM [67]:

$$N = \frac{(t_{measured} - 0.4)}{0.335} \quad 2.27$$

where $t_{measured}$ is the measured thickness via AFM and the nominal 0.4 value is subtracted to account for increases in measured thickness related to substrate–graphene and graphene–tip interactions [170]. The value of 0.4 is arbitrary and can be inaccurate by up to 1 nm (equivalent to three graphene layers assuming a 0.335 nm spacing) [170].

The variation in the thickness measurements of the single graphene layers may be attributed to the change in the tip–sample interaction as the tapping tip scans over the surface. Observations of distortions in the thickness of nanoparticles, measured with TM-AFM in amplitude modulation, are well known [163], [176]. Anomalous nanoparticle height measurements, dependent on the free amplitude of the cantilever and material properties of the sample, were reported earlier [177]–[179]. However, the inconsistencies in using AM-AFM to measure graphene layer thicknesses can be due to two physical phenomena:

1. Under ambient conditions, the interface between hydrophobic graphene and various hydrophilic substrates including mica, silicon dioxide, and silicon carbide is subjected to water adsorption [180]–[182]. When prepared in a high humidity environment water adlayers have been observed between mica and graphene [183], [184].
2. AM-AFM is prone to contrast artifacts on heterogeneous samples with alternation hydrophilic and hydrophobic regions [179], [185], [186].

The accurate measurement of graphene thickness using AFM is very important, in particular when considering the substantial variation in graphene properties with the number of layers. One option that has been explored has been optimizing the free amplitude of oscillation in the tapping mode AFM such that the effect of nanomaterial–tip interactions can be effectively negated [177], [178]. When applied to the imaging of graphene, changes to the free amplitude have resulted in measured single layer graphene thickness from 0.4–1.7 nm (Table 2.1) [163].

Table 2.1. Summary of selected results for measured single layer graphene thickness measured by AFM with preparation method, AFM method, substrate and whether SLG was confirmed by Raman spectroscopy. Adapted from [170]

Measured thickness (nm)	Preparation method	SPM method	Substrate	SLG confirmed by Raman?	Reference
0.9+-0.2	Mechanical exfoliation	AC-AFM	Si/SiO_2	Y	[187]
0.4	Mechanical exfoliation	UHV NC-AFM	Si/SiO_2 (300 nm)	N	[33]
0.4-0.9	Mechanical exfoliation	TM-AFM	Mica	Y	[181], [188]
0.4-1.7	Mechanical exfoliation	TM-AFM	Si/SiO_2	Y	[163]
0.9	Mechanical exfoliation	C-AFM	Si/SiO_2	N	[189]
0.4-1	Mechanical exfoliation	C-AFM	Si/SiO_2	N	[2]
1.19+-0.1	Mechanical exfoliation	IC-AFM	Si/SiO_2 (300 nm)	Y	[190]
0.7	Mechanical exfoliation	C-AFM	Si/SiO_2 (300 nm)	Y	[191]
1	Mechanical exfoliation	C-AFM	Si (111)	Y	[192]
1.8	CVD	TM-AFM	Si/SiO_2	Y	[162]
1.44	RGO	TM-AFM	HOPG	N	[193]
0.8-1.5	RGO	TM-AFM	Si/SiO_2 (300 nm)	N	[194]
1.1+-0.1	GO and RGO	TM-AFM	HOPG	N	[195]
0.9-1.7	GO and RGO	TM and C-AFM	HOPG	N	[196]
0.8-1.1	GO	TM-AFM	Si/SiO_2 (300 nm)	N	[197]

IC and AC = Intermittent contact mode

UHV = ultra high vacuum

C = contact mode

NC = non-contact mode

TM = tapping mode

The process to determine the optimal free amplitude and imaging set-point is somewhat time consuming and laborious. This optimization of TM also requires the acquisition of amplitude versus distance curves which can result in tip damage, especially considering TM probes have relatively high spring constants (on the order of 5–50 N m^{-1}) and small radii (typically less than 10 nm). Furthermore, it does not take into account substrate-graphene interactions which are likely to be a greater source of inaccuracy. Calculating the exact imaging force in TM is also more complicated than other imaging modes and therefore reproducibility of results can be difficult [198]. Contact

mode AFM can also been used to determine the number of layers of graphene films but differences in height have been observed between forward and reverse scans [163]. These differences have been attributed to the high lateral forces, typical of contact mode, which can result in inaccurate estimation of N.

The likely cause of the overestimation of graphene height by AFM is adlayers between graphene and the substrate creating a buffer between graphene and substrate. Previous works, report the effect of relative humidity (RH) on the graphene thickness measurements. Measured thickness of graphene as a function of RH is shown in Figure 2.37. The results show an overall trend of increasing measured thickness with the increasing RH with a distinct feature of decreasing seen in the region of Middle RH.

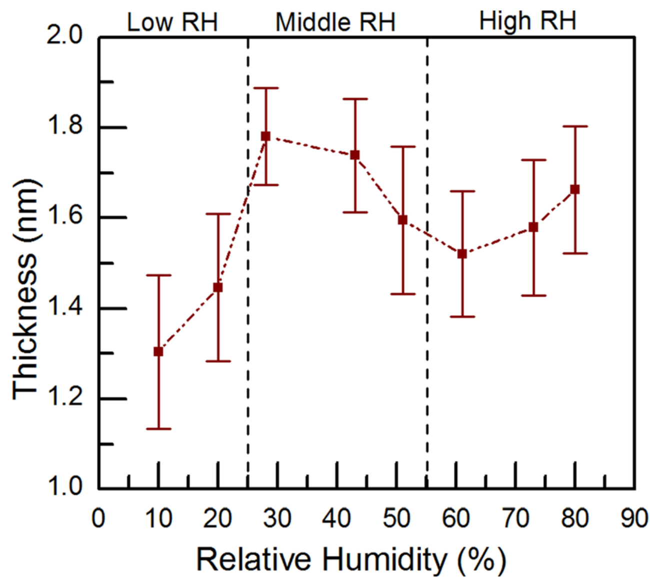

Figure 2.37. Typical measured thickness of graphene as a function of RH. The RH range is divided into three approximate sections: Low, Middle, and High RH [161].

In the Middle RH range, the adhesion force is the greatest, and then the measured thickness increases. This behavior is due to adhesion forces that change with the molecular structure evolution of the adsorbed water layer on the SiO_2 substrate as RH changes. A water adlayer between graphene and SiO_2 substrate is supposed [161]. The hypothesized structure of graphene/water/SiO2 sandwich is shown in Figure 2.38.

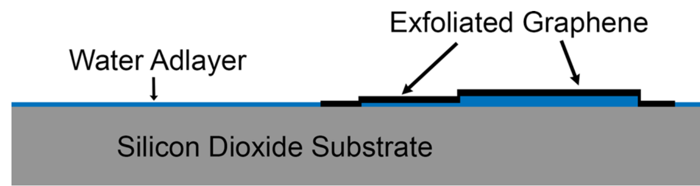

Figure 2.38. Structure of exfoliated FLG trapping the water adlayer on the oxide substrate. Figure not shown to scale [161].

These adlayers have been observed also by Novoselov in 2004 [2]. Shearer et al. suggest that it is possible to accurately measure graphene height if either (1) high applied force is used or (2) no buffer layer is present between substrate and graphene. To avoid the inclusion of buffer layers between substrate and graphene, the sample can be prepared in a water free environment such as a nitrogen glove box or under vacuum [192], [199], [200]. A key parameter for accurate determination of graphene thickness is the applied pressure of the tip on the sample. As represented schematically in Figure 2.39, when imaging with low applied pressure (Figure 2.39a), the tip lightly presses into the graphene and the measured height is a combination of the thickness of the buffer layer and the graphene.

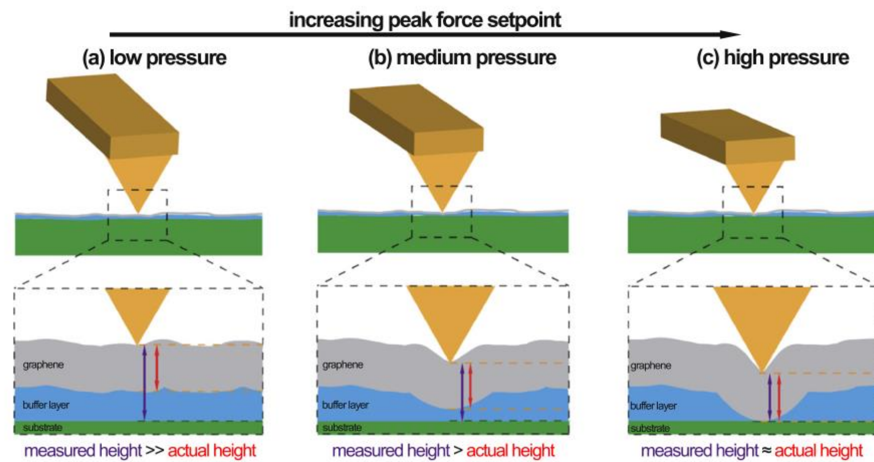

Figure 2.39. Schematic mechanism of improving AFM imaging accuracy with increasing peak force set point. As the pressure applied increases from (a) low to (b) medium to (c) high the AFM tip is able to disrupt the underlying buffer layer and subsequently measure a more accurate value for graphene height [170].

By applying more pressure (Figure 2.39b), the tip presses into the graphene and forces it into the buffer layer, reducing the measured height but still measuring a height greater than the actual thickness of graphene. Finally, when applying a high pressure (Figure 2.39c), the tip presses the graphene

through the entire buffer layer and onto the underlying substrate and measures a height approximately equal to the true thickness of graphene.

2.5.4 Simultaneous AFM-Raman

The instrumentation used to characterize the graphene samples in this thesis allowed to perform simultaneous AFM-Raman measurements. AIST-NT SPM microscope is coupled to LabRamHR Evolution HORIBA Scientific as showed in Figure 2.40a, while a schematic overview of the mechanism is shown in Figure 2.40b.

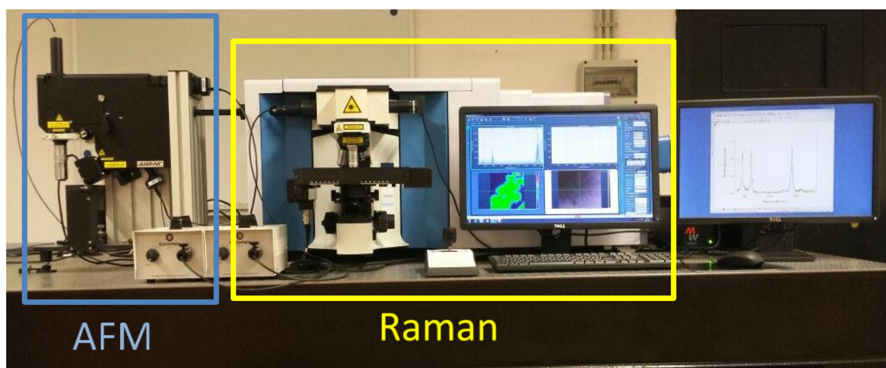

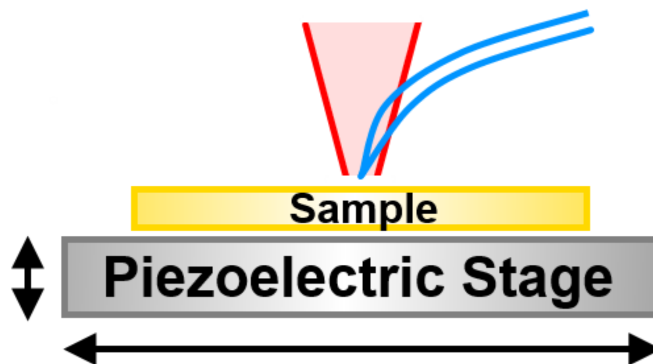

Figure 2.40. (a) Schematic of AIST-NT SPM AFM integrated with LabRamHR Evolution HORIBA Scientific Raman system for simultaneous AFM-Raman. (b) The Raman laser (red shaded area) and AFM probe (blue) are both focused onto the same area of the sample and held in a fixed position.

Simultaneous AFM-Raman measurements were performed by first aligning the AFM probe and the Raman laser spot onto the same location on the surface of a sample, once aligned the probe was held in position. The tip-sample separation was maintained by setting the phase feedback to determine

the z position of the piezoelectric stage as shown in Figure 2.40. The stage was then allowed to move in the x-y plane so that the sample could be scanned. First, an AFM map was specified then Raman measurements were performed.

2.6 Kelvin Probe Force Microscopy (KPFM)

Kelvin probe force microscopy, or KPFM, was introduced as a tool to measure the local contact potential difference between an AFM tip and the sample, thereby mapping the work function or surface potential of the sample with high spatial resolution. Since its first introduction by Nonnenmacher et al. in 1991 [201], KPFM has been used extensively as a unique method to characterize the nano-scale electronic/electrical properties of metal/semiconductor surfaces and semiconductor devices. Recently, KPFM has also been used to study the electrical properties of organic materials/devices [202]–[204] and biological materials [205], [206]. KPFM can be used to image potential distributions on the surface with sub-nanometer resolution, making KPFM the best technique, at present, for characterizing the electrical properties of nanostructures. KPFM measures a contact potential difference (CPD) between the sample surface and the tip. A notable application of KPFM is the imaging of operational electrical devices to provide the high-resolution potential profiles. These measurements provide critical, near-atomic scale information on processing induced defects and their effects to the performance of the electrical devices.

KPFM is primarily based on the instrumentation of an AFM system. The KPFM measures CPD between a conducting AFM tip and a sample. The CPD (V_{CPD}) between the tip and sample is defined as:

$$V_{CPD} = \frac{\phi_{tip} - \phi_{sample}}{-e} \tag{2.28}$$

where ϕ_{sample} and ϕ_{tip} are the work functions of the sample and tip, and e is the electronic charge. When an AFM tip is brought close to the sample surface, an electrical force is generated between the tip and sample surface, due to the

differences in their Fermi energy levels. Figure 2.41 shows the energy level diagram of the tip and sample surface when ϕ_{sample} and ϕ_{tip} are different.

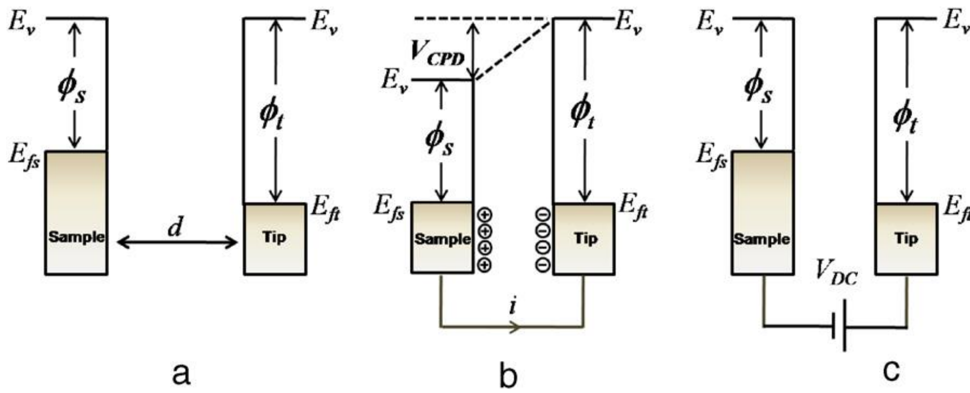

Figure 2.41. Electronic energy levels of the sample and AFM tip for three cases: (a) tip and sample are separated by distance d with no electrical contact, (b) tip and sample are in electrical contact, and (c) external bias ($\boldsymbol{V_{dc}}$) is applied between tip and sample to nullify the CPD and, therefore, the tip–sample electrical force. $\boldsymbol{E_v}$ is the vacuum energy level. $\boldsymbol{E_{fs}}$ and $\boldsymbol{E_{ft}}$ are Fermi energy levels of the sample and tip, respectively.

Figure 2.41a depicts the energy levels of the tip and sample surface when separated by a distance d and not electrically connected (note, the vacuum levels are aligned but Fermi energy levels are different). Equilibrium requires Fermi levels to line-up at steady state, if the tip and sample surface are close enough for electron tunnelling. Upon electrical contact, the Fermi levels will align through electron current flow, and the system will reach an equilibrium state, Figure 2.41b. The tip and sample surface will be charged, and an apparent V_{CPD} will form (note, the Fermi energy levels are aligned but vacuum energy levels are no longer the same, and a V_{CPD} between the tip and sample has formed). An electrical force acts on the contact area, due to the V_{CPD}. As shown in Figure 2.41c, this force can be nullified. If an applied external bias (V_{DC}) has the same magnitude as the V_{CPD} with opposite direction, the applied voltage eliminates the surface charge in the contact area. The amount of applied external bias (V_{DC}) that nullifies the electrical force due to the V_{CPD} is equal to the work function difference between the tip and sample; therefore, the work function of the sample can be calculated when the tip work function is known.

For a semiconductor surface, the measured CPD is related to the surface potential, which differs from the work function of semiconductor materials, due to the Space-charge-Layer near the semiconductor surface.

2.7 Graphene Field Effect Transistor (GFET) for mobility measurements

Electric field effect on graphene was one of the outstanding results showed by Novoselov et al. [2]. As a consequence, extensive amount of research has been done on graphene field effect transistors (GFETs) in which graphene is used as the channel material [207], [208]. In the beginning, back-gate devices were being fabricated from exfoliated graphene on Si/SiO_2 substrate in which silicon and silicon dioxide served as back gate electrode and dielectric respectively. However, top-gate devices are much more desirable for applications [208]. Figure 2.42 shows the schematic cross section of a GFET [207].

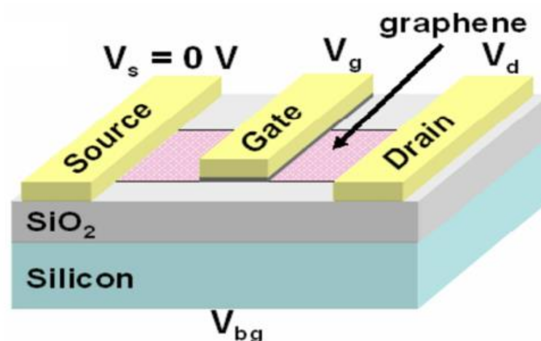

Figure 2.42. Schematic cross section of a GFET [207].

Because of the gapless property of graphene, typical GFETs exhibit ambipolar behaviour in which charge carriers change from electrons to holes and vice versa at a minimum conductivity Dirac neutrality point. In an ideal case, the transfer characteristic of GFET should be quasi ballistic. However, device fabrication and structure introduce limitations and then it is possible to use drift-diffusion model to describe drain current.

In recent years, several models for current-voltage characteristics of GFETs have been proposed [61], [209]–[211]. For instance, a model tries to fit

current voltage characteristics of GFET to that of conventional MOSFET. In this model, at low drain voltages ($V_D < V_{GS} - V_0$), drain current can be described by Eq. 2.29 in which a constant charge carrier mobility is assumed:

$$I_D = \frac{W_{ch}}{L_{ch}} \mu C_{ox} \left[(V_{GS} - V_0)V_D - \frac{V_D^2}{2} \right] \qquad 2.29$$

This equation is the same as MOSFET drain equation except for V_0 which is the Dirac neutrality point in GFETs. In addition, there is always a minimum conductivity point much larger than the universal minimum conductivity $4e^2/h$ due to inhomogeneity and thermal excitations [11]. Figure 2.43 shows the transfer characteristic of graphene field effect transistor using Eq. 2.29, and a minimum conductivity. The V-shape of transfer characteristics reflects the ambipolar transport behaviour of GFETs.

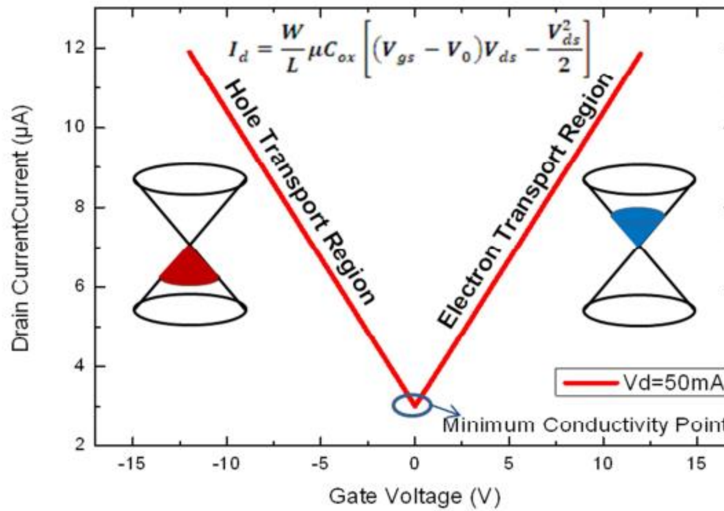

Figure 2.43. Ideal drain current versus gate voltage.

The field effect mobility can be extracted from the transfer characteristics. The drift current can be write as

$$\vec{J} = qn\mu\vec{\varepsilon} \qquad 2.30$$

and

$$\vec{J} = \sigma\vec{\varepsilon} \qquad 2.31$$

Carrier concentration can be calculated as

$$qn = C_{ox}(V_{GS} - V_D) \qquad 2.32$$

with

$$C_{ox} = \frac{\varepsilon_r \varepsilon_0}{d} \qquad 2.33$$

Where $C_{ox}$and V_D are geometrical capacitance and gate voltage at minimum conductivity point respectively. Thus, carrier mobility can be expressed by

$$\mu = \frac{\sigma}{qn} = \frac{I_D L}{V_D W C_{ox}(V_{GS} - V_D)} \qquad 2.34$$

However, since there is always a nonzero minimum conductivity for graphene, using $\frac{I_D}{(V_{GS}-V_D)}$ results in mobility over estimation [212]. For this reason, it is more accurate to use the transconductance

$$g_{mt} = \frac{dI_D}{dV_{GS}} \qquad 2.35$$

That represents the slope of linear part of Current-voltage curve as reported in Figure 2.44 [61]. Replacing $\frac{I_{ds}}{(V_{gs}-V_D)}$ with transconductance g_{mt}, the field-effect mobility can be expressed as

$$\mu_{FE} = \frac{L_{ch}}{W_{ch}C_G V_{DS}}\left(\frac{dI_D}{dV_{GS}}\right) \qquad 2.36$$

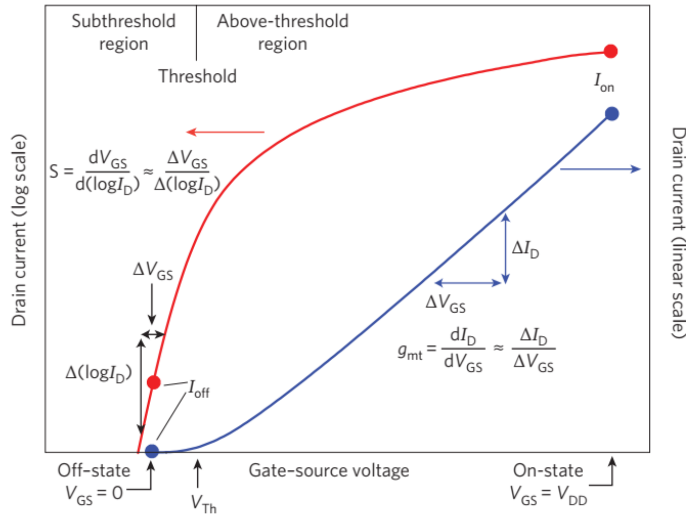

Figure 2.44. FET transfer characteristics showing I_D (on a logarithmic scale on the left and a linear scale on the right) versus the gate–source voltage V_{GS}. Above threshold, the change in I_D for a given change in V_{GS} is called the terminal transconductance, g_{mt} [61].

2.8 Solar Cell Characterization

In chapter 4, a Schottky Barrier Solar Cell based on graphene on n-Silicon junction will be discussed. The parameters used to characterize the device as solar cell are reported here.

2.8.1 External Quantum Efficiency (EQE)

The external quantum efficiency (EQE) is defined as the ratio, at a specific wavelength, of the number of carriers collected to the number of incident photons. Hence, if the cell collects a current I for an incident photon beam of f photons, the EQE is given by

$$EQE(\lambda) = \frac{I}{q\,f} \qquad 2.37$$

where q is the electric charge. This ratio is by definition taken when no voltage is applied on the solar cell. EQE measurements were carried out without and with an appropriate white-light bias (optical bias, OB) to bring the cell close to the operation condition with a Bentham PVE300 apparatus (Reading, U.K.) calibrated with a Si detector and using a probe light with a spot size much smaller than the cell area.

2.8.2 Photovoltaic Parameters

The four parameters used to evaluate a solar cell's performance are power conversion efficiency (PCE), short circuit current (J_{SC}), open circuit voltage (V_{OC}), and fill factor (FF) and can be extracted from J-V curves acquired under illumination in standard condition (Figure 2.45).

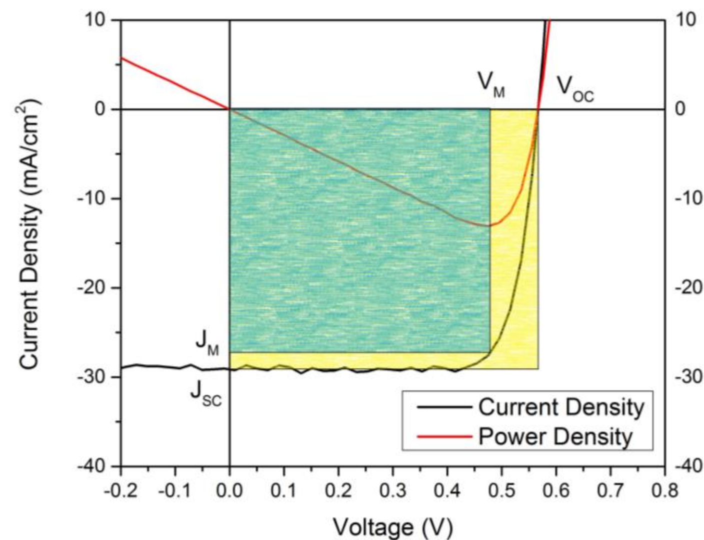

Figure 2.45. J-V curves acquired under illumination with photovoltaic parameters.

The bias voltage where the photocurrent is equal and opposite to the diode current (ie, J_{total} = 0) is called the open circuit voltage, V_{OC}. The output current when V_{bias}= 0 V is defined as the short circuit current density, J_{SC}. An overall measure for the efficiency of a cell, PCE is defined as a ratio of the maximum power generated by the cell to the power of the incident radiation on the active area of the device. The short circuit current density is taken directly from the

J-V curve and is approximately equal to the photocurrent (the dark diode current is generally orders of magnitude smaller). The V_{OC} is defined as the voltage at which the photocurrent is equal and opposite to the diode current, $J_{photo} = J_{diode}$:

$$J_{photo} = J_0 \left[\exp\left(\frac{qV_{OC}}{kT} - 1 \right) \right] \qquad 2.38$$

Solving for V_{OC} yields:

$$V_{OC} = \frac{kT}{q} \ln\left(\frac{J_{photo}}{J_0} + 1 \right) \qquad 2.39$$

The V_{OC} is extracted directly from the J-V and can be used to calculate other parameters, such as the dark current (and subsequently Schottky barrier height).This equation elucidates the factors contributing to a high or low V_{OC}, namely and increase in short circuit current and/or a decrease in dark current. Increasing V_{OC} by increasing the light intensity is a well known phenomena exploited through solar concentrators, though the semiconducting material must have high enough mobilities to avoid carrier saturation (and inversion). The inverse logarithmic dependence on dark current points to a reduction in junction recombination as another way to increase the V_{OC}. The fill factor is a measure of how much the solar cell functions as an ideal diode, with a FF of 1 corresponding to a completely square shaped J-V curve in the fourth quadrant.

$$FF = \frac{V_M J_M}{V_{OC} J_{SC}} \qquad 2.40$$

V_M and J_M are the voltage and current density corresponding to the maximum power point: the point on the J-V curve where the maximum power is generated by the solar cell. This is found by graphing the power density vs voltage and solving for $\frac{dP}{dV} = 0$.

The power generated at the maximum power point is represented by the blue square in Figure 2.45.

With those parameters defined, we can now solve for the PCE:

$$\eta = \frac{J_M V_M}{P_{incid}} = \frac{J_{SC} V_{OC} FF}{P_{incid}} \quad 2.41$$

Note that this is the efficiency at the maximum power point; the efficiency will be lower at other equivalent loads in the fourth quadrant. Consequently, maximizing the power extracted from a solar cell involves matching the load to the resistance at the maximum power point.

Other important parameters are Series and Shunt Resistance. Both series and shunt resistance have a detrimental effect on solar cell performance, with the best performance extracted by minimizing the former and maximizing the latter. The expression for the total current can be rewritten to include both series and shunt resistance:

$$J_{total} = J_{photo} - J_0 \exp\left[\frac{q(V + IR_S)}{\eta kT}\right] - \frac{V + IR_S}{R_{SH}} \quad 2.42$$

Series resistance is the resistance encountered by carriers as they are extracted from the device. Series resistance should ideally be as low as possible; high series resistances lead to a lower FF and ultimately lower PCE. High series resistances can be due to employing poorly conductive contacts or having insufficient electrical contact such that the photogenerated carriers cannot be efficiently extracted. Shunt resistance is ideally as high as possible, as it represents all current paths that carry the charges through a circuit in parallel with the load, i.e., the photogenerated carriers do no useful work and do not contribute to the overall efficiency. One possible contributor to low shunt resistance in both p-n junctions and Schottky junctions is losing photogenerated carriers out the edge of a device. Figure 2.46 shows the degradation of the J-V curve with large series and small shunt resistances.

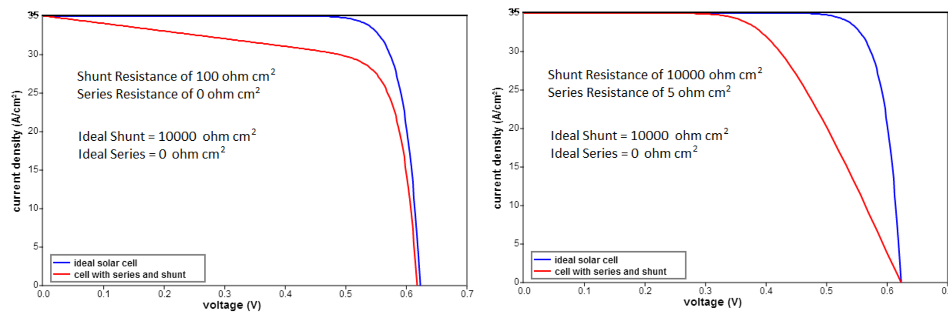

Figure 2.46. The effects of series and shunt resistance on the J-V curve. Optimal values are $\boldsymbol{R_{series}}$ = 0 ohm cm^2 and $\boldsymbol{R_{shunt}}$ = ∞ ohm cm^2.

Illuminated J–V characteristics were performed with a Keithley 228a voltage/current source (Keithley Instruments Inc., Cleveland, USA) and HP 3478A multimeter measure unit (Palo Alto, USA). White light illumination was provided by a class AAA solar simulator from WACOM (model WXS- 155S-L2) equipped with a 1000 W Xenon lamp and a 400 W Halogen lamp. The light intensity was calibrated using a mono-Si reference cell in standard test conditions (25 °C, AM1.5G, 1000 W m^{-2}).

3

Ethanol-CVD synthesis of large graphene domains

Analysis of growth parameters in ethanol Chemical Vapour Deposition process will be presented in this chapter. Growth parameters will be analyzed and optimized in order to control and obtain the growth of large graphene domains. First, CVD apparatus designed at ENEA Casaccia and CVD process steps followed to grow graphene will be introduced. A brief description and some results on the transfer method based on cyclododecane optimized in collaboration with Yonsei University will be presented. Then the complete analysis of growth parameters used to obtain large graphene domains will be reported. The graphene characterization performed to obtain information on structural and electronic properties and on thickness and morphology of each sample will be discussed.

3.1 Introduction

As reported in Chapter 2, graphene films do not exist in nature, but it is possible to extract it from graphite by mechanical exfoliation [2] or grow it by Chemical Vapor Deposition (CVD) [107]. The superior electrical properties of graphene are normally achieved in single-crystal exfoliated graphene, but it has proven hard to match those properties in large-area samples produced by CVD. Contrarily to exfoliated graphene, samples grown by CVD are typically made of polycrystalline graphene, and the presence of grain boundaries are known to have a negative impact on graphene's physical properties, such as mobility, electron conductivity, and mechanical strength [213]–[215]. For this reason, it is important to suppress the formation of grain boundaries and increase the size of graphene grains, mainly by decreasing the nucleation density. In fact, if a few graphene nuclei are widely spaced, they can grow as isolated single crystals and eventually merge into a continuous graphene film with reduced grain

boundaries. Alternatively, all graphene nuclei were reported to grow with the same crystalline orientation on hydrogen-terminated Ge substrates [95]: Being them epitaxially correlated on an identically-oriented surface, they grow aligned along the same crystalline direction and ultimately merge into a single-crystal film without grain boundaries. However, this approach is still too difficult to use in the case of a polycrystalline Cu foil substrate, which is widely used for graphene growth due to a low price combined with a high graphene quality. On polycrystalline Cu foil, in case of methane CVD growth of graphene, the nucleation density was initially in the order of $\sim 10^6$ nuclei/cm^2 [216]. The CVD process is highly sensitive to many growth parameters such as precursor used, metallic substrate, growth temperature, substrate pre-treatment, precursors flow and total pressure. To minimize the high nucleation density, the CVD parameters were finely modulated by using high temperature (1000 ~ 1077 °C, close to the melting point of Cu (1084 °C)) [96], [97], [217], low precursor partial pressure [97], [218], and high hydrogen-to-methane ratio [216], [217], [219], [220]. To further control the nucleation sites, the Cu substrates were pre-treated by thermal annealing [221], [222], electrochemical polishing [223], and pre-oxidation [107], [221], [224]. These efforts finally enabled the growth of millimeter-sized graphene grains [216], [222]. Although methane represent the preferential carbon source for the CVD growth of graphene on Cu, ethanol can be considered as valid alternative. Being an efficient carbon precursor, ethanol can be used instead of methane and provide various advantages. Being liquid at Standard Ambient Temperature and Pressure (SATP), ethanol is safer than methane and can decompose at a lower temperature, accelerating the growth [80], [225]. Continuous graphene films were grown on Cu foils at low partial pressures of ethanol (< 2 Pa) in seconds i.e., much faster than conventional growth times (in the order of minutes) of methane-based CVD processes [82]–[85], [107]. Shorter growth times are crucial for industrial production and can also limit growth kinetic issues related to Cu sublimation [226], which can pollute the internal furnace walls during the CVD process, limiting the throughput [227]. Such an extremely fast growth of graphene occurs with an ethanol vapor flow as small as 0.1 sccm, one order of magnitude lower than those typical for methane. It is then challenging to increase the size

of individual graphene grains above 5 μm without a specific strategy aimed at limiting the nucleation density [228]. The pre-oxidation of the Cu foils is an effective way for reducing the nucleation sites and obtain large single-crystal graphene samples [85], [216], [222], [224], [229]–[231]. By pre-oxidizing the Cu foils at 250 °C, the nucleation density became as low as ∼ 1 nucleus/cm^2, five orders of magnitude smaller than that reported for untreated Cu foils [85], [222], [229]–[232]. When the Cu foil is covered by an oxide layer, its surface is passivated and the presence of impurities acting as nucleation seeds is abated [216], [221], [224], [233]–[236]. However, it should be noted that an unwanted amount of oxygen is often uncontrollably introduced into the CVD chamber for several potential reasons: i) imperfect vacuum sealing, ii) use of hydrolyzers for the production of H_2 gas [237]. Other than the presence of residual oxygen, the different quality and processing of Cu foils, depending on the production process (cold-rolled or soft-annealed) and the degree of purity (oxygen-free or oxygen-rich) [54], [224], [238]–[243] are associated with a confirmed difficulty to reproduce results.

Most of the recent studies on the growth of large single crystal graphene covered the CVD of methane [97], while ethanol as a carbon source has not been investigated in this respect yet. Up to date, only one group reported the growth of mm-sized single crystal graphene by CVD of ethanol with pre-oxidized Cu "enclosures" [85]. The enclosure approach is not ideal because it introduces uncertainties to the CVD process: It is impossible to define the gaseous environment inside the enclosure's internal surfaces. If the enclosures are physically sealed and gas-tight, then carbon would be either present as a contaminant on the copper surface, or it would diffuse inside across the Cu foils bulk, possibly along grain boundaries [224]. Instead, if the enclosures are not perfectly sealed, then the precursors could flow in and out, along the uncertain "pliers-crimped edges". In this framework, it is crucial to optimize the early nucleation stages on a flat Cu surface directly exposed to the gas atmosphere. In this chapter, the CVD growth of isolated graphene grains larger than 350 μm by using ethanol and pre-oxidized flat Cu foils will be reported. By varying total pressure and ethanol flow, the nucleation site density was reduced. By optimizing the growth parameters, it was possible to abate the

nucleation density and tune the CVD parameters to control the growth process for a time long enough (an hour) to produce sub-mm graphene grains with high crystallinity and few defects.

3.2 The CVD system at ENEA

The CVD system used to grow graphene is based on a hot-wall quartz tube furnace which allows the rapid sample insertion/ extraction in/from the hot zone without breaking the vacuum [79], [84], [244]. The system was modified with inner screens of alumina and tantalum to avoid the quartz contamination [227]. The CVD system was designed and built at ENEA Casaccia Research Center and consists of a high-vacuum fitted tube furnace, a rotary vane pump, digitally controlled mass flow meters for allowing the gases into the chamber, and a needle valve for setting the reactor pressure. The scheme of the CVD system is shown in Figure 3.47.

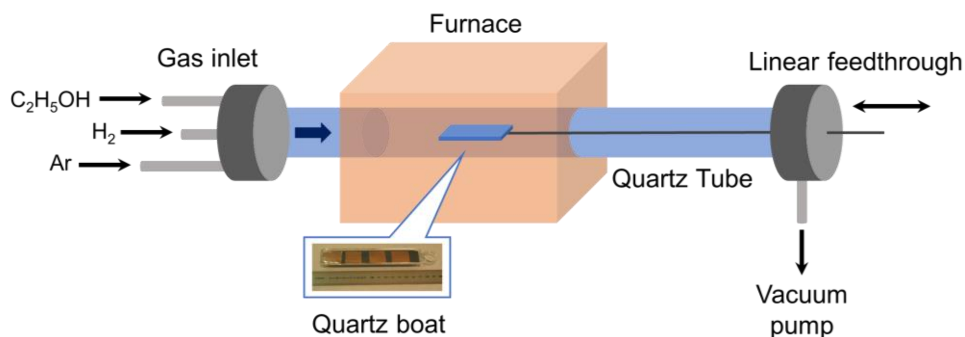

Figure 3.47. Scheme of CVD apparatus at ENEA.

The reaction chamber consisted of a 40-mm-outer-diameter, 2-m-long quartz tube that allowed the quartz sled containing the growth samples to be inserted and extracted from the hot zone under vacuum tight conditions. Rapid extraction from the hot zone into a cold part of the long quartz tube implemented a fast cooling system (and fast heating upon insertion), providing very fast initial cooling of the samples because of the intense radiation and the low thermal mass of the sled. Graphene was synthesized on polycrystalline Cu foil (SE Cu 58, cold worked Oxygen Free Copper 99.95%) using low-pressure

CVD. Before the growth, Cu foils cut into 2x2 cm substrates, were washed in a cycle of ultrasonic baths (5 min each in acetone and ethanol). For the pre-oxidation treatment, the Cu substrates were heated on a hot plate at 250°C in air (from 0 to 150 min as reported, with ramping rate of 8 °C/min). Then Cu substrates were slowly cooled down at room temperature to prevent the formation of micro-cracks in the copper oxide layer, which could expose bare metal. The oxidized Cu substrates were inserted inside the quartz-tube furnace under controlled pressure (from 800 to 65 Pa), and quickly moved from the room-temperature zone into the hot zone without breaking the vacuum when the growth temperature was reached. During the growth phase H_2, Ar (20sccm) and ethanol vapor were supplied. The H_2 and ethanol vapor flows ranged between 10-100 sccm and 1.5×10^{-3}-0.1 sccm, respectively. Before the introduction of ethanol vapors in the chamber, the Cu substrates were thermalized in Ar atmosphere (20 sccm) at the same growth temperature for a given annealing time (1-20 min). The growth time was defined between the onset of the precursor flow and the extraction of the sample from the hot zone. Ethanol vapor was fed with Ar carrier gas by using a pressurized bubbler kept at 0°C in an iced water bath, so that the partial pressure of ethanol was 15 mbar (1.5×10^3 Pa) in 3 bar (3×10^4 Pa) Ar. Negligible ethanol condensation in the gas line after the mass flow controller was expected, because the line was at a higher temperature than the bubbler. At the end of the growth process, the sample holder is rapidly extracted from the hot zone and cooled down to room temperature under Ar flow (750 sccm).

A typical graphene growth process is a six step process as summarized by the temperature-time diagram in Figure 3.48.

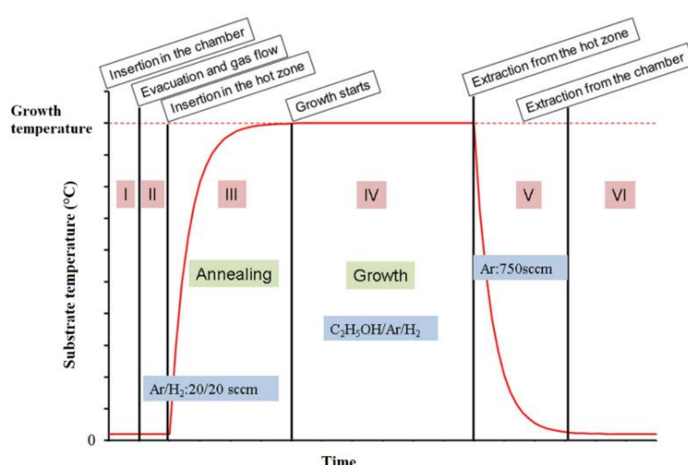

Figure 3.48. Temperature-time profile during a typical growth. (I) Insertion in the chamber, (II) evacuation and setting of the gas flows for annealing (Ar, H_2), (III) insertion in the furnace hot zone and annealing, (IV) growth, (V) extraction from the hot zone and rapid cooling under Ar, (VI) filling with Ar and extraction from the chamber. Adapted from [227].

3.3 Optimized Cyclododecane-based graphene transfer method

After the growth on Cu foils, graphene has to be transferred for analysis onto target substrates. First, the graphene grown on the back side of the Cu foils was removed by using O_2 plasma etching and then the Cu foil is removed using an etchant solution of ammonium persulfate ($(NH_4)_2S_2O_8$). The best results come with a series of three ($(NH_4)_2S_2O_8$) baths. Post Cu etching the sample is rinsed using three ultra-pure water baths, with the graphene in contact with the liquid surface, for optimum removal of residual etchant reaction impurities. The atomic-thick and highly hydrophobic layers of graphene can be easily fractured or folded, making the post-growth processing a delicate task, especially for device fabrication. A protective layer of a suitable material can be cast on graphene during this phase to assist the removal from the growth substrate: Poly(methyl methacrylate) (PMMA), a typical photoresist in the silicon industry, was first chosen and has since become the standard to transfer CVD graphene [245]. The established PMMA-transfer procedure for CVD graphene grown on Cu foil provides the spin-coating of a thin layer of PMMA on the graphene/Cu substrate before starting the chemical etching of Cu. In this way,

PMMA support the graphene in all the post growth process, until the transfer of the graphene film to the substrate of interest (e.g., a SiO_2/Si wafer). PMMA residues and contaminants are removed washing-off in acetone the system and with a thermal treatment. Researchers have refined the process steps in recent years, with the aim of retaining at most the electronic properties of graphene; however, the general outcome of such transfer process is still far from ideal. Although PMMA is highly effective in providing mechanical strength to the film and keeping it intact, its residues are known to induce defects on graphene and/or affect its electronic mobility [116]. A thin layer (1–2 nm) of PMMA was observed to remain adsorbed on graphene even after wash-off in acetone, giving the film a mild p-type doping [246]. A thermal annealing is generally required to ultimately get rid of any PMMA trace, but this further step can itself damage the film: Radicals created by the thermal scission of PMMA chains can locally modify the hybridization of carbons from sp^2 to sp^3 , or even make the residues more resilient, so hindering removal [247]. Other thin polymeric layers have also been tested to assist the transfer of graphene, but they all require the use of a solvent for the final removal of the polymer [248], [249]. Any additional chemical treatment can introduce defects or modify the graphene film and thus, ideally, should be avoided. Moreover, using a solvent-free transfer process makes it possible to apply graphene onto a wide range of polymeric substrates also. To avoid the problems related to PMMA, cyclododecane transfer method was used in this thesis [117], [250]. Cyclododecane transfer method is simple, effective, and capable of maintaining intact the intrinsic features of graphene films. Cyclododecane ($C_{12}H_{24}$) is a cyclic hydrocarbon, appearing as a white waxy solid made of large translucent crystals (Figure 3.49). It is readily soluble in non-polar and aromatic solvents, while it is insoluble in polar solvents such as water, being highly hydrophobic. This non-toxic and eco-friendly organic compound is solid at room temperature, has a low density (0.82 g/cm^3 at 80 °C) and a high vapor pressure (1.33 kPa at 100 °C). Its melting point is 60.7 °C, while the boiling point is 247 °C [117].

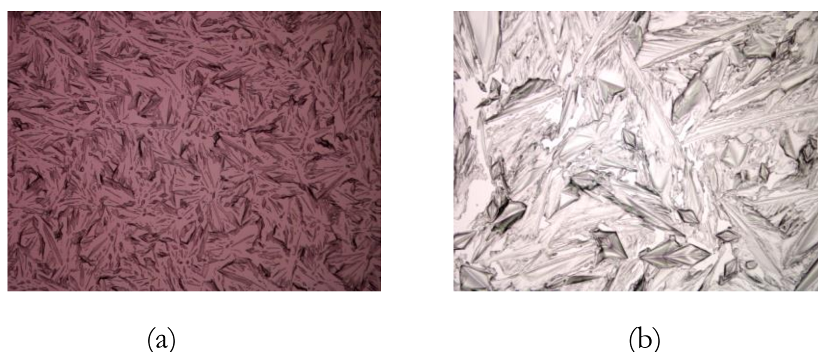

(a) (b)

Figure 3.49. 10X optical image of cyclododecane diluted in hexane (a) 20mg/ml and (b) 200mg/ml spin coated at 1000rpm for 40s.

Thanks to these characteristics, cyclododecane completely sublimates upon air exposure and is therefore often used by art restorers as a temporary, clean support material for transferring frescoes or other fragile art pieces. Commercially available cyclododecane was spin coated from a hexane solution (20 mg/ml) to form a compact layer on the surface of chemical vapor deposited graphene on copper samples. Other apolar and aprotic solvents (e.g., isooctane, cyclohexane and ethyl acetate) were also previously tested and gave comparable results. Cyclododecane support graphene during the Cu foils etching preventing damages to the film. After the full etching of the Cu, the free-floating carbon film was scooped up using a thermally oxidized silicon wafer and transferred into a clean bath of distilled water to remove the acid bath residues. It is important that the "scooping" substrate be highly wettable in water (with a low contact angle), so as not to create tension in the floating film through the formation of drops. The graphene film floating in water can then be scooped up for subsequent characterization and use. The complete removal of cyclododecane does not require solvents, but a mild thermal heating at 60 °C was used to speed up the sublimation. A scheme of graphene transfer method by using cyclododecane is reported in Figure 3.50. Different experiments were performed to test the optimal concentration of CDD in hexane to transfer monolayer films and monolayer islands. Solution of 40%, 44% and 40% of CDD in hexane were tested to transfer different sample. Monolayer films and monolayer islands require different concentration of CDD.

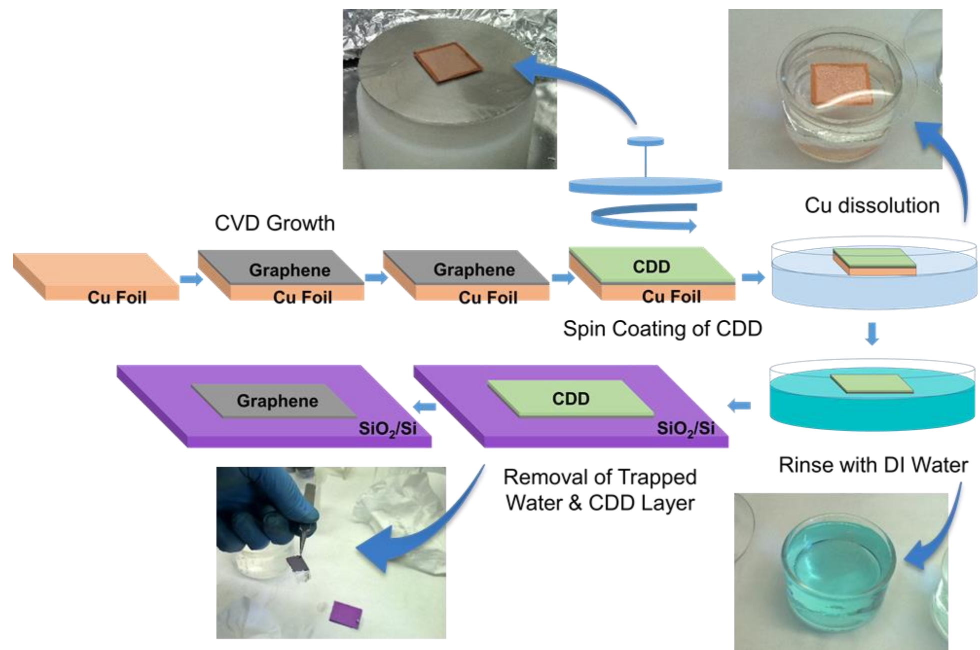

Figure 3.50. Scheme of cyclododecane transfer method process of graphene, from Cu native substrate to Si/SiO_2 substrate.

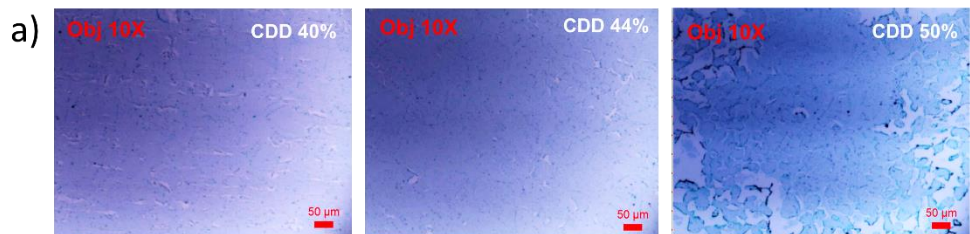

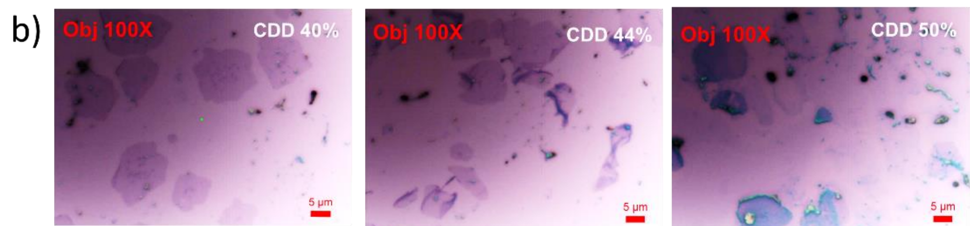

Figure 3.51. (a) Monolayer graphene films and (b) graphene islands transferred with different concentration 0f 40%, 44% and 50% of CDD in hexane.

Monolayer film need more support during the transfer procedure to prevent crack and avoid tears and wrinkles and then a concentration of CDD at 44% is used. A higher concentration of 50%, instead, damages the film

increasing tears and residues (Figure 3.51a). To transfer individual islands of monolayer graphene, instead, a lower concentration of CDD is required. A 40% solution of CDD can support the monolayer graphene and leaves less residues (Figure 3.51b). The AFM and Raman characterizations of graphene samples transferred with optimal concentration of CDD are shown in Figure 3.52. AFM image of monolayer graphene shows that the CDD transfer method can reduce the tears and the wrinkles (Figure 3.52a). Some etch bath residues that contaminate the film are present. These contaminations are due to ambient condition, because the CDD transfer results very sensitive to temperature. The Raman maps acquired on a greater region of 50x50 μm (step size 0.5 μm) in Figure 3.52b confirm a homogeneous graphene with low defect density ($I_D/I_G \approx 0.5 \div 0.6$) and low thickness ($I_{2D}/I_G \approx 2 \div 3$). CDD transfer method permits to transfer isolated graphene domains from Cu to SiO_2 substrate without alter shape and order of the islands (Figure 3.52c). AFM images show the presence of etch bath residues but show how the CDD transfer reduce the fold and wrinkles in graphene domains smaller than 10 μm. Raman maps acquired on a region greater than 15x15 μm (step size 0.15 μm) show that the transfer does not alter graphene properties (Figure 3.52d).

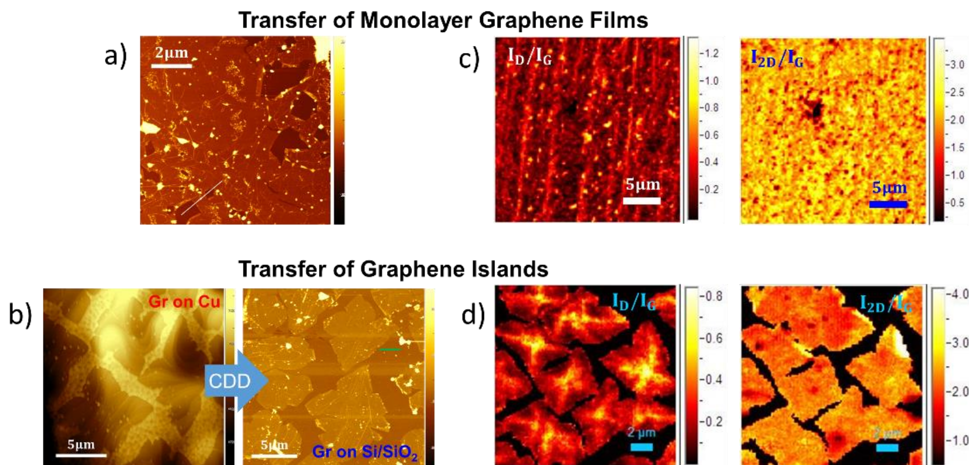

Figure 3.52. (a) and (b) AFM characterization of monolayer graphene film and graphene islands, respectively, (c) and (d) Raman maps of I_D/I_G and I_{2D}/I_G ratios of monolayer graphene film and graphene islands, respectively.

Graphene islands of few tens of microns successfully transferred show low defect density ($I_D/I_G \approx 0.4 \div 0.6$) and low thickness ($I_{2D}/I_G \approx 2 \div 3$),

without folds and wrinkles. Unlike PMMA, CDD allows to transfer graphene domains of few μm preserving graphene properties and small domains order.

3.4 Initial stages of the growth of graphene

The graphene growth by ethanol is rapid and efficient so that a continuous polycrystalline film is ready in a time as short as few seconds, less than 60 s [82]. However, these continuous films are not single layer and show a residual Raman defect related D peak, implying that the fast Cu coverage occurs at the expense of the crystalline quality of the film. Many experiments were performed in order to decelerate the graphene growth and observe the initial growth stages. It is important to study the graphene before the continuous film is formed and in particular observe the individual graphene islands before they merge in the continuous film. The shape and orientation of individual domains can give information about the quality of the film. Many small graphene domains, with irregular shape and without preferential orientation forms a monolayer films with many boundary defects and then a low quality monolayer film with low electron mobility. To improve the quality of graphene film it is relevant to improve the crystallinity. To secure crystallinity, it is necessary to increase the grain size by decreasing the nucleation density (δ_n) and tune the growth rate to reduce the defectiveness within each grain (Figure 3.53).

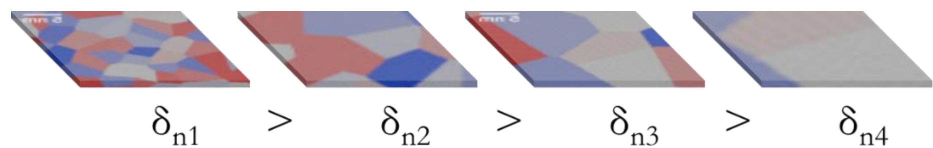

Figure 3.53. Schematic representation of reduction of nucleation density and increase of crystallinity.

Since both these goals can be achieved by throttling the precursors, the ethanol flow rate (Q_{eth}) was varied from 0.1 to 2.5×10^{-2} sccm and the total pressure from 800 to 65 Pa (**Table 3.2.** Graphene growth conditions and Raman parameters.Table 3.2). Graphene grown for 30 s (Figure 3.54, the black curves) showed a stronger D peak than that grown for 1800 s (the red curves) and for

30 s with more precursor (the blue curves): but now graphene is mostly single layer. This indicates that the initial defects are cured during the longer growth process and by the growth of additional layers.

Table 3.2. Graphene growth conditions and Raman parameters.

Growth Type		T (° C)	Time (s)	P (Pa)	Q_{eth} (sccm)	H_2 (sccm)	A_D/A_G	I_{2D}/I_G
Standard	(a)	1000	1800	800	0.1	100	0.22	0.91
	(d)	1070	1800	400	0.1	10	0.31	1.97
Rapid	(b)	1000	30	800	0.1	100	0.48	1.18
	(e)	1070	30	400	0.1	10	0.42	0.99
Reduced P/Eth	(c)	1000	30	130	2.5×10^{-2}	100	0.91	2.03
	(f)	1070	30	65	2.5×10^{-2}	10	0.60	1.90

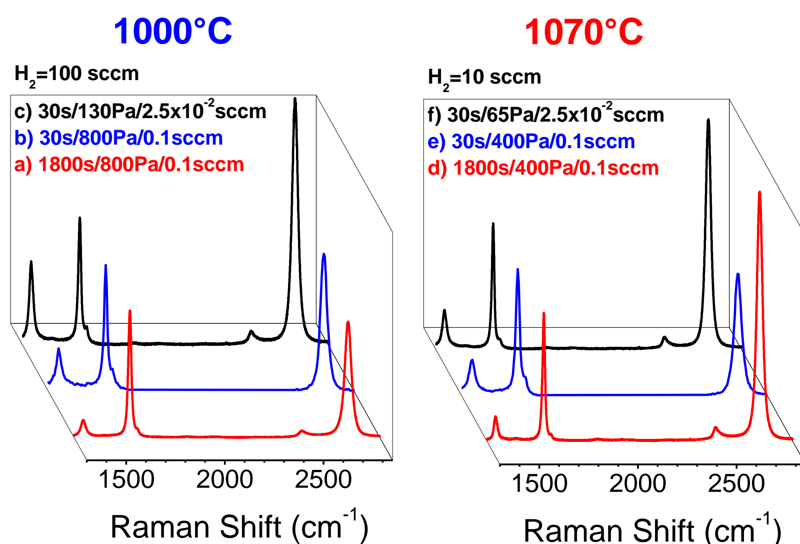

Figure 3.54. Raman spectra of graphene samples grown in the conditions of **Table 3.2**; the graphene was grown in different conditions (Temperature, growth time, pressure, flow of ethanol) [251].

However, at lower temperature, the growth is decelerated and the sample consists of small (< 5 μm) islands not fully interconnected. At 1070°C, where graphene was less defective, we had to reduce the growth time down to 15 s (**Figure 3.47**Figure 3.54) to observe the individual graphene islands. With Q_{eth} = 0.1 sccm, a continuous graphene film was still produced, while isolated graphene islands of 1 - 3 μm size were observed at the $Q_{eth} = 1.5\times10^{-2}$ sccm as shown in Figure 3.55a and Figure 3.55d.

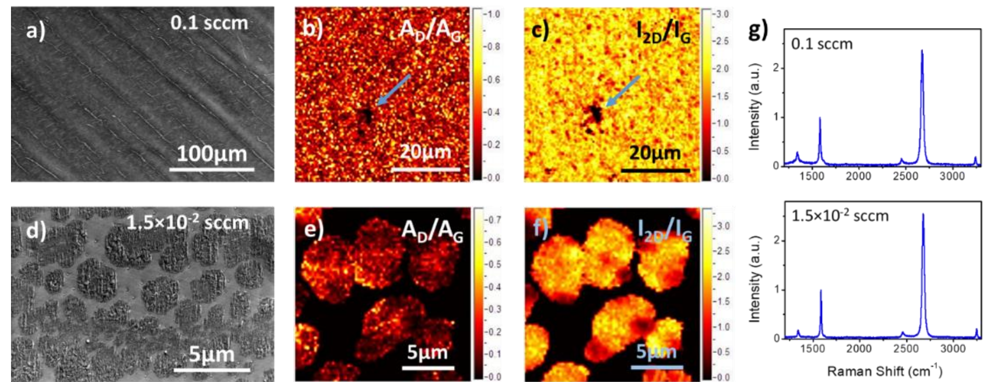

Figure 3.55. Graphene grown at 1070°C and 65 Pa for 15 s with (a-c) Q_{eth} = 0.1 sccm and (d-f) Q_{eth} = 1.5×10^{-2} sccm with g) averaged Raman spectra. (a,d) SEM micrographs of the as-grown graphene on the Cu substrates. (b,c) Raman mapping images (50 x 50 µm in size, 0.5 µm resolution) for A_D/A_G and I_{2D}/I_G after transfer on SiO_2/Si. The blue arrow indicates tear caused by transfer. (e,f) Raman mapping images (17 x 17 µm in size, 0.25 µm resolution) for A_D/A_G and I_{2D}/I_G of graphene islands after transfer on SiO_2/Si. The sample is composed of isolated monolayer graphene grains of 1 - 3 µm with smaller disorder level [251].

The I_{2D}/I_G (peak intensity ratio) maps in Figure 3.55c and Figure 3.55f show that both samples are made of homogeneous monolayer graphene ($I_{2D}/I_G \sim 2.7$ for the continuous graphene grown at 0.1 sccm and $I_{2D}/I_G > 2.3$ for isolated graphene islands grown at 1.5×10^{-2} sccm). In the case of these very short growth, the continuous film at Q_{eth} = 0.1 sccm has $A_D/A_G \cong 0.5$ (peak integrated intensity ratio), which is higher than that of graphene islands (~ 0.3) grown at Q_{eth} = 1.5×10^{-2} sccm. This implies that the monolayer film is less defective with a lower ethanol flow. The morphology of the islands after transfer onto a SiO_2/Si substrate was measured by AFM (Figure 3.56). The Cu foils used as substrates in the current study were polycrystalline and underwent substantial recrystallization during the CVD processes. The AFM map of the as-grown graphene on the Cu foils reveals that most islands do not have well-defined geometric shapes, it is nevertheless possible to appreciate differences in shape and orientation on different facets of the heavily-re-crystallized Cu grains and the presence of few hexagonally shaped grains possibly favored by Cu (111) facets [252].

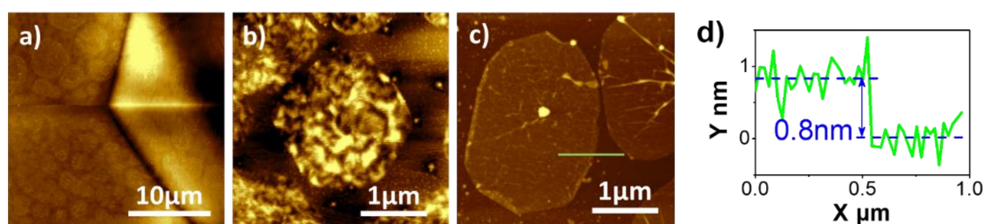

Figure 3.56. (a) AFM image of the graphene grains on copper foil facets (t = 15 s, T = 1070 °C, P = 65 Pa, and Q_{eth} = 1.5×10^{-2} sccm). (b) Higher resolution AFM image of a single grain on Cu. Some grains show hexagonal shape with rounded corners. c) AFM image after transfer on SiO_2/Si. (d) Height profile from (c) shows a step of 0.8 nm [251].

AFM measurements (Figure 3.56c) show that the islands are homogeneous with the presence of some wrinkles and contaminations due to transfer. The line profile reported in Figure 3.56d shows a step of 0.8 nm, typical for monolayer graphene on Si/SiO_2 and in line with Raman of Figure 3.55f.

Reducing ethanol from 0.1 sccm to 1.5×10^{-2} sccm graphene growth can be decelerated and the growth of few-micron-sized grains with low defect density is permitted, still in few seconds. However, although the islands show hints of faceting, from rectangular to hexagonal, they have neither a well-defined polygonal shape nor straight and sharp edges. Low precursor flow not only decelerate the growth, but also allows to the graphene single-crystal grains to become progressively regular [252].

3.5 Large graphene domains growth

Although low precursor flow and low temperature allow observing the initial growth stage, graphene domains grown for few second are too small. In order to obtain large and regular grains acting on the nucleation density is necessary, since individual crystals cannot outgrow their mutual average distance.

3.5.1 Nucleation density reduction

Substrate pretreatment before the CVD growth can reduce the nucleation density, in particular the preoxidation. To grow grains larger than a few microns

pre-oxidation treatments to the substrates was applied and the correlation of total pressure and ethanol flow on the nucleation density (δ_n) reduction was investigated. When the Cu foil is covered by an oxide layer, its surface is passivated and the presence of impurities acting as nucleation seeds is abated [216], [221], [224], [233]–[236]. As pre-oxidation treatment, the Cu foils were annealed in air at 250 °C for a time (t_{ox}) ranging from 0 to 150 min (Figure 3.57).

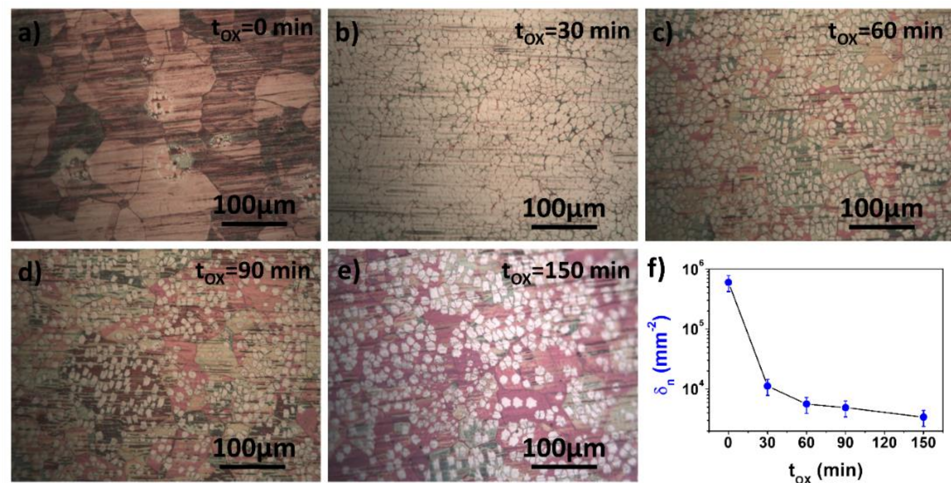

Figure 3.57. Nucleation density of graphene grown on Cu substrate with different pre-oxidation (250°C in air) time (t_{OX}) ranging from 0 to 150 min. (a-e) Optical microscopy of the graphene grown on Cu in the various cases. (f) Nucleation density trend *vs* pre-oxidation time. Adapted by [251].

With no pre-oxidation (t_{ox} = 0 min), the δ_n = 6×10^5 nuclei/mm^2 (Figure 3.57a). For t_{ox} = 30 min, the nucleation density drastically decrease (δ_n = 1.1×10^4 nuclei/mm^2). At longer times, δ_n keeps on slightly decreasing, reaching δ_n = 3.4×10^3 nuclei/mm^2 at t_{ox} = 150 min: Such nucleation density is more than two orders of magnitude smaller than the value obtained on non-oxidized Cu. The grains grow in size at a growth rate of ~0.08 µm/s and reached an average size of ~20 µm (Figure 3.57e).

Before the growth, the Cu substrate is normally annealed in hydrogen gas to remove the remaining native oxides on the surface. Annealing is completed prior to CVD growth of graphene on the Cu catalyst substrate to allow for grain expansion of the Cu, minimizing grain boundary density and the effects they have on graphene growth and the properties of graphene. The Cu grain

growth at the annealing temperature is driven by the thermodynamically favorable minimization of the Gibbs free energy by reduction of the grain boundary enthalpy [253], [254]. This procedure can increase the size of Cu domains and reduce Cu defects [88] where the nucleation of multi-layer graphene would happen. Having set the duration of the pre-oxidation treatment to 150 min, we investigated the effect of the Ar annealing on the growth (Figure 3.58). The Ar annealing was done in vacuum just before the CVD growth in the furnace. By varying the Ar annealing time from 1 to 20 min, we discovered that such pre-oxidation treatment was effective in reducing the nucleation density only with an Ar annealing of 1 min before the CVD growth. With a Ar annealing time longer than 1 min. the effect of the pre-oxidation on the nucleation suppression was cancelled and continuous graphene resumed growing.

Figure 3.58. (a-c) Nucleation density of graphene grown on pre-oxidized Cu substrate (250°C in air for 150min) with different pre-growth Ar annealing times (t_{ann}). Isolated grains grew only with 1 min Ar annealing, while in the other cases continuous films grew. Adapted by [251].

The combined effect of pre-oxidation and Ar annealing can be explained in terms of copper reconstruction and sublimation [226]. During the pre-oxidation treatment, both cupric oxide (CuO) and cuprous oxide (Cu_2O) are formed on the Cu surface [85]. At AFM analysis, the pre-oxidized Cu surface appears highly roughened due to typical clusters of sub-µm Cu oxide spheroids (Figure 3.59a) [85]. The annealing process converts almost all the CuO into Cu_2O, which has higher decomposition temperature and then is more stable at high-temperature [255]. It has been suggested that the initial presence of inactive Cu2O [10] inhibits the nucleation and growth. However, above 1000 °C in vacuum, the Ar annealing rids the Cu surface of oxides in a few seconds (as predicted by the Cu/O_2 phase diagram in Figure 3.59b [52]); this should

restore the catalytic activity of metallic Cu, but the reconstructed surface is very smooth and offers fewer nucleation sites, such as defects and carbon contaminations, than the original Cu foil [28, 53]. When the Ar annealing lasts for longer times ($t_{ann} > 1$ min), the intense Cu sublimation and re-deposition induce new nucleation sites and thus the growth of continues films resumes [28]. In conclusion, during the complex Cu reconstructive processes during pre-oxidation, annealing and growth, the nucleation sites are effectively although not permanently removed.

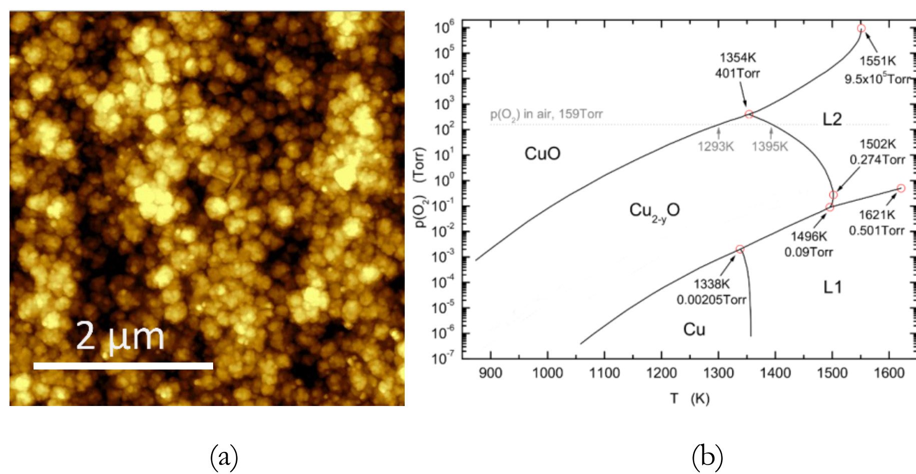

(a) (b)

Figure 3.59. (a) AFM image of pre-oxidized Cu foil, (b) the effect of oxygen on copper. Reprinted from [256].

3.5.2 Effect of ethanol flow: Towards large graphene grains

After determining the optimal substrate pretreatment for reduction of nucleation density and the growth of individual grains (Cu pre-oxidation at 250°C in air for 150 min, Ar annealing in vacuum for 1 min), the CVD parameters were optimized to obtain crystalline graphene grain of sub-mm size. The CVD parameters used are reported in Table 3.3.

Table 3.3. Optimization of the CVD conditions to make large-area, single-crystal graphene grains via ethanol-CVD on pre-oxidized, flat Cu substrates.

Process	T (°C)	Time (s)	P (Pa)	Q_{eth} (sccm)	H_2 (sccm)	A_D/A_G	I_{2D}/I_G	δ_n (nuclei/mm²)	Size (µm)
P1	1000	1800	130	1.5×10^{-2}	100	0.6±0.1	2.4±0.1	3.7×10^2	40±12
P2	1000	1800	130	1.5×10^{-3}	100	0.3±0.1	2.4±0.3	3	45.4±5.5
P3	1070	1800	130	1.5×10^{-3}	10	0.3±0.1	2.5±0.2	<3	90.3±8.9
P4	1070	1800	400	1.5×10^{-3}	10	0.2±0.1	2.5±0.4	<3	216.0±20.2
P5	1070	3600	400	1.5×10^{-3}	10	0.1±0.1	2.4±0.1	<3	359.6±75.3

At first, the effect of the ethanol flow on the grain size was further investigated by comparing the growth at 1.5×10^{-2} and 1.5×10^{-3} sccm. By decreasing the flow, the nucleation density turned from 3.7×10^2 (P1, Figure 3.60a) to δ_n = 3 nuclei/mm² (P2, Figure 3.60b). In the latter case, monolayer grains ($I_{2D}/I_G \approx 2.4$) grew larger than 40 µm and with low defect density (A_D/A_G from 0.6 to 0.3). The use of a smaller ethanol flow on oxidized Cu successfully decelerated the growth rate and favored the appearance of grains with regular and well-defined shape [97].

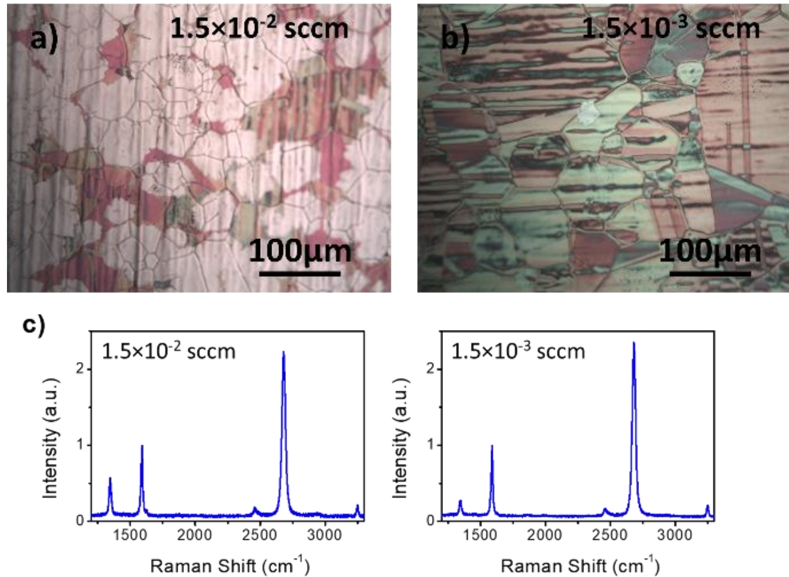

Figure 3.60. Optical images of graphene (30 min, 1000° C, 130 Pa) grown on pre-oxidized Cu foil with (a) 1.5×10^{-2} sccm and (b) 1.5×10^{-3} sccm of ethanol. (c) The corresponding Raman spectra. [251]

A detailed characterization of one 50-µm grain (130 Pa and 1.5×10^{-3} sccm) was carried out by AFM and Raman mapping (Figure 3.61). In line with Figure 3.60c, the A_D/A_G map (Figure 3.61c) shows that the ratio is < 0.2, with peak values of ~ 0.3 on artifacts caused by the transfer process. Also the I_{2D}/I_G map (mean value of ~ 2.4, Figure 3.61d) reveals the overall uniformity. The AFM (Figure 3.61b) measurements are in line with Raman mapping: the average thickness is ~ 1 nm (Figure 3.61b inset), pointing out to a monolayer, confirming the monolayer thickness previously inferred by Raman spectroscopy. The value is larger than the inter-plane spacing of graphite (0.335 nm) due to intercalated molecules and to the interaction forces between graphene-substrate-tip, as found for CVD-graphene on SiO_2/Si measured in similar experimental and environmental (relative humidity) conditions [161]–[163].

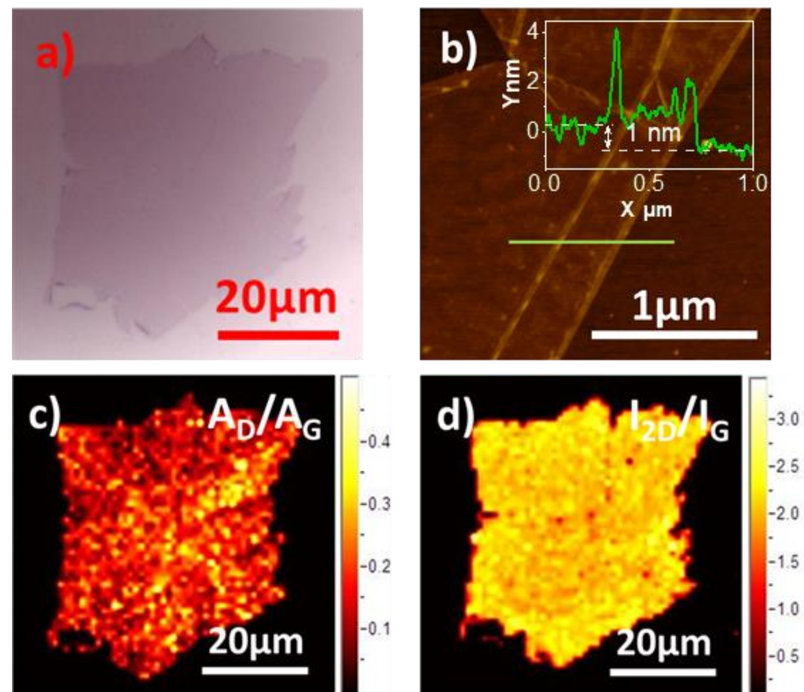

Figure 3.61. Analysis of a 50-µm grain (sample P2) after transfer onto Si/SiO_2. (a) Optical micrograph of the grain, (b) AFM topography image with thickness line profile of ~ 1 nm. The value is larger than the inter-plane spacing of graphite (0.335 nm) due to intercalated molecules and to the interaction forces between graphene-substrate-tip, as found for CVD-graphene in similar experimental and environmental (relative humidity) conditions [161]–[163]. Raman mapping images of (b) A_D/A_G and (c) I_{2D}/I_G peak ratio (60 µm × 60 µm area, 0.5 µm spatial resolution) [251].

The results show that such a low ethanol flow rate, together with preoxidation, is the key to the controlled-growth of isolated large graphene grains on Cu. The initial annealing time should be shorter than 60 s to grant a low nucleation density. Despite both annealing and growth are capable of removing the copper oxide the growth process can be extended up to 60 min and more, still guaranteeing low nucleation density. Our conclusion is that during the growth process, the supplied carbon atoms dissociated from ethanol are very efficiently and effectively incorporated into the few early formed graphene grains without contributing to nucleation.

3.5.3 High-temperature growth of large graphene grains

After setting the ethanol flow to 1.5×10^{-3} sccm, the CVD temperature was raised from 1000°C to 1070°C, to fully exploit the fast growth kinetics granted by ethanol aiming at increasing the grain size and crystallinity (Figure 3.62).

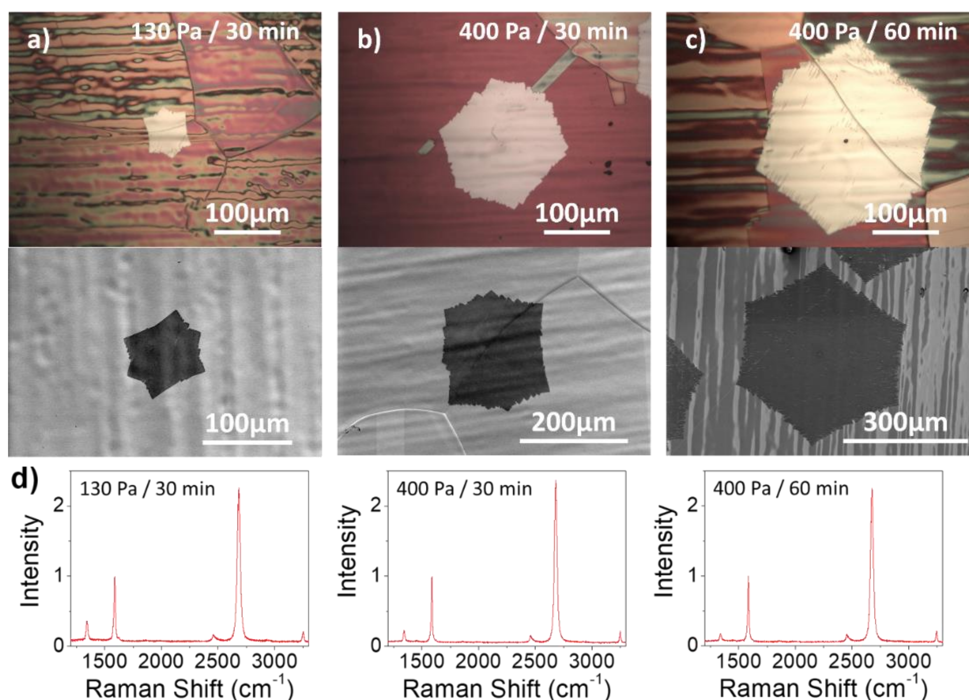

Figure 3.62. Optical and SEM images of the single-crystal graphene grains grown at 1070 °C with 1.5×10^{-3} sccm of ethanol: (a) 130 Pa, 30 min (P3); (b) 400 Pa, 30 min (P4); (c) 400Pa, 60 min (P5). (d) Raman spectra of the samples transferred onto Si/SiO_2[251].

At 1070 °C, single-crystal grain reached sizes over 90 μm (P3, Figure 3.62a). Raman analysis shows $I_{2D}/I_G = 2.5$ and $A_D/A_G = 0.3$, a typical Raman signature of crystalline monolayer graphene, with lower defect level than at 1000°C (Figure 3.62d). By raising the gas total pressure (400 Pa) during the growth, the graphene grains extended their sizes to more than 200 μm (P4, Figure 3.62b). In these conditions, by bringing the growth time to 60 min, sub-mm grains (larger than 350 μm) grew with regular geometric shape and sharply defined edges (P5, Figure 3.62c). The Raman spectra in Figure 3.62d shows $I_{2D}/I_G = 2.5$ [135], [136] and $A_D/A_G < 0.1$. Graphene grown for 60 min showed the lowest defect related D peak intensity, which was probably induced by the transfer process.

Figure 3.63a shows the edge morphology of a graphene grain (P5, 350 μm in size) on Cu substrate.

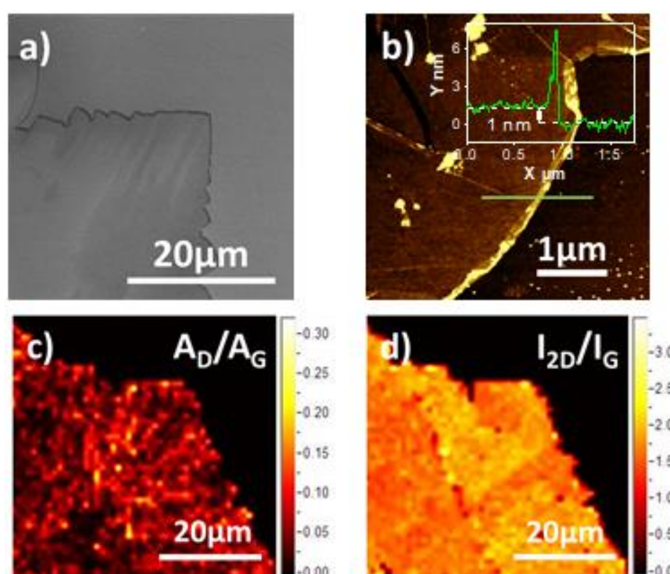

Figure 3.63. Analysis of a 350-μm graphene grain (P5: 1.5×10^{-3} sccm ethanol, 1070° C, 130 Pa, 60 min). (a) SEM image and (b) AFM topography image with thickness line profile of the grain edge. Raman mapping images of (c) A_D/A_G and (d) I_{2D}/I_G [251].

The thickness measured by AFM is ~ 1 nm, compatible with monolayer graphene on Si/SiO_2 (Figure 3.63b). Raman mapping images (50 × 50 μm) acquired on the grain edge highlight the uniformity of the sample, with $A_D/A_G \leq 0.1$ (Figure 3.63c). Small regions with $A_D/A_G > 0.2$ correspond to

minor contaminations, wrinkles and folds due to transfer process. The Raman peak ratio $I_{2D}/I_G > 2$ confirms the monolayer thickness (Figure 3.63d).

To summarize, the optimization steps led to a concurrent decrease in nucleation density and to a major increase in grain size, as reported in Figure 3.64. The successful growth of large single-crystal graphene by ethanol-CVD might be possibly attributed to oxygen atoms dissociated from ethanol, which would act as nucleation inhibitors by suppressing the formation of new nucleation sites [224]. However, in ethanol-CVD, oxygen might also act as a growth enhancer promoting the quick growth of graphene on a Cu substrate [82]. Therefore, this growth platform would deserve further investigations in order to fully understand the overall effect of oxygen on the nucleation and growth of graphene.

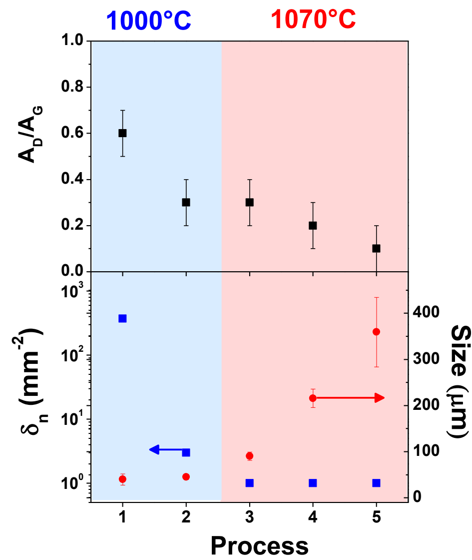

Figure 3.64. Optimization steps performed to reduce nucleation density δ_n according to Table 1. Grain size and A_D/A_G are also reported.

3.5.4 Electrical properties of sub-mm graphene grains by ethanol-CVD

To investigate electrical properties of the large grains (P5), we fabricated devices with transmission line method (TLM) geometry, as shown in Figure 3.65a. Figure 3.65b shows transfer curve (I_D-V_G) of a representative graphene device. The charge neutral point is shifted to ~ 50 V, indicating that graphene

is highly p-doped. The p-doping behaviour of graphene can be caused by various extrinsic factors, such as residues from the wet-transfer process, charged impurities on the SiO_2 substrate, and trapped molecule between graphene channel and substrate [257], [258]. The inset shows linear output curves (I_D-V_D) with gate voltage dependence, demonstrating Ohmic contact between graphene and metal electrodes.

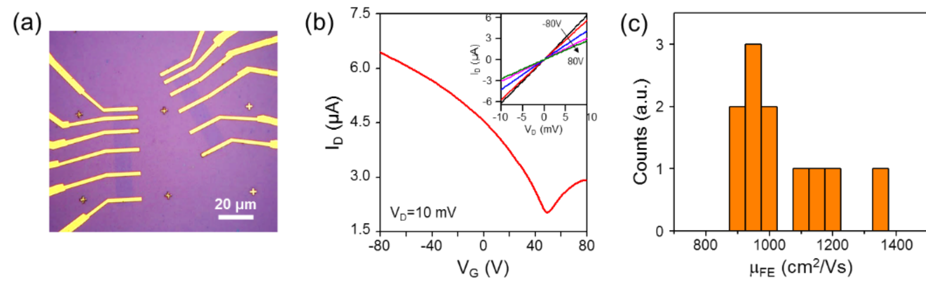

Figure 3.65. (a) Optical image of graphene devices with TLM geometry. (b) Transfer curve (I_D-V_G) of a representative graphene device. The inset shows the output curves (I_D-V_D) at different gate voltages. (c) Histogram of field-effect mobilities measured from eleven graphene devices [251].

The field-effect mobility (μ_{FE}) of graphene was calculated by using the equation,

$$\mu_{FE} = \frac{L}{WC_iV_D}\left(\frac{dI_D}{dV_G}\right) \qquad 3.43$$

where L, W and C_i are channel length, width and capacitance of SiO_2, respectively. As shown in Figure 3.65c, the extracted filed-effect mobility ranges from 912 to 1355 cm^2/Vs, which are much higher to the mobility values of polycrystalline graphene films grown by any alcohol-type precursors [83], [259]. In the case of isolated grains (transferred onto Si/SiO_2), to date a few works reported higher mobility values for methane-CVD growth [54], [217], [260]–[262], but no one ever disclosed mobility values of ethanol-grown grains [85], [111]. We further calculated sheet resistances (R_{sh}) of the graphene grains at V_G = 0 V (no electrical doping): The best samples attained a sheet resistance of 550-610 Ω/□, highlighting the potential of ethanol-grown graphene as a transparent conducting material [251].

4

Graphene based derivative interlayer in Graphene on Silicon Schottky Barrier Solar Cells

The role of a non conductive graphene based derivative (GBD) as interlayer in Graphene on Silicon Schottky Barrier Solar Cell (SBSC) will be presented in this chapter. First, an introduction to Schottky junction theory will be reported, and then the experimental activity, carried out at the ENEA Portici and ENEA Casaccia Research Centers concerning design, fabrication and characterization of the Graphene/GBD/Silicon Schottky Barrier Solar Cell will be investigated in detail.
The effect of GBD interlayer on the electrical and photovoltaic solar cell parameters will be discussed.

4.1 Introduction

Schottky junction solar cells are similar to p-n junction solar cells in which one of the semiconductors is replaced with a metal. Schottky junctions benefit from being the majority carrier devices fabricated with low temperature processes, but up until the mid-1970s suffered from a lower open circuit voltage (V_{OC}) with respect to p-n junction solar cells [263]. This low V_{OC} is partly due to the high dark current inherent in devices that rely on thermionic emission of majority carriers due to the transport across the junctions (as in Schottky junctions). Additionally, surface states that pin the Fermi level are also responsible for increased recombination and a corresponding increase in dark current. A low V_{OC} and a corresponding low power conversion efficiency (PCE) kept Schottky junction devices away from competing with p-n solar cells until Godfrey and Green developed a 17.6 metal-insulator-semiconductor (MIS) PV cell with an open circuit voltage of over 0.65 V [264], [265]. This excellent performance was realized through a thin (< 2 nm) insulating layer placed between the metal and semiconducting layer, passivating the silicon

surface and reducing recombination while negligibly affecting current transport.

Due to its important advantage of being naturally compatible with thin film processing, graphene is easy to integrate into existing semiconductor device technologies. It is readily scalable, has low contact resistance with most common metals as Ti, Cr, Ni, Pa [266]–[269], and can form rectifying junctions with several semiconductor materials. The graphene–semiconductor (Gr/Si) junction is one of the simplest conceivable devices in a hybrid graphene–semiconductor technology. The understanding of its properties and the mastering of its fabrication process are important prerequisites towards a graphene integrated electronics. The challenge in the fabrication is the ability to establish an intimate Gr/Si contact by avoiding chemical–structural modifications to the semiconductor while simultaneously preserving the superior properties of graphene.

The Gr/Si junction offers great opportunity to study the physics occurring at the interface between a 2D and a 3D material, as well as between a zero and a definite bandgap system, and can be a convenient platform to investigate electronic properties and transport mechanisms. Surprisingly, it has become the subject of systematic investigation only in the last years. The Gr/Si junction has already been demonstrated as a rectifying or a barrier-variable device, a photovoltaic cell, a bias-tunable photodetector, a chemical sensor and as a building-block of more complex graphene-based electronic systems, such as Schottky-barrier based field-effect transistors (FETs) or high-electron-mobility transistors (HEMTs) [270]. While the current–voltage (*I–V*) behaviour of a Gr/Si junction can be roughly described by the well-known ideal diode equation, the details of the measured characteristics often require modifications of the standard thermionic theory and the consideration of additional effects. As for conventional metal/semiconductor diodes, the quality of the interface dramatically affects the junction properties. Impurities and defects may significantly alter the *I–V* curve. Additionally, there are important effects, which origin from the peculiar band structure and density of states of graphene and from its two-dimensional nature. The low density of states close to the neutrality point makes the graphene Fermi level extremely sensitive to

the amount of carriers injected into or from the semiconductor. The position of the Fermi level affects the Schottky barrier height (SBH), which in turn controls the current–voltage relationship. These features make the current of the Gr/Si junction tunable in several ways and can be conveniently exploited in practical applications. The role of a low conductive graphene based derivative interlayer in a standard Gr/Si junction is presented in the following chapter.

4.2 The Schottky junction

The intimate contact between a metal and a semiconductor can result in two ideal devices: the ohmic junction or the rectifying junction also called Schottky. In an ideal ohmic junction, the current I varies linearly with the applied voltage V and the ratio V/I is the combination of the contact (R_C) and the series (R_S) resistance:

$$\frac{V}{I} = R_C + R_S \qquad (4.1)$$

Ideal Schottky junction acts as a perfect diode with high current and very low contact resistance in one direction (forward direction) and negligible current or infinite resistance in the opposite direction (reverse direction). Real metal/semiconductor (M/S) junctions are neither perfectly ohmic nor perfectly rectifying [271]. Due to its simple structure, a Schottky diode is a basic component for several devices. Recently, graphene has been demonstrated to form junctions with semiconductor materials showing rectifying characteristics. The main novelty of this sort of devices, where graphene operates as a metal, is the tunable Schottky barrier height (SBH), a feature which makes the graphene/semiconductor junction suitable for applications even in other fields such as photo-detection, high-speed communications and solar cells [270].

4.2.1 The Schottky barrier

A metal-semiconductor (M/S) junction is formed at the interface between a metal and a semiconductor. Figure 4.66 represents the Schottky model of the junction. The vacuum level or the free-electron energy, E_0, is the energy state of electrons with zero kinetic energy outside the material, either metal or semiconductor. The difference between E_0 and the Fermi level E_F in any material is called work function Φ:

$$\Phi = E_0 + E_F \qquad 4.2$$

The Fermi energy E_F represents the highest occupied electron energy state at T = 0 K in a metal. In a non-degenerate semiconductor it lies in the gap between the valence and the conduction band (Figure 4.66b), and it separates the occupied states from the unoccupied ones at T = 0 K. E_F appears in the Fermi–Dirac distribution function

$$f(E) = \frac{1}{1 + e^{(E-E_F)/kT}} \qquad 4.3$$

which expresses the probability that an electron occupies a state with energy E at the temperature T ($k = 8.62\times10^{-5}$ eV/K is the Boltzmann constant). According to Eq. 4.3, for T > 0 K, electrons can occupy levels above the Fermi level with a rapidly decreasing probability as the energy moves away from E_F. For metals, the work function $\Phi_{\mathrm{M}} = E_0 - E_{FM}$ is the energy needed to move an electron from the Fermi level E_{FM} to the vacuum and has a value which depends only on the type of metal. In a given semiconductor, the position of E_{FS} depends on the doping: E_{FS} is closer to E_C (the lowest allowed energy level of the conduction band, ≈ 4.05 eV for silicon (Si)) for a n-type semiconductor or closer to E_V (the highest allowed energy level of the valence band, ≈ 5.17 eV for Si) for p-type doping, as shown in Figure 4.66d and e. The electron and hole densities in a semiconductor, denoted by n and p respectively, are related to the Fermi energy by the relations:

$$n = N_c e^{-(E_C - E_{FS})/kT} \quad 4.4$$

and

$$p = N_v e^{-(E_{FS} - E_v)/kT} \quad 4.5$$

where $N_c = 2(2\pi m_e^* \, kT/h^2)^{3/2}$ and $N_v = 2\left(2\pi m_p^* \, kT/h^2\right)^{3/2}$ are the effective densities of states in the conduction and valence band, and m_e^* and m_p^* are the effective masses of electrons and holes, respectively. h = 4.136 × 10^{-15} eV s is the Planck constant. Since the Fermi level is not fixed, the work function, $\Phi_S = E_0 - E_{FS}$, in a semiconductor varies according to the doping. To characterize a semiconductor can be used the electron affinity χ that represents the difference between the vacuum level and the conduction band edge:

$$\chi = E_0 - E_C \quad 4.6$$

(examples of electron affinity are: 4.05 eV for Si, 4.07 eV for gallium arsenide (GaAs), 4.0 eV for germanium (Ge)).

When a metal with work function Φ_M is established in intimate contact with a semiconductor having a different work function Φ_S ($\Phi_M > \Phi_S$ in the example of Figure 4.66a–d), charge transfer occurs until the respective Fermi levels are aligned at equilibrium. In Figure 4.66a and b, the different position of the Fermi levels implies that electrons in the n-type semiconductor have an average total energy higher than that in the metal; after the contact, the disparity in average energy causes the transfer of electrons from the semiconductor to the metal. The transfer of charge results in the formation of a layer at the semiconductor interface depleted of free charge carriers, called depletion layer or space charge region. The removal of electrons (and similarly of holes for p-type substrates) leaves the space immobile charge of the uncompensated dopant ions. In Figure 4.66c such layer of immobile positive ions is shown over a distance w from the junction and corresponds in the band diagram of Figure

4.66d to the region with bands bent upwards. In the depletion layer with up-bent bands of Figure 4.66d, the Fermi level is close to neither E_c nor E_v as should be according to Eqs.4.4 and 4.5 in the region with reduced values of n and p.

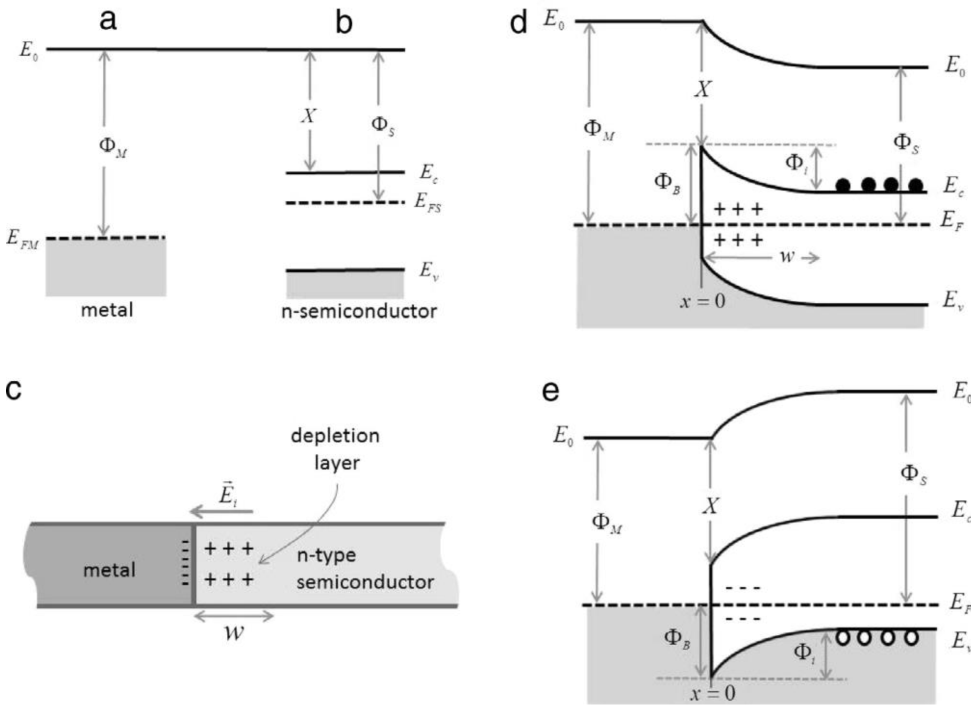

Figure 4.66. (a) Work function Φ_M and Fermi energy E_{FM} in a metal and (b) work function Φ_S, electron affinity X and band structure with a bandgap between E_c and E_v and Fermi energy E_{FS} in a n-type semiconductor. (c) Charge at the metal/semiconductor junction. (d) Schematics of equilibrium band diagram for the junction. The junction is set at x = 0. Φ_i is the energy barrier to the flow of electrons (black dots) from the semiconductor to the metal, while Φ_B is the Schottky barrier height (SBH) for the electron flow in the opposite direction. w is the extension of the depletion layer. (e) Schematics of equilibrium band diagram of a metal with a p-type semiconductor under the assumption that $\Phi_M < \Phi_S$ (empty circles represent holes). [270]

The formation of a depletion region in the semiconductor is a necessary condition for the achievement of a Schottky rectifying junction. The contact between a metal and a n-type semiconductor with $\Phi_M < \Phi_S$ would result in electron injection from the metal to the semiconductor. No depletion layer will be formed in this case, since the metal can be considered an infinite electron reservoir, and the junction would be ohmic. When a depletion layer is formed in the semiconductor, the space charge is mirrored by a very thin layer of

opposite-sign charge at the metal surface (Figure 4.66c). These two layers of opposite charge give rise to an electric field $\vec{E}_i$ and to a potential $\varphi_i = \Phi_i/e$ (e = 1.6×10^{-19} C the electron charge) at the junction (Figure 4.66d), which prevent further net charge diffusion between the semiconductor and the metal. Φ_i (expressed in V) is called built-in potential; the corresponding energy, $\Phi_i = e\varphi_i$ (in eV), which is the energy barrier against the diffusion of electrons from the semiconductor to the metal, is obtained as

$$\Phi_i = \Phi_M - \Phi_S \qquad 4.7$$

The electric field $\vec{E}_i = -\vec{\nabla}\varphi_i$ is the built-in electric field and opposes to the motion of electrons from the semiconductor to the metal. It has the maximum value at the physical M/S interface (x = 0 in Figure 4.66) and decreases with distance until it vanishes at the edge of the depletion layer (i.e. at x = w). The most important feature of the M/S energy diagram at the equilibrium, as shown in Figure 4.66d for the n-type semiconductor, is the appearance of a discontinuity of the allowed energy states, which results in the formation of an energy barrier at the M/S interface, Φ_B, known as the Schottky barrier (SB). Φ_B is the barrier seen by the electron's flow from the metal to the n-type semiconductor and plays a similar role as Φ_i. While Φ_i can be modified by the application of an external voltage bias, Φ_B is unaffected by the voltage bias. Φ_B is called the Schottky barrier height (SBH) and can be related to the metal work function and to the semiconductor electron affinity (Figure 4.66d):

$$\Phi_B = |\Phi_M - \mathrm{X}| \qquad 4.8$$

Eq.4.8 is known as the Schottky–Mott relation. Φ_M and X are both properties of the crystal lattice and cannot be modified by normal level doping or by a voltage bias and so is the SBH.

A similar barrier, for the flow of holes from the metal to the semiconductor is formed at the metal/p-type semiconductor junction when

$\Phi_M < \Phi_S$, as shown in Figure 4.66e. The Schottky-Mott relation of a MSJ on a p-type substrate, can be written as

$$\Phi_B = E_g - |\Phi_M - \mathrm{X}| \qquad 4.9$$

where

$$E_g = E_C - E_v \qquad 4.10$$

is the bandgap of the semiconductor. According to Eqs.4.8 and 4.9, the sum of the SBHs for electrons and holes of a given metal on a n- and p-doped semiconductor are expected to be equal to the bandgap:

$$\Phi_{B,n} + \Phi_{B,p} = E_g. \qquad 4.11$$

The Schottky barrier is the most important feature of a M/S rectifying junction and the SBH, according to 4.8 and 4.9, is controllable by the choice of materials and is independent of the semiconductor doping level. A larger SBH is usually achieved with elevated work function metals on n-type semiconductors or with low work function metals on p-type semiconductors and results in better rectifying characteristics. However, experimental measurements show that the relation 4.8 or 4.9 are only qualitatively valid, with SBH often nearly independent of metal work function [272]–[274]. Theoretical value of SBH is lowered by Schottky effect. When an electron is at a distance x close to a metal, a positive charge is induced at the metal surface. This charge generates a force which is equivalent to that obtained with an equal positive charge (image charge) at distance -x inside the metal. The interaction between the electron and its image charge corresponds to a potential energy $-e^2/(16\pi\varepsilon_0 x^2)$. This energy, combined with the electron potential energy in an external electric field $\vec{E}$ at the metal surface tending to pull electrons from the metal, $-e|\vec{E}|x$, results in an effective lowering of the barrier height (Figure 4.67).

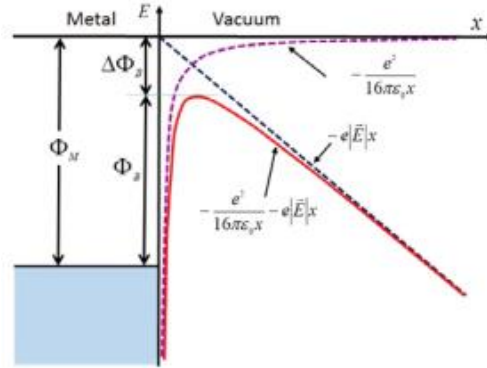

Figure 4.67. Energy band diagram between a metal surface and vacuum, showing (red continuous line) how the application of an external electric field $\vec{\boldsymbol{E}}$ lowers the effective barrier height by the amount $\boldsymbol{\Delta\Phi_B}$

When the metal is in contact with a semiconductor, the appropriate interface electric field has to be considered and the free-space dielectric constant has to be replaced by the dielectric constant of the semiconductor $\varepsilon_s = k_s\varepsilon_0$ (k_s is the relative permittivity, ~11.7 for Si). In this case, the SBH lowering can be expressed as

$$\Delta\Phi_B = \sqrt{\frac{e^3|\vec{E}_{max}|}{4\pi\varepsilon_s}} \qquad 4.12$$

where $\vec{E}_{max}$ is the maximum electric field at the M/S junction [271]. If a voltage bias V is applied to the junction, since $\vec{E}_{max}$ is related to the bias V by the relation

$$|\vec{E}_{max}| = \sqrt{\frac{2eN}{\varepsilon_s}(\varphi_i - V - kT/e)} \qquad 4.13$$

where N is the doping density per volume, the Schottky effect of Eq. 4.12 introduces a dependence of the SBH on the fourth root of the applied voltage. Eqs. 4.12 and 4.13 make the SBH to depend also on the substrate doping level. This dependence enables a fine tuning of $\Delta\Phi_B$ and a SBH adjustment though

the control of N, which is practically performed by ion implantation in a thin layer (~10 nm or less) over the semiconductor surface. However, the Schottky effect in a M/S structure is less important than in a metal-vacuum system, because of the larger value of ε_S.

4.2.2 Thermionic emission and I–V characteristic

Differently from a p–n junction, the current transport in a M/S junction is mainly due to majority carriers, that are electrons for n-type and holes for p-type semiconductors. With the moderately doped semiconductors which are employed to fabricate the Schottky diodes (N≤5×10^{+17} cm^{-3}), the emission of thermally excited electrons (or holes) from the semiconductor to the metal over the potential barrier Φ_i (thermionic emission, TE) is the dominating process contributing to the MSJ current (Figure 4.68a).

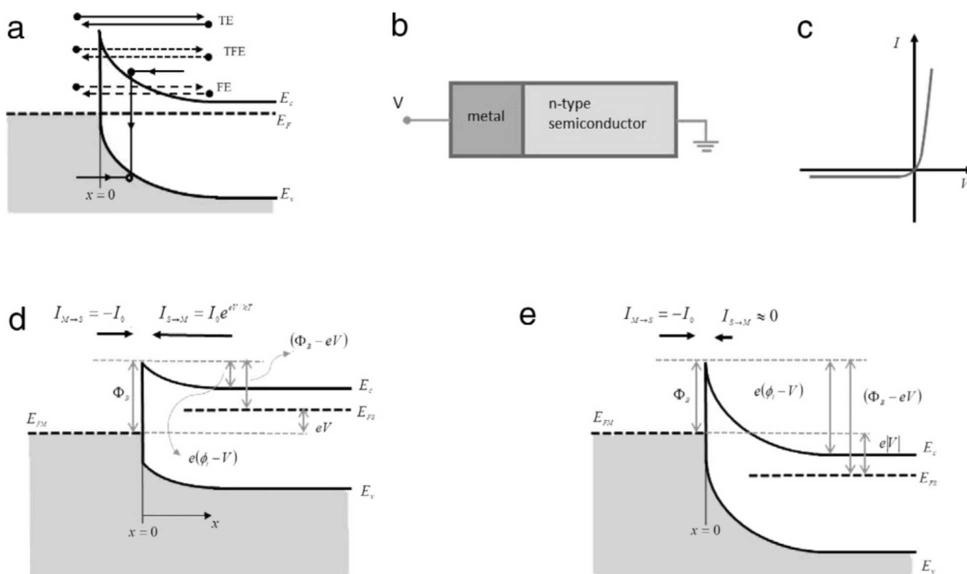

Figure 4.68. (a) Principal transport processes across a Schottky junction: TE = thermionic emission, TFE = thermionic field emission, FE = field emission and electron–hole recombination. (b) Schematic of the voltage bias of the junction. (c) Ideal I–V characteristic of a Schottky junction. (d) Band diagrams at the ideal metal/n-type semiconductor Schottky junction in forward bias (V > 0) and in (e) reverse bias (V < 0). The arrows associated with currents in (d) and (e) indicate the direction of the electron flow [270].

Accordingly, the I–V characteristics of Schottky junctions (Figure 4.68c) are quite accurately reproduced using the thermionic emission theory. Other conduction mechanisms are the thermionic field emission (TFE) or field emission (FE), which include tunneling through the barrier (Figure 4.68a). The relative contribution of the conduction mechanism depends on the doping N in the semiconductor as well as on the temperature T [275], [276]. Other mechanisms that may contribute to the M/S current are generation/recombination in the space-charge region, diffusion of electrons in the depletion region or injection of holes from the metal that diffuse in the semiconductor and recombine in the neutral region. In addition, there may be edge leakage current due to high electric field at the metal-contact periphery or interface current due to traps at the M/S interface. Figure 4.68d and e show the energy band diagrams when a positive (forward) or negative (reverse) voltage bias V is applied to the metal with respect to a n-type semiconductor (Figure 4.68b). V affects the width of the depletion layer which is narrowed (widened) in forward (reverse) bias according to:

$$w = \sqrt{\frac{2\varepsilon_s}{eN}(\varphi_i - V - kT/e)} \qquad 4.14$$

where φ_i is the built-in potential (kT/e ≈ 26 mV at room temperature is often neglected) [271]. In the reverse (forward) bias, the Fermi energy of the bulk semiconductor E_{FS} shifts down (up) with respect to that of the metal, E_{FM}, allowing an increase (decrease) of the potential barrier $\varphi_i - V$, that results in rectification. At the interface, the work function of the metal is independent of voltage bias due to the high density of states of the metal at the Fermi level. E_{FM} is practically unaffected by the bias and is pinned to a level Φ_M from the vacuum E_0. With reference to Figure 4.68d, the thermionic emission theory assumes that the Fermi energy in the semiconductor is flat all the way to x = 0. Then, according to Eq. 4.4, the electron density at x = 0 can be expressed as

$$n = N_c e^{-(E_c - E_F)/kT} = N_c e^{-(\Phi_B - eV)/kT}. \qquad 4.15$$

The current density, $I_{S\to M}$, due to electrons flowing from the semiconductor to the metal can be obtained as

$$I_{S\to M} = A\frac{4\pi e m^* k^2}{h^3}T^2 \exp\left(-\frac{\Phi_B - eV}{kT}\right) \quad 4.16$$

According to Eq. 4.16, $I_{S\to M}$depends on the SBH, but is independent of the shape of the barrier. However, it strongly depends on the applied voltage bias, being exponentially increased (decreased) by a positive (negative) V. The total current through the junction can be obtained by adding to $I_{S\to M}$the current $I_{M\to S}$ corresponding to the flow of electrons from the metal to the semiconductor. At zero bias, there is no net flow of current: the electron current from the semiconductor to the metal is balanced by the current in the opposite direction:

$$I_{S\to M} + I_{M\to S} = 0 \quad 4.17$$

or

$$\begin{aligned} I_{S\to M} = -I_{M\to S} &= A\frac{4\pi e m^* k^2}{h^3}T^2 \exp\left(-\frac{\Phi_B}{kT}\right) \\ &= AA^* T^2 \exp\left(-\frac{\Phi_B}{kT}\right) \end{aligned} \quad 4.18$$

where

$$A^* = \frac{4\pi e m^* k^2}{h^3} \quad 4.19$$

is known as the Richardson constant (≈ 112 $Acm^{-2}K^{-2}$ for n-Si). Although the Richardson constant should depends only on the material properties of the semiconductor, it has been shown that the metal can cause some variations in its value [277]. Variations in A^* can also be caused by inhomogeneity in SBH, by interfacial layers, quantum mechanical reflections and tunnel of carriers

[278]–[280]. Since the application of a bias does not change the Fermi level of the metal, Φ_B, is unaffected by a bias and so is the flow of electrons from the metal to the semiconductor $I_{M\rightarrow S}$. Finally, by adding Eqs. 4.16 and 4.17, the total current though the junction with the applied voltage bias V results:

$$I_{total} = I_{S\rightarrow M} + I_{M\rightarrow S} = I_0 \left[\exp\left(\frac{eV}{kT}\right) - 1 \right] \tag{4.20}$$

with

$$I_0 = A^* T^2 \exp\left(-\frac{\Phi_B}{kT}\right) \tag{4.21}$$

as the reverse saturation current or diode leakage current or dark current. I_0 is an important figure of merit: the lower it is the better is the diode. It strongly depends on the temperature and the SBH: even a small change $\delta\Phi_B$ can have observable effects on it.

Eq. 4.20 is the ideal diode equation, which is valid both in forward and reverse bias, and describes the qualitative behavior of the I–V curve of a Schottky junction (Figure 4.68c). Accordingly, in forward bias, the current is dominated by $I_{S\rightarrow M}$ and increases exponentially with the voltage V, while for V < 0 the current is almost constant and is given by $I_{M\rightarrow S} = -I_0$. Deviations from the ideal behavior are often observed in real devices. In forward bias, the rise of the current can be better reproduced by inserting a phenomenological parameter η in the exponential of Eq. 4.20. Also, at higher currents a series resistance R_S, which includes the lump resistance of the semiconductor, metal and contacts, becomes important since it lowers the effective voltage applied to the junction:

$$V_{eff} = V - R_S I \tag{4.22}$$

Eq. 4.20 can then be rewritten as

$$I = I_0\left(e^{\frac{e(V-R_SI)}{\eta kT}} - 1\right). \qquad 4.23$$

η is called ideality factor and is another important metric of the Schottky junction ($\eta \approx 1.0 \div 1.2$ correspond to good quality real junction). This equation can be written as [276], [281]

$$I = I_0 e^{e\left(\frac{V-R_SI}{\eta kT}\right)}\left(1 - e^{\frac{e(V-R_SI)}{\eta kT}}\right). \qquad 4.24$$

It measures the deviation from the thermionic emission, taking into account the degree to which defects and other additional non-thermionic effects mediate the transport. The assumption $\eta = 1$ may be inappropriate for several reasons:

1. It can be affected (increased) by image force lowering and the presence of interface states [271], [282]. Nevertheless, if the transport current is due to thermionic mechanism, expression 4.21 is still valid, but with η>1.
2. A mode of carrier transport other than thermionic emission might dominate. Depending on doping levels, temperature, and barrier height, the current transport mechanism takes shapes [271], [281], [282] other than the thermionic one such as generation-recombination current [282], tunneling across the interface [282] and the injection of minority carriers into the semiconductor.
3. η>1 can be the result of barrier inhomogeneities at the Schottky contact [283].

Such effects include thermionic field emission and field emission, generation/recombination, image-force-lowering of the SBH, Schottky barrier inhomogeneity, bias-dependence of the SBH, edge leakage, etc. [284], [285].

Despite these possible complications, the I-V characteristic of a real diode is often described within the thermionic emission theory regardless of the η value. Consequently, the barrier height Φ_B, determined from Eq. 4.21, is only the result of a calculation, and has no real physical

meaning if the thermionic current ($\eta = 1$) is not the dominant regime. An accurate determination of Schottky parameters is therefore required to understand the behavior of the interface and to correctly model the transport properties of the Schottky barrier

4.2.3 Analysis of I-V characteristic

Several methods have been proposed to extract the different parameters of Schottky diodes [283], [286], [295], [296], [287]–[294]. The method used in this thesis consisted in fitting the experimental I-V curves with Eqs. 4.21 and 4.23, where the three fit parameters are R_s , η, and Φ_B. The hypothesis are that $\Phi_B$is determined by Eq. 4.21 even if $\eta \geq 1$, Φ_B and η are voltage independent. For $V \rightarrow 0$ the linear behaviour of the semi-log plot is lost due to the "-1" in Eq. 4.23. However, according to Eq. 4.24 a straight line all the way to $V = 0$ is obtained with a semi-log plot of $I/(1 - e^{eV/kT})$ vs. V, provided that $V \gg R_S I$:

$$\ln \frac{1}{1 - e^{eV/kT}} = \ln I_s + \frac{eV}{\eta kT}. \qquad 4.25$$

In both cases the slope and the y-axis intercept of the straight line can be used to estimate η and I_0, respectively. This plot is used in the standard method [271], [281], [282], [297]. As R, increases, this linear region shrinks. When the series resistance R_s becomes important at high current, in forward bias, and for V high enough to neglect the "-1", taking the logarithm, Eq. 4.23 can be written as $V = \frac{\eta kT}{e} \ln \frac{I}{I_0} + R_s I$ which, derived with respect to I and using the equality $\frac{dI}{I} = d(\ln I)$, yields:

$$\frac{dV}{d(\ln I)} = \frac{\eta kT}{e} + R_s I \qquad 4.26$$

allowing the evaluation of η and R_s from the intercept and the slope of the straight line by fitting $dV/d(\ln I\,)$ vs. I plot [296].

4.3 Graphene on Silicon Schottky junction with GBD interlayer

In the field of silicon photovoltaics, Schottky barrier solar cells (SBSCs) based on graphene/n-Si junctions (Gr/Si) represent an innovative and interesting case of study for the integration of two-dimensional materials into consolidated cell architectures and fabrication processes. The engineering of the interface between absorber and front electrode is crucial for reducing the dark current, blocking the majority carriers injected into the electrode, and reducing surface recombination [298]. All these effects reflect into an improvement of the device performance. Interfacial layer between the semiconductor and the metal realized with a low thermal budget is highly desirable in solar cell processing technology.

4.3.1 Graphene on Silicon Schottky junction

Graphene and related materials are ideally suited for the fabrication of stacked structures, either in novel device configurations or in conjunction with "classic" photovoltaic (PV) materials [299]. Schottky Barrier Solar Cells based on graphene/n-Si junctions represent a low-cost and high-efficient alternative to traditional Si solar cells based on p-n junctions [300]–[302]. Graphene in the SBSC serves not only as transparent conductive electrode, but can also contribute as an active layer for carrier separation and hole transport [303]–[308]. These cells can be fabricated by simply transferring a graphene film onto n-Si substrate at room temperature, making the fabrication process less expensive and easier in comparison to traditional Si solar cells. Power conversion efficiency (PCE) of graphene/n-Si SBSCs passed from 1.5 % [303] to 15.6 % [309] in only five years, by implementing various kinds of graphene films and optimization strategies: multilayer films [310], [311], chemical doping treatments [312]–[316], the introduction of antireflection coatings or light-trapping layers [244], [314], [315], [317], [318], the engineering of interface between graphene and Si [309], [319]–[323]. Nevertheless, the PCE of these cells are still much lower than that of state-of-the-art crystalline Si solar cells.

An exhaustive theory of the Gr/Si Schottky junction does not exist to-date, although few phenomenological models, explaining particular experimental features, have been proposed. A first attempt to model the Gr/Si junction was done by S. Tongay et al. [324] who proposed a simple modification of the thermionic emission theory to include the dependence of the graphene Fermi level E_F on the voltage bias and explain the bias-driven increase of the reverse saturation current. In M/S diodes, the Fermi level of the metal stays constant upon applied voltage due to the high density of states of the metal. When the metal is replaced by graphene, a charge exchange between the 2D graphene, with limited density of states, and the 3D semiconductor induces a shift of the graphene Fermi level [325]. To show how this works, let us consider graphene on a n-type semiconductor and let us assume that at zero bias the Fermi level of graphene is at the Dirac point (Figure 4.69a). In forward bias, E_F shifts down since the negative charge in graphene required to mirror the positive charge of the depletion layer of the semiconductor (Figure 4.69b). This effect is small since a low forward bias is usually applied. In reverse bias, the depletion layer of the semiconductor increases substantially and so does the negative charge in graphene. This shifts the Fermi level upwards (Figure 4.69c).

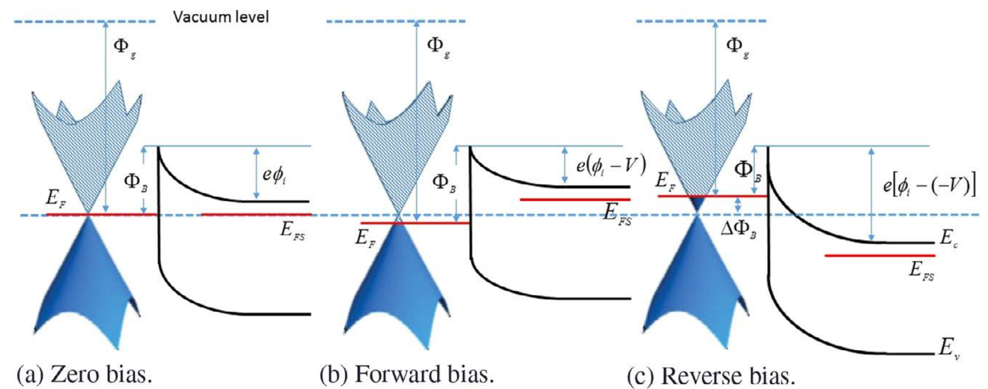

Figure 4.69. Band diagrams of an ideal Gr/Si junction at (a) zero, (b) forward and (c) reverse bias [270].

The variation of the graphene Fermi level (and hence of the work function Φ_g) modifies the SBH. As shown in Figure 4.69, Φ_g is slightly increased in forward bias and decreased in reverse bias. The decrease of Φ_g in reverse bias causes the dependence on V of the reverse current. The bias

induced variation of the graphene Fermi level, ΔE_F, and it can be easily included in the thermionic model of the Schottky diode, by replacing the constant SBH in Eqs. 4.21 and 4.23 with a voltage dependent $\Phi_B(V)$. In such way, the original functional form of the diode equation is preserved and is generalized to allow the estimation of the SBH at any given voltage. If the band alignment of Figure 4.69a holds at zero bias, the density of carriers per unit area induced in graphene by the application of a voltage V, n_{in}, can be expressed considering that this density is opposite to the variation of the density of the positive donor ions per unit area in the depletion layer of the n-type semiconductor. n_{in} is given by

$$\begin{aligned} n_{in}(V) &= -\Delta n_{depl} \\ &= -\left(\sqrt{2\varepsilon_s N(\varphi_i - V - kT/e)/e} \right. \\ &\quad \left. - \sqrt{2\varepsilon_s N(\varphi_i - kT/e)/e}\right). \end{aligned} \tag{4.27}$$

When V>0, n_{in} is positive, and graphene is hole doped (Figure 4.69b); in reverse bias, V<0 and n_{in}<0, and the doping is n-type (Figure 4.69c). Considering the Fermi level

$$E_F = \mp \frac{h}{2\sqrt{\pi}} v_F \sqrt{n}, \tag{4.28}$$

n_{in} corresponds to the Fermi level variation, $\Delta E_F(V)$, given by

$$\Delta E_F(V) = \mp \frac{h}{2\sqrt{\pi}} v_F \sqrt{|n_{in}(V)|}, \tag{4.29}$$

where the -/+ signs correspond to the down/up shift of E_F in forward or reverse bias, respectively.

If graphene has a doping with density n_0 at zero bias (n_0 is negative for electrons and positive for holes), then the zero bias Fermi level is initially shifted with respect to the Dirac point by an amount given by Eq. 4.29 with n_{in} replaced by n_0. This doping can be due to the synthesis/transfer process, to interaction with the substrate, to exposure to air, etc. In this case, referring

to the situation of Figure 4.69 with positive spatial charge region for the semiconductor, the total carrier density per area in graphene caused by the application of a bias is

$$n_g(V) = n_0 + n_{in}(V) = -\sqrt{2\varepsilon_s N(\varphi_i - V - kT/e)/e}, \tag{4.30}$$

where $n_{in}(V)$ is the bias induced contribution to carriers. n_{in} results in a variation of the Fermi level that can be expressed as

$$\begin{aligned} \Delta E_F(V) &= \frac{h}{2\sqrt{\pi}} v_F \left(\sqrt{|n_g(V)|} - \sqrt{|n_0|}\right) \\ &= \frac{h}{2\sqrt{\pi}} v_F \left(\sqrt{|n_0 + n_{in}(V)|} - \sqrt{|n_0|}\right). \end{aligned} \tag{4.31}$$

Obviously, $\Delta E_F = 0$ at zero bias, when $n_g = n_0 = -\sqrt{2\varepsilon_s N(\varphi_i - V - kT/e)/e}$. Under the assumption that $n_{in} \ll n_0$, ΔE_F can be expressed as

$$\Delta E_F(V) = \frac{h}{4\sqrt{\pi}} v_F \frac{n_{in}}{\sqrt{|n_0|}}, \tag{4.32}$$

which, using the expression for n_g, becomes

$$\begin{aligned} \Delta E_F(V) &= \frac{h}{4\sqrt{\pi}} v_F \frac{1}{\sqrt{n_0}} (n_g - n_0) \\ &= a\left(\sqrt{\varphi_i - V - kT/e} - \sqrt{\varphi_i - kT/e}\right) \end{aligned} \tag{4.33}$$

with

$$a \equiv \frac{h}{4\sqrt{\pi}} v_F \sqrt{\frac{\varepsilon_s N}{2en_0}}. \tag{4.34}$$

The variation of the graphene Fermi level corresponds to an opposite variation of the SBH, $\Delta\Phi_B(V) = -\Delta E_F(V)$, as can be seen from Figure 4.69. If Φ_B^0 and $\Delta\Phi_B$ are the zero bias SBH and the correction due to the applied voltage V (whether forward or reverse), then the voltage dependent Schottky barrier height can be written as:

$$\Phi_B(V) = \Phi_B^0 + \Delta\Phi_B(V) = \Phi_B^0 - \Delta E_F(V) = \Phi_B^0 - a(\sqrt{(\varphi_i - V - kT/e)} - \sqrt{(\varphi_i - kT/e)}). \quad 4.35$$

In the Schottky model, the constant Φ_B^0 appears in the expression of the reverse saturation current. By replacing there Φ_B^0 with $\Phi_B(V)$, the Schottky model equations can be finally rewritten as

$$I_0 = AA^*T^2 e^{-\frac{1}{kT}(\Phi_B^0 + \Delta\Phi_B(V))} = AA^*T^2 e^{-\frac{1}{kT}[\Phi_B^0 - a(\sqrt{(\varphi_i - V - kT/e)} - \sqrt{(\varphi_i - kT/e)})]} \quad 4.36$$

and

$$I_0 = I_0\left(e^{\frac{e(V-R_sI)}{\eta kT}} - 1\right) = AA^*T^2 e^{-\frac{1}{kT}\left[\Phi_B^0 - a\left(\sqrt{\left(\varphi_i - V - \frac{kT}{e}\right)} - \sqrt{\left(\varphi_i - \frac{kT}{e}\right)}\right)\right]}\left(e^{\frac{e(V-R_sI)}{\eta kT}} - 1\right). \quad 4.37$$

According to Eq. 4.36, since $\Delta\Phi_B(V=0) = 0$, Φ_B^0 can still be evaluated from the reverse saturation current I_0 at zero bias (extrapolation to $V = 0$ of forward bias current); however, once Φ_B^0 is known, measurements of the reverse current at given V can be used to estimate the correction $\Delta\Phi_B(V)$. Eq. 4.37 maintains the general form of the diode equation and includes the bias dependence of the reverse saturation current resulting from the Schottky barrier variation caused by the limited number of states of graphene around the Dirac point.

4.3.2 The interface engineering in Schottky junction

Interface engineering is crucial in Schottky heterostructures based on graphene, as already reported for graphene/GaAs [326]–[329], graphene/InP [330] and graphene/CdTe solar cell [331]–[334]. The performance of graphene/n-Si SBSCs is highly affected by the recombination of the charge carriers at the interface between graphene and Si due to the low Schottky barrier height (~0.6–0.7 eV), much smaller than that of traditional Si solar cells, which causes a large leakage current and thus a low open circuit voltage (V_{OC}) [300]. One approach to reduce charge recombination at the interface and improve the performance of the cell consists in engineering the interface by adding interfacial layers. Such layers can play a key role in suppressing the charge recombination and improving the V_{OC} of the cell. A thin native oxide layer (~2 nm) between Si and graphene can act as a passivation layer, reducing the influence of surface defects and reverse dark saturation current, thus improving the Voc. By optimizing the thickness of the native oxide layer a high PCE of 15.6 % has been achieved [309]. The insertion of an insulating layer in the graphene/n-Si junction forms a metal-insulator semiconductor (MIS) structure [305]. In MIS configuration, the additional insulating layer works as an electron blocking layer preventing the diffusion of electrons (majority carriers) from n-Si to graphene and thus reducing the carrier recombination. An appropriate band alignment between the insulating layer and the n-Si can also reduce the effect of hole (minority carrier) transport from n-Si to graphene, but the insulating layer should be uniform and very thin (down to atomic thickness) to avoid increasing the series resistance (R_s). SBSCs with optimized interfacial layers of aluminium oxide (Al_2O_3) [322], [335] or hafnium oxide (HfO_2) [323] have been reported to achieve stable, high-efficiency graphene/n-Si junction. 2D materials have been also investigated as interfacial layers: it was reported that MoS_2 monolayer [321], [336] and hexagonal boron nitride (h-BN) [328], [337] work as effective electron-blocking/hole-transporting layers, and graphene oxide (GO) [320], [338] could effectively suppress the interface recombination of graphene/Si solar cells and increase the V_{OC}.

Recently, carbon nanomaterials have been engineered and efficiently introduced in the architecture of innovative PV technology [339], such as

organic [225], [340]–[342] and perovskite-based solar cells [343]–[345]. Among the many carbon nanomaterials, graphene-based derivatives [55], [346]–[348] are particularly relevant in the PV context, given the possibility of fine-tuning their properties (*e.g.,* optical, electronic, mechanical, etc.) according to the device requirements [349].

4.3.3 Device realization

SBSC with single and double graphene based derivative (GBD) interlayers were tested and the results have been compared with a standard SBSC without interfacial layers. The devices were realized and tested in partnership with ENEA Portici and ENEA Casaccia Research Centers [350][351]. The work consisted in several steps:

1. the preparation of the silicon substrate
2. the realization of both the Ti/Pd/Ag cathode and Cr/Au anode
3. the growth of few layer graphene (FLG) and graphene based derivative (GBD) films
4. the transfer of the films on the silicon substrate
5. the solar cell test

Steps 1, 2 and 5 were performed at ENEA Portici, while the steps 3 and 4 at ENEA Casaccia Research Center.

Substrate preparation

The synthesis of the substrate follows the procedure used to realize substrate for gas sensor based on Gr/Si Schottky junction [352], [353]. The substrate used for the realization of the device was an n-type commercially available polished Si substrates ([100]-oriented, 1 Ω cm), with thermally grown SiO_2 layer (300 nm) [244]. After the cleaning of the surface, the back ohmic contact was realized with a titanium/palladium/silver alloy (Ti/Pd/Ag). As reported in literature, titanium provides a low rate of recombination at the surface, palladium protects titanium from oxidation while the last layer of silver provides a low contact resistance and chemical resistance [354]. Thin metal films deposition over semiconductor substrates is a basic process in the

realization of electronic devices. It is commonly used to realize rectifying or ohmic contacts, to form thermal and chemical barrier coatings or to modify surface properties (as for reflectivity in optic applications). The deposition process can be mainly classified into chemical vapor deposition (CVD) and physical vapor deposition (PVD). In CVD, the film growth takes place at high temperatures involving chemical reactions that usually lead to undesired products with the formation of possible impurities in the film. The PVD process is instead characterized by lower deposition temperatures without any kind of impurities even if deposition rates are slower. Among the available techniques, the electron beam physical vapor deposition was used. Metals deposition was realized by the Roth and Rau MS-600 e-beam evaporator. Basically, an electron beam is generated from a filament and accelerated to a high kinetic energy by the combination of both magnetic and electric fields, within a vacuum environment (less than 10^{-7} mbar). The e-beam is directed towards the source materials, contained in particular crucibles characterized by both thermal and chemical compatibility with the process temperature and the evaporation materials, respectively. The thermal energy that is produced heats up the material causing it to sublimate. As soon as temperature and vacuum level are sufficiently high, the resulting vapor creates a coating on the substrate surfaces positioned above the evaporating materials. A schematic illustration of the e-beam evaporator is shown in Figure 4.70. The three metals were loaded inside the e-beam evaporator. The possibility to load a number of crucibles with different metals allowed to preserve the vacuum conditions and to make the process faster, since materials evaporation could be carried out in sequence. The deposition parameters, growth rate and film thickness, were set for each metal and systematically checked during the deposition since their variation can negatively affect the final characteristics of the thin film.

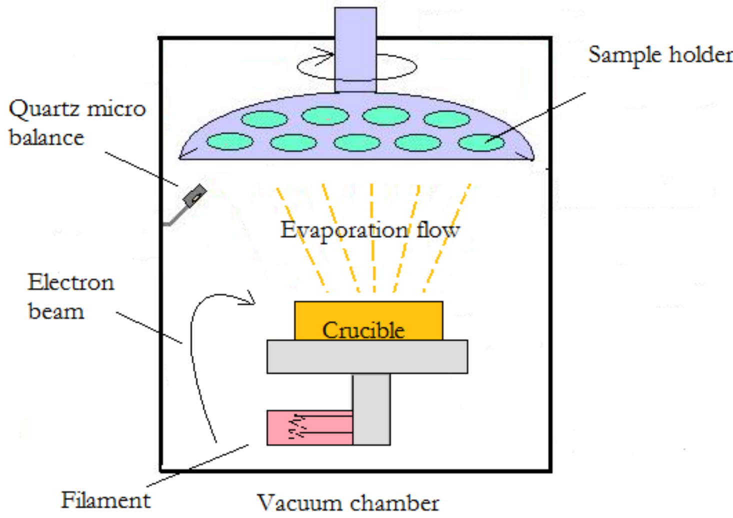

Figure 4.70. Schematic representation of the e-beam evaporator.

The film thickness was precisely monitored using a quartz micro balance which, upon the change in frequency of a quartz crystal resonator, measures the mass variation per unit area caused by the film deposition on the surface of the acoustic resonator. The relation between the film thickness and material physical parameters is expressed as [355]:

$$l_f = -\frac{N_q \rho_q \Delta\nu}{\rho_f \upsilon_q^2} \tag{4.38}$$

where l_f and ρ_f are the evaporated film thickness and density, respectively; $N_q = l_q \upsilon_q$ is the frequency constant; l_q, υ_q and ρ_q are the quartz crystal thickness, resonant frequency and density, respectively; $\Delta\nu = \upsilon_c - \upsilon_q$ with υ_c the system frequency after the evaporation process. Thickness values of 35 nm, 35 nm and 1000 nm were established for Ti, Pd and Ag, respectively. After the evaporation and condensation processes, a further heat treatment was carried out for 20 minutes at 350°C.

Silicon dioxide (SiO_2) was evaporated on the top of the structure. This deposition was masked to leave an area of exposed Si of 3x3 mm^2 as cathode of the junction. To this purpose a layer of PDMS (Polydimethylsiloxane) was used as a mask tanks to its remarkable resistance to temperature, chemical

attack and oxidation. PDMS was mixed with a liquid curing agent in the ratio 10:1. The mixture was maintained under vacuum and heated up to 100°C for 1 hour. Then, it was uniformly spread on a substrate and cut to obtain the mask of appropriate size (3 mm side). The square mask was then placed in the center of the silicon substrate pieces. Then, a 300 nm SiO_2 thick layer was deposited at a low evaporation rate. After the evaporation process (the same as previously described for metals evaporation), the mask was removed leaving exposed the underlying Si substrate (Figure 4.71a-c). Successively, a second mask was applied to the substrates in order to create a metallic ring (Figure 4.71d-f). A wider PDMS mask of $5x5mm^2$ was used to cover the center of the structure again, whereas an hollow squared mask was used for the external region. Thereafter, 30 nm of chromium and 120 nm of gold were evaporated in sequence as previously explained. Chromium was used as interface layer, because of the lack of grip between Au and SiO_2.

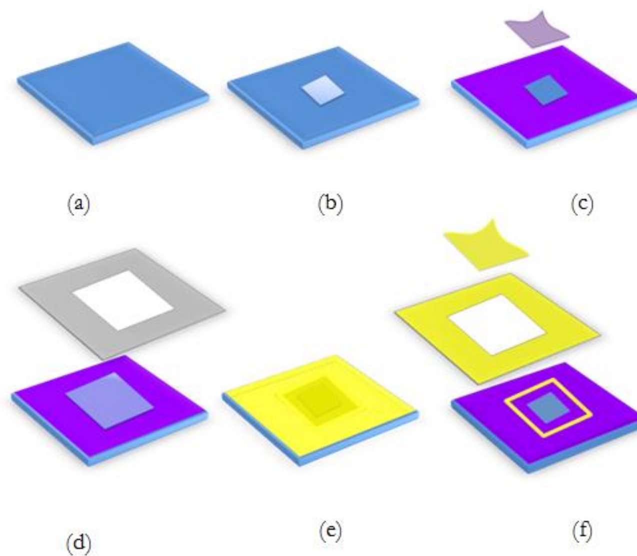

Figure 4.71. Schematic illustration of (a) silicon wafer, (b) PDMS mask 3 mm of side on the silicon substrate, (c) SiO_2 layer surrounding the silicon window, (d) hollow squared and 5 mm of side PDMS masks on the substrate, (e) Cr-Au evaporated contact, (f) final device.

Films growth and transfer on substrate

Conductive graphene (few layer graphene or thin graphite) and graphene based derivative (GBD) interlayer were grown by ethanol CVD onto Cu

substrates respectively at 1070 °C and 790 °C with growth parameters reported in previous works [84], [225] and summarized in Table 4.4.

Table 4.4. Growth parameters for FLG and GBD

Layer	$\Phi_{EtOH/Ar}$ (SCCM)	T (° C)	P (torr)	Φ_{H2} (SCCM)	Growth (min)
FLG	2.8	1070	10	10	10
GBD	2.8	790	3	0	30

The CVD reactor used to grow graphene films consists of a cold chamber, made of a quartz tube, equipped with an inductively coupled graphite susceptor heater (Figure 4.72). The heater is excited by a 3 kW maximum power radio frequency current source, which is modulated according to the signal from a thermocouple buried inside the graphite susceptor itself. Among the advantages of the system are the avoidance of heating the quartz tube and of the entire CVD assembly [227], the fast heating and start-up time for the whole system and the possibility to reach higher temperatures than with more conventional, coaxial quartz tube furnaces. Samples are placed inside the susceptor boat. The system temperature was initially calibrated by bringing Cu foils to melting (1084.6 °C).

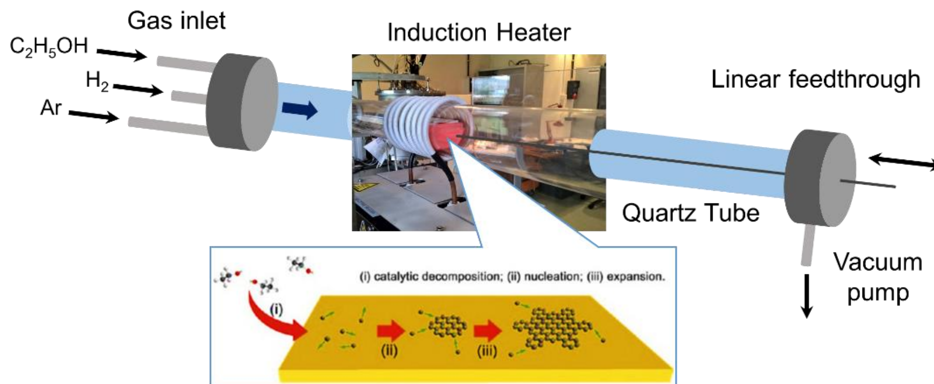

Figure 4.72. The inductively heated CVD reactor used to grow FLG and GBD

After growth, both FLG and GBD samples were transferred onto the cell substrates by cyclododecane-transfer method [117]. First, the graphene grown on the back of the Cu foil is removed by oxygen plasma, and then a protective cyclododecane film is spin coated onto the graphene/Cu foil. The foil is then

etched by ammonium persulfate, and the floating graphene films are first transferred to distilled water (for rinsing) and then onto the solar cell.

The last step carried out to complete the devices was layers transfer by using cyclododecane method [117]. Before the transfer of the graphene-based films, HF was used to remove native Si oxide from active area of the cell (Fig 2a). Multiple layers were transferred by this method and after each transfer the cell was heated for 60 min at 60°C to help cyclododecane removal, and then to 90°C for 20 min for final drying. Cells were made of stacks of two or more layers, with graphene as electrode and GBD as interlayer between graphene and n-silicon.

SBSCs with two configurations were fabricated to study the effects of GBD interlayer in the cell architecture: (i) reference cell with FLG as top conductive electrode (FLG/n-Si); (ii) cell with a GBD interlayer (FLG/GBD/n-Si). Unlike the top graphene that entirely covered the Au/Ti front electrode, the GBD was removed from the Au electrode and covered only the active area. The device schematics is reported in **Figure 2**. A control cell with a double GBD interlayer (*i.e.,* two GBD film transferred sequentially) was also fabricated to verify the effect of the GBD thickness on the device performance.

The same transfer procedure was applied for transferring each layer onto target substrates for characterizations.

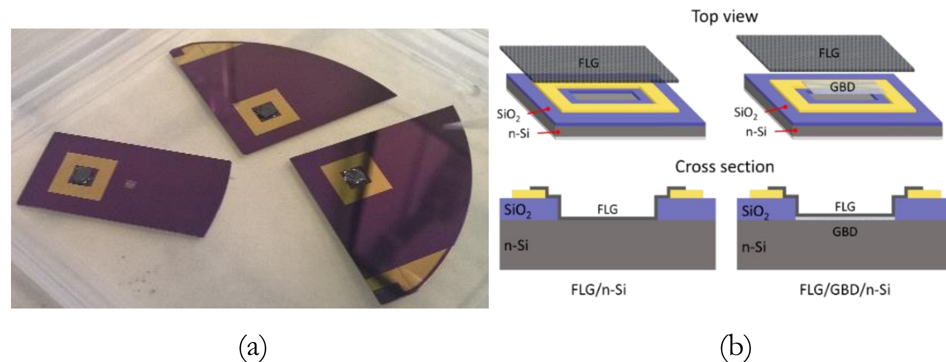

(a) (b)

Figure 4.73. (a) Silicon substrate with HF on active area just before the layers transfer, (b) Schematic illustration of the fabricated devices left, reference solar cell based on FLG/n-Si junction (FLG/n-Si), right, solar cell with single GBD between single FLG and n-Si (FLG/GBD/n-Si) [351].

4.3.4 GBD and Few Layer Graphene characterization

Raman spectra of the FLG and GBD films are reported in Figure 4.74a. Both spectra exhibit the characteristic D, G and 2D peaks, respectively at ~ 1350 cm^{-1}, ~ 1580 cm^{-1}, ~ 2700 cm^{-1} [135]. D to G (I_D/I_G) and 2D to G (I_{2D}/I_G) intensity ratios are used to provide quantitative information on graphene's defect density and thickness, respectively [135], [146]. The spectrum of FLG reported in Figure 4.74a has $I_{2D}/I_G < 1$ and $I_D/I_G \sim 0.13$, confirming the formation of few-layer graphene [356] with low defect density [146]. The spectrum of GBD is also reported and confirms the structural characteristics of films grown in the same conditions [225]. The D, G and 2D peaks are still present, but in this case the D peak strongly intensifies and the defect-related D' peak at ~ 1620 cm^{-1} appears [82], [135], [136], [225]. The high value of I_D/I_G intensity ratio (~ 3.2) is typical of defective carbonaceous film [356]. A similar very sharp D peak was already observed in functionalized graphene [357], and in hydrogenated graphene grown at 650° C by plasma-CVD [358]. Raman analysis showed that the GBD film is less crystalline on long-range, having sp^2 graphene domains with lateral size of a few tens of nm, and a high percentage of sp^3 carbons along grain boundaries. A detailed analysis on the nature of the defect in the GBD film can be found in a previous work [225]. AFM measurements performed on a FLG/GBD stack on SiO_2 give information about the thickness of each layer (Figure 4.74b). These measurements showed that the thickness of FLG and GBD are 2.2 nm and 1.1 nm, respectively. These values are compatible to 4-6 layers for FLG and 1-2 layers for GBD, in agreement with the results extracted from Raman spectroscopy. The measured thickness values take into account the presence of water buffers between the stack and SiO_2 and between each layers of the stack [161]–[163]. We measured the UV-vis absorption of FLG/GBD stack transferred onto quartz substrate and the result has been compared with the absorption of graphene (Figure 4.74c). The absorption spectrum of the stack is dominated by a pronounced peak at ~ 270 nm (4.6 eV). At the same wavelength, graphene shows a peak due to electron-hole (excitonic) interactions and interband transition from the bonding to the antibonding π-states. The transmittance of the stack has the maximum value of ~ 85 % in the

UV region, below 250 nm (~ 5 eV), while is ~ 80 % for 600 nm < λ < 800 nm. Work function scanning of FLG onto Si is reported in Figure 4.74d. The resulting work function for FLG is 4.7 eV, a higher value with respect to the theoretical calculations [359] since the Cu etching process can have a slight p-doping effect on graphene [360].

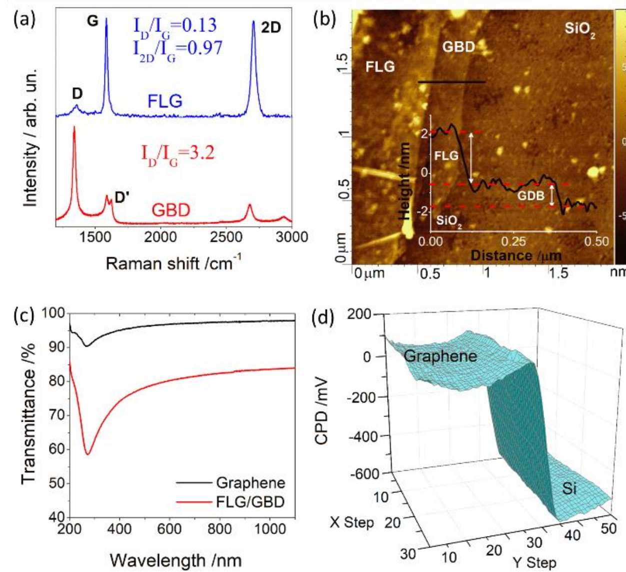

Figure 4.74. (a) Raman spectra of FLG and GBD, (b) AFM measurement on FLG/GBD stack on Si/SiO2 with relative height profile, (c) transmittance of FLG/GBD stack onto quartz substrates, compared with transmittance of graphene, (d) scanning work function of FLG onto Si substrate [351].

In order to have a detailed characterization of the films, AFM, KPFM and Raman mapping are performed on a 10x10 μm region with a stack composed of FLG and GBD on SiO_2 (Figure 4.75). AFM images show a region composed by the three different materials (Figure 4.75a). In order to identify each material, Raman maps were used. Evaluating I_{2D}, I_D/I_G and I_{2D}/I_G maps, it was possible to distinguish each material. The region with high I_{2D} signal (yellow region in Figure 4.75c) corresponded to a region with low I_D/I_G (dark region in Figure 4.75d) and high I_{2D}/I_G (brighter region in Figure 4.75e). These characteristics were related to a carbonaceous material of good quality, with low defect density and then this region corresponded to FLG. On the other side, the region with low I_{2D} signal (dark region in Figure 4.75c), high I_D/I_G (yellow region in Figure 4.75d) and low I_{2D}/I_G (darker region in Figure 4.75e)

corresponded to a carbonaceous material with high defect density and then it was attributed to GBD. The black portion in the Raman maps corresponded to SiO_2.

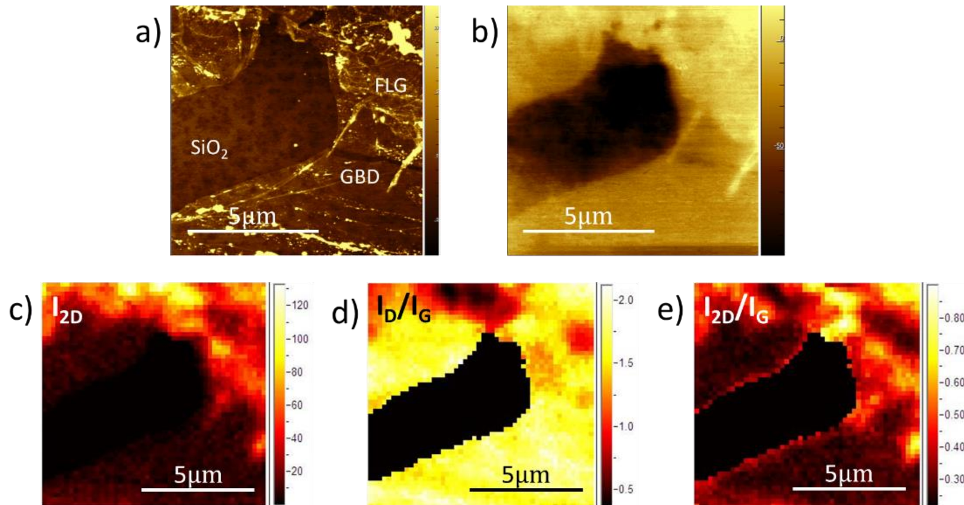

Figure 4.75. (a) AFM and (b) CPD maps, Raman mapping images of (c) 2D intensity, (d) I_D/I_G and (e) I_{2D}/I_G.

From CPD map shown in Figure 4.75b it was also extracted the work function of GBD. CPD map reported a mean value of -0.020mV for GBD. Considering from Kelvin probe analysis that

$$\phi_{sample} = \phi_{tip} - eV_{CPD} \tag{4.39}$$

and that $\phi_{tip} = 4{,}88\ eV$ after calibration with HOPG and Cu[100] samples [298], [361], [362], GBD work function resulted of 4.90 eV, in good agreement with the values measured in previous experiments [225].

Finally, the sheet resistance measured for FLG and GBD films were 0.5 and 124 kΩ/□, respectively confirming the lower conductivity of GBD.

4.4 Solar cell characterization

4.4.1 Electrical characterization

J-V characteristic under dark condition and the corresponding ln(J)/V curves of FLG/GBD/n-Si compared with FLG/n-Si SBSC are reported in Figure 4.76.

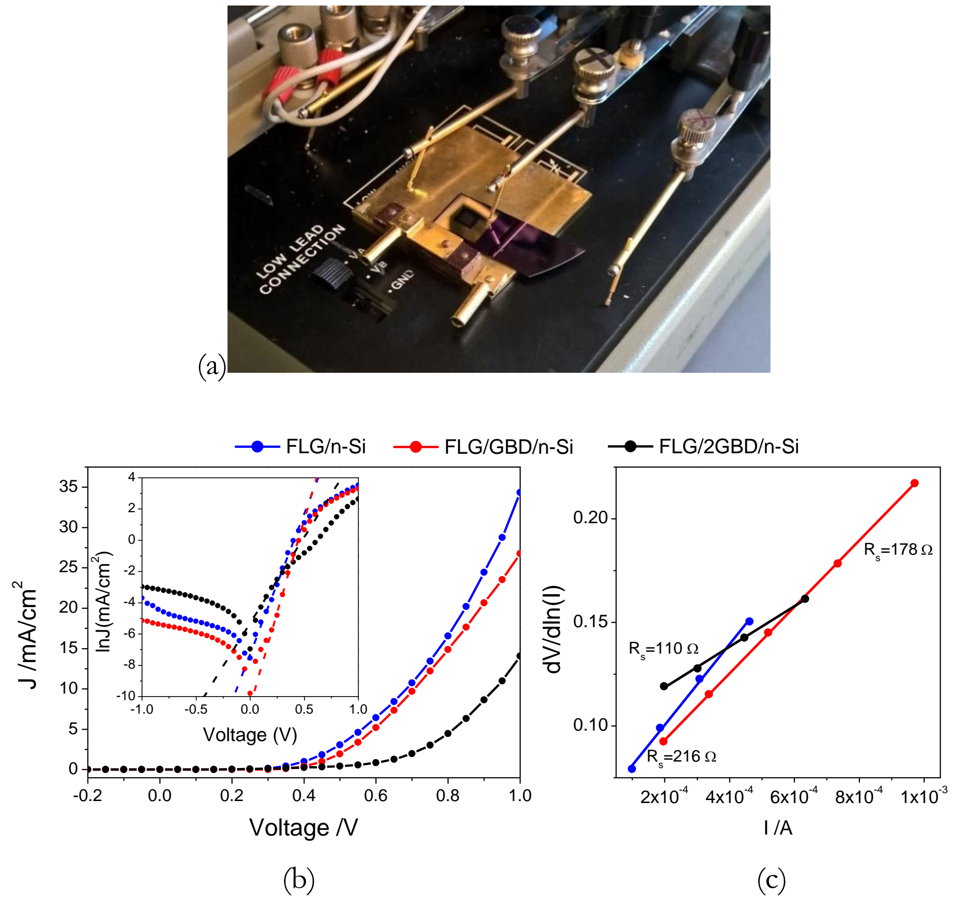

Figure 4.76. (a) Experimental setup, (b) Dark ln(J)-V characteristics with corresponding lnJ-V curves (inset) and (c) plots of dV/dln(I) versus I for FLG/n-Si (blue), FLG/GBD/n-Si (red) and FLG/2GBD/n-Si SBSCs (black curve) SBSCs [351].

The reverse saturation current density (J_0) is estimated to be 8.9×10^{-4} mA/cm^2 in FLG/n-Si cell, while it decreases to 4×10^{-4} mA/cm^2 in FLG/GBD/n-Si cell. This highlights that the carrier recombination is reduced thanks to the GBD interlayer in the junction. On the contrary, when adding two GBD films as interlayer (FLG/2GBD/n-Si), J_0 increases to 3.8×10^{-3} mA/cm^2 indicating the presence of a large quantity of trap states among the interfaces. The series resistances R_S have been extracted from the slope of the

linear fitting of the curves dV/d(lnI) *vs* I (Figure 3b) [363]. R_S is reduced from 216 Ω to 178 Ω with the GBD interlayer (110 Ω in case of two GBD films). To understand the physical mechanism behind the SBSC behaviour, the band diagram of the cells is depicted in Figure 4.77.

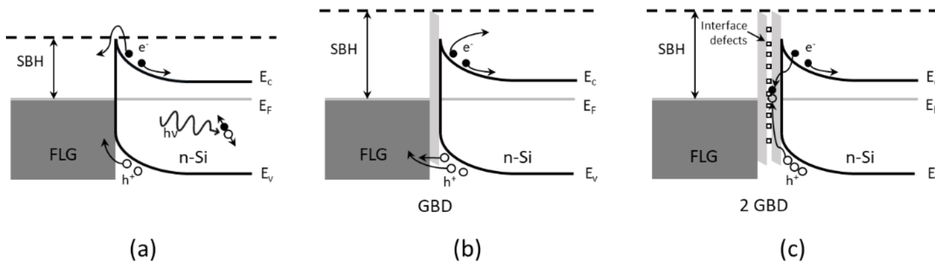

Figure 4.77. Schematics of band diagrams for (a) FLG/n-Si, (b) FLG/GBD/n-Si and (c) FLG/2GBD/n-Si SBSCs [351].

The GBD interlayer has a valance band maximum of 4.9 eV, while n-Si has the conduction band minimum and valence band maximum of 4.05 and 5.17 eV, respectively. Upon irradiation, electron−hole pairs generated in Si diffuse across FLG/n-Si interface, where they are separated by the built-in electric field of the heterojunction (Figure 4.77a). The presence of thin GBD interlayer modifies the band alignments increasing the SBH [309] (Figure 4.77b). This increase hinders the photo-generated electron transport in Si, hence reducing the leakage current. In addition, the valence band bending facilitates the photo-generated hole transport, reducing the loss due to carrier recombination. In summary, the interlayer works as an hole transport layer, while also acting as an electron blocking layer and reducing the carrier recombination at the anode. Therefore, the interlayer lowers the saturation current density and hence increases the open circuit voltage of the device. If the interlayer thickness is doubled (as in the case of two GBD films), the probability of charge carrier tunnelling lowers, causing the accumulation of holes near the interface; this results in high recombination. The recombination centres are further increased by the GBD transfer process that introduce interface defects, as already seen in graphene/h-BN/GaAs heterostructures [328]. The schematics diagram of carrier separation processes in FLG/2GBD/n-Si SBSCs is shown in Figure 4.77c. The analysis of the dark J-

V characteristics gives information on the diode characteristics of the cells. The diode characteristics of a Schottky junction is described by thermionic emission theory of majority carriers over the Schottky barrier according to equation [312]

$$J = J_0 \left[\exp\left(\frac{qV}{\eta kT}\right) - 1\right] \tag{4.40}$$

where η is the ideality factor, R_S the series resistance, k is Boltzmann's constant (k=8.62×10^{-5} eV/K), T is the temperature in Kelvin, q is the electronic charge (1.6×10^{-19} C) and the saturation current density J_0 is described by the equation

$$J_0 = A^* T^2 \exp\left(-\frac{q(SBH)}{kT}\right) \tag{4.41}$$

where A^* is the effective Richardson constant. The SBH values, evaluated by taking the slope at the forward bias linear region of ln(J)-V curve (inset of Figure 4.76b), are reported in Table 4.5.

Table 4.5. The diode characteristics of Schottky junctions reported in Figure 4.76

Device	SBH [eV]	η	R_S [Ω]
FLG/n-Si	0.78	2.1	216
FLG/GBD/n-Si	0.87	1.6	178
FLG/2GBD/n-Si	0.70	3.5	110

For FLG/n-Si, the SBH is estimated to be 0.78 eV. The SBH increases when the GBD interlayer is added (0.87 eV). The η values were also extracted from ln(J)-V curve: the introduction of the interlayer reduces η from 2.1 to 1.6, as previously reported for undoped FLG/n-Si diodes [312]. With two GBD films as interlayer, the diode curve showed a non-linearity at the lower bias. This is due to the presence of leakage currents usually attributed to generation and recombination of carriers in the charge space region, field emission and thermionic field emission or surface/edge effects that may lead to local barrier lowering [284], [285]. In this case the SBH is 0.70 eV, lower than the SBH found for the other cell configurations, and η increases to 3.5 [283].

4.4.2 Photovoltaic characterization

Additional characterization is presented in Figure 4.78, which shows the EQE of the cells acquired with and without OB.

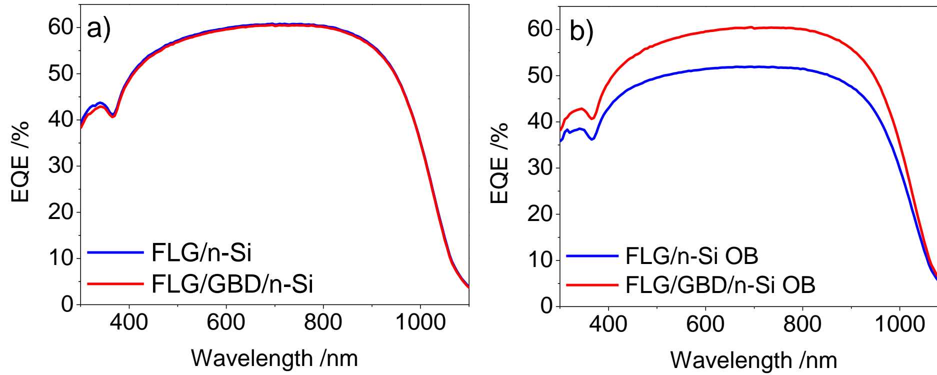

Figure 4.78. EQE curves without (a) and with (b) OB of G /n-Si (blue) and FLG/GBD/n-Si (red) SBSCs [351].

The EQE curves acquired without OB are identical for the two cells (Figure 4.78a). They reach a value of ~60 % in the wavelength range 600 nm < λ < 800 nm, in line with state-of-the-art Si solar cells [312]. Evaluating EQE with OB, the cells show a different behaviour: FLG/GBD/n-Si shows an unchanged EQE curve with maximum efficiency at ~ 60 %, while FLG/n-Si shows a low efficiency of ~ 50% (Figure 4.78b). This result indicates that the introduction of the GBD interlayer significantly improves the electron-hole pair separation and collection by the corresponding electrodes. Since the photogeneration for the device without and with the interlayer is identical, the higher EQE observed with the GBD is due to more efficient charge separation and charge collection as a result of increased SBH and reduced recombination centres at the interfaces. Otherwise in SBSC with two GBD layers a significative EQE reduction in OB condition (under than 10%) was observed, indicating an activation of recombination centers responsible for the entrapment of photogenerated carriers. Probably, in this case, the wet fabrication process and film transfer procedures introduce some contamination at the interfaces and these defects then increase the recombination centers, reducing the EQE measured in OB condition.

4.5 Doping treatment

Molecular doping was performed by exposing the top part of the cell to nitric acid (HNO_3) vapor (from a 70 % solution diluted 1:1 in deionized water) at ambient conditions for 3 min [364]. Schematic of doping process is reported in Figure 4.79. Details of the doping process can be found in a previous work [364], [365].

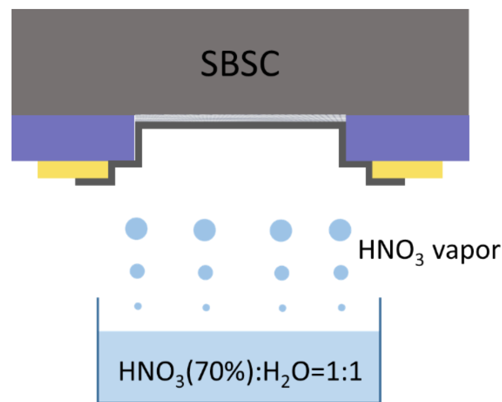

Figure 4.79. Schematic diagrams of the Gr/Si solar cell and HNO_3 doping. Adapted from [364].

Doping treatment can induce modification in the graphene lattice, resulting in an effect on the vibrational modes probed by Raman spectroscopy [80], [135]. It is possible to obtain information about carriers concentration and strain by evaluating the G and 2D bands frequency [23], [46], [366]. FLG layer after doping was largely discussed in previous work, confirming a p-doping with a doping level of ~ 2×10^{13} cm^{-2} [365]. To evaluate the effects of doping on GBD, the correlation between the Raman shift of the G and 2D band was studied [366]. Points in the map in Figure 4.80 corrispond to Raman spectra acquired on the GBD films transferred on Si/SiO_2, before and after the doping treatment. The points are located between two axes that describe the pure strain with a slope of 2.45 [46] (solid black line in Figure 4.80) and the pure doping with a slope of 0.7 [23] (solid grey line in Figure 4.80). The origin of this coordinate system (1582 cm^{-1}, 2670 cm^{-1}) corresponds to undoped and unstrained graphene for excitation energy equal to 2.33 eV [367]. The point distribution in the map is due to in-homogeneity of the sample but it was

possible to extimate doping and strain evaluating the center of point cluster [367].

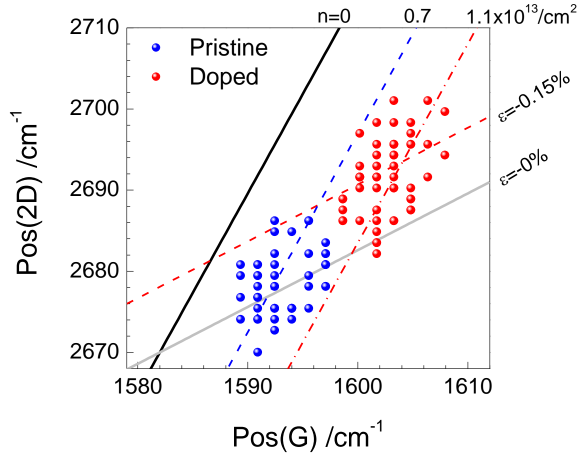

Figure 4.80. G-2D Correlation map for GBD layer. The solid black line and the solid grey line represent the pure strain and pure doping, respectively. The dashed line represent the projection on strain and doping axes [351].

Pristine GBD appears characterized by an intrinsic doping of ~ 0.7 × 10^{13} cm^{-2} due to the different nature of GBD with respect to the pristine graphene. After doping treatment, the point distribution moves to a compressive strain of -0.15% and doping of ~ 1.1 × 10^{13} cm^{-2}. This result shows that the doping treatment works differently on the two layers, with a less significant doping on GBD. The J-V characteristics under illumination were acquired on FLG/GBD/n-Si with best EQE performance. The curves were acquired before and after the doping treatment with HNO_3 [244]. The effect of the doping treatments on FLG/GBD/n-Si J-V curves is reported in Figure 4.81 and the photovoltaics parameters are summarized in Table 4.6.

Table 4.6. Photovoltaic parameters calculated from curves reported in **Figure 4.81** for FLG/GBD/n-Si SBSC

Process step	J_{sc} [MA/CM²]	V_{oc} [V]	FF [%]	PCE [%]	R_s [Ω]
Pristine	23.1	0.52	39.4	4.8	17.5
Doped HNO3 3min	23.3	0.53	54.2	6.7	7.8

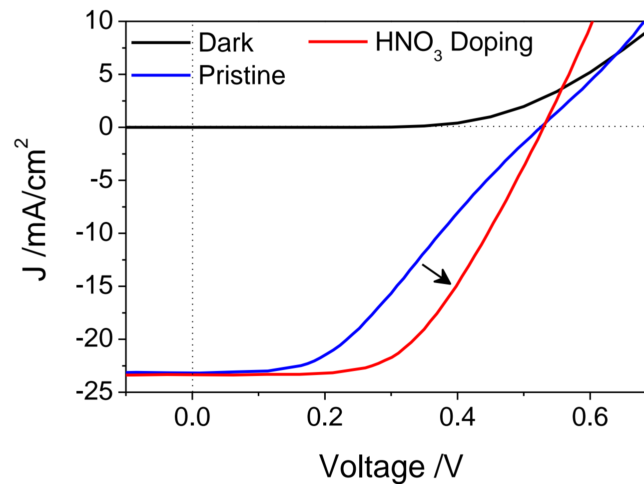

Figure 4.81. J-V curve of FLG/GBD/n-Si under illumination in standard condition, before and after doping treatment with HNO_3 [351]

The pristine cell under illumination shows good photovoltaic characteristics with short circuit current density (J_{SC}), open circuit voltage (V_{OC}), fill factor (FF), PCE and series resistance of 23.1 mA/cm^2, 0.52 V, 39.4 %, 4.8 %, 17.5 Ω, respectively. The molecular doping improves the cell performance in particular in term of PCE and FF, while reducing the R_S: the FF increases to 54.2 % and consequently the PCE reaches 6.7 %, while the R_S decreases to 7.8 Ω. The influence of doping on the short-circuit current density (J_{SC}) is negligible, as already observed in literature [313], [365]. The improvement in the cell photovoltaic parameters by HNO_3 treatment can be attributed to different factors. The molecular doping is expected to decrease the sheet resistance of graphene [313], [316] and this leads to a proportional decrease in the R_S of the solar cell, and to a concomitant increase in the FF. Beside the significant decrease in the graphene sheet resistance, a volatile oxidant treatment such as the exposure to HNO_3 vapor is expected to improve the uniformity of the Schottky junction by saturating defects at the interfaces. This should also contribute to decrease the cell R_S, further increasing its FF [313]. The effects of ageing on the doping treatment and on the cell performance were also investigated and are showed in Figure 4.82.

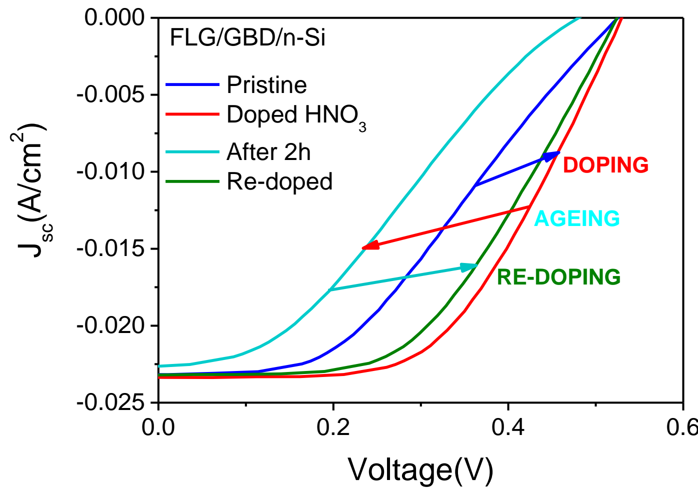

Figure 4.82. Doping, ageing and recovery effect on illuminated J-V curve of FLG/GBD/n-Si SBSC: before the doping (blue), immediately after doping (red), after 2 hours (light) and after re-doping process (green)

Table 4.7. Photovoltaic parameters calculated from curves reported in Figure 4.82

Process step	J_{sc} (mA/cm²)	V_{OC} (V)	FF (%)	PCE (%)	R_s (Ω)
Pristine	23.1	0.52	39.4	4.8	17.5
Doped HNO_3 3min	23.3	0.53	54.2	6.7	7.8
After 2h	22.6	0.48	32.7	3.5	32.3
Re-doped HNO_3 3min	23.2	0.52	50.7	6.2	9.0

The long-term stability of solar cells is a very important factor in view of commercialization [368]. The light blue curve in Figure 4.82 shows the ageing effect on the cell. After 2 hours, the photovoltaic parameters show a worsening. Ageing degrades the V_{OC} (reaching 0.48 V) and FF parameters and PCE decrease respectively at 32.7 and 3.5 %. A quasi-complete recovery of photovoltaic parameters is possible upon repeating the exposure to HNO_3 (green curve in Figure 4.82). The comparison between the relative electrical parameters is reported in Table 4.7. As reported in our previous work on a FLG/n-Si SBSC, ageing leads to the degradation of the Voc and FF parameters and to the increase of "the S shape" of the I-V curve [244]. This effect was due to the instability of graphene doping by volatile compounds (HNO_3), which lowered the SBH and hence decreased the value of V_{OC} [313], [317]. After three weeks of storage in air, the final effect on PCE was a 70% reduction with respect to the freshly doped cell, but a complete recovery was possible upon repeating the doping procedure by exposure to HNO_3 vapors. A similar

degradation and recovery behaviour was observed in the present study on FLG/GBD/n-Si SBSC.

Conclusions

In summary, this thesis was aimed at providing a contribute in the CVD growth of graphene by using ethanol. The growth parameters were varied to optimize graphene synthesis as well as to endow it with peculiar electric characteristics. Graphene films, supplied with different structure and conductivity, were used to realize photovoltaics devices based on graphene on silicon Schottky junction. Indeed, graphene, characterized by outstanding electrical properties, is considered a good substitute of silicon in the fabrication of electronic devices and it is highly integrating with modern silicon technology. In this view, CVD represents the most promising and successful method to grow high quality large graphene films.

In this work, graphene was properly synthesized and its properties were suitably tailored to photovoltaic applications. A detailed characterization of the obtained products was also performed by Raman spectroscopy and optical, electric and atomic force microscopy.

The growth of sub-mm, highly crystalline monolayer graphene grains by ethanol CVD on Cu foils with direct exposition of metallic substrate was demonstrated. The growth was performed without using Cu enclosures or other artifices to limit the nucleation density. The study systematically explored the ethanol-CVD parameters to afford the growth of graphene on flat Cu foils with full control over nucleation rate, grain size and crystallinity. The importance of Cu foil pre-oxidation was shown: without Cu pre-oxidation, the high nucleation density granted by ethanol-CVD prevented the growth of grains larger than 1-3 μm; by using Cu pre-oxidation, it was possible to optimize the growth process by tuning the CVD parameters. A combination of Cu pre-oxidation, quick Ar annealing (1 min, pre-growth) and low ethanol flow rate (1.5×10^{-3} sccm) have been identified as the key to the growth of isolated large graphene grains on plain Cu with size in excess of 300 μm. When used in field-effect transistors, these large grains attained field-effect mobility up to 1355 cm^2Vs. With these optimized CVD conditions, a few nucleation sites were

formed and the carbon atoms dissociated from ethanol were preferentially incorporated into the growing *nuclei* instead of further contributing to the nucleation. In these conditions, the growth process could be extended to 60 min to increase the grain size while retaining a low nucleation density. Overall, the growth of sub-mm single-crystal grains with low defects on flat Cu surfaces is very significant for technologic applications. Having a reproducible production method, these crystalline grains can be made in large numbers to be used as building blocks for electronic devices. Further, crystalline grains as such could serve as seeds for the formation of continuous large-area, single-crystal graphene films, which are actively sought after in the materials community.

A few-layer graphene (FLG) on silicon Schottky barrier solar cell with an interlayer of low-conductivity graphene based derivative (GBD) was realized, electrically characterized and tested as photovoltaic device demonstrating the effect of interfacial layer in the junction. J-V curves and external quantum efficiency measurements confirmed that the GBD interlayer reduces charge traps, added by interface states and recombination centres. The interlayer leads to a decrease of the saturation current and series resistance, bringing the Schottky barrier height from 0.78 to 0.87 V. Analysis of the diode characteristics, showed that the ideality factor is also reduced from 2.1 to 1.6, demonstrating the reduction of interface recombination processes. The improvements derived by the insertion of a GBD interlayer in the FLG/n-Si junction, were confirmed by the ~ 20% increase in external quantum efficiency (measured under white-light bias to keeping the cell closer to the operation condition). The insertion of a GBD interlayer with doubled thickness (made by sequentially transferring two GBD films) resulted in charge accumulation at the interface, acting as detrimental recombination centres. This proved that the GBD film has intrinsically an optimal thickness (~ 1.1 nm) to work as hole transport layer in this cell architecture. The effect of a doping treatment by HNO_3 vapour on the cell was also investigated and proved an improvement of all photovoltaic parameters, raising the power conversion efficiency from 4.8 % up to 6.7 %. The results reported in this thesis set the basis for the exploration of Si Schottky-barrier solar cells fabricated with graphene-based

films with selected properties (*e.g.,* layers number, work function, charge transport behaviour, doping level, etc.) and in different configurations, towards improved cell performance.

References

[1] P. R. Wallace, "The Band Theory of Graphite," *Phys. Rev.*, vol. 71, no. 9, pp. 622–634, May 1947.

[2] K. S. Novoselov, A. K. Geim, S. V Morozov, D. Jiang, Y. Zhang, S. V Dubonos, I. V Grigorieva, and A. A. Firsov, "Electric Field Effect in Atomically Thin Carbon Films," *Science (80-.).*, vol. 306, no. 5696, p. 666 LP-669, Oct. 2004.

[3] A. K. Geim, "Nobel Lecture: Random walk to graphene," *Rev. Mod. Phys.*, vol. 83, no. 3, pp. 851–862, Aug. 2011.

[4] A. Jorio, "Raman Spectroscopy in Graphene-Based Systems: Prototypes for Nanoscience and Nanometrology," *ISRN Nanotechnol.*, vol. 2012, no. 234216, pp. 1–16, 2012.

[5] M. O. Goerbig, "Electronic properties of graphene in a strong magnetic field," *Rev. Mod. Phys.*, vol. 83, no. 4, pp. 1193–1243, Nov. 2011.

[6] A. H. Castro Neto, F. Guinea, N. M. R. Peres, K. S. Novoselov, and A. K. Geim, "The electronic properties of graphene," *Rev. Mod. Phys.*, vol. 81, no. 1, pp. 109–162, Jan. 2009.

[7] A. K. Geim and A. H. MacDonald, "Graphene: Exploring carbon flatland," *Phys. Today*, vol. 60, no. 8, pp. 35–41, Aug. 2007.

[8] P. Allain and J. Fuchs, "Klein tunneling in graphene: optics with massless electrons," *Eur. Phys. J. B Condens. Matter Complex Syst.*, vol. 83, no. 3, pp. 301–317, 2011.

[9] K. S. Novoselov, A. K. Geim, S. V Morozov, D. Jiang, M. I. Katsnelson, I. V Grigorieva, S. V Dubonos, and A. A. Firsov, "Two-dimensional gas of massless Dirac fermions in graphene," *Nature*, vol. 438, p. 197, Nov. 2005.

[10] F. Bonaccorso, Z. Sun, T. Hasan, and A. C. Ferrari, "Graphene photonics and optoelectronics," *Nat. Photonics*, vol. 4, p. 611, 2010.

[11] A. K. Geim and K. S. Novoselov, "The rise of graphene," *Nat. Mater.*, vol. 6, p. 183, Mar. 2007.

[12] I. Snyman and C. W. J. Beenakker, "Ballistic transmission through a graphene bilayer," *Phys. Rev. B*, vol. 75, no. 4, p. 45322, Jan. 2007.

[13] D. C. Elias, R. V Gorbachev, A. S. Mayorov, S. V Morozov, A. A. Zhukov, P. Blake, L. A. Ponomarenko, I. V Grigorieva, K. S. Novoselov, F. Guinea, and A. K. Geim, "Dirac cones reshaped by interaction effects in suspended graphene," *Nat. Phys.*, vol. 7, p. 701, Jul. 2011.

[14] S. V Morozov, K. S. Novoselov, M. I. Katsnelson, F. Schedin, D. C. Elias, J. A. Jaszczak, and A. K. Geim, "Giant Intrinsic Carrier Mobilities in Graphene and Its Bilayer," *Phys. Rev. Lett.*, vol. 100, no. 1, p. 16602, Jan. 2008.

[15] K. I. Bolotin, K. J. Sikes, J. Hone, H. L. Stormer, and P. Kim, "Temperature-Dependent Transport in Suspended Graphene," *Phys. Rev. Lett.*, vol. 101, no. 9, p. 96802, Aug. 2008.

[16] P. Avouris, "Graphene: Electronic and Photonic Properties and Devices," *Nano Lett.*, vol. 10, no. 11, pp. 4285–4294, Nov. 2010.

[17] J.-H. Chen, C. Jang, S. Xiao, M. Ishigami, and M. S. Fuhrer, "Intrinsic and extrinsic performance limits of graphene devices on SiO2," *Nat. Nanotechnol.*, vol. 3, p. 206, Mar. 2008.

[18] J.-H. Chen, C. Jang, M. Ishigami, S. Xiao, W. G. Cullen, E. D. Williams, and M. S. Fuhrer, "Diffusive charge transport in graphene on SiO2," *Solid State Commun.*, vol. 149, no. 27, pp. 1080–1086, 2009.

[19] J. Xue, J. Sanchez-Yamagishi, D. Bulmash, P. Jacquod, A. Deshpande, K. Watanabe, T. Taniguchi, P. Jarillo-Herrero, and B. J. LeRoy, "Scanning tunnelling microscopy and spectroscopy of ultra-flat graphene on hexagonal boron nitride," *Nat. Mater.*, vol. 10, p. 282, Feb. 2011.

[20] C. R. Dean, A. F. Young, I. Meric, C. Lee, L. Wang, S. Sorgenfrei, K. Watanabe, T. Taniguchi, P. Kim, K. L. Shepard, and J. Hone, "Boron nitride substrates for high-quality graphene electronics," *Nat. Nanotechnol.*, vol. 5, p. 722, Aug. 2010.

[21] J. C. Meyer, C. Kisielowski, R. Erni, M. D. Rossell, M. F. Crommie, and A. Zettl, "Direct Imaging of Lattice Atoms and Topological

Defects in Graphene Membranes," *Nano Lett.*, vol. 8, no. 11, pp. 3582–3586, Nov. 2008.

[22] Y. Zhang, V. W. Brar, C. Girit, A. Zettl, and M. F. Crommie, "Origin of spatial charge inhomogeneity in graphene," *Nat. Phys.*, vol. 5, p. 722, Aug. 2009.

[23] A. Das, S. Pisana, B. Chakraborty, S. Piscanec, S. K. Saha, U. V Waghmare, K. S. Novoselov, H. R. Krishnamurthy, A. K. Geim, A. C. Ferrari, and A. K. Sood, "Monitoring dopants by Raman scattering in an electrochemically top-gated graphene transistor," *Nat. Nanotechnol.*, vol. 3, p. 210, Mar. 2008.

[24] Y.-M. Lin, C. Dimitrakopoulos, K. A. Jenkins, D. B. Farmer, H.-Y. Chiu, A. Grill, and P. Avouris, "100-GHz Transistors from Wafer-Scale Epitaxial Graphene," *Science (80-.).*, vol. 327, no. 5966, p. 662 LP-662, Feb. 2010.

[25] K. I. Bolotin, K. J. Sikes, Z. Jiang, M. Klima, G. Fudenberg, J. Hone, P. Kim, and H. L. Stormer, "Ultrahigh electron mobility in suspended graphene," *Solid State Commun.*, vol. 146, no. 9, pp. 351–355, 2008.

[26] S. Adam, E. H. Hwang, V. M. Galitski, and S. Das Sarma, "A self-consistent theory for graphene transport," *Proc. Natl. Acad. Sci. U. S. A.*, vol. 104, no. 47, pp. 18392–18397, Nov. 2007.

[27] T. Ando, "Screening Effect and Impurity Scattering in Monolayer Graphene," *J. Phys. Soc. Japan*, vol. 75, no. 7, p. 74716, Jul. 2006.

[28] K. Nomura and A. H. MacDonald, "Quantum Transport of Massless Dirac Fermions," *Phys. Rev. Lett.*, vol. 98, no. 7, p. 76602, Feb. 2007.

[29] J.-H. Chen, C. Jang, S. Adam, M. S. Fuhrer, E. D. Williams, and M. Ishigami, "Charged-impurity scattering in graphene," *Nat. Phys.*, vol. 4, p. 377, Apr. 2008.

[30] E. H. Hwang, S. Adam, and S. Das Sarma, "Carrier Transport in Two-Dimensional Graphene Layers," *Phys. Rev. Lett.*, vol. 98, no. 18, p. 186806, May 2007.

[31] K. M.I and G. A.K, "Electron scattering on microscopic corrugations in graphene," *Philos. Trans. R. Soc. A Math. Phys. Eng. Sci.*, vol. 366, no. 1863, pp. 195–204, Jan. 2008.

[32] S. V Morozov, K. S. Novoselov, M. I. Katsnelson, F. Schedin, L. A. Ponomarenko, D. Jiang, and A. K. Geim, "Strong Suppression of Weak Localization in Graphene," *Phys. Rev. Lett.*, vol. 97, no. 1, p. 16801, Jul. 2006.

[33] M. Ishigami, J. H. Chen, W. G. Cullen, M. S. Fuhrer, and E. D. Williams, "Atomic Structure of Graphene on SiO2," *Nano Lett.*, vol. 7, no. 6, pp. 1643–1648, Jun. 2007.

[34] E. Stolyarova, K. T. Rim, S. Ryu, J. Maultzsch, P. Kim, L. E. Brus, T. F. Heinz, M. S. Hybertsen, and G. W. Flynn, "High-resolution scanning tunneling microscopy imaging of mesoscopic graphene sheets on an insulating surface," *Proc. Natl. Acad. Sci.*, vol. 104, no. 22, p. 9209 LP-9212, May 2007.

[35] R. R. Nair, P. Blake, A. N. Grigorenko, K. S. Novoselov, T. J. Booth, T. Stauber, N. M. R. Peres, and A. K. Geim, "Fine Structure Constant Defines Visual Transparency of Graphene," *Science (80-.).*, vol. 320, no. 5881, p. 1308 LP-1308, Jun. 2008.

[36] I. Hamberg and C. G. Granqvist, "Evaporated Sn-doped In2O3 films: Basic optical properties and applications to energy-efficient windows," *J. Appl. Phys.*, vol. 60, no. 11, pp. R123–R160, Dec. 1986.

[37] F. Wang, Y. Zhang, C. Tian, C. Girit, A. Zettl, M. Crommie, and Y. R. Shen, "Gate-Variable Optical Transitions in Graphene," *Science (80-.).*, vol. 320, no. 5873, p. 206 LP-209, Apr. 2008.

[38] A. A. Balandin, S. Ghosh, W. Bao, I. Calizo, D. Teweldebrhan, F. Miao, and C. N. Lau, "Superior Thermal Conductivity of Single-Layer Graphene," *Nano Lett.*, vol. 8, no. 3, pp. 902–907, Mar. 2008.

[39] C. Faugeras, B. Faugeras, M. Orlita, M. Potemski, R. R. Nair, and A. K. Geim, "Thermal Conductivity of Graphene in Corbino Membrane Geometry," *ACS Nano*, vol. 4, no. 4, pp. 1889–1892, Apr. 2010.

[40] J. H. Seol, I. Jo, A. L. Moore, L. Lindsay, Z. H. Aitken, M. T. Pettes, X. Li, Z. Yao, R. Huang, D. Broido, N. Mingo, R. S. Ruoff, and L. Shi, "Two-Dimensional Phonon Transport in Supported Graphene," *Science (80-.).*, vol. 328, no. 5975, p. 213 LP-216, Apr. 2010.

[41] S. Chen, Q. Wu, C. Mishra, J. Kang, H. Zhang, K. Cho, W. Cai, A. A.

Balandin, and R. S. Ruoff, "Thermal conductivity of isotopically modified graphene," *Nat. Mater.*, vol. 11, p. 203, Jan. 2012.

[42] W. Cai, A. L. Moore, Y. Zhu, X. Li, S. Chen, L. Shi, and R. S. Ruoff, "Thermal Transport in Suspended and Supported Monolayer Graphene Grown by Chemical Vapor Deposition," *Nano Lett.*, vol. 10, no. 5, pp. 1645–1651, May 2010.

[43] S. Ghosh, I. Calizo, D. Teweldebrhan, E. P. Pokatilov, D. L. Nika, A. A. Balandin, W. Bao, F. Miao, and C. N. Lau, "Extremely high thermal conductivity of graphene: Prospects for thermal management applications in nanoelectronic circuits," *Appl. Phys. Lett.*, vol. 92, no. 15, p. 151911, Apr. 2008.

[44] K. L. Grosse, M.-H. Bae, F. Lian, E. Pop, and W. P. King, "Nanoscale Joule heating, Peltier cooling and current crowding at graphene–metal contacts," *Nat. Nanotechnol.*, vol. 6, p. 287, Apr. 2011.

[45] C. Lee, X. Wei, J. W. Kysar, and J. Hone, "Measurement of the elastic properties and intrinsic strength of monolayer graphene," *Science (80-.).*, vol. 321, no. 5887, pp. 385–388, 2008.

[46] J. Zabel, R. R. Nair, A. Ott, T. Georgiou, A. K. Geim, K. S. Novoselov, and C. Casiraghi, "Raman Spectroscopy of Graphene and Bilayer under Biaxial Strain: Bubbles and Balloons," *Nano Lett.*, vol. 12, no. 2, pp. 617–621, Feb. 2012.

[47] W. Tian, X. Zhang, and Z. C. and H. Ji, "A Review of Graphene on NEMS," *Recent Patents on Nanotechnology*, vol. 10, no. 1. pp. 3–10, 2016.

[48] Z.-S. Wu, W. Ren, L. Gao, J. Zhao, Z. Chen, B. Liu, D. Tang, B. Yu, C. Jiang, and H.-M. Cheng, "Synthesis of Graphene Sheets with High Electrical Conductivity and Good Thermal Stability by Hydrogen Arc Discharge Exfoliation," *ACS Nano*, vol. 3, no. 2, pp. 411–417, Feb. 2009.

[49] A. Peigney, C. Laurent, E. Flahaut, R. R. Bacsa, and A. Rousset, "Specific surface area of carbon nanotubes and bundles of carbon nanotubes," *Carbon N. Y.*, vol. 39, no. 4, pp. 507–514, 2001.

[50] F. Schedin, A. K. Geim, S. V Morozov, E. W. Hill, P. Blake, M. I. Katsnelson, and K. S. Novoselov, "Detection of individual gas

molecules adsorbed on graphene," *Nat. Mater.*, vol. 6, p. 652, Jul. 2007.

[51] R. Muszynski, B. Seger, and P. V Kamat, "Decorating Graphene Sheets with Gold Nanoparticles," *J. Phys. Chem. C*, vol. 112, no. 14, pp. 5263–5266, Apr. 2008.

[52] K. P. Loh, Q. Bao, P. K. Ang, and J. Yang, "The chemistry of graphene," *J. Mater. Chem.*, vol. 20, no. 12, pp. 2277–2289, 2010.

[53] D. R. Dreyer, S. Park, C. W. Bielawski, and R. S. Ruoff, "The chemistry of graphene oxide," *Chem. Soc. Rev.*, vol. 39, no. 1, pp. 228–240, 2010.

[54] X. Li, W. Cai, J. An, S. Kim, J. Nah, D. Yang, R. Piner, A. Velamakanni, I. Jung, E. Tutuc, S. K. Banerjee, L. Colombo, and R. S. Ruoff, "Large-Area Synthesis of High-Quality and Uniform Graphene Films on Copper Foils," *Science (80-.).*, vol. 324, no. 5932, pp. 1312–1314, 2009.

[55] M. Pumera and C. H. A. Wong, "Graphane and hydrogenated graphene," *Chem. Soc. Rev.*, vol. 42, no. 14, pp. 5987–5995, 2013.

[56] D. C. Elias, R. R. Nair, T. M. G. Mohiuddin, S. V Morozov, P. Blake, M. P. Halsall, A. C. Ferrari, D. W. Boukhvalov, M. I. Katsnelson, A. K. Geim, and K. S. Novoselov, "Control of Graphene's Properties by Reversible Hydrogenation: Evidence for Graphane," *Science (80-.).*, vol. 323, no. 5914, p. 610 LP-613, Jan. 2009.

[57] R. R. Nair, W. Ren, R. Jalil, I. Riaz, V. G. Kravets, L. Britnell, P. Blake, F. Schedin, A. S. Mayorov, S. Yuan, M. I. Katsnelson, H.-M. Cheng, W. Strupinski, L. G. Bulusheva, A. V Okotrub, I. V Grigorieva, A. N. Grigorenko, K. S. Novoselov, and A. K. Geim, "Fluorographene: A Two-Dimensional Counterpart of Teflon," *Small*, vol. 6, no. 24, pp. 2877–2884, Nov. 2010.

[58] J. Zhou, M. M. Wu, X. Zhou, and Q. Sun, "Tuning electronic and magnetic properties of graphene by surface modification," *Appl. Phys. Lett.*, vol. 95, no. 10, p. 103108, Sep. 2009.

[59] J. Baringhaus, M. Ruan, F. Edler, A. Tejeda, M. Sicot, A. Taleb-Ibrahimi, A.-P. Li, Z. Jiang, E. H. Conrad, C. Berger, C. Tegenkamp, and W. A. de Heer, "Exceptional ballistic transport in epitaxial

graphene nanoribbons," *Nature*, vol. 506, p. 349, Feb. 2014.

[60] J. Moser, A. Barreiro, and A. Bachtold, "Current-induced cleaning of graphene," *Appl. Phys. Lett.*, vol. 91, no. 16, p. 163513, Oct. 2007.

[61] F. Schwierz, "Graphene transistors," *Nat. Nanotechnol.*, vol. 5, p. 487, May 2010.

[62] K. S. Novoselov, Z. Jiang, Y. Zhang, S. V Morozov, H. L. Stormer, U. Zeitler, J. C. Maan, G. S. Boebinger, P. Kim, and A. K. Geim, "Room-Temperature Quantum Hall Effect in Graphene," *Science (80-.).*, vol. 315, no. 5817, p. 1379 LP-1379, Mar. 2007.

[63] Y. Zhang, Y.-W. Tan, H. L. Stormer, and P. Kim, "Experimental observation of the quantum Hall effect and Berry's phase in graphene," *Nature*, vol. 438, p. 201, Nov. 2005.

[64] V. P. Gusynin and S. G. Sharapov, "Unconventional Integer Quantum Hall Effect in Graphene," *Phys. Rev. Lett.*, vol. 95, no. 14, p. 146801, Sep. 2005.

[65] S. Bae, H. Kim, Y. Lee, X. Xu, J.-S. Park, Y. Zheng, J. Balakrishnan, T. Lei, H. Ri Kim, Y. Il Song, Y.-J. Kim, K. S. Kim, B. Özyilmaz, J.-H. Ahn, B. H. Hong, and S. Iijima, "Roll-to-roll production of 30-inch graphene films for transparent electrodes," *Nat. Nanotechnol.*, vol. 5, p. 574, 2010.

[66] J. S. Bunch, S. S. Verbridge, J. S. Alden, A. M. van der Zande, J. M. Parpia, H. G. Craighead, and P. L. McEuen, "Impermeable Atomic Membranes from Graphene Sheets," *Nano Lett.*, vol. 8, no. 8, pp. 2458–2462, Aug. 2008.

[67] A. C. Ferrari, F. Bonaccorso, V. Fal'ko, K. S. Novoselov, S. Roche, P. Bøggild, S. Borini, F. H. L. Koppens, V. Palermo, N. Pugno, J. A. Garrido, R. Sordan, A. Bianco, L. Ballerini, M. Prato, E. Lidorikis, J. Kivioja, C. Marinelli, T. Ryhänen, A. Morpurgo, J. N. Coleman, V. Nicolosi, L. Colombo, A. Fert, M. Garcia-Hernandez, A. Bachtold, G. F. Schneider, F. Guinea, C. Dekker, M. Barbone, Z. Sun, C. Galiotis, A. N. Grigorenko, G. Konstantatos, A. Kis, M. Katsnelson, L. Vandersypen, A. Loiseau, V. Morandi, D. Neumaier, E. Treossi, V. Pellegrini, M. Polini, A. Tredicucci, G. M. Williams, B. Hee Hong, J.-

H. Ahn, J. Min Kim, H. Zirath, B. J. van Wees, H. van der Zant, L. Occhipinti, A. Di Matteo, I. A. Kinloch, T. Seyller, E. Quesnel, X. Feng, K. Teo, N. Rupesinghe, P. Hakonen, S. R. T. Neil, Q. Tannock, T. Löfwander, and J. Kinaret, "Science and technology roadmap for graphene, related two-dimensional crystals, and hybrid systems," *Nanoscale*, vol. 7, no. 11, pp. 4598–4810, 2015.

[68] K. S. Novoselov, V. I. Fal'ko, L. Colombo, P. R. Gellert, M. G. Schwab, and K. Kim, "A roadmap for graphene," *Nature*, vol. 490, p. 192, Oct. 2012.

[69] W. Wang, S. Dai, X. Li, J. Yang, D. J. Srolovitz, and Q. Zheng, "Measurement of the cleavage energy of graphite," *Nat. Commun.*, vol. 6, p. 7853, Aug. 2015.

[70] F. Bonaccorso, A. Lombardo, T. Hasan, Z. Sun, L. Colombo, and A. C. Ferrari, "Production and processing of graphene and 2d crystals," *Mater. Today*, vol. 15, no. 12, pp. 564–589, 2012.

[71] Y. Huang, E. Sutter, N. N. Shi, J. Zheng, T. Yang, D. Englund, H.-J. Gao, and P. Sutter, "Reliable Exfoliation of Large-Area High-Quality Flakes of Graphene and Other Two-Dimensional Materials," *ACS Nano*, vol. 9, no. 11, pp. 10612–10620, Nov. 2015.

[72] A. K. Geim, "Graphene: Status and Prospects," *Science (80-.).*, vol. 324, no. 5934, p. 1530 LP-1534, Jun. 2009.

[73] J. N. Coleman, "Liquid Exfoliation of Defect-Free Graphene," *Acc. Chem. Res.*, vol. 46, no. 1, pp. 14–22, Jan. 2013.

[74] F. La Via, M. Camarda, and A. La Magna, "Mechanisms of growth and defect properties of epitaxial SiC," *Appl. Phys. Rev.*, vol. 1, no. 3, p. 31301, Sep. 2014.

[75] K. V Emtsev, A. Bostwick, K. Horn, J. Jobst, G. L. Kellogg, L. Ley, J. L. McChesney, T. Ohta, S. A. Reshanov, J. Röhrl, E. Rotenberg, A. K. Schmid, D. Waldmann, H. B. Weber, and T. Seyller, "Towards wafer-size graphene layers by atmospheric pressure graphitization of silicon carbide," *Nat. Mater.*, vol. 8, p. 203, Feb. 2009.

[76] C. Virojanadara, A. A. Zakharov, R. Yakimova, and L. I. Johansson, "Buffer layer free large area bi-layer graphene on SiC(0001)," *Surf. Sci.*,

vol. 604, no. 2, pp. L4–L7, 2010.

[77] J. A. Robinson, M. Hollander, M. LaBella, K. A. Trumbull, R. Cavalero, and D. W. Snyder, “Epitaxial Graphene Transistors: Enhancing Performance via Hydrogen Intercalation,” *Nano Lett.*, vol. 11, no. 9, pp. 3875–3880, Sep. 2011.

[78] E. Pallecchi, F. Lafont, V. Cavaliere, F. Schopfer, D. Mailly, W. Poirier, and A. Ouerghi, “High Electron Mobility in Epitaxial Graphene on 4H-SiC(0001) via post-growth annealing under hydrogen,” *Sci. Rep.*, vol. 4, p. 4558, Apr. 2014.

[79] S. Santangelo, G. Messina, A. Malara, N. Lisi, T. Dikonimos, A. Capasso, L. Ortolani, V. Morandi, and G. Faggio, “Taguchi optimized synthesis of graphene films by copper catalyzed ethanol decomposition,” *Diam. Relat. Mater.*, vol. 41, pp. 73–78, 2014.

[80] A. Capasso, T. Dikonimos, F. Sarto, A. Tamburrano, G. De Bellis, M. S. Sarto, G. Faggio, A. Malara, G. Messina, and N. Lisi, “Nitrogen-doped graphene films from chemical vapor deposition of pyridine: influence of process parameters on the electrical and optical properties,” *Beilstein J. Nanotechnol.*, vol. 6, pp. 2028–2038, 2015.

[81] G. Faggio, A. Capasso, A. Malara, E. Leoni, M. A. Nigro, S. Santangelo, G. Messina, T. Dikonimos, F. Buonocore, and N. Lisi, “Fast growth of polycrystalline graphene by chemical vapor deposition of ethanol on copper,” in *2014 IEEE 9th Nanotechnology Materials and Devices Conference (NMDC)*, 2014, pp. 69–72.

[82] N. Lisi, F. Buonocore, T. Dikonimos, E. Leoni, G. Faggio, G. Messina, V. Morandi, L. Ortolani, and A. Capasso, “Rapid and highly efficient growth of graphene on copper by chemical vapor deposition of ethanol,” *Thin Solid Films*, vol. 571, pp. 139–144, 2014.

[83] A. Guermoune, T. Chari, F. Popescu, S. S. Sabri, J. Guillemette, H. S. Skulason, T. Szkopek, and M. Siaj, “Chemical vapor deposition synthesis of graphene on copper with methanol, ethanol, and propanol precursors,” *Carbon N. Y.*, vol. 49, no. 13, pp. 4204–4210, 2011.

[84] G. Faggio, A. Capasso, G. Messina, S. Santangelo, T. Dikonimos, S. Gagliardi, R. Giorgi, V. Morandi, L. Ortolani, and N. Lisi, “High-

Temperature Growth of Graphene Films on Copper Foils by Ethanol Chemical Vapor Deposition," *J. Phys. Chem. C*, vol. 117, no. 41, pp. 21569–21576, Oct. 2013.

[85] X. Chen, P. Zhao, R. Xiang, S. Kim, J. Cha, S. Chiashi, and S. Maruyama, "Chemical vapor deposition growth of 5mm hexagonal single-crystal graphene from ethanol," *Carbon N. Y.*, vol. 94, pp. 810–815, 2015.

[86] Y. Xue, B. Wu, Y. Guo, L. Huang, L. Jiang, J. Chen, D. Geng, Y. Liu, W. Hu, and G. Yu, "Synthesis of large-area, few-layer graphene on iron foil by chemical vapor deposition," *Nano Res.*, vol. 4, no. 12, pp. 1208–1214, 2011.

[87] M. Batzill, "The surface science of graphene: Metal interfaces, CVD synthesis, nanoribbons, chemical modifications, and defects," *Surf. Sci. Rep.*, vol. 67, no. 3, pp. 83–115, 2012.

[88] X. Li, W. Cai, L. Colombo, and R. S. Ruoff, "Evolution of Graphene Growth on Ni and Cu by Carbon Isotope Labeling," *Nano Lett.*, vol. 9, no. 12, pp. 4268–4272, Dec. 2009.

[89] K. S. Kim, Y. Zhao, H. Jang, S. Y. Lee, J. M. Kim, K. S. Kim, J.-H. Ahn, P. Kim, J.-Y. Choi, and B. H. Hong, "Large-scale pattern growth of graphene films for stretchable transparent electrodes," *Nature*, vol. 457, p. 706, Jan. 2009.

[90] L. Huang, Q. H. Chang, G. L. Guo, Y. Liu, Y. Q. Xie, T. Wang, B. Ling, and H. F. Yang, "Synthesis of high-quality graphene films on nickel foils by rapid thermal chemical vapor deposition," *Carbon N. Y.*, vol. 50, no. 2, pp. 551–556, 2012.

[91] M. Losurdo, M. M. Giangregorio, P. Capezzuto, and G. Bruno, "Graphene CVD growth on copper and nickel: role of hydrogen in kinetics and structure," *Phys. Chem. Chem. Phys.*, vol. 13, no. 46, pp. 20836–20843, 2011.

[92] S. J. Chae, F. Güneş, K. K. Kim, E. S. Kim, G. H. Han, S. M. Kim, H.-J. Shin, S.-M. Yoon, J.-Y. Choi, M. H. Park, C. W. Yang, D. Pribat, and Y. H. Lee, "Synthesis of Large-Area Graphene Layers on Poly-Nickel Substrate by Chemical Vapor Deposition: Wrinkle Formation," *Adv.*

Mater., vol. 21, no. 22, pp. 2328–2333, Jun. 2009.

[93] A. Reina, X. Jia, J. Ho, D. Nezich, H. Son, V. Bulovic, M. S. Dresselhaus, and J. Kong, "Large Area, Few-Layer Graphene Films on Arbitrary Substrates by Chemical Vapor Deposition," *Nano Lett.*, vol. 9, no. 1, pp. 30–35, Jan. 2009.

[94] W. Liu, H. Li, C. Xu, Y. Khatami, and K. Banerjee, "Synthesis of high-quality monolayer and bilayer graphene on copper using chemical vapor deposition," *Carbon N. Y.*, vol. 49, no. 13, pp. 4122–4130, 2011.

[95] J.-H. Lee, E. K. Lee, W.-J. Joo, Y. Jang, B.-S. Kim, J. Y. Lim, S.-H. Choi, S. J. Ahn, J. R. Ahn, M.-H. Park, C.-W. Yang, B. L. Choi, S.-W. Hwang, and D. Whang, "Wafer-Scale Growth of Single-Crystal Monolayer Graphene on Reusable Hydrogen-Terminated Germanium," *Science (80-.).*, Apr. 2014.

[96] H. Kim, C. Mattevi, M. R. Calvo, J. C. Oberg, L. Artiglia, S. Agnoli, C. F. Hirjibehedin, M. Chhowalla, and E. Saiz, "Activation Energy Paths for Graphene Nucleation and Growth on Cu," *ACS Nano*, vol. 6, no. 4, pp. 3614–3623, Apr. 2012.

[97] X. Li, C. W. Magnuson, A. Venugopal, J. An, J. W. Suk, B. Han, M. Borysiak, W. Cai, A. Velamakanni, Y. Zhu, L. Fu, E. M. Vogel, E. Voelkl, L. Colombo, and R. S. Ruoff, "Graphene Films with Large Domain Size by a Two-Step Chemical Vapor Deposition Process," *Nano Lett.*, vol. 10, no. 11, pp. 4328–4334, Nov. 2010.

[98] L. Gao, W. Ren, J. Zhao, L.-P. Ma, Z. Chen, and H.-M. Cheng, "Efficient growth of high-quality graphene films on Cu foils by ambient pressure chemical vapor deposition," *Appl. Phys. Lett.*, vol. 97, no. 18, p. 183109, Nov. 2010.

[99] L. Liu, H. Zhou, R. Cheng, Y. Chen, Y.-C. Lin, Y. Qu, J. Bai, I. A. Ivanov, G. Liu, Y. Huang, and X. Duan, "A systematic study of atmospheric pressure chemical vapor deposition growth of large-area monolayer graphene," *J. Mater. Chem.*, vol. 22, no. 4, pp. 1498–1503, 2012.

[100] J. Sun, N. Lindvall, M. T. Cole, K. T. T. Angel, T. Wang, K. B. K. Teo, D. H. C. Chua, J. Liu, and A. Yurgens, "Low Partial Pressure Chemical

Vapor Deposition of Graphene on Copper," *IEEE Trans. Nanotechnol.*, vol. 11, no. 2, pp. 255–260, 2012.

[101] J. C. and A. T. N. and M. E. and C. B. and D. W. and N. B. and F.-J. M. zu H. and R. van G. and B. P. and T. Michely, "Growth of graphene on Ir(111)," *New J. Phys.*, vol. 11, no. 2, p. 23006, 2009.

[102] T. A. Land, T. Michely, R. J. Behm, J. C. Hemminger, and G. Comsa, "STM investigation of single layer graphite structures produced on Pt(111) by hydrocarbon decomposition," *Surf. Sci.*, vol. 264, no. 3, pp. 261–270, 1992.

[103] H. Ueta, M. Saida, C. Nakai, Y. Yamada, M. Sasaki, and S. Yamamoto, *Highly oriented monolayer graphite formation on Pt(111) by a supersonic methane beam*, vol. 560. 2004.

[104] P. Sutter, J. T. Sadowski, and E. Sutter, "Graphene on Pt(111): Growth and substrate interaction," *Phys. Rev. B*, vol. 80, no. 24, p. 245411, Dec. 2009.

[105] J. M. W. and E. S. and A. L. W. and S. N. and A. B. and N. C. B. and K. T. and E. R. and K. F. M. and O. D. Dubon, "Extraordinary epitaxial alignment of graphene islands on Au(111)," *New J. Phys.*, vol. 14, no. 5, p. 53008, 2012.

[106] T. Oznuluer, E. Pince, E. O. Polat, O. Balci, O. Salihoglu, and C. Kocabas, "Synthesis of graphene on gold," *Appl. Phys. Lett.*, vol. 98, no. 18, p. 183101, May 2011.

[107] X. Li, C. W. Magnuson, A. Venugopal, R. M. Tromp, J. B. Hannon, E. M. Vogel, L. Colombo, and R. S. Ruoff, "Large-Area Graphene Single Crystals Grown by Low-Pressure Chemical Vapor Deposition of Methane on Copper," *J. Am. Chem. Soc.*, vol. 133, no. 9, pp. 2816–2819, Mar. 2011.

[108] H. I. Rasool, E. B. Song, M. J. Allen, J. K. Wassei, R. B. Kaner, K. L. Wang, B. H. Weiller, and J. K. Gimzewski, "Continuity of Graphene on Polycrystalline Copper," *Nano Lett.*, vol. 11, no. 1, pp. 251–256, Jan. 2011.

[109] S. Nie, A. L. Walter, N. C. Bartelt, E. Starodub, A. Bostwick, E. Rotenberg, and K. F. McCarty, "Growth from Below: Graphene

Bilayers on Ir(111)," *ACS Nano*, vol. 5, no. 3, pp. 2298–2306, Mar. 2011.

[110] X. Chen, R. Xiang, P. Zhao, H. An, T. Inoue, S. Chiashi, and S. Maruyama, "Chemical vapor deposition growth of large single-crystal bernal-stacked bilayer graphene from ethanol," *Carbon N. Y.*, vol. 107, pp. 852–856, 2016.

[111] P. Zhao, A. Kumamoto, S. Kim, X. Chen, B. Hou, S. Chiashi, E. Einarsson, Y. Ikuhara, and S. Maruyama, "Self-Limiting Chemical Vapor Deposition Growth of Monolayer Graphene from Ethanol," *J. Phys. Chem. C*, vol. 117, no. 20, pp. 10755–10763, May 2013.

[112] D. S. Choi, K. S. Kim, H. Kim, Y. Kim, T. Kim, S. Rhy, C.-M. Yang, D. H. Yoon, and W. S. Yang, "Effect of Cooling Condition on Chemical Vapor Deposition Synthesis of Graphene on Copper Catalyst," *ACS Appl. Mater. Interfaces*, vol. 6, no. 22, pp. 19574–19578, Nov. 2014.

[113] J. Cai, P. Ruffieux, R. Jaafar, M. Bieri, T. Braun, S. Blankenburg, M. Muoth, A. P. Seitsonen, M. Saleh, X. Feng, K. Müllen, and R. Fasel, "Atomically precise bottom-up fabrication of graphene nanoribbons," *Nature*, vol. 466, p. 470, Jul. 2010.

[114] J. Hackley, D. Ali, J. DiPasquale, J. D. Demaree, and C. J. K. Richardson, "Graphitic carbon growth on Si(111) using solid source molecular beam epitaxy," *Appl. Phys. Lett.*, vol. 95, no. 13, p. 133114, Sep. 2009.

[115] S. Dhar, A. R. Barman, G. X. Ni, X. Wang, X. F. Xu, Y. Zheng, S. Tripathy, Ariando, A. Rusydi, K. P. Loh, M. Rubhausen, A. H. C. Neto, B. Őzyilmaz, and T. Venkatesan, "A new route to graphene layers by selective laser ablation," *AIP Adv.*, vol. 1, no. 2, p. 22109, Apr. 2011.

[116] Y. Ahn, H. Kim, Y.-H. Kim, Y. Yi, and S.-I. Kim, "Procedure of removing polymer residues and its influences on electronic and structural characteristics of graphene," *Appl. Phys. Lett.*, vol. 102, no. 9, p. 91602, Mar. 2013.

[117] A. Capasso, M. De Francesco, E. Leoni, T. Dikonimos, F. Buonocore,

L. Lancellotti, E. Bobeico, M. S. Sarto, A. Tamburrano, G. De Bellis, and N. Lisi, "Cyclododecane as support material for clean and facile transfer of large-area few-layer graphene," *Appl. Phys. Lett.*, vol. 105, no. 11, p. 113101, Sep. 2014.

[118] I. Jung, M. Pelton, R. Piner, D. A. Dikin, S. Stankovich, S. Watcharotone, M. Hausner, and R. S. Ruoff, "Simple Approach for High-Contrast Optical Imaging and Characterization of Graphene-Based Sheets," *Nano Lett.*, vol. 7, no. 12, pp. 3569–3575, Dec. 2007.

[119] L. Gao, W. Ren, F. Li, and H.-M. Cheng, "Total Color Difference for Rapid and Accurate Identification of Graphene," *ACS Nano*, vol. 2, no. 8, pp. 1625–1633, Aug. 2008.

[120] L. A. Falkovsky, "Optical properties of graphene," *J. Phys. Conf. Ser.*, vol. 129, no. 1, p. 12004, 2008.

[121] A. B. Kuzmenko, E. van Heumen, F. Carbone, and D. van der Marel, "Universal Optical Conductance of Graphite," *Phys. Rev. Lett.*, vol. 100, no. 11, p. 117401, Mar. 2008.

[122] P. Blake, E. W. Hill, A. H. Castro Neto, K. S. Novoselov, D. Jiang, R. Yang, T. J. Booth, and A. K. Geim, "Making graphene visible," *Appl. Phys. Lett.*, vol. 91, no. 6, p. 63124, Aug. 2007.

[123] M. Schriver, W. Regan, W. J. Gannett, A. M. Zaniewski, M. F. Crommie, and A. Zettl, "Graphene as a Long-Term Metal Oxidation Barrier: Worse Than Nothing," *ACS Nano*, vol. 7, no. 7, pp. 5763–5768, Jul. 2013.

[124] C. W. Oatley, "The early history of the scanning electron microscope," *J. Appl. Phys.*, vol. 53, no. 2, pp. R1–R13, Feb. 1982.

[125] M. von Ardenne, "The scanning electron microscope: Theoretical fundamentals," *Z. Phys.*, vol. 109, p. 553, 1938.

[126] K. C. A. Smith and C. W. Oatley, "The scanning electron microscope and its fields of application," *Br. J. Appl. Phys.*, vol. 6, p. 391, 1955.

[127] J. Goldstein, D. E. Newbury, P. Echlin, D. C. Joy, A. D. J. Romig, C. E. Lyman, C. Fiori, and E. Lifshin, *Scanning Electron Microscopy and X-Ray Microanalysis*, 2nd ed. Springer US, 1992.

[128] H. H. and H. M. and K. Tsukagoshi, "Determination of the Number

of Graphene Layers: Discrete Distribution of the Secondary Electron Intensity Stemming from Individual Graphene Layers," *Appl. Phys. Express*, vol. 3, no. 9, p. 95101, 2010.

[129] Z. Qi, H. Shi, M. Zhao, H. Jin, S. Jin, X. Kong, R. S. Ruoff, S. Qin, J. Xue, and H. Ji, "Chemical Vapor Deposition Growth of Bernal-Stacked Bilayer Graphene by Edge-Selective Etching with H2O," *Chem. Mater.*, vol. 30, no. 21, pp. 7852–7859, Nov. 2018.

[130] C. V RAMAN and K. S. KRISHNAN, "A New Type of Secondary Radiation," *Nature*, vol. 121, p. 501, Mar. 1928.

[131] R. L. McCreery, *Raman Spectroscopy for Chemical Analysis*. Hoboken, NJ, USA: John Wiley & Sons, Inc., 2000.

[132] S. Califano, "Theory of Vibrational Energy States," *Anal. Chem.*, vol. 48, no. 13, p. 1087A–1092A, Nov. 1976.

[133] E. Le Ru and P. G Etchegoin, *Principles of Surface-Enhanced Raman Spectroscopy*, vol. 29. 2009.

[134] A. C. Ferrari and J. Robertson, "Interpretation of Raman spectra of disordered and amorphous carbon," *Phys. Rev. B*, vol. 61, no. 20, pp. 14095–14107, May 2000.

[135] A. C. Ferrari, J. C. Meyer, V. Scardaci, C. Casiraghi, M. Lazzeri, F. Mauri, S. Piscanec, D. Jiang, K. S. Novoselov, S. Roth, and A. K. Geim, "Raman Spectrum of Graphene and Graphene Layers," *Phys. Rev. Lett.*, vol. 97, no. 18, p. 187401, Oct. 2006.

[136] L. M. Malard, M. A. Pimenta, G. Dresselhaus, and M. S. Dresselhaus, "Raman spectroscopy in graphene," *Phys. Rep.*, vol. 473, no. 5, pp. 51–87, 2009.

[137] W. Hayes and R. Loudon, *Scattering of light by crystals / William Hayes, Rodney Loudon*. 2018.

[138] D. F. Edwards, "Raman scattering in crystals," 1988.

[139] M. S. Dresselhaus, G. Dresselhaus, R. Saito, and A. Jorio, "Raman spectroscopy of carbon nanotubes," *Phys. Rep.*, vol. 409, no. 2, pp. 47–99, 2005.

[140] D. M. Basko, S. Piscanec, and A. C. Ferrari, "Electron-electron interactions and doping dependence of the two-phonon Raman

intensity in graphene," *Phys. Rev. B*, vol. 80, no. 16, p. 165413, Oct. 2009.

[141] A. C. Ferrari and D. M. Basko, "Raman spectroscopy as a versatile tool for studying the properties of graphene," *Nat. Nanotechnol.*, vol. 8, p. 235, Apr. 2013.

[142] A. C. Ferrari and J. Robertson, "Resonant Raman spectroscopy of disordered, amorphous, and diamondlike carbon," *Phys. Rev. B*, vol. 64, no. 7, p. 75414, Jul. 2001.

[143] F. Tuinstra and J. L. Koenig, "Raman Spectrum of Graphite," *J. Chem. Phys.*, vol. 53, no. 3, pp. 1126–1130, Aug. 1970.

[144] L. G. Cançado, A. Jorio, E. H. M. Ferreira, F. Stavale, C. A. Achete, R. B. Capaz, M. V. O. Moutinho, A. Lombardo, T. S. Kulmala, and A. C. Ferrari, "Quantifying Defects in Graphene via Raman Spectroscopy at Different Excitation Energies," *Nano Lett.*, vol. 11, no. 8, pp. 3190–3196, Aug. 2011.

[145] A. Eckmann, A. Felten, A. Mishchenko, L. Britnell, R. Krupke, K. S. Novoselov, and C. Casiraghi, "Probing the Nature of Defects in Graphene by Raman Spectroscopy," *Nano Lett.*, vol. 12, no. 8, pp. 3925–3930, Aug. 2012.

[146] M. A. Pimenta, G. Dresselhaus, M. S. Dresselhaus, L. G. Cancado, A. Jorio, and R. Saito, "Studying disorder in graphite-based systems by Raman spectroscopy," *Phys. Chem. Chem. Phys.*, vol. 9, no. 11, pp. 1276–1290, 2007.

[147] V. Yu, E. Whiteway, J. Maassen, and M. Hilke, "Raman spectroscopy of the internal strain of a graphene layer grown on copper tuned by chemical vapor deposition," *Phys. Rev. B*, vol. 84, no. 20, p. 205407, Nov. 2011.

[148] S. Piscanec, M. Lazzeri, F. Mauri, A. C. Ferrari, and J. Robertson, "Kohn Anomalies and Electron-Phonon Interactions in Graphite," *Phys. Rev. Lett.*, vol. 93, no. 18, p. 185503, Oct. 2004.

[149] S. Pisana, M. Lazzeri, C. Casiraghi, K. S. Novoselov, A. K. Geim, A. C. Ferrari, and F. Mauri, "Breakdown of the adiabatic Born–Oppenheimer approximation in graphene," *Nat. Mater.*, vol. 6, p. 198,

Feb. 2007.

[150] V. Carozo, C. M. Almeida, E. H. M. Ferreira, L. G. Cançado, C. A. Achete, and A. Jorio, "Raman Signature of Graphene Superlattices," *Nano Lett.*, vol. 11, no. 11, pp. 4527–4534, Nov. 2011.

[151] A. K. Gupta, Y. Tang, V. Crespi, and P. C. Eklund, *Nondispersive Raman D band activated by well-ordered interlayer interactions in rotationally stacked bilayer graphene*, vol. 82. 2010.

[152] R. Rao, R. Podila, R. Tsuchikawa, J. Katoch, D. Tishler, A. M. Rao, and M. Ishigami, "Effects of Layer Stacking on the Combination Raman Modes in Graphene," *ACS Nano*, vol. 5, no. 3, pp. 1594–1599, Mar. 2011.

[153] C. Cong, T. Yu, R. Saito, G. F. Dresselhaus, and M. S. Dresselhaus, "Second-Order Overtone and Combination Raman Modes of Graphene Layers in the Range of 1690−2150 cm−1," *ACS Nano*, vol. 5, no. 3, pp. 1600–1605, Mar. 2011.

[154] P. H. Tan, W. P. Han, W. J. Zhao, Z. H. Wu, K. Chang, H. Wang, Y. F. Wang, N. Bonini, N. Marzari, N. Pugno, G. Savini, A. Lombardo, and A. C. Ferrari, "The shear mode of multilayer graphene," *Nat. Mater.*, vol. 11, p. 294, Feb. 2012.

[155] G. Binnig and H. Rohrer, "Scanning Tunneling Microscopy," *IBM J. Res. Dev.*, vol. 30, no. 4, pp. 355–369, 1986.

[156] G. Binnig, C. F. Quate, and C. Gerber, "Atomic Force Microscope," *Phys. Rev. Lett.*, vol. 56, no. 9, pp. 930–933, Mar. 1986.

[157] S. Masubuchi, M. Ono, K. Yoshida, K. Hirakawa, and T. Machida, "Fabrication of graphene nanoribbon by local anodic oxidation lithography using atomic force microscope," *Appl. Phys. Lett.*, vol. 94, no. 8, p. 82107, Feb. 2009.

[158] K. K. Gomes, W. Mar, W. Ko, F. Guinea, and H. C. Manoharan, "Designer Dirac fermions and topological phases in molecular graphene," *Nature*, vol. 483, p. 306, Mar. 2012.

[159] C. Lee, Q. Li, W. Kalb, X.-Z. Liu, H. Berger, R. W. Carpick, and J. Hone, "Frictional Characteristics of Atomically Thin Sheets," *Science (80-.).*, vol. 328, no. 5974, p. 76 LP-80, Apr. 2010.

[160] W. Melitz, J. Shen, A. C. Kummel, and S. Lee, "Kelvin probe force microscopy and its application," *Surf. Sci. Rep.*, vol. 66, no. 1, pp. 1–27, 2011.

[161] K. Jinkins, J. Camacho, L. Farina, and Y. Wu, "Examination of humidity effects on measured thickness and interfacial phenomena of exfoliated graphene on silicon dioxide via amplitude modulation atomic force microscopy," *Appl. Phys. Lett.*, vol. 107, no. 24, p. 243107, Dec. 2015.

[162] W. Jung, J. Park, T. Yoon, T.-S. Kim, S. Kim, and C.-S. Han, "Prevention of Water Permeation by Strong Adhesion Between Graphene and SiO2 Substrate," *Small*, vol. 10, no. 9, pp. 1704–1711, May 2014.

[163] P. Nemes-Incze, Z. Osváth, K. Kamarás, and L. P. Biró, "Anomalies in thickness measurements of graphene and few layer graphite crystals by tapping mode atomic force microscopy," *Carbon N. Y.*, vol. 46, no. 11, pp. 1435–1442, 2008.

[164] D. Rugar and P. Hansma, "Atomic Force Microscopy," *Phys. Today*, vol. 43, no. 10, pp. 23–30, Oct. 1990.

[165] G. Binnig, C. Gerber, E. Stoll, T. R. Albrecht, and C. F. Quate, "Atomic resolution with atomic force microscope," *Surf. Sci.*, vol. 189–190, pp. 1–6, 1987.

[166] T. R. Albrecht and C. F. Quate, "Atomic resolution with the atomic force microscope on conductors and nonconductors," *J. Vac. Sci. Technol. A*, vol. 6, no. 2, pp. 271–274, Mar. 1988.

[167] R. Garcı□ a and R. Pérez, "Dynamic atomic force microscopy methods," *Surf. Sci. Rep.*, vol. 47, no. 6, pp. 197–301, 2002.

[168] R. Erlandsson, L. Olsson, and P. Mårtensson, "Inequivalent atoms and imaging mechanisms in ac-mode atomic-force microscopy of Si(111)7\ifmmode\times\else\texttimes\fi{}7," *Phys. Rev. B*, vol. 54, no. 12, pp. R8309–R8312, Sep. 1996.

[169] T. Junno, S.-B. Carlsson, H. Xu, L. Montelius, and L. Samuelson, "Fabrication of quantum devices by Ångström-level manipulation of nanoparticles with an atomic force microscope," *Appl. Phys. Lett.*, vol.

72, no. 5, pp. 548–550, Feb. 1998.

[170] C. J. Shearer, A. D. Slattery, A. J. Stapleton, J. G. Shapter, and C. T. Gibson, “Accurate thickness measurement of graphene,” *Nanotechnology*, vol. 27, no. 12, p. 125704, Mar. 2016.

[171] H. Shioyama, “The interactions of two chemical species in the interlayer spacing of graphite,” *Synth. Met.*, vol. 114, no. 1, pp. 1–15, 2000.

[172] A. Gupta, G. Chen, P. Joshi, S. Tadigadapa, and P. C. Eklund, “Raman Scattering from High Frequency Phonons in Supported n-Graphene Layer Films,” *Nano Lett.*, vol. 6, no. 12, pp. 1–21, 2006.

[173] Z. Chen, Y.-M. Lin, M. J. Rooks, and P. Avouris, “Graphene nano-ribbon electronics,” *Phys. E Low-dimensional Syst. Nanostructures*, vol. 40, no. 2, pp. 228–232, 2007.

[174] A. N. Sidorov, M. M. Yazdanpanah, R. Jalilian, P. J. Ouseph, R. W. Cohn, and G. U. Sumanasekera, “Electrostatic deposition of graphene,” *Nanotechnology*, vol. 18, no. 13, p. 135301, Apr. 2007.

[175] C. Casiraghi, A. Hartschuh, E. Lidorikis, H. Qian, H. Harutyunyan, T. Gokus, K. S. Novoselov, and A. C. Ferrari, “Rayleigh Imaging of Graphene and Graphene Layers,” *Nano Lett.*, vol. 7, no. 9, pp. 2711–2717, Sep. 2007.

[176] Y. K. Koh, M.-H. Bae, D. G. Cahill, and E. Pop, “Reliably Counting Atomic Planes of Few-Layer Graphene (n > 4),” *ACS Nano*, vol. 5, no. 1, pp. 269–274, Jan. 2011.

[177] Á. Mechler, J. Kopniczky, J. Kokavecz, A. Hoel, C.-G. Granqvist, and P. Heszler, “Anomalies in nanostructure size measurements by AFM,” *Phys. Rev. B*, vol. 72, no. 12, p. 125407, Sep. 2005.

[178] Á. Mechler, J. Kokavecz, P. Heszler, and R. Lal, “Surface energy maps of nanostructures: Atomic force microscopy and numerical simulation study,” *Appl. Phys. Lett.*, vol. 82, no. 21, pp. 3740–3742, May 2003.

[179] A. Kühle, A. H. Sorensen, J. B. Zandbergen, and J. Bohr, “Contrast artifacts in tapping tip atomic force microscopy,” *Appl. Phys. A Mater. Sci. Process.*, vol. 66, no. 7, pp. S329–S332, Mar. 1998.

[180] T. L. Burnett, R. Yakimova, and O. Kazakova, “Identification of

epitaxial graphene domains and adsorbed species in ambient conditions using quantified topography measurements," *J. Appl. Phys.*, vol. 112, no. 5, p. 54308, Sep. 2012.

[181] K. Xu, P. Cao, and J. R. Heath, "Graphene Visualizes the First Water Adlayers on Mica at Ambient Conditions," *Science (80-.).*, vol. 329, no. 5996, p. 1188 LP-1191, Sep. 2010.

[182] J. Song, Q. Li, X. Wang, J. Li, S. Zhang, J. Kjems, F. Besenbacher, and M. Dong, "Evidence of Stranski–Krastanov growth at the initial stage of atmospheric water condensation," *Nat. Commun.*, vol. 5, p. 4837, Sep. 2014.

[183] P. Cao, K. Xu, J. O. Varghese, and J. R. Heath, "Atomic Force Microscopy Characterization of Room-Temperature Adlayers of Small Organic Molecules through Graphene Templating," *J. Am. Chem. Soc.*, vol. 133, no. 8, pp. 2334–2337, Mar. 2011.

[184] O. Ochedowski, B. K. Bussmann, and M. Schleberger, "Graphene on Mica - Intercalated Water Trapped for Life," *Sci. Rep.*, vol. 4, p. 6003, Aug. 2014.

[185] L. Zitzler, S. Herminghaus, and F. Mugele, "Capillary forces in tapping mode atomic force microscopy," *Phys. Rev. B*, vol. 66, no. 15, p. 155436, Oct. 2002.

[186] A. Knoll, R. Magerle, and G. Krausch, "Tapping Mode Atomic Force Microscopy on Polymers: Where Is the True Sample Surface?," *Macromolecules*, vol. 34, no. 12, pp. 4159–4165, Jun. 2001.

[187] U. Schmidt, T. Dieing, W. Ibach, and O. Hollricher, "A Confocal Raman-AFM Study of Graphene," *Micros. Today*, vol. 19, no. 6, pp. 30–33, 2011.

[188] P. Cao, "Surface chemistry at the nanometer scale," California Institute of Technology, 2011.

[189] K. S. Novoselov, D. Jiang, F. Schedin, T. J. Booth, V. V Khotkevich, S. V Morozov, and A. K. Geim, "Two-dimensional atomic crystals," *Proc. Natl. Acad. Sci.*, vol. 102, no. 30, pp. 10451–10453, Jul. 2005.

[190] N. Hosoya, M. Tanimura, and M. Tachibana, "Effect of laser irradiation on few-layer graphene in air probed by Raman

spectroscopy,” *Trans. Mater. Res. Soc. Japan*, vol. 38, no. 4, pp. 579–583, 2013.

[191] E. A. Obraztsova, A. V Osadchy, E. D. Obraztsova, S. Lefrant, and I. V Yaminsky, “Statistical analysis of atomic force microscopy and Raman spectroscopy data for estimation of graphene layer numbers,” *Phys. status solidi*, vol. 245, no. 10, pp. 2055–2059, Oct. 2008.

[192] O. Ochedowski, G. Begall, N. Scheuschner, M. El Kharrazi, J. Maultzsch, and M. Schleberger, “Graphene on Si(111)7×7,” *Nanotechnology*, vol. 23, no. 40, p. 405708, Oct. 2012.

[193] C. E. Giusca, V. Panchal, M. Munz, V. D. Wheeler, L. O. Nyakiti, R. L. Myers-Ward, D. K. Gaskill, and O. Kazakova, “Water Affinity to Epitaxial Graphene: The Impact of Layer Thickness,” *Adv. Mater. Interfaces*, vol. 2, no. 16, p. 1500252, Nov. 2015.

[194] S. Eigler, F. Hof, M. Enzelberger-Heim, S. Grimm, P. Müller, and A. Hirsch, “Statistical Raman Microscopy and Atomic Force Microscopy on Heterogeneous Graphene Obtained after Reduction of Graphene Oxide,” *J. Phys. Chem. C*, vol. 118, no. 14, pp. 7698–7704, Apr. 2014.

[195] J. I. Paredes, S. Villar-Rodil, P. Solís-Fernández, A. Martínez-Alonso, and J. M. D. Tascón, “Atomic Force and Scanning Tunneling Microscopy Imaging of Graphene Nanosheets Derived from Graphite Oxide,” *Langmuir*, vol. 25, no. 10, pp. 5957–5968, May 2009.

[196] P. Solís-Fernández, J. I. Paredes, S. Villar-Rodil, A. Martínez-Alonso, and J. M. D. Tascón, “Determining the thickness of chemically modified graphenes by scanning probe microscopy,” *Carbon N. Y.*, vol. 48, no. 9, pp. 2657–2660, 2010.

[197] R. Jalili, S. H. Aboutalebi, D. Esrafilzadeh, K. Konstantinov, S. E. Moulton, J. M. Razal, and G. G. Wallace, “Organic Solvent-Based Graphene Oxide Liquid Crystals: A Facile Route toward the Next Generation of Self-Assembled Layer-by-Layer Multifunctional 3D Architectures,” *ACS Nano*, vol. 7, no. 5, pp. 3981–3990, May 2013.

[198] N. A. B. and O. P. B. and F. O. and G. G. and P.-J. G. and D. G. and E. D. and A. J. K. and H. M. P. and G. A. D. Briggs, “How does a tip tap?,” *Nanotechnology*, vol. 8, no. 2, p. 67, 1997.

[199] O. Ochedowski, B. K. Bußmann, and M. Schleberger, "Laser cleaning of exfoliated graphene," *MRS Proc.*, vol. 1455, pp. mrss12-1455-ii08-06, Jan. 2012.

[200] C. H. Lui, L. Liu, K. F. Mak, G. W. Flynn, and T. F. Heinz, "Ultraflat graphene," *Nature*, vol. 462, no. 7271, pp. 339–341, Nov. 2009.

[201] M. Nonnenmacher, M. P. O'Boyle, and H. K. Wickramasinghe, "Kelvin probe force microscopy," *Appl. Phys. Lett.*, vol. 58, no. 25, pp. 2921–2923, Jun. 1991.

[202] H. Hoppe, T. Glatzel, M. Niggemann, A. Hinsch, M. C. Lux-Steiner, and N. S. Sariciftci, "Kelvin Probe Force Microscopy Study on Conjugated Polymer/Fullerene Bulk Heterojunction Organic Solar Cells," *Nano Lett.*, vol. 5, no. 2, pp. 269–274, Feb. 2005.

[203] T. H. and C. M. D. and T. M. and M. A. and H. Sirringhaus, "A scanning Kelvin probe study of charge trapping in zone-cast pentacene thin film transistors," *Nanotechnology*, vol. 20, no. 2, p. 25203, 2009.

[204] L. Liu and G. Li, "Electrical characterization of single-walled carbon nanotubes in organic solar cells by Kelvin probe force microscopy," *Appl. Phys. Lett.*, vol. 96, no. 8, p. 83302, Feb. 2010.

[205] N. G. Clack, K. Salaita, and J. T. Groves, "Electrostatic readout of DNA microarrays with charged microspheres," *Nat. Biotechnol.*, vol. 26, p. 825, Jun. 2008.

[206] E. Finot, Y. Leonenko, B. Moores, L. Eng, M. Amrein, and Z. Leonenko, "Effect of Cholesterol on Electrostatics in Lipid−Protein Films of a Pulmonary Surfactant," *Langmuir*, vol. 26, no. 3, pp. 1929–1935, Feb. 2010.

[207] M. C. Lemme, "Current Status of Graphene Transistors," *Solid State Phenom.*, vol. 156–158, pp. 499–509, 2010.

[208] M. C. Lemme, T. J. Echtermeyer, M. Baus, and H. Kurz, "A Graphene Field-Effect Device," *IEEE Electron Device Lett.*, vol. 28, no. 4, pp. 282–284, 2007.

[209] S. A. Thiele, J. A. Schaefer, and F. Schwierz, "Modeling of graphene metal-oxide-semiconductor field-effect transistors with gapless large-area graphene channels," *J. Appl. Phys.*, vol. 107, no. 9, p. 94505, May

2010.

[210] H. Wang, A. Hsu, J. Kong, D. A. Antoniadis, and T. Palacios, "Compact Virtual-Source Current–Voltage Model for Top- and Back-Gated Graphene Field-Effect Transistors," *IEEE Trans. Electron Devices*, vol. 58, no. 5, pp. 1523–1533, 2011.

[211] S. Kim, J. Nah, I. Jo, D. Shahrjerdi, L. Colombo, Z. Yao, E. Tutuc, and S. K. Banerjee, "Realization of a high mobility dual-gated graphene field-effect transistor with Al2O3 dielectric," *Appl. Phys. Lett.*, vol. 94, no. 6, p. 62107, Feb. 2009.

[212] Z. Chen and J. Appenzeller, "Mobility extraction and quantum capacitance impact in high performance graphene field-effect transistor devices," in *2008 IEEE International Electron Devices Meeting*, 2008, pp. 1–4.

[213] Y. Ogawa, K. Komatsu, K. Kawahara, M. Tsuji, K. Tsukagoshi, and H. Ago, "Structure and transport properties of the interface between CVD-grown graphene domains," *Nanoscale*, vol. 6, no. 13, pp. 7288–7294, 2014.

[214] H. Ago, S. Fukamachi, H. Endo, P. Solís-Fernández, R. Mohamad Yunus, Y. Uchida, V. Panchal, O. Kazakova, and M. Tsuji, "Visualization of Grain Structure and Boundaries of Polycrystalline Graphene and Two-Dimensional Materials by Epitaxial Growth of Transition Metal Dichalcogenides," *ACS Nano*, vol. 10, no. 3, pp. 3233–3240, Mar. 2016.

[215] P. Y. Huang, C. S. Ruiz-Vargas, A. M. van der Zande, W. S. Whitney, M. P. Levendorf, J. W. Kevek, S. Garg, J. S. Alden, C. J. Hustedt, Y. Zhu, J. Park, P. L. McEuen, and D. A. Muller, "Grains and grain boundaries in single-layer graphene atomic patchwork quilts," *Nature*, vol. 469, no. 7330, pp. 389–392, Jan. 2011.

[216] H. Zhou, W. J. Yu, L. Liu, R. Cheng, Y. Chen, X. Huang, Y. Liu, Y. Wang, Y. Huang, and X. Duan, "Chemical vapour deposition growth of large single crystals of monolayer and bilayer graphene.," *Nat. Commun.*, vol. 4, p. 2096, 2013.

[217] Z. Yan, J. Lin, Z. Peng, Z. Sun, Y. Zhu, L. Li, C. Xiang, E. L. Samuel,

C. Kittrell, and J. M. Tour, “Toward the Synthesis of Wafer-Scale Single-Crystal Graphene on Copper Foils,” *ACS Nano*, vol. 6, no. 10, pp. 9110–9117, Oct. 2012.

[218] Y. H. Zhang, Z. Y. Chen, B. Wang, Y. W. Wu, Z. Jin, X. Liu, and G. H. Yu, *Controllable growth of millimeter-size graphene domains on Cufoil*, vol. 96. 2013.

[219] A. Mohsin, L. Liu, P. Liu, W. Deng, I. N. Ivanov, G. Li, O. E. Dyck, G. Duscher, J. R. Dunlap, K. Xiao, and G. Gu, “Synthesis of Millimeter-Size Hexagon-Shaped Graphene Single Crystals on Resolidified Copper,” *ACS Nano*, vol. 7, no. 10, pp. 8924–8931, Oct. 2013.

[220] R. M. Jacobberger and M. S. Arnold, “Graphene Growth Dynamics on Epitaxial Copper Thin Films,” *Chem. Mater.*, vol. 25, no. 6, pp. 871–877, Mar. 2013.

[221] G. Eres, M. Regmi, C. M. Rouleau, J. Chen, I. N. Ivanov, A. A. Puretzky, and D. B. Geohegan, “Cooperative Island Growth of Large-Area Single-Crystal Graphene on Copper Using Chemical Vapor Deposition,” *ACS Nano*, vol. 8, no. 6, pp. 5657–5669, Jun. 2014.

[222] L. Gan and Z. Luo, “Turning off Hydrogen To Realize Seeded Growth of Subcentimeter Single-Crystal Graphene Grains on Copper,” *ACS Nano*, vol. 7, no. 10, pp. 9480–9488, Oct. 2013.

[223] Z. Luo, Y. Lu, D. W. Singer, M. E. Berck, L. A. Somers, B. R. Goldsmith, and A. T. C. Johnson, “Effect of Substrate Roughness and Feedstock Concentration on Growth of Wafer-Scale Graphene at Atmospheric Pressure,” *Chem. Mater.*, vol. 23, no. 6, pp. 1441–1447, Mar. 2011.

[224] Y. Hao, M. S. Bharathi, L. Wang, Y. Liu, H. Chen, S. Nie, X. Wang, H. Chou, C. Tan, B. Fallahazad, H. Ramanarayan, C. W. Magnuson, E. Tutuc, B. I. Yakobson, K. F. McCarty, Y.-W. Zhang, P. Kim, J. Hone, L. Colombo, and R. S. Ruoff, “The Role of Surface Oxygen in the Growth of Large Single-Crystal Graphene on Copper,” *Science (80-.).*, vol. 342, no. 6159, p. 720 LP-723, Nov. 2013.

[225] A. Capasso, L. Salamandra, G. Faggio, T. Dikonimos, F. Buonocore,

V. Morandi, L. Ortolani, and N. Lisi, "Chemical Vapor Deposited Graphene-Based Derivative As High-Performance Hole Transport Material for Organic Photovoltaics," *ACS Appl. Mater. Interfaces*, vol. 8, no. 36, pp. 23844–23853, Sep. 2016.

[226] I. Vlassiouk, S. Smirnov, M. Regmi, S. P. Surwade, N. Srivastava, R. Feenstra, G. Eres, C. Parish, N. Lavrik, P. Datskos, S. Dai, and P. Fulvio, "Graphene Nucleation Density on Copper: Fundamental Role of Background Pressure," *J. Phys. Chem. C*, vol. 117, no. 37, pp. 18919–18926, Sep. 2013.

[227] N. Lisi, T. Dikonimos, F. Buonocore, M. Pittori, R. Mazzaro, R. Rizzoli, S. Marras, and A. Capasso, "Contamination-free graphene by chemical vapor deposition in quartz furnaces," *Sci. Rep.*, vol. 7, no. 1, p. 9927, 2017.

[228] A. K. SINGH and A. K. GUPTA, "Facet-dependent study of efficient growth of graphene on copper by ethanol-CVD," *Bull. Mater. Sci.*, vol. 38, no. 7, pp. 1723–1729, 2015.

[229] V. Miseikis, D. Convertino, N. Mishra, M. Gemmi, T. Mashoff, S. Heun, N. Haghighian, F. Bisio, M. Canepa, V. Piazza, and C. Coletti, "Rapid CVD growth of millimetre-sized single crystal graphene using a cold-wall reactor," *2D Mater.*, vol. 2, no. 1, p. 14006, 2015.

[230] J. Li, X.-Y. Wang, X.-R. Liu, Z. Jin, D. Wang, and L.-J. Wan, "Facile growth of centimeter-sized single-crystal graphene on copper foil at atmospheric pressure," *J. Mater. Chem. C*, vol. 3, no. 15, pp. 3530–3535, 2015.

[231] S. Suzuki, K. Kiyosumi, T. Nagamori, K. Tanaka, and M. Yoshimura, "Low Density Growth of Graphene by Air Introduction in Atmospheric Pressure Chemical Vapor Deposition," *e-Journal Surf. Sci. Nanotechnol.*, vol. 13, pp. 404–409, 2015.

[232] D. Ding, P. Solís-Fernández, H. Hibino, and H. Ago, "Spatially Controlled Nucleation of Single-Crystal Graphene on Cu Assisted by Stacked Ni," *ACS Nano*, vol. 10, no. 12, pp. 11196–11204, Dec. 2016.

[233] C. W. Magnuson, X. Kong, H. Ji, C. Tan, H. Li, R. Piner, C. A. Ventrice, and R. S. Ruoff, "Copper oxide as a 'self-cleaning' substrate

for graphene growth," *J. Mater. Res.*, vol. 29, no. 3, pp. 403–409, 2014.

[234] J. Pang, A. Bachmatiuk, L. Fu, C. Yan, M. Zeng, J. Wang, B. Trzebicka, T. Gemming, J. Eckert, and M. H. Rummeli, "Oxidation as A Means to Remove Surface Contaminants on Cu Foil Prior to Graphene Growth by Chemical Vapor Deposition," *J. Phys. Chem. C*, vol. 119, no. 23, pp. 13363–13368, Jun. 2015.

[235] A. J. Strudwick, N. E. Weber, M. G. Schwab, M. Kettner, R. T. Weitz, J. R. Wünsch, K. Müllen, and H. Sachdev, "Chemical Vapor Deposition of High Quality Graphene Films from Carbon Dioxide Atmospheres," *ACS Nano*, vol. 9, no. 1, pp. 31–42, Jan. 2015.

[236] J. Kraus, M. Böbel, and S. Günther, "Suppressing graphene nucleation during CVD on polycrystalline Cu by controlling the carbon content of the support foils," *Carbon N. Y.*, vol. 96, pp. 153–165, 2016.

[237] S. Choubak, M. Biron, P. L. Levesque, R. Martel, and P. Desjardins, "No Graphene Etching in Purified Hydrogen," *J. Phys. Chem. Lett.*, vol. 4, no. 7, pp. 1100–1103, Apr. 2013.

[238] L. Tao, H. Guangyu, H. Guowei, K. Yuhan, F. Weifei, C. Hongzheng, W. Qi, I. Hideo, F. Daisuke, L. Yingchun, and X. Mingsheng, "Graphene Nucleation Preferentially at Oxygen-Rich Cu Sites Rather Than on Pure Cu Surface," *Adv. Mater.*, vol. 27, no. 41, pp. 6404–6410, Sep. 2015.

[239] P. Braeuninger-Weimer, B. Brennan, A. J. Pollard, and S. Hofmann, "Understanding and Controlling Cu-Catalyzed Graphene Nucleation: The Role of Impurities, Roughness, and Oxygen Scavenging," *Chem. Mater.*, vol. 28, no. 24, pp. 8905–8915, Dec. 2016.

[240] N. Reckinger, X. Tang, F. Joucken, L. Lajaunie, R. Arenal, E. Dubois, B. Hackens, L. Henrard, and J.-F. Colomer, "Oxidation-assisted graphene heteroepitaxy on copper foil," *Nanoscale*, vol. 8, no. 44, pp. 18751–18759, 2016.

[241] L. F. and J. Z. and Z. L. and X. L. and K. W. and J. W. and M. Z. and D. W. and Z. X. and H. Zhu, "Topology evolution of graphene in chemical vapor deposition, a combined theoretical/experimental approach toward shape control of graphene domains," *Nanotechnology*,

vol. 23, no. 11, p. 115605, 2012.

[242] J. M. Wofford, S. Nie, K. F. McCarty, N. C. Bartelt, and O. D. Dubon, "Graphene Islands on Cu Foils: The Interplay between Shape, Orientation, and Defects," *Nano Lett.*, vol. 10, no. 12, pp. 4890–4896, Dec. 2010.

[243] L. Zhiqiang, Y. Ting, S. Jingzhi, W. Yingying, L. Sanhua, L. Lei, G. G. G., S. Zexiang, and L. Jianyi, "Large-Scale Synthesis of Bi-layer Graphene in Strongly Coupled Stacking Order," *Adv. Funct. Mater.*, vol. 21, no. 5, pp. 911–917, Jan. 2011.

[244] L. Lancellotti, E. Bobeico, A. Capasso, E. Lago, P. Delli Veneri, E. Leoni, F. Buonocore, and N. Lisi, "Combined effect of double antireflection coating and reversible molecular doping on performance of few-layer graphene/n-silicon Schottky barrier solar cells," *Sol. Energy*, vol. 127, no. Supplement C, pp. 198–205, 2016.

[245] X. Li, Y. Zhu, W. Cai, M. Borysiak, B. Han, D. Chen, R. D. Piner, L. Colombo, and R. S. Ruoff, "Transfer of Large-Area Graphene Films for High-Performance Transparent Conductive Electrodes," *Nano Lett.*, vol. 9, p. 4359, 2009.

[246] A. Pirkle, J. Chan, A. Venugopal, D. Hinojos, C. W. Magnuson, S. McDonnell, L. Colombo, E. M. Vogel, R. S. Ruoff, and R. M. Wallace, "The effect of chemical residues on the physical and electrical properties of chemical vapor deposited graphene transferred to SiO2," *Appl. Phys. Lett.*, vol. 99, no. 12, p. 122108, Sep. 2011.

[247] Y. C. Lin, C. C. Lu, C. H. Yeh, C. Jin, K. Suenaga, and P. W. Chiu, "Graphene Annealing: How Clean Can It Be?," *Nano Lett.*, vol. 12, p. 414, 2012.

[248] H. J. Park, J. Meyer, S. Roth, and V. Skákalová, "Growth and properties of few-layer graphene prepared by chemical vapor deposition," *Carbon N. Y.*, vol. 48, no. 4, pp. 1088–1094, 2010.

[249] C. Mattevi, H. Kim, and M. Chhowalla, "A review of chemical vapour deposition of graphene on copper," *J. Mater. Chem.*, vol. 21, no. 10, pp. 3324–3334, 2011.

[250] I. Brückle, J. Thornton, K. Nichols, and G. Strickler, "Cyclododecane:

Technical Note on Some Uses in Paper and Objects Conservation," *J. Am. Inst. Conserv.*, vol. 38, no. 2, pp. 162–175, Jan. 1999.

[251] A. Gnisci, G. Faggio, G. Messina, J. Kwon, J.-Y. Lee, G.-H. Lee, T. Dikonimos, N. Lisi, and A. Capasso, "Ethanol-CVD Growth of Sub-mm Single-Crystal Graphene on Flat Cu Surfaces," *J. Phys. Chem. C*, vol. 122, no. 50, pp. 28830–28838, Dec. 2018.

[252] E. Meca, J. Lowengrub, H. Kim, C. Mattevi, and V. B. Shenoy, "Epitaxial Graphene Growth and Shape Dynamics on Copper: Phase-Field Modeling and Experiments," *Nano Lett.*, vol. 13, no. 11, pp. 5692–5697, Nov. 2013.

[253] V. Y. Gertsman and R. Birringer, "On the room-temperature grain growth in nanocrystalline copper," *Scr. Metall. Mater.*, vol. 30, no. 5, pp. 577–581, 1994.

[254] K. Hoehne and R. Sizmann, "Volume and surface self-diffusion measurements on copper by thermal surface smoothing," *Phys. Status Solidi*, vol. 5, no. 3, pp. 577–589, Jun. 1971.

[255] A. G. and Y. N. Trehan, "The Thermal Decomposition of Cupric Oxide in vacuo," *Proc. Phys. Soc. Sect. B*, vol. 70, no. 10, p. 1005, 1957.

[256] F. Biccari, "Defects And Doping In Cu2O," Sapienza - University of Rome, 2012.

[257] S. Goniszewski, M. Adabi, O. Shaforost, S. M. Hanham, L. Hao, and N. Klein, "Correlation of p-doping in CVD Graphene with Substrate Surface Charges," *Sci. Rep.*, vol. 6, no. 1, p. 22858, Sep. 2016.

[258] H. Xu, Y. Chen, J. Zhang, and H. Zhang, "Investigating the Mechanism of Hysteresis Effect in Graphene Electrical Field Device Fabricated on SiO2 Substrates using Raman Spectroscopy," *Small*, vol. 8, no. 18, pp. 2833–2840, Jun. 2012.

[259] G. Wang, M. Zhang, Y. Zhu, G. Ding, D. Jiang, Q. Guo, S. Liu, X. Xie, P. K. Chu, Z. Di, and X. Wang, "Direct Growth of Graphene Film on Germanium Substrate," *Sci. Rep.*, vol. 3, p. 2465, Aug. 2013.

[260] N. Petrone, C. R. Dean, I. Meric, A. M. van der Zande, P. Y. Huang, L. Wang, D. Muller, K. L. Shepard, and J. Hone, "Chemical Vapor Deposition-Derived Graphene with Electrical Performance of

Exfoliated Graphene," *Nano Lett.*, vol. 12, no. 6, pp. 2751–2756, Jun. 2012.

[261] Y. Zhang, L. Zhang, P. Kim, M. Ge, Z. Li, and C. Zhou, "Vapor Trapping Growth of Single-Crystalline Graphene Flowers: Synthesis, Morphology, and Electronic Properties," *Nano Lett.*, vol. 12, no. 6, pp. 2810–2816, Jun. 2012.

[262] H.-T. Chin, J.-J. Lee, M. Hofmann, and Y.-P. Hsieh, "Impact of growth rate on graphene lattice-defect formation within a single crystalline domain," *Sci. Rep.*, vol. 8, no. 1, p. 4046, 2018.

[263] D. L. Pulfrey, "MIS solar cells: A review," *IEEE Trans. Electron Devices*, vol. 25, no. 11, pp. 1308–1317, 1978.

[264] R. B. Godfrey and M. A. Green, "Enhancement of MIS solar-cell "efficiency" by peripheral collection," *Appl. Phys. Lett.*, vol. 31, no. 10, pp. 705–707, Nov. 1977.

[265] R. B. Godfrey and M. A. Green, "655 mV open-circuit voltage, 17.6% efficient silicon MIS solar cells," *Appl. Phys. Lett.*, vol. 34, no. 11, pp. 790–793, Jun. 1979.

[266] W. S. Leong, H. Gong, and J. T. L. Thong, "Low-Contact-Resistance Graphene Devices with Nickel-Etched-Graphene Contacts," *ACS Nano*, vol. 8, no. 1, pp. 994–1001, Jan. 2014.

[267] F. Xia, V. Perebeinos, Y. Lin, Y. Wu, and P. Avouris, "The origins and limits of metal–graphene junction resistance," *Nat. Nanotechnol.*, vol. 6, p. 179, Feb. 2011.

[268] A. Di Bartolomeo, S. Santandrea, F. Giubileo, F. Romeo, M. Petrosino, R. Citro, P. Barbara, G. Lupina, T. Schroeder, and A. Rubino, "Effect of back-gate on contact resistance and on channel conductance in graphene-based field-effect transistors," *Diam. Relat. Mater.*, vol. 38, pp. 19–23, 2013.

[269] S. Russo, M. F. Craciun, M. Yamamoto, A. F. Morpurgo, and S. Tarucha, "Contact resistance in graphene-based devices," *Phys. E Low-dimensional Syst. Nanostructures*, vol. 42, no. 4, pp. 677–679, 2010.

[270] A. Di Bartolomeo, "Graphene Schottky diodes: An experimental review of the rectifying graphene/semiconductor heterojunction,"

Phys. Rep., vol. 606, pp. 1–58, 2016.

[271] S. M. Sze and K. K. Ng, *Physics of Semiconductor Device*, Third ed. New Jersey, 2007.

[272] A. M. Cowley and S. M. Sze, "Surface States and Barrier Height of Metal-Semiconductor Systems," *J. Appl. Phys.*, vol. 36, no. 10, pp. 3212–3220, Oct. 1965.

[273] E. Hökelek and G. Y. Robinson, "A study of Schottky contacts on indium phosphide," *J. Appl. Phys.*, vol. 54, no. 9, pp. 5199–5205, Sep. 1983.

[274] K. A. Rickert, A. B. Ellis, J. K. Kim, J.-L. Lee, F. J. Himpsel, F. Dwikusuma, and T. F. Kuech, "X-ray photoemission determination of the Schottky barrier height of metal contacts to n–GaN and p–GaN," *J. Appl. Phys.*, vol. 92, no. 11, pp. 6671–6678, Nov. 2002.

[275] F. A. Padovani and R. Stratton, "Field and thermionic-field emission in Schottky barriers," *Solid. State. Electron.*, vol. 9, no. 7, pp. 695–707, 1966.

[276] D. K. Schroder, *Semiconductor Material and Device Characterization*. Hoboken, NJ, USA: John Wiley & Sons, Inc., 2005.

[277] A. Modinos, "Secondary Electron Emission Spectroscopy," in *Field, Thermionic, and Secondary Electron Emission Spectroscopy*, Boston, MA: Springer US, 1984, pp. 327–345.

[278] Z. J. Horváth, "Comment on 'Analysis of I-V measurements on CrSi2□ Si Schottky structures in a wide temperature range,'" *Solid. State. Electron.*, vol. 39, no. 1, pp. 176–178, 1996.

[279] İ. Dökme, Ş. Altindal, and M. M. Bülbül, "The barrier height inhomogeneity in Al/p-Si Schottky barrier diodes with native insulator layer," *Appl. Surf. Sci.*, vol. 252, no. 22, pp. 7749–7754, 2006.

[280] İ. Taşçıoğlu, U. Aydemir, and Ş. Altındal, "The explanation of barrier height inhomogeneities in Au/n-Si Schottky barrier diodes with organic thin interfacial layer," *J. Appl. Phys.*, vol. 108, no. 6, p. 64506, Sep. 2010.

[281] E. H. Rhoderick, "Metal-semiconductor contacts," *IEE Proc. I - Solid-State Electron Devices*, vol. 129, no. 1, p. 1, 1982.

[282] S. S. Cohen and G. Sh. Gildenblat, *Metal-Semiconductor Contacts and Devices*, vol. 87. 1986.

[283] J. H. Werner and H. H. Güttler, "Barrier inhomogeneities at Schottky contacts," *J. Appl. Phys.*, vol. 69, no. 3, pp. 1522–1533, Feb. 1991.

[284] R. T. Tung, "Recent advances in Schottky barrier concepts," *Mater. Sci. Eng. R Reports*, vol. 35, no. 1, pp. 1–138, 2001.

[285] R. T. Tung, "The physics and chemistry of the Schottky barrier height," *Appl. Phys. Rev.*, vol. 1, no. 1, p. 11304, Jan. 2014.

[286] V. Aubry and F. Meyer, "Schottky diodes with high series resistance: Limitations of forward I-V methods," *J. Appl. Phys.*, vol. 76, no. 12, pp. 7973–7984, Dec. 1994.

[287] D. Donoval, J. de Sousa Pires, P. A. Tove, and R. Harman, "A self consistent approach to IV-measurements on rectifying metal-semiconductor contacts," *Solid. State. Electron.*, vol. 32, no. 11, pp. 961–964, 1989.

[288] E. K. Evangelou, L. Papadimitriou, C. A. Dimitriades, and G. E. Giakoumakis, "Extraction of Schottky diode (and p−n junction) parameters from I–V characteristics," *Solid. State. Electron.*, vol. 36, no. 11, pp. 1633–1635, 1993.

[289] H. Norde, "A modified forward I-V plot for Schottky diodes with high series resistance," *J. Appl. Phys.*, vol. 50, no. 7, pp. 5052–5053, Jul. 1979.

[290] C.-. Lien, F. C. T. So, and M.-. Nicolet, "An improved forward I-V method for nonideal Schottky diodes with high series resistance," *IEEE Trans. Electron Devices*, vol. 31, no. 10, pp. 1502–1503, 1984.

[291] K. Sato and Y. Yasumura, "Study of forward I-V plot for Schottky diodes with high series resistance," *J. Appl. Phys.*, vol. 58, no. 9, pp. 3655–3657, Nov. 1985.

[292] J. -C. Manifacier, N. Brortryb, R. Ardebili, and J. -P. Charles, "Schottky diode: Comments concerning the diode parameters determination from the forward I-V plot," *J. Appl. Phys.*, vol. 64, no. 5, pp. 2502–2504, Sep. 1988.

[293] K. E. Bohlin, "Generalized Norde plot including determination of the

ideality factor," *J. Appl. Phys.*, vol. 60, no. 3, pp. 1223–1224, Aug. 1986.

[294] R. M. Cibils and R. H. Buitrago, "Forward I-V plot for nonideal Schottky diodes with high series resistance," *J. Appl. Phys.*, vol. 58, no. 2, pp. 1075–1077, Jul. 1985.

[295] T. C. Lee, S. Fung, C. D. Beling, and H. L. Au, "A systematic approach to the measurement of ideality factor, series resistance, and barrier height for Schottky diodes," *J. Appl. Phys.*, vol. 72, no. 10, pp. 4739–4742, Nov. 1992.

[296] S. K. Cheung and N. W. Cheung, "Extraction of Schottky diode parameters from forward current-voltage characteristics," *Appl. Phys. Lett.*, vol. 49, no. 2, pp. 85–87, Jul. 1986.

[297] P. G. Shewmon, "Thin films-interdiffusion and reactions, J. M. Poate, K. N. Tu, and J. W. Mayer, Eds., Wiley-Interscience, New York, 1978, 578 pp.," *J. Polym. Sci. Polym. Lett. Ed.*, vol. 17, no. 1, p. 39, Jan. 1979.

[298] N. K. S. and S. S. and H. M. Ghule, "The role of the interfacial layer in Schottky barrier solar cells," *J. Phys. D. Appl. Phys.*, vol. 12, no. 5, p. 765, 1979.

[299] K. S. Novoselov, A. Mishchenko, A. Carvalho, and A. H. Castro Neto, "2D materials and van der Waals heterostructures," *Science (80-.).*, vol. 353, no. 6298, Jul. 2016.

[300] Y. Lin, X. Li, D. Xie, T. Feng, Y. Chen, R. Song, H. Tian, T. Ren, M. Zhong, K. Wang, and H. Zhu, "Graphene/semiconductor heterojunction solar cells with modulated antireflection and graphene work function," *Energy Environ. Sci.*, vol. 6, no. 1, pp. 108–115, 2013.

[301] L. Tao, Z. Chen, X. Li, K. Yan, and J.-B. Xu, "Hybrid graphene tunneling photoconductor with interface engineering towards fast photoresponse and high responsivity," *npj 2D Mater. Appl.*, vol. 1, no. 1, p. 19, 2017.

[302] X. Li, M. Zhu, M. Du, Z. Lv, L. Zhang, Y. Li, Y. Yang, T. Yang, X. Li, K. Wang, H. Zhu, and Y. Fang, "High Detectivity Graphene-Silicon Heterojunction Photodetector," *Small*, vol. 12, no. 5, pp. 595–601, Dec. 2015.

[303] X. Li, H. Zhu, K. Wang, A. Cao, J. Wei, C. Li, Y. Jia, Z. Li, X. Li, and

D. Wu, "Graphene-On-Silicon Schottky Junction Solar Cells," *Adv. Mater.*, vol. 22, no. 25, pp. 2743–2748, Jul. 2010.

[304] K. Ihm, J. T. Lim, K.-J. Lee, J. W. Kwon, T.-H. Kang, S. Chung, S. Bae, J. H. Kim, B. H. Hong, and G. Y. Yeom, "Number of graphene layers as a modulator of the open-circuit voltage of graphene-based solar cell," *Appl. Phys. Lett.*, vol. 97, no. 3, p. 32113, Jul. 2010.

[305] Y. Ye and L. Dai, "Graphene-based Schottky junction solar cells," *J. Mater. Chem.*, vol. 22, no. 46, pp. 24224–24229, 2012.

[306] X. An, F. Liu, and S. Kar, "Optimizing performance parameters of graphene–silicon and thin transparent graphite–silicon heterojunction solar cells," *Carbon N. Y.*, vol. 57, pp. 329–337, 2013.

[307] X. Yu, L. Yang, Q. Lv, M. Xu, H. Chen, and D. Yang, "The enhanced efficiency of graphene-silicon solar cells by electric field doping," *Nanoscale*, vol. 7, no. 16, pp. 7072–7077, 2015.

[308] E. Singh and H. S. Nalwa, "Graphene-Based Bulk-Heterojunction Solar Cells: A Review," *J. Nanosci. Nanotechnol.*, vol. 15, no. 9, pp. 6237–6278, 2015.

[309] Y. Song, X. Li, C. Mackin, X. Zhang, W. Fang, T. Palacios, H. Zhu, and J. Kong, "Role of Interfacial Oxide in High-Efficiency Graphene–Silicon Schottky Barrier Solar Cells," *Nano Lett.*, vol. 15, no. 3, pp. 2104–2110, Mar. 2015.

[310] X. Li, D. Xie, H. Park, T. H. Zeng, K. Wang, J. Wei, M. Zhong, D. Wu, J. Kong, and H. Zhu, "Anomalous Behaviors of Graphene Transparent Conductors in Graphene–Silicon Heterojunction Solar Cells," *Adv. Energy Mater.*, vol. 3, no. 8, pp. 1029–1034, Aug. 2013.

[311] Y. F. Li, W. Yang, Z. Q. Tu, Z. C. Liu, F. Yang, L. Q. Zhang, and R. Hatakeyama, "Schottky junction solar cells based on graphene with different numbers of layers," *Appl. Phys. Lett.*, vol. 104, no. 4, p. 43903, Jan. 2014.

[312] X. Miao, S. Tongay, M. K. Petterson, K. Berke, A. G. Rinzler, B. R. Appleton, and A. F. Hebard, "High Efficiency Graphene Solar Cells by Chemical Doping," *Nano Lett.*, vol. 12, no. 6, pp. 2745–2750, Jun. 2012.

[313] T. Cui, R. Lv, Z.-H. Huang, S. Chen, Z. Zhang, X. Gan, Y. Jia, X. Li, K. Wang, D. Wu, and F. Kang, "Enhanced efficiency of graphene/silicon heterojunction solar cells by molecular doping," *J. Mater. Chem. A*, vol. 1, no. 18, pp. 5736–5740, 2013.

[314] C. Xie, X. Zhang, K. Ruan, Z. Shao, S. S. Dhaliwal, L. Wang, Q. Zhang, X. Zhang, and J. Jie, "High-efficiency, air stable graphene/Si micro-hole array Schottky junction solar cells," *J. Mater. Chem. A*, vol. 1, no. 48, pp. 15348–15354, 2013.

[315] X. Zhang, C. Xie, J. Jie, X. Zhang, Y. Wu, and W. Zhang, "High-efficiency graphene/Si nanoarray Schottky junction solar cells via surface modification and graphene doping," *J. Mater. Chem. A*, vol. 1, no. 22, pp. 6593–6601, 2013.

[316] X. Li, D. Xie, H. Park, M. Zhu, T. H. Zeng, K. Wang, J. Wei, D. Wu, J. Kong, and H. Zhu, "Ion doping of graphene for high-efficiency heterojunction solar cells," *Nanoscale*, vol. 5, no. 5, pp. 1945–1948, 2013.

[317] E. Shi, H. Li, L. Yang, L. Zhang, Z. Li, P. Li, Y. Shang, S. Wu, X. Li, J. Wei, K. Wang, H. Zhu, D. Wu, Y. Fang, and A. Cao, "Colloidal Antireflection Coating Improves Graphene–Silicon Solar Cells," *Nano Lett.*, vol. 13, no. 4, pp. 1776–1781, Apr. 2013.

[318] T. Feng, D. Xie, Y. Lin, Y. Zang, T. Ren, R. Song, H. Zhao, H. Tian, X. Li, H. Zhu, and L. Liu, "Graphene based Schottky junction solar cells on patterned silicon-pillar-array substrate," *Appl. Phys. Lett.*, vol. 99, no. 23, p. 233505, Dec. 2011.

[319] D. Xu, X. Yu, L. Zuo, and D. Yang, "Interface engineering and efficiency improvement of monolayer graphene-silicon solar cells by inserting an ultra-thin LiF interlayer," *RSC Adv.*, vol. 5, no. 58, pp. 46480–46484, 2015.

[320] L. Yang, X. Yu, M. Xu, H. Chen, and D. Yang, "Interface engineering for efficient and stable chemical-doping-free graphene-on-silicon solar cells by introducing a graphene oxide interlayer," *J. Mater. Chem. A*, vol. 2, no. 40, pp. 16877–16883, 2014.

[321] Y. Tsuboi, F. Wang, D. Kozawa, K. Funahashi, S. Mouri, Y. Miyauchi,

T. Takenobu, and K. Matsuda, "Enhanced photovoltaic performances of graphene/Si solar cells by insertion of a MoS2 thin film," *Nanoscale*, vol. 7, no. 34, pp. 14476–14482, 2015.

[322] M. F. Bhopal, K. Akbar, M. A. Rehman, D. won Lee, A. ur Rehman, Y. Seo, S.-H. Chun, and S. H. Lee, "High-κ dielectric oxide as an interfacial layer with enhanced photo-generation for Gr/Si solar cells," *Carbon N. Y.*, vol. 125, pp. 56–62, 2017.

[323] A. Alnuaimi, I. Almansouri, I. Saadat, and A. Nayfeh, "High performance graphene-silicon Schottky junction solar cells with HfO2 interfacial layer grown by atomic layer deposition," *Sol. Energy*, vol. 164, pp. 174–179, 2018.

[324] S. Tongay, M. Lemaitre, X. Miao, B. Gila, B. R. Appleton, and A. F. Hebard, "Rectification at Graphene-Semiconductor Interfaces: Zero-Gap Semiconductor-Based Diodes," *Phys. Rev. X*, vol. 2, no. 1, p. 11002, Jan. 2012.

[325] G. Giovannetti, P. A. Khomyakov, G. Brocks, V. M. Karpan, J. van den Brink, and P. J. Kelly, "Doping Graphene with Metal Contacts," *Phys. Rev. Lett.*, vol. 101, no. 2, p. 026803, Jul. 2008.

[326] W. Jie, F. Zheng, and J. Hao, "Graphene/gallium arsenide-based Schottky junction solar cells," *Appl. Phys. Lett.*, vol. 103, no. 23, p. 233111, Dec. 2013.

[327] X. Li, W. Chen, S. Zhang, Z. Wu, P. Wang, Z. Xu, H. Chen, W. Yin, H. Zhong, and S. Lin, "18.5% efficient graphene/GaAs van der Waals heterostructure solar cell," *Nano Energy*, vol. 16, pp. 310–319, 2015.

[328] X. Li, S. Lin, X. Lin, Z. Xu, P. Wang, S. Zhang, H. Zhong, W. Xu, Z. Wu, and W. Fang, "Graphene/h-BN/GaAs sandwich diode as solar cell and photodetector," *Opt. Express*, vol. 24, no. 1, pp. 134–145, 2016.

[329] H. He, X. Yu, Y. Wu, X. Mu, H. Zhu, S. Yuan, and D. Yang, "13.7% Efficiency graphene-gallium arsenide Schottky junction solar cells with a P3HT hole transport layer," *Nano Energy*, vol. 16, pp. 91–98, 2015.

[330] P. Wang, X. Li, Z. Xu, Z. Wu, S. Zhang, W. Xu, H. Zhong, H. Chen, E. Li, J. Luo, Q. Yu, and S. Lin, "Tunable graphene/indium phosphide heterostructure solar cells," *Nano Energy*, vol. 13, pp. 509–517, 2015.

[331] S. Lin, X. Li, S. Zhang, P. Wang, Z. Xu, H. Zhong, Z. Wu, and H. Chen, "Graphene/CdTe heterostructure solar cell and its enhancement with photo-induced doping," *Appl. Phys. Lett.*, vol. 107, no. 19, p. 191106, Nov. 2015.

[332] N. E. Gorji, "Degradation of ultrathin CdTe films with SWCNT or Graphene back contact," *Phys. E Low-Dimensional Syst. Nanostructures*, vol. 70, pp. 84–89, 2015.

[333] J. Liang, H. Bi, D. Wan, and F. Huang, "Novel Cu Nanowires/Graphene as the Back Contact for CdTe Solar Cells," *Adv. Funct. Mater.*, vol. 22, no. 6, pp. 1267–1271, Mar. 2012.

[334] H. Bi, F. Huang, J. Liang, X. Xie, and M. Jiang, "Transparent Conductive Graphene Films Synthesized by Ambient Pressure Chemical Vapor Deposition Used as the Front Electrode of CdTe Solar Cells," *Adv. Mater.*, vol. 23, no. 28, pp. 3202–3206, May 2011.

[335] M. A. Rehman, I. Akhtar, W. Choi, K. Akbar, A. Farooq, S. Hussain, M. A. Shehzad, S.-H. Chun, J. Jung, and Y. Seo, "Influence of an Al2O3 interlayer in a directly grown graphene-silicon Schottky junction solar cell," *Carbon N. Y.*, vol. 132, pp. 157–164, 2018.

[336] J. Ma, H. Bai, W. Zhao, Y. Yuan, and K. Zhang, "High efficiency graphene/MoS2/Si Schottky barrier solar cells using layer-controlled MoS2 films," *Sol. Energy*, vol. 160, pp. 76–84, 2018.

[337] J.-H. Meng, X. Liu, X.-W. Zhang, Y. Zhang, H.-L. Wang, Z.-G. Yin, Y.-Z. Zhang, H. Liu, J.-B. You, and H. Yan, "Interface engineering for highly efficient graphene-on-silicon Schottky junction solar cells by introducing a hexagonal boron nitride interlayer," *Nano Energy*, vol. 28, pp. 44–50, Aug. 2016.

[338] L. Lancellotti, L. Sansone, E. Bobeico, E. Lago, M. D. Noce, P. D. Veneri, A. Borriello, M. Casalino, G. Coppola, M. Giordano, and M. Iodice, "Graphene oxide as an interfacial layer in silicon based Schottky barrier solar cells," in *2015 Fotonica AEIT Italian Conference on Photonics Technologies*, 2015, pp. 1–4.

[339] N. Balis, E. Stratakis, and E. Kymakis, "Graphene and transition metal dichalcogenide nanosheets as charge transport layers for solution

processed solar cells," *Mater. Today*, vol. 19, no. 10, pp. 580–594, 2016.

[340] E. Kymakis, M. M. Stylianakis, G. D. Spyropoulos, E. Stratakis, E. Koudoumas, and C. Fotakis, "Spin coated carbon nanotubes as the hole transport layer in organic photovoltaics," *Sol. Energy Mater. Sol. Cells*, vol. 96, pp. 298–301, 2012.

[341] A. Capasso, L. Salamandra, A. Di Carlo, J. M. Bell, and N. Motta, "Low-temperature synthesis of carbon nanotubes on indium tin oxide electrodes for organic solar cells," *Beilstein J. Nanotechnol.*, vol. 3, pp. 524–532, Jul. 2012.

[342] A. Capasso, L. Salamandra, A. Chou, A. Di Carlo, and N. Motta, "Multi-wall carbon nanotube coating of fluorine-doped tin oxide as an electrode surface modifier for polymer solar cells," *Sol. Energy Mater. Sol. Cells*, vol. 122, pp. 297–302, 2014.

[343] A. Capasso, F. Matteocci, N. Leyla, M. Prato, J. Buha, L. Cinà, V. Pellegrini, A. Di Carlo, and F. Bonaccorso, "Solar Cells: Few-Layer MoS2 Flakes as Active Buffer Layer for Stable Perovskite Solar Cells (Adv. Energy Mater. 16/2016)," *Adv. Energy Mater.*, vol. 6, no. 16, p. 1600920, Aug. 2016.

[344] Q. Van Le, J.-Y. Choi, and S. Y. Kim, "Recent advances in the application of two-dimensional materials as charge transport layers in organic and perovskite solar cells," *FlatChem*, vol. 2, pp. 54–66, 2017.

[345] J. Bouclé and N. Herlin-Boime, "The benefits of graphene for hybrid perovskite solar cells," *Synth. Met.*, vol. 222, pp. 3–16, 2016.

[346] J. O. Sofo, A. S. Chaudhari, and G. D. Barber, "Graphane: A two-dimensional hydrocarbon," *Phys. Rev. B*, vol. 75, no. 15, p. 153401, Apr. 2007.

[347] F. Buonocore, A. Capasso, and N. Lisi, "An ab initio study of hydroxylated graphane," *J. Chem. Phys.*, vol. 147, no. 10, p. 104705, Sep. 2017.

[348] F. Buonocore, A. Capasso, and N. Lisi, "Interface of graphane with copper: a van der Waals density-functional study," *Mater. Res. Express*, vol. 1, no. 1, p. 15608, 2014.

[349] Q. Etienne, F. Roux, F. Emieux, P. Faucherand, E. Kymakis, G.

Volonakis, F. Giustino, B. Martín-García, I. Moreels, S. A. Gürsel, A. B. Yurtcan, V. Di Noto, A. Talyzin, I. Baburin, D. Tranca, G. Seifert, L. Crema, G. Speranza, V. Tozzini, P. Bondavalli, G. Pognon, C. Botas, D. Carriazo, G. Singh, T. Rojo, G. Kim, W. Yu, C. P. Grey, and V. Pellegrini, "Graphene-based technologies for energy applications, challenges and perspectives," *2D Mater.*, vol. 2, no. 3, p. 30204, 2015.

[350] A. Gnisci, G. Faggio, G. Messina, L. Lancellotti, E. Bobeico, P. D. Veneri, A. Capasso, T. Dikonimos, and N. Lisi, "Graphene-based derivative as interfacial layer in graphene / n-Si Schottky barrier solar cells," *Adv. Model. Anal. A*, vol. 55, no. 3, pp. 144–150, 2018.

[351] A. Gnisci, G. Faggio, L. Lancellotti, G. Messina, R. Carotenuto, E. Bobeico, P. Delli Veneri, A. Capasso, T. Dikonimos, and N. Lisi, "The Role of Graphene-Based Derivative as Interfacial Layer in Graphene/n-Si Schottky Barrier Solar Cells," *Phys. status solidi*, vol. 0, no. 0, p. 1800555, Dec. 2018.

[352] T. Polichetti, F. Ricciardella, F. Fedi, M. L. Miglietta, R. Miscioscia, E. Massera, S. De Vito, G. Di Francia, M. A. Nigro, G. Faggio, A. Malara, and G. Messina, "Graphene-based Schottky Device Detecting NH3 at ppm level in Environmental Conditions," *Procedia Eng.*, vol. 87, pp. 232–235, 2014.

[353] T. Polichetti, F. Ricciardella, F. Fedi, M. L. Miglietta, R. Miscioscia, E. Massera, G. Di Francia, M. A. Nigro, G. Faggio, A. Malara, and G. Messina, "Graphene-Si Schottky diode in environmental conditions at low NH<inf>3</inf> ppm level," in *2014 IEEE 9th Nanotechnology Materials and Devices Conference (NMDC)*, 2014, pp. 23–26.

[354] C. S. Solanki, *Solar Photovoltaics; Fundamentals, Technologies and Applications*. 2012.

[355] C. Lu and O. Lewis, "Investigation of film-thickness determination by oscillating quartz resonators with large mass load," *J. Appl. Phys.*, vol. 43, no. 11, pp. 4385–4390, Nov. 1972.

[356] A. C. Ferrari, "Raman spectroscopy of graphene and graphite: Disorder, electron–phonon coupling, doping and nonadiabatic effects," *Solid State Commun.*, vol. 143, no. 1, pp. 47–57, 2007.

[357] M. Seifert, J. E. B. Vargas, M. Bobinger, M. Sachsenhauser, A. W. Cummings, S. Roche, and J. A. Garrido, “Role of grain boundaries in tailoring electronic properties of polycrystalline graphene by chemical functionalization,” *2D Mater.*, vol. 2, no. 2, p. 24008, 2015.

[358] Y. Wang, X. Xu, J. Lu, M. Lin, Q. Bao, B. Özyilmaz, and K. P. Loh, “Toward High Throughput Interconvertible Graphane-to-Graphene Growth and Patterning,” *ACS Nano*, vol. 4, no. 10, pp. 6146–6152, Oct. 2010.

[359] O. L. and B. P. and F. M. P. and A. V. and C. Van Haesendonck, “The work function of few-layer graphene,” *J. Phys. Condens. Matter*, vol. 29, no. 3, p. 35003, 2017.

[360] M. Wang, E. H. Yang, R. Vajtai, J. Kono, and P. M. Ajayan, “Effects of etchants in the transfer of chemical vapor deposited graphene,” *J. Appl. Phys.*, vol. 123, no. 19, p. 195103, May 2018.

[361] W. N. Hansen and G. J. Hansen, “Standard reference surfaces for work function measurements in air,” *Surf. Sci.*, vol. 481, no. 1–3, pp. 172–184, 2001.

[362] R. C. Weast, 1928- Lide David R., and U. of Rhode Island. Coastal Resources Center, “CRC handbook of chemistry and physics,” 1978.

[363] A. Di Bartolomeo, G. Luongo, F. Giubileo, N. Funicello, G. Niu, T. Schroeder, M. Lisker, and G. Lupina, “Hybrid graphene/silicon Schottky photodiode with intrinsic gating effect,” *2D Mater.*, vol. 4, no. 2, p. 25075, 2017.

[364] L. Lancellotti, E. Bobeico, A. Capasso, M. Della Noce, T. Dikonimos, N. Lisi, and P. D. Veneri, “Effects of HNO3 molecular doping in graphene/Si Schottky barrier solar cells,” in *2014 Fotonica AEIT Italian Conference on Photonics Technologies*, 2014, pp. 1–3.

[365] L. Lancellotti, E. Bobeico, A. Castaldo, P. Delli Veneri, E. Lago, and N. Lisi, “Effects of different graphene dopants on double antireflection coatings/graphene/n-silicon heterojunction solar cells,” *Thin Solid Films*, vol. 646, pp. 21–27, 2018.

[366] J. E. Lee, G. Ahn, J. Shim, Y. S. Lee, and S. Ryu, “Optical separation of mechanical strain from charge doping in graphene,” *Nat. Commun.*,

vol. 3, p. 1024, Aug. 2012.

[367] T. G. A. Verhagen, K. Drogowska, M. Kalbac, and J. Vejpravova, "Temperature-induced strain and doping in monolayer and bilayer isotopically labeled graphene," *Phys. Rev. B*, vol. 92, no. 12, p. 125437, Sep. 2015.

[368] E. Singh and H. S. Nalwa, "Stability of graphene-based heterojunction solar cells," *RSC Adv.*, vol. 5, no. 90, pp. 73575–73600, 2015.

List of Publications

1. Gnisci, A.; Faggio, G.; Messina, G.; Kwon, J.; Lee, J.-Y.; Lee, G.-H.; Dikonimos, T.; Lisi, N.; Capasso, A. Ethanol-CVD Growth of Sub-Mm Single-Crystal Graphene on Flat Cu Surfaces. J. Phys. Chem. C 2018, 122 (50), 28830–28838. https://doi.org/10.1021/acs.jpcc.8b10094.
2. Gnisci, A.; Faggio, G.; Lancellotti, L.; Messina, G.; Carotenuto, R.; Bobeico, E.; Delli Veneri, P.; Capasso, A.; Dikonimos, T.; Lisi, N. The Role of Graphene-Based Derivative as Interfacial Layer in Graphene/n-Si Schottky Barrier Solar Cells. Phys. status solidi 2018, 0 (0), 1800555. https://doi.org/10.1002/pssa.201800555.
3. Faggio, G.; Gnisci, A.; Messina, G.; Lisi, N.; Capasso, A.; Lee, G. H.; Armano, A.; Sciortino, A.; Messina, F.; Cannas, M.; et al. Carbon Dots Dispersed on Graphene/SiO 2 /Si: A Morphological Study. Phys. status solidi 2019, 1800559. https://doi.org/10.1002/pssa.201800559.
4. Gnisci, A.; Faggio, G.; Messina, G.; Lancellotti, L.; Bobeico, E.; Veneri, P. D.; Capasso, A.; Dikonimos, T.; Lisi, N. Graphene-Based Derivative as Interfacial Layer in Graphene / n-Si Schottky Barrier Solar Cells. Adv. Model. Anal. A 2018, 55 (3), 144–150. https://doi.org/10.18280/ama_a.550307.
5. Loise, V.; Vuono, D.; Policicchio, A.; Teltayev, B.; Gnisci, A.; Messina, G.; Oliviero Rossi, C. The Effect of Multiwalled Carbon Nanotubes on the Rheological Behaviour of Bitumen. Colloids Surfaces A Physicochem. Eng. Asp. 2019, 566, 113–119. https://doi.org/10.1016/j.colsurfa.2019.01.021.
6. Capasso, A., Buonocore, F., Faggio, G., Gnisci, A., Messina, G., Kim, M. J., Lee, G. H., Placidi, E., Dikonimos, T., Lisi, N. Thermodynamically stable hydrogenated graphene grown by chemical vapor deposition of ethanol, SUBMITTED
7. Caridi, F., Santangelo, S., Faggio, G., Gnisci, A., Messina, G., Marcianò, G., Belmusto, G., Compositional and mineralogical analysis of marine sediments from Calabrian selected areas, southern Italy, *The European Physical Journal Plus*, 2018, SUBMITTED

Acknowledgments

I am deeply grateful to my supervisor… mmm no, too direct…. *Firstly, I would like to express my deepest appreciation to…* ehi ehi ehi! Ok, but too formal!!! *I would like to thank my adviser…* "I would like"?? This is my thesis! I can do what I want, finally! …retry… *My interest in technological innovations started at a young age when my father…*no no no too long in time, we have not so much time!! Go to the focal point! Just one last attempt… *There are many people who contributed to my personal and professional development during my PhD study and undoubtedly, all of them deserve my acknowledgments….* It sounds very good, but there is something that goes bad…mmm…I found it!!! È l'accento che non va! Forse queste ultime righe andrebbero scritte e lette con la mia lingua, i miei accenti, le mie cadenZe, cosicché risultino più familiari e chiare a tutti…rompendo gli schemi ancora una volta e senza perdere l'irriverenza che ha segnato questo percorso. Sono tante le persone che in un modo o nell'altro mi hanno accompagnato in questi 3 anni e meritano un pensiero e di rimanere ricordate tra queste pagine. Prima di tutto un grazie speciale alla Prof.ssa Faggio (Giuliana!) e al Prof. Messina, per avermi accolto nel loro gruppo di ricerca e nel loro laboratorio, avermi coinvolto nella loro ricerca e trasferito parte delle loro conoscenze. Grazie per gli stimoli, i confronti e l'autonomia che mi hanno dato, per avermi dato la possibilità di mettermi alla prova e confrontarmi con ricercatori di rilevanza nazionale e internazionale. Grazie a Giuliana, punto di riferimento in una città non mia. Grazie per i confronti (a volte anche accesi), per la stima, per avermi sempre coinvolto nelle attività più disparate e avermi fatto vivere l'Università a 360°, nella sua completezza, per le discussioni in lingua napoletana o con qualsiasi altro accento italiano. Grazie al Dott. Nicola Lisi e al team dell'ENEA Casaccia, per la splendida esperienza trascorsa presso i suoi laboratori, per le quasi giornaliere discussioni scientifiche, per le spiegazioni e le interpretazioni fisiche dei dati. Grazie al Dott. Ing. Andrea Capasso, per le idee e la costanza scientifica, per la fiducia e per avermi spronato a migliorare ogni giorno un po' di più. Grazie alla Dott.ssa Laura Lancellotti e al team dell'ENEA di Portici, per la sua simpatia partenopea e la sua professionalità. La risposta alla sua

domanda forse era semplicemente "Qui, ai piedi del Vesuvio". Grazie all'Ing. Malara e all'Ing. Pangallo, i primi dottorandi che ho incontrato nel mio percorso all'Università Mediterranea. Grazie per avermi accompagnato nel muovere i primi passi in un'università piccola ma piena di contraddizioni. In particolare grazie alla Dott. Ing. Malara, al tempo stesso mia dottoranda e mia tutor, nonché guida che mi ha trasferito le sue competenze tecniche e mostrato i trucchi per districarmi nei meandri del DIIES. Dal primo giorno mi ha preso sotto la sua ala e mi ha guidato senza lasciarmi mai. Memoria storica del laboratorio e instancabile ricercatrice, ha sempre avuto la risposta giusta a qualsiasi domanda, soprattutto se iniziava con la formula "Angela, ricordi per caso….?". Grazie alla mia famiglia, che mi ha sempre supportato e che troppe volte non ho ascoltato, paradossalmente neanche quando mi dicevano di ascoltare solo me stesso. Grazie a mamma Valeria e papà Carlo. Se mi limitassi alla pura osservazione, potrei dire che questi ultimi anni li hanno vissuti affacciati ad un terrazzo: erano lì a salutarmi ogni volta che partivo, ed erano lì ad accogliermi ogni volta che tornavo….grazie! Grazie a mia sorella Emanuela che mi ha spronato a lasciare qualche volta da parte la razionalità per seguire il cuore. Grazie ad Angela, Fabiola, Roberta ed Emilia, le mie amiche e colleghe della pausa pranzo e non solo. Grazie per ogni panino, ogni caffè, ogni pausa, ogni passeggiata, ogni sfogo, ogni brindisi. Per rubare una citazione, "grazie per essere state la mia famiglia rrrreggina", per esserci state sempre e soprattutto nei momenti più importanti. Meritereste un grazie particolare ciascuno, e visto che ci siamo, perché no? Grazie ad Angela per la calma e la pazienza, per la serenità con cui mi ha aiutato a superare i momenti di *susta* (susta = fastidio), per quei minuti alla fine di una lunga giornata necessari per riordinare i pensieri e riallinearsi al mondo. Per ogni pausa caffè presa, per ogni fotocopia fatta, per ogni volta che qualcosa non è andata come doveva ma che poi ha ritrovato la giusta direzione. Grazie a Roberta, la più furba, il cui sguardo deciso e la sicurezza sono stati di aiuto difronte alle scelte importanti. Risolutiva in ogni circostanza. Grazie ad Emilia, la piccola del gruppo, per la spensieratezza e lo scialla. Grazie a Fabiola per i momenti di svago e le grasse risate, oltre per avermi avviato verso la conoscenza dei dolci veramente buoni. Grazie ad Enza per quel pizzico di follia, per la sua integrità morale e per le vicende della sua

“caserma” (anche se alla fine lo *sfincione* non lo abbiamo assaggiato!). Grazie a Giada, dapprima solo un nome su una tesi, poi una folta chioma che non permette di vedere la lavagna a lezione e infine una degna compagna di pranzo che non si tira mai indietro. Grazie a tutto il gruppo di chimica che ha avuto sempre la pazienza di vedermi passeggiare per i laboratori. Grazie a Francesco, testardo nel voler creare un gruppo di giovani dottorandi e ricercatori, testimone della nascita di quel gruppo che facilmente ha affiancato all’amore per la ricerca la passione per il cibo e non solo. Grazie alla Dott.ssa Frontera, al prof. Donato e al prof Bonaccorsi per la stima riposta e mostrata nei miei confronti. Grazie ai miei tesisti Caterina e Danilo, un’esperienza davvero incredibile. Ho rivisto nei loro occhi la mia passione per la ricerca e la scoperta (nonostante fossero degli ingegneri). Grazie ai “miei studenti” tutti, e alle loro improbabili risposte agli esami, avevo paura di loro prima di ogni esercitazione, non ne potevo fare a meno quando avevo finito. Grazie alle mie giovanissime studentesse Federica e Giovanna, e ai pomeriggi infiniti per cercare di recuperare i brutti voti in matematica e fisica. Mentre loro recuperavano nozioni scolastiche io provavo a recuperare il tempo perso. Grazie a tutti i ragazzi che mi hanno regalato un ricordo piacevole in questo percorso, Antonio, Sofia, Umberto, Lavinia. Grazie ai miei colleghi di avventura, i miei colleghi di ciclo con cui ho condiviso incertezze, dubbi e paure, grazie a Giuseppe per le lunghissime chiacchierate, a Filippo, Rosario e Pasquale (anche se ci siamo visti in tutto 4 volte in 3 anni). Grazie ai ragazzi del bar, Giovanna, Paolo, Angelica e Jessica, al loro caffè, con o senza crema caffè, con o senza nutella, alla loro chiacchiera, a quei momenti di svago tra una misura e l’altra. Vorrei dedicare un ultimo grazie ad Angi. Chiamata in causa già più volte in questi ringraziamenti con nomi diversi, perché meritava un grazie abbastanza complesso e sotto tanti aspetti. Da semplice dottoranda ed amica a compagna. Grazie per ogni cosa, per la pace, la serenità e la forza che mi hai dato, per ogni risata e ogni consiglio, per ogni momento di sfogo, per i consigli scientifici, per ogni momento trascorso, per aver sempre creduto in me, per non avermi allontanato quando sembravo un fastidioso dottorando che ti seguiva ovunque, fino ad avermi dato la possibilità di guardare il mondo riflesso nei tuoi occhi verdi… Grazie di cuore, per quello che hai fatto in questi 3 anni e per quello

che stai continuando a fare, nonostante la mia tendenza a prendere sempre la strada più complicata.

E infine il mio grazie più grande lo riservo a chi non c'è più. Stavolta sono sicuro che non leggerai queste mie pagine, non mi dirai magari che il mio inglese è contorto e al più sbagliato. Ma c'eri quando ho messo piede il primo giorno a Reggio, c'eri ogni mattina, ogni sera e ogni momento. Mi hai guidato in ogni scelta e nel tuo pensiero mi sono ricordato di non perdermi mai. Spero di essere stato all'altezza almeno in parte di quello che mi hai lasciato. Grazie Daniela, tutto questo non è solo mio, ma è anche e soprattutto tuo…. Grazie….

… e niente, quindi questo…GraZie a tutti,

Andrea